A Search for Supernova Relic Neutrinos

A Dissertation Presented

by

Matthew Samir Malek

to

The Graduate School

in Partial Fulfillment of the Requirements

for the Degree of

Doctor of Philosophy

in

Physics and Astronomy

State University of New York
at
Stony Brook

August 2003

State University of New York
at Stony Brook

The Graduate School

Matthew Samir Malek

We, the dissertation committee for the above candidate for the Doctor of Philosophy degree, hereby recommend acceptance of the dissertation.

Dr. Chang Kee Jung
Advisor
Professor of Physics

Dr. Paul Grannis
Professor of Physics

Dr. James Lattimer
Professor of Astronomy

Dr. John Beacom
Physicist, Fermi National Accelerator Laboratory

This dissertation is accepted by the Graduate School.

Dean of the Graduate School

Abstract of the Dissertation
A Search for Supernova Relic Neutrinos

by

Matthew Samir Malek

Doctor of Philosophy

in

Physics and Astronomy

State University of New York at Stony Brook

2003

A search for the relic neutrinos from all past core-collapse supernovae was conducted using 1496 days of data from the Super-Kamiokande-I detector. This analysis searched for electron-type anti-neutrino interactions that produce a positron with an energy greater than 18 MeV. No appreciable signal for such interactions was found. In the absence of a signal, 90% C.L. upper bounds on the total flux were set for several theoretical models; the limits ranged from 20 to 130 $\bar{\nu}_e$ cm^{-2} s^{-1}. These results are a factor of 40 times better than the best limits set in previous experiments, and they can eliminate certain models. Additionally, a model-insensitive upper bound of 1.2 $\bar{\nu}_e$ cm^{-2} s^{-1} was obtained for the supernova relic neutrino flux in the energy region $E_\nu > 19.3$ MeV. This limit is two orders of magnitude more stringent than the best previous limit.

Dedicated to my sweet Lisa
who stood by me
who believed in me
and who waited for me to come home.

Contents

List of Figures

List of Tables

Acknowledgements

At the time of this writing, I have spent approximately one quarter of my life in graduate school. Thus, it is not surprising that I should owe a debt of gratitude to many people that I have known, both personally and professionally. Without their support and assistance, this thesis could never have reached completion. Although mere recognition does not sufficiently convey the extent of my gratitude, I will try not to be stingy in expressing my appreciation here.

First, I thank my advisor, Chang Kee Jung. He recruited me into the Stony Brook neutrino group after my second year in graduate school, while I was wondering how to choose between particle physics and astronomy. I had little idea that astro-particle physics existed, much less that it was quickly becoming an exciting area of study. I could not have asked for a more interesting thesis experiment than Super-Kamiokande, and without Chang Kee, I would never have been a part of it. During the five years that I have been his student, I have come to have great respect for Chang Kee's style of advising. He does not micro-manage his students, but neither does he abandon them in Japan to fend for themselves. Besides his concern for my development as a physicist, Chang Kee has also been interested in my well-being as a person. Several unusual crises occurred in my life while I was a graduate student, and Chang Kee was understanding as I dealt with them. Finally, I will be the first to admit that there were times when I was not quite the ideal graduate student. Chang Kee was patient with me during those times and offered guidance, from which I was able to learn. In short, I do not think that I could have asked for a better advisor.

Next, I would like to thank Kai Martens, who was a post-doc with our group when I joined. I mentioned that Chang Kee does not send new students to Japan without resources; Kai was my initial guide at Super-Kamiokande. As the only other member of the Stony Brook group who studied stellar neutrinos, it was Kai's job to orient me when I first landed in Japan. However, Kai did much more than what was required of him, and he became something like an older brother to me. Besides teaching me physics and FORTRAN, he taught

me about how to live and work in Japan. Most importantly, Kai was often the only person in Japan that I could depend upon during the stresses that accompanied my first year on the experiment.

Along with Chang Kee and Kai, no one has taught me more about neutrino physics than Masayuki Nakahata. When I joined the collaboration, Nakahata-sensei was the head of the general calibration group and the LINAC group. Soon afterwards, he also became responsible for the water purification and radon reduction groups. Late in my Super-K years, his duties expanded further and he became the convener of the low energy analysis group (i.e. the people who study stellar neutrinos). I have often wondered if there is anything about Super-Kamiokande that Nakahata-sensei does not know. Equally often, I have been amazed that a man with so many responsibilities can take time out to explain both physics and the detector in detail to a new graduate student.

Special acknowledgements are due to Lisa Makros, my beloved partner, and to Pam Williams, my best friend. Besides their personal support, which I will thank them for below, these two women devoted a considerable amount of time to editing the language of this thesis. Both Lisa and Pam have worked as professional editors, so their comments and suggestions have proven invaluable in making this dissertation coherent. Additionally, Lisa's many humorous comments made the tedious process of revision somewhat bearable.

Although Lisa and Pam are masters of the English language, they are not physicists. They could check the form of my thesis, but not the content. Thus, I must thank Chiaki Yanagisawa and Kenkou Kobayashi for performing this task. Chiaki is a senior research scientist at Stony Brook, and I have known him ever since I joined Chang Kee's group. Kenkou was a Japanese graduate student that I knew only peripherally until he came to Stony Brook as a post-doc in 2002. They both read through my draft and made valuable suggestions that were incorporated before this thesis was sent to my dissertation committee.

On the topic of my dissertation committee, I must say that I have been quite lucky to have Paul Grannis, Jim Lattimer, and John Beacom as committee members. I feel that this combination of experts in both astronomy and particle physics was perfect for reviewing a thesis that exists at the point of intersection between these two fields. In particular, I would like to express deep gratitude to John Beacom who, as my external committee member, had to make a somewhat contorted travel arrangement in order to attend my thesis defense.

Nearly all physics experiments are a collaborative effort; this is especially true in particle physics. Super-Kamiokande is a successful experiment through the efforts of many people. Most helpful to me were the other members of the

low energy analysis group. In particular, I would like to thank Yasuo Takeuchi, Yoshiyuki Fukuda, and Yusuke Koshio for being the backbone of this group. On the "American" side of the collaboration, I have benefited greatly from discussions with Michael Smy and Gene Guillian. My exchanges with Hirokazu Ishino have been infrequent, but also invaluable, especially during the early stages of my analysis. Similarly, my occasional contacts with Bob Svoboda and Steve Dazely have always been fruitful.

Traditionally, the Super-Kamiokande collaboration has had separate analysis groups for studying high and low energy neutrinos. Although I have worked with the low energy group, the supernova relic neutrino search was conducted in a middle energy range; therefore, it was sometimes necessary to learn about the high energy analysis. Most of what I needed to learn about the high energy tools was shown to me by Kate Scholberg, for which I thank her. Discussions with Alec Habig also aided the progress of my thesis.

An old cliche says that a team is only as strong as its leader. Although I do not think that this is generally true, I can certainly say that the SK low energy group benefited from the capable leadership provided by Yoichiro Suzuki. For most of my time on Super-Kamiokande, Suzuki-sensei was the low energy convener, and he guided the group with insight and clear vision. I have the utmost respect for him, and I was pleased to see that he was promoted to spokesperson of the entire experiment in 2002. Another leader worth mentioning is our former spokesperson, Yoji Totsuka, who presided over the experiment during its most difficult times. The destruction of Super-Kamiokande in November 2001 was devastating to the entire collaboration, and I am thankful that Totsuka-sensei was able to ensure that SK would be rebuilt and fully restored.

Japan is a beautiful country, and I am lucky to have spent over two years living there. Nevertheless, I often missed my friends and my community on the other side of the Pacific Ocean. Fortunately, there have been many fine graduate students in the SK collaboration, and they have made my time in Kamioka more enjoyable. Thus, I must thank Dean Takemori, Erik Blaufuss, and Nobuyuki Sakurai, whom I viewed as my "upper classmen." They showed me how to have fun in Japan. I must also thank Shantanu Desai, Dawei Liu, Dusan Turcan, Yoshihito Gando, Chikaori Mitsuda, and Jonghee Yoo; they all joined SK shortly after I arrived, and we have had some good times together. I must not forget to mention Andrew Clough, Kristine Washburn, and John Parker Cravens, all of whom are relatively recent arrivals; I have already enjoyed their company greatly and I regret that I will not have more time to spend with them.

My final thanks on the Eastern side of the Pacific go to Hans Berns,

who was always exceptional company; and to the US group secretaries: Yoko Koshizawa, Mihoko Okinaka, and Kiyoko Hirose. The efforts of these three women have been vital to the entire US group working in Japan.

Back at Stony Brook, there are many deserving of my thanks and recognition. Besides those already mentioned, I am grateful to the other members of the Stony Brook Neutrino and Nucleon Decay (NN) group. Jim Hill and Clark McGrew were both post-docs when I joined the group. Although they have now assumed professorships, their advice and company were welcomed and appreciated.

Brett Viren was the first graduate student in the Stony Brook NN group. He graduated soon after I joined the group, and so we did not get to spend as much time together as I would have liked. Besides providing stimulating late night discussions in our apartment, fellow graduate student Christopher Mauger was our resident expert on all things Japanese; based on his advice, I planned a highly successful tour of Japan in 2001. Eric Sharkey did his graduate work at KEK, so he and I rarely crossed paths. Nonetheless, the times that we did meet were pleasant, and Eric did me the favor of covering my detector shifts in February 2000, when a family emergency required my immediate departure from Japan.

People who joined the NN group after me include the German exchange student Markus Ackermann, with whom I formed a valuable and enduring friendship, as well as PhD students Fumi Kato and Dan Kerr. In 2002, Antony Sarrat joined our group as a new post-doc and he has been a fine companion.

Outside of Chang Kee's NN group many of the other Stony Brook graduate students contributed significantly towards efforts to keep me sane – especially during my first year at Stony Brook. My old officemate, Jay Dickerson, deserves special recognition here, as does our next-door neighbor, Dan Kaplan. Likewise, Kunegunda Belle (in Astronomy) and Jenny Routh (in Chemistry) were fast friends who were reliable for help with work *or* for help getting away from work. Sergey Pflyuk, my partner-in-crime for the infamous grad lab class, must also be thanked; many late nights did we suffer together. Without a doubt, the most important graduate student to thank is Satish Desai, who has been both a colleague and a dear friend; indeed, he is practically family. Satish has been present throughout some of the happiest times in my life, and he has been very supportive during several of the crises. I wish him well with the completion of his own thesis, and I look forward to many more years of his company.

At Stony Brook, I have been taught by many excellent professors. However, none are as noteworthy as Peter Kahn. Peter looked out for the struggling first-year grad students, and taught us physics and how to survive the year

intact. Having attended a highly non-traditional undergraduate institution, Hampshire College, I had quite a difficult time re-adapting to traditional education. Peter's extra classes for us first-years felt much more like what I had grown accustomed to at Hampshire, which made the transition infinitely more tolerable.

It is not possible to overestimate the importance of the Stony Brook administrative staff. In the main physics office, Diane Siegel was helpful on many important occasions. It is no exaggeration to say that Pat Peiliker has been a mother to all of us physics graduate students, and for that I will be forever grateful. The high energy group could not function without the help of Alice Dugan and Joan Napolitano, for which I now applaud them.

Contrary to what some may believe, physicists are human, too. Thus, there are a number of personal relations that deserve recognition here. Although they may not have contributed directly to my thesis, their efforts were still vital to the completion of this work.

First and foremost, I must thank my life-partner, Lisa Makros. Whatever I could say about her here, it could not possibly be enough. Lisa and I have been partnered for my entire adult life, and she has supported me through the best and the worst of times. I doubt that I would have even considered spending six months in Japan each year if she had not been receptive to the idea – and willing to stay behind to keep our household running smoothly in my absence.

Pam Williams is my best friend. Besides editing this thesis, she gets credit for keeping me together when my worlds seemed to be flying apart at the seams. She is a unique and wonderful person who just deserves lots of general thanks and my heartfelt gratitude.

I wish to acknowledge my mother, Beth, for raising me and for putting me through college despite a time of hardship. Without her efforts, I have no idea where I would be today. I am certain that it would be someplace quite different. I would also like to thank my father, Samir, for the financial support that he provided during my years as a graduate student. My Uncle Magdi is a chemist and he has always expressed interest in my work; I have enjoyed talking with his as one scientist to another. And I should thank my younger brother, Eric, for being my brother.

In 2001, Lisa moved to Arizona and I followed her. Since I was still enrolled at Stony Brook, this move made life interesting. Due to the efforts of Susan Crane and her housemates, Bethany and Steve Ehrlich, life was thankfully made a little *less* interesting: These three often welcomed me into their home and provided me with a bed to sleep in when I was spending time at Stony Brook. One cannot properly emphasize the value of having access to a warm

bed and a shower.

Although they did not play a strong role in my graduate career, I should acknowledge the educators and mentors who played a significant role in my pre-Stony Brook life. Herb Bernstein of Hampshire College is the man who made me decide to pursue a career in physics. Besides being my teacher, he was my advisor, my employer, and a second father to me. The late Sandra Stone was my high school biology teacher, and the first person to have faith in my potential as a scientist. I deeply regret that she did not live to see me obtain my doctorate. My interest in science was encouraged from a young age by Anthony Stark, who has been an older friend of mine since childhood. Other educators who have helped me reach my PhD have been Peter Taubman and Louise Forsythe, both of whom taught me when I was in high school. Although neither of them are scientists, their guidance and advice have stayed with me to this day.

Other friends worth mentioning are Jon Wolfe, without whom I may have gone insane long ago; Jim Carlson; Craig Counterman, and Reynard Roxbury. They have supported me during life in general, and specifically during the writing of this dissertation. And I am always thankful for my six cats. When the process of writing this thesis was slowly driving me mad, I knew that my adorable kitties would always be eager to provide a welcome distraction. Needless to say, this was a mutually beneficial arrangement.

Finally, my last acknowledgement is for William Wattenberg, my maternal grandfather who died when I was only halfway through my time as a graduate student. Grandpa was always encouraging and supportive of me in many different ways, and I dearly wish that he could have lived to see me reach the end of this successful journey.

Chapter 1

Introduction

On 23 February 1987, observers on Earth saw a blue supergiant star named Sanduleak -69° 202 explode in the Large Magellanic Cloud. The death of this star formed the brightest supernova detected since the invention of the telescope, and the first supernova visible with the unaided eye since the 1604 explosion recorded by Kepler. Sanduleak -69° 202 was rechristened supernova 1987A (SN1987A), and its remnant has become one of the most extensively observed objects in the history of astronomy.

Photons from SN1987A were observed across a wide range of frequencies, from gamma rays to radio waves. Most remarkably, as predicted by theory, neutrinos from the supernova were detected in two large underground water Cherenkov detectors [1, 2], opening a new arena in the field of neutrino astronomy. SN1987A was the first time that neutrinos originating outside of this solar system had been observed; sixteen years later, it remains the only such detection to date. Twelve interactions of neutrinos from SN1987A were observed within the Kamiokande detector [3], and eight neutrino interactions were seen in the Irvine-Michigan-Brookhaven (IMB) experiment [4]. During the past decade and a half, hundreds of publications have been written about these twenty neutrino events.

Much has already been learned about the stellar interior from the SN1987A neutrinos. A new generation of neutrino detectors now await the next burst of neutrinos from a supernova in the Milky Way or one of its satellite galaxies. Meanwhile, the neutrinos from distant supernova have not stopped traveling; they have merely spread out and become diffuse. Measurements of these supernova relic neutrinos would provide information about the history of supernova explosions in the universe, and the evolution of the universe itself.

1.1 Supernovae

Some stars, particularly massive ones, end their active lives as supernovae, which are among the most energetic explosive events in the universe. Supernovae are broadly categorized into two types based on whether hydrogen lines can be seen when they are viewed through a spectrograph. Type I supernovae do not appear to have hydrogen lines, and Type II do. Additionally, Type I supernovae can be further sub-divided by their spectra: Type Ia supernovae have a large silicon spectral line; Type Ib contain neither hydrogen nor silicon, but helium lines are present; and Type Ic spectra are devoid of hydrogen, helium, and silicon.

Supernovae can also be categorized into two classes based on the mechanism that triggers the explosion [5]. The progenitor stars for either class of supernova spend the majority of their active existence on the main sequence, fusing hydrogen into helium. At this stage, the outward pressure from hydrogen burning is in equilibrium with the inward force of gravity; thus, the star is stable. When the hydrogen in the dense core of the star is depleted, the core begins to collapse under gravity. This collapse causes the temperature of the core to increase to the point where helium fusion begins. The star, now a red giant, is fueled by the fusion of helium into carbon and oxygen. Eventually, the helium supply is also depleted and the core begins to collapse once again, heating up as it does so. At this point in the process, the progenitor stars separate into two different classes, based upon the mass of the star.

In a star that contains less than approximately eight solar masses, the core will not become hot enough to begin fusing carbon and oxygen into heavier elements. Each time the core collapses, the outer envelope of the star expands, causing the surface temperature to drop and the luminosity to increase. Eventually, the envelope of a low mass star will be pushed away from the core by pressure from the stellar wind and the photons emitted by the core. The departing envelope will leave behind a core composed of carbon and oxygen, called a white dwarf, that is supported against gravity by electron degeneracy pressure. If the white dwarf is a member of a binary star system, it may accrete matter from its companion star. When the white dwarf grows more massive than the Chandrashekhar limit of 1.4 solar masses, it becomes unstable. The carbon in the star ignites in a thermonuclear explosion, which is one of the two mechanisms for creating a supernova.

In a star that contains more than approximately eight solar masses, the core of the red giant will rise to temperatures that are sufficient to initiate the fusion of carbon and oxygen into progressively heavier elements. This process ends when the core has been fused into iron, which has a highly compact and

stable nucleus. Creating elements that are heavier than iron does not release energy; on the contrary, it requires that external energy be consumed. Without a new source of fusion energy, the star continues to contract under gravity. Eventually, nuclear degeneracy in the core counters the gravitational force, triggering what is known as a "core-collapse" supernova. These supernovae end by forming either a neutron star or a black hole. The mechanics of a core-collapse supernova will be discussed in greater detail in Section 1.2.

Unfortunately, the original scheme for sorting supernovae based on spectroscopic characteristics does not parallel the actual mechanisms of the explosions. Type Ia supernovae are caused by carbon deflagration, whereas Type II, Ib, and Ic are all believed to be produced by core-collapse. Further subdivisions of Type II supernovae have been made; however, those distinctions are not relevant to this thesis.

1.2 Supernova Neutrinos

1.2.1 Emission

Neutrino emission from Type Ia supernova is believed to be negligible, according to information obtained from x-ray observations. In contrast, core-collapse supernovae emit copious amounts of neutrinos [6]. During such a supernova explosion, approximately 10^{53} ergs of energy are released, about 99% of which are in the form of neutrinos; only 1% of the energy is kinetically released in the explosion. The neutrinos are produced and scattered via the following interactions:

$$
\begin{array}{lrcl}
\textbf{(a)} & e^- + A(N,Z) & \longleftrightarrow & \nu_e + A(N+1,Z-1) \\
\textbf{(b)} & \nu + A(N,Z) & \longleftrightarrow & \nu + A(N,Z) \\
\textbf{(c)} & e^- + p & \longleftrightarrow & \nu_e + n \\
\textbf{(d)} & e^+ + n & \longleftrightarrow & \bar{\nu}_e + p \\
\textbf{(e)} & e^- + e^+ & \longleftrightarrow & \nu + \bar{\nu} \\
\textbf{(f)} & e^\pm + N & \longleftrightarrow & e^\pm + N + \nu + \bar{\nu} \\
\textbf{(g)} & N + N & \longleftrightarrow & N + N + \nu + \bar{\nu} \\
\textbf{(h)} & \gamma^* & \longleftrightarrow & \nu + \bar{\nu} \\
\textbf{(i)} & \gamma^* + e^\pm & \longleftrightarrow & e^\pm + \nu + \bar{\nu}
\end{array}
$$

In these reactions, $\bar{\nu}$ indicates all three flavors of anti-neutrinos. When it appears in the same reaction as $\bar{\nu}$, ν denotes all three flavors of neutrinos; when listed alone, ν is used to represent both neutrinos and anti-neutrinos of all flavors. In reactions **(h,i)**, γ^* represents a plasmon.

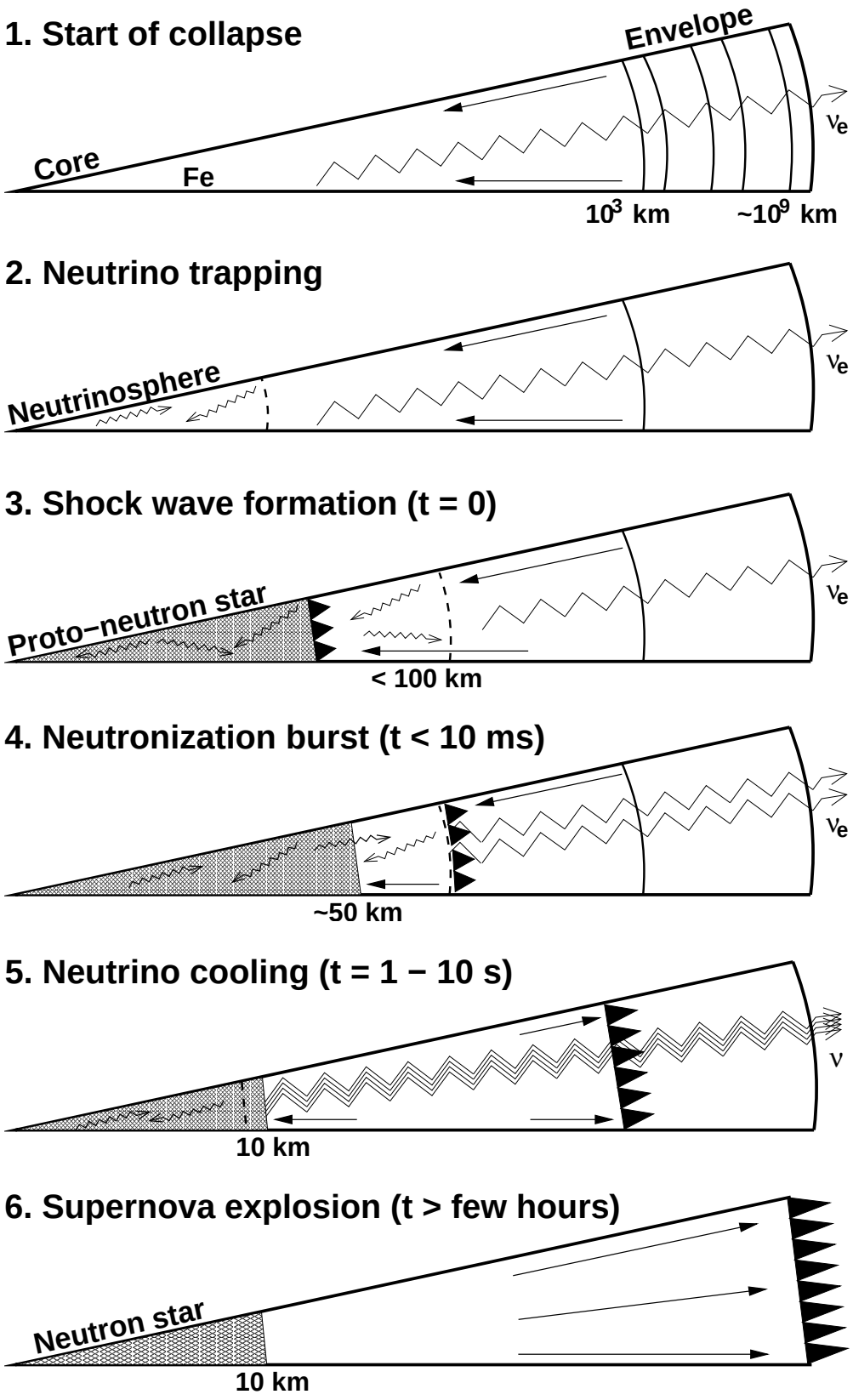

Figure 1.1: The stages of a core-collapse supernova that involve neutrino emission. The final stage, where the supernova actually explodes, is included for completeness. This figure is based on a diagram from reference [8].

The chronological process of neutrino emission from a core-collapse supernova [7] is summarized in Figure 1.1 and in the description below:

1. At the start of the collapse, ν_e are produced when electrons are captured by nuclei **(a)**. The diffusive time scale of the neutrinos is much smaller than the characteristic time scale for the collapse; thus, these neutrinos promptly escape from the core.

2. The core density increases during the collapse, causing the mean free path of the neutrinos to become continually smaller due to interactions with stellar matter. When the core becomes sufficiently dense, the neutrinos can no longer escape; they become trapped by coherent scattering off of nuclei **(b)**. At this stage, the only neutrino emission comes from the low density (10^{11} g/cm^3) region of the mantle, where the mean free path is larger than the radius of the core. The spherical shell surrounding the volume where neutrinos are contained through coherent scattering interactions is called the "neutrinosphere."

3. The inner core completes its collapse when it has reached nuclear densities. Neutron degeneracy counters the gravitational attraction, causing the inner core to rebound with a shock wave that propagates through the infalling outer core.

4. The shock wave heats the matter that it passes through. This heating process leads to nuclear dissociation; the shock wave loses about 8 MeV per dissociated nucleon, which weakens the shock wave and gradually causes it to stall. When the shock wave passes through the neutrinosphere, a large number of ν_e are produced by neutronization, as electrons are captured on newly dissociated protons **(c)**. These ν_e promptly leave the star in a burst that has a duration of $\sim$10 ms. The peak luminosity of this neutronization burst exceeds 10^{53} erg/s, and the total energy carried away by these ν_e is on the order of 10^{51} erg. The core left behind after the bounce shock is called a proto-neutron star.

5. Matter from outside of the core collects onto the proto-neutron star, eventually leading to an accretion shock. During the infall of matter, approximately 10^{53} ergs of gravitational energy are transformed into thermal energy; the temperature in the hot core of the proto-neutron star is about 40 MeV. Neutrinos and anti-neutrinos of all flavors are produced **(c,d,e,f,g,h,i)**, and the hot proto-neutron star is cooled as these neutrinos carry thermal energy out of the star on a time scale of 10 s.

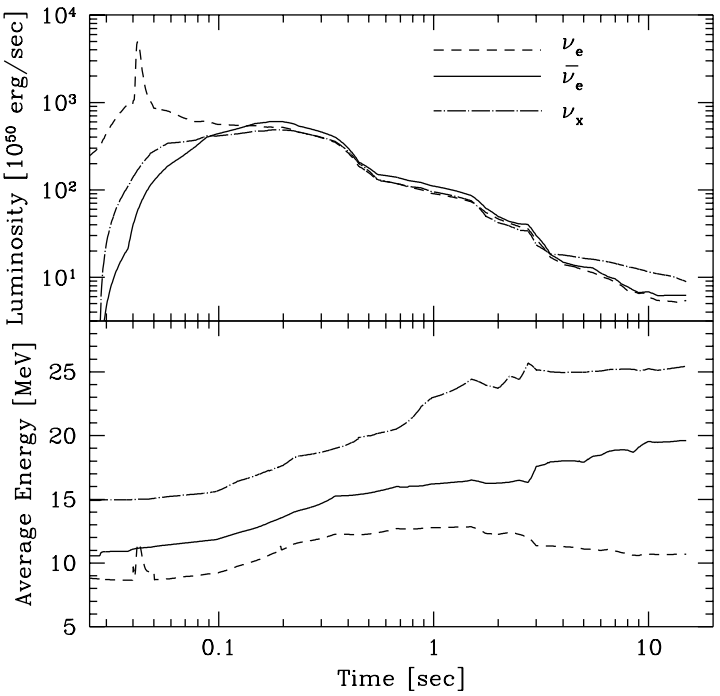

Figure 1.2: The time evolution of neutrino luminosity (top) and average energy (bottom) is shown for a core-collaspe supernova [10]. The neutronization burst manifests as a sharp peak in the ν_e emission.

The de-leptonization and cooling of the proto-neutron star produces a neutron star, which remains after the supernova explosion.

The energy carried away from the supernova is distributed almost evenly amongst the six species of neutrinos. Although only ν_e are emitted in the initial collapse and in the neutronization burst, the total energy released in these stages ($O(10^{51})$ erg) is small compared to the energy radiated away by the thermal neutrinos ($O(10^{53})$ erg). This is illustrated by Figure 1.2, where the neutronization burst is seen as a strong peak in the ν_e luminosity and as a weaker peak in the average ν_e energy.

The average energy of individual neutrinos depends upon the neutrino species [9], as shown in the bottom part of Figure 1.2. The ν_μ, $\bar{\nu}_\mu$, ν_τ, and $\bar{\nu}_\tau$ (hereafter collectively referred to as ν_x) only interact via the neutral current and do not undergo reactions **(c,d)**. Thus, these flavors decouple from the neutrinosphere more easily than the ν_e and the $\bar{\nu}_e$. Essentially, the effective radius of the neutrinosphere is smaller for the ν_x than it is for the ν_e and the $\bar{\nu}_e$.

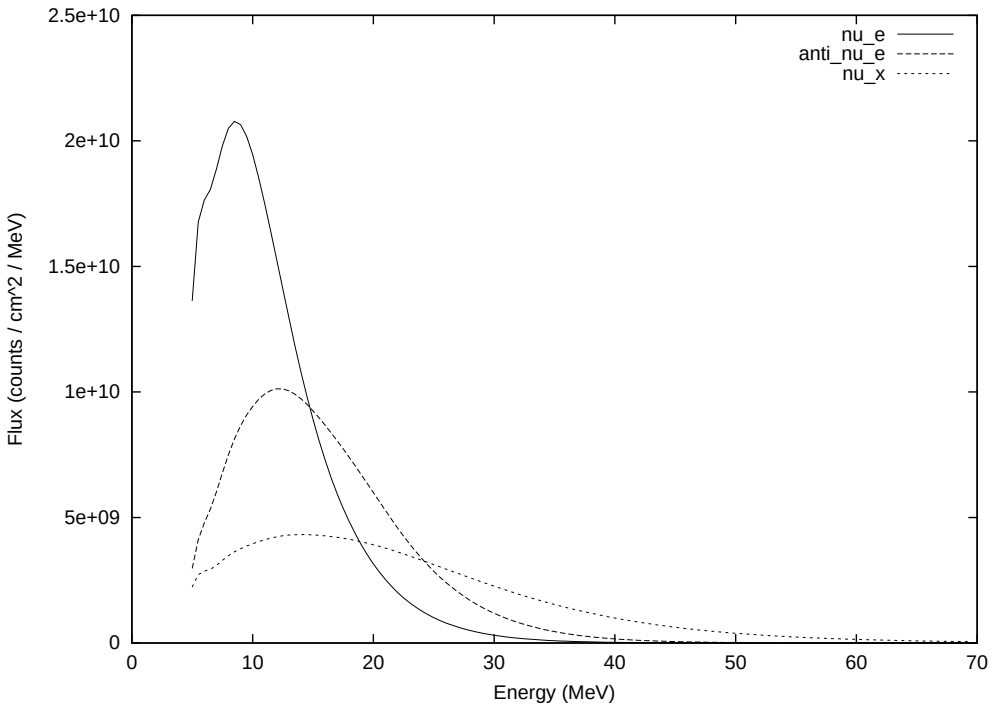

Figure 1.3: The time-integrated energy spectra of supernova neutrinos are shown for the different neutrino species [11].

As a result, the ν_x are emitted from a deeper and hotter layer of the supernova, causing the mean energy of these neutrinos to be higher than that of the ν_e or $\bar{\nu}_e$. The opacities of the ν_e and the $\bar{\nu}_e$ are dominated, respectively, by reactions **(c)** and **(d)**. Since the mantle of the proto-neutron star contains more neutrons than protons, the effective radius of the neutrinosphere is smaller for the $\bar{\nu}_e$ than it is for the ν_e, and the average energy of an emitted $\bar{\nu}_e$ is higher than that of an emitted ν_e. Figure 1.3 shows the time-integrated energy spectra for the different neutrino species. The average energy for each species is:

$$\begin{aligned} <\mathrm{E}_{\nu_e}> &= 11 \text{ MeV} \\ <\mathrm{E}_{\bar{\nu}_e}> &= 16 \text{ MeV} \\ <\mathrm{E}_{\nu_x}> &= 23 \text{ MeV} \end{aligned}$$

These species-dependent differences in the neutrino energy spectra affect the detection of supernova neutrinos, especially when neutrino oscillation is considered (see Section 1.3.3).

1.2.2 Detection

Observing a burst of supernova neutrinos is important because these neutrinos are a unique tool for probing the stellar interior during a core-collapse. Unlike other particles, neutrinos only experience weak interactions, so they can escape from the supernova quickly, without losing all information about the collapse. The twenty neutrinos that were observed from SN1987A provided knowledge about the temperature of the burst, as well as the time-evolution of the star immediately following the collapse. With the large Super-Kamiokande detector now in place, thousands of neutrinos could be observed from a supernovae occurring within the Milky Way galaxy. Such high statistics would provide information about the processes involved in the collapse, such as shock wave stall and subsequent reheating; degenerate states of matter; nucleosynthesis; and stellar atmospherics.

The rate at which core-collapses occur in the Milky Way and its satellite galaxies has been estimated to be about 3 ± 1 supernovae per century [13]. Most of the stars in the Milky Way are obscured by interstellar dust; if one of these stars becomes a supernova, the light that it emits may not be visible on Earth. However, neutrinos are not affected by dust, so neutrino detectors are sensitive to supernovae throughout the entire galaxy. Furthermore, the thermal neutrinos are emitted several hours before the photons; if a burst of supernova neutrinos is detected, the astronomical community can be alerted to watch for light from the explosion. It may even be possible for neutrino detectors to triangulate the position of the supernova for astronomers [12], though they may never see anything optically if it was a dust-obscured star that collapsed.

Both Kamiokande and IMB were water Cherenkov detectors, as are some of their successor experiments; the observation method used by water Cherenkov detectors is described in Section 2.1. For an explosion at the center of the Milky Way, about 10 kpc distant, approximately 400 neutrino events are expected per kiloton of water. These events are primarily created by the following three interactions:

Inverse beta decay (89%): $\bar{\nu}_e + p \rightarrow e^+ + n$

Water Cherenkov detectors are most likely to see the positrons created from inverse β decay. At the energies relevant for supernova neutrino observation, the cross section for this reaction is an order of magnitude greater than that of any other interaction. By measuring the energy spectrum of these events, information about the time evolution of the burst can be obtained.

Neutral current interaction with ^{16}O (8%): $\nu_x + {}^{16}\mathrm{O} \rightarrow \nu_x + \gamma + \mathrm{X}$
The most energetic supernova neutrinos can eject a nucleon from ^{16}O, producing either ^{15}O or ^{15}N in an excited nuclear state. Upon de-excitation, these nuclei emit mono-energetic γ-rays with energy between 5 MeV and 10 MeV. The γ-rays produce peaks on an otherwise smooth energy distribution; the height of these neutral current peaks corresponds to the temperature of the ν_μ and ν_τ in the stellar core [14].

Elastic scattering (3%): $\nu + e^- \rightarrow \nu + e^-$
Neutrino-electron elastic scattering interactions are directional; the recoil electrons preserve the direction of the incoming neutrinos. With sufficient statistics, these events may allow a single detector to determine the position of the supernova in the sky to a precision of $\pm 1.5^\circ$ [12].

In addition to providing information about the stellar interior, a burst of supernova neutrino could be used to study the properties of neutrinos. Potentially, neutrino flavor mixing parameters as well as the absolute masses and magnetic moments of the different neutrino types could all be measured from a supernova burst [15].

1.3 Supernova Relic Neutrinos (SRN)

Valuable information can be obtained by studying supernova neutrinos; unfortunately, bursts from nearby supernovae are quite rare. To date, the only observed instance has been SN1987A. It is generally believed that core-collapse supernovae have been happening throughout the universe since shortly after star formation began. As a consequence, there should exist a diffuse background of neutrinos originating from all of the supernovae that have previously occurred [16, 17, 18]. The distribution of these supernova relic neutrinos (SRN) should be isotropic, as the contribution from any particular supernova is minimal. It is not possible to view the stellar interior by observing the SRN, as the characteristic time structure has been lost and the neutrinos from distant supernovae have been redshifted considerably. However, observation of the SRN would offer insight about the history of supernova explosions in the universe and related cosmological quantities (see Section 1.3.1).

Although all six neutrino species carry away approximately the same amount of thermal energy from a core-collapse supernova, some species of SRN are easier to detect than others. At a water Cherenkov experiment, the $\bar{\nu}_e$ is most likely to be observed (see Section 1.2.2). Figure 1.4 shows the relative event rates expected for the dominant interaction modes of each neutrino species.

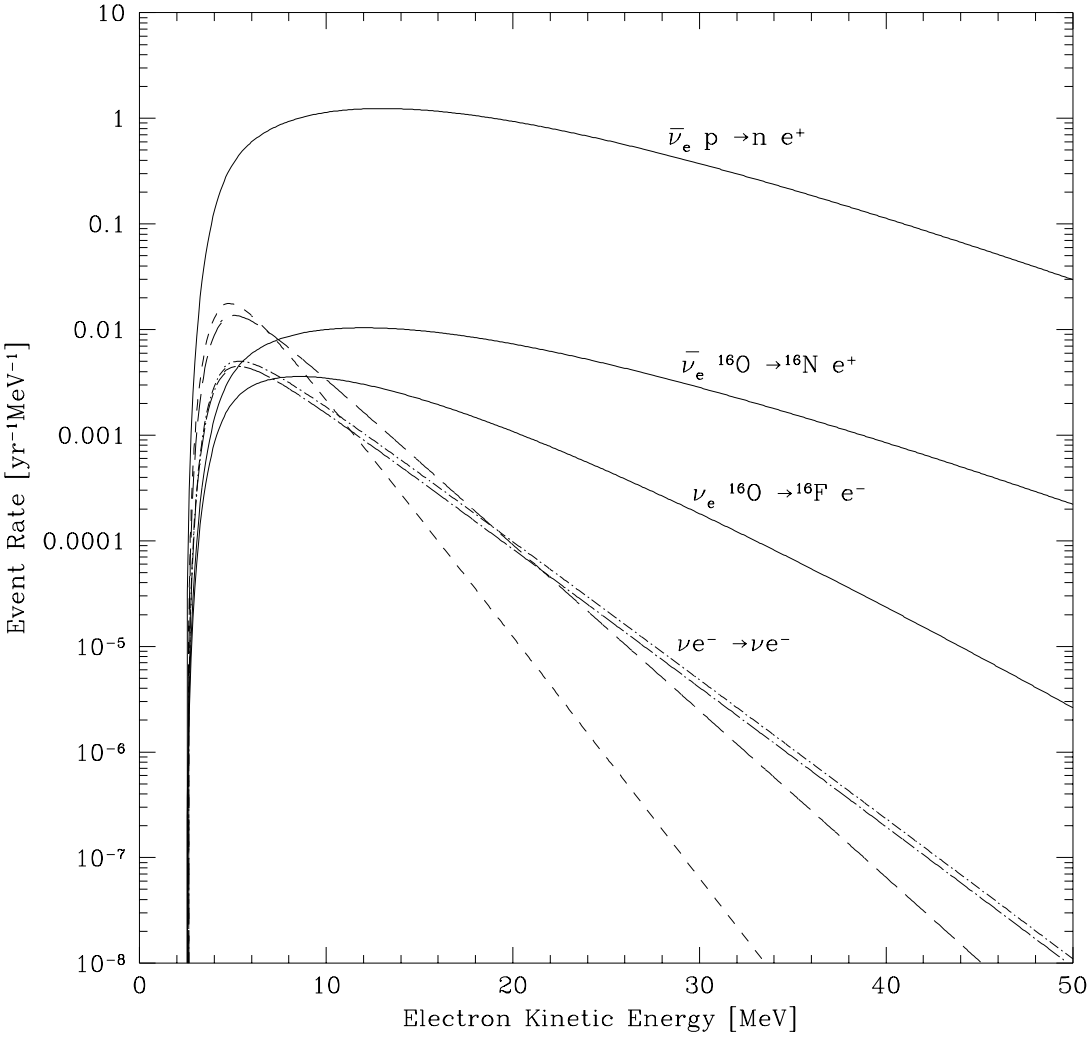

Figure 1.4: The relative event rates are shown for different supernova relic neutrino modes [19]. The solid lines are explicitly labeled in the figure with the interaction mode that they represent. The four broken lines represent neutrino-electron elastic scattering: the short dashed line denotes the ν_e events, the long dashed line indicates the $\bar{\nu}_e$ events, the short dot-dashed line marks the ν_x events, and the long dot-dashed line shows the $\bar{\nu}_x$ events. The absolute scale of the ordinate assumes a water Cherenkov detector with a 22.5 kton fiducial volume.

The figure shows that the $\bar{\nu}_e$ interact primarily through inverse β decay, which has a cross section that is $\sim$2 orders of magnitude greater than that of neutrino-electron elastic scattering. It is clear that the primary SRN signal will come from $\bar{\nu}_e$ undergoing inverse β interactions with free protons [19, 20]. Therefore, in this thesis, all further discussion of the SRN refers only to the $\bar{\nu}_e$ and this specific interaction mode.

1.3.1 Cosmological Implications

Determining the total SRN flux, integrated over all energies, would serve as a measurement of the core-collapse supernova rate integrated over the history of the universe. The importance of observing the SRN has been described by theorists Hartmann and Woosley as follows: "An actual detection would of course be an invaluable observational accomplishment because it would be a direct measure of the global supernova rate." [22]

Neutrinos from distant supernovae have had their energy redshifted, according to the following relation:

$$\frac{E_{detect}}{E_{emit}} = \frac{1}{1+z} \tag{1.1}$$

where E_{emit} is the emitted neutrino energy, E_{detect} is the energy of the neutrino when it reaches Earth, and z is the redshift parameter. Redshifting lowers the average energy of the SRN, relative to the average energy of neutrinos emitted from a single supernova, and causes the width of the energy distribution to become broader, since supernovae at all different z values contribute to the SRN flux. Therefore, measuring the energy distribution of the SRN would be equivalent to an observation of the average supernova rate as a function of the redshift parameter. The sensitivity of such an observation would depend on the lower energy threshold of the SRN spectrum measurement; a smaller threshold would allow larger values of z to be probed.

Besides serving as a direct measurement of the global supernova rate, precision measurements of the SRN would provide insight into related quantities, such as the universal star formation rate. All stars containing more than eight solar masses are expected to end their active lives in a core-collapse. Therefore, the supernova rate should be closely related to the formation rate of these massive stars. The history of star formation is only well understood from a redshift of $z \approx 1$ to the present; at earlier times, it is largely uncertain [23]. Observation of the SRN could offer new information about star formation in the early universe. Furthermore, it is believed that as a galaxy evolves, its star formation rate varies; young galaxies may have produced stars at a much

higher rate than what is seen in the current epoch. Thus, the SRN may also serve as a new tool for learning about the evolution of galaxies [15]. Finally, it is believed that elements heavier than oxygen are predominantly synthesized within core-collapse supernovae, so measurements of the supernova rate may also provide information on cosmic chemical evolution [22].

1.3.2 SRN Models and Predictions

The SRN were first discussed in theoretical papers published before neutrinos from SN1987A had been observed [16]; early calculations provided only rough estimates of the SRN flux [17, 18]. Without any experimental data on neutrino emission from core-collapse supernovae, these early models primarily focused on the flux contributed from individual supernovae and made simple assumptions about the supernova rate, namely that it has been constant with time. Later models, published years after SN1987A, have used more sophisticated methods to calculate the SRN flux and spectrum [19, 20, 21, 22, 23, 24]. These models have produced flux predictions that range from $2 - 54\ \bar{\nu}_e\ \mathrm{cm}^{-2}\ \mathrm{s}^{-1}$.

The first paper to make a somewhat sophisticated modeling of the supernova rate also included calculations based on the assumption of a constant supernova rate [19]. The constant model expectations were included to illustrate the effect that an evolving supernova rate has on the SRN flux and spectrum. A constant supernova rate was also assumed by previous experimenters when setting limits on the SRN flux (see Section 1.3.4). In this thesis, several theoretical models of the SRN flux and spectrum are evaluated. Though it is no longer regarded as a realistic model, the constant supernova prediction is still considered for this analysis. The reasons for including this model are primarily historical, as it permits a direct comparison of current and previous results. The total flux allowed by the constant model prediction was normalized using a nucleosynthesis constraint: Since oxygen is created within the massive stars that eventually become supernovae, the observed abundances of oxygen can be used to estimate the total number of core-collapse supernovae. Oxygen created in stars of lower mass can be neglected from this estimate, as these stars fuse oxygen to create iron during Type Ia supernovae.

A more advanced set of predictions was later published by the same authors of the previous model [20]. In their second publication, the SRN flux and spectrum were calculated with a population synthesis model of galaxy evolution. Star formation within a galaxy, $C(t)$, was approximated with the function:

$$C(t) \;=\; v\, f^n(t) \tag{1.2}$$

where the coefficient v and the power index n were constrained by observation. Different parameter values were obtained for elliptical galaxies and four sub-classes of spiral galaxies: S_{ab}, S_{bc}, S_{cd}, and S_{dm}. Essentially, this method evaluated the supernova rate within each galaxy type, then used data from surveys of faint galaxies to estimate the number of each galaxy type as a function of redshift. Together, this information enabled predictions of the SRN flux. Several sets of cosmological parameters were considered; SRN flux and spectrum predictions were produced for each set. In this thesis, the flux predictions from the population syntheis model were derived using the cosmological parameters $(h,\Omega,\lambda) = (0.8,0.2,0.8)$, where h is the Hubble parameter, Ω is the energy density relative to the critical density ($\Omega = \rho/\rho_c$), and λ represents the cosmological constant.

Another model uses the redshift evolution of cosmic gas, as determined from observations of absorption lines in quasi-stellar objects, to calculate the supernova rate [21]. In general, the evolution of cosmic gas can be described as the transformation of gas into stars and back into gas again. In addition to this simple system, an infall of cool gas is also allowed for redshifts of $z \leq 2$; the infall is taken to be a constant multiple of the star formation rate. This model predicts a supernova rate that is lower than any of the other models considered. In particular, the supernova rate in the modern epoch seems to be abnormally low in comparison to observation. The inclusion of gas infall effects partially offsets the low supernova rate that is expected by this model for small redshift values. However, this method still predicts the most steeply falling spectrum for SRN with energies above 10 MeV, which originate from recent supernovae.

SRN predictions calculated using a cosmic chemical evolution model were published at the same time as the gas infall model described above. Observations of damped Lyman α systems, which are believed to be the progenitors of galaxies, and faint redshift surveys of galaxies were used to estimate the global star formation history. This paper [22] made multiple predictions; besides using a "standard" supernova model, predictions were made by using a cooling function to allow the neutrino temperature to change during the course of the supernova. Yet another calculation produced a constant rate model, with the flux normalization obtained by assuming that the supernova rate observed in the modern epoch has been true since star formation began; the total flux estimated in this manner is an order of mangitude lower than the estimates obtained via the nucleosynthesis constraint [19]. Further results were produced by using a large initial neutrino temperature of 7 MeV, and by altering the cosmological parameter Ω. For evaluation within this thesis, the standard model from this paper was selected. The standard model assumes a

Theoretical model	Predicted flux
Constant supernova rate [19]	52 $\bar{\nu}_e$ cm^{-2} s^{-1}
Population synthesis [20]	44 $\bar{\nu}_e$ cm^{-2} s^{-1}
Cosmic gas infall [21]	5.4 $\bar{\nu}_e$ cm^{-2} s^{-1}
Cosmic chemical evolution [22]	8.3 $\bar{\nu}_e$ cm^{-2} s^{-1}
Heavy metal abundance [23]	< 54 $\bar{\nu}_e$ cm^{-2} s^{-1}
Large mixing angle osc. [24]	11 $\bar{\nu}_e$ cm^{-2} s^{-1}

Table 1.1: The total flux of the SRN, calculated by six theoretical models.

neutrino temperature of 4 MeV and a supernova rate that evolves over time; it does not include the effects of a cooling function on the neutrino spectrum.

More recently, a theoretical upper bound was estimated for the detectable SRN flux [23]. In this model, the observed abundances of heavy metals in the local universe were used to calculate the supernova rate from $z \approx 1$ to the present. It was assumed that all heavy metals are synthesized within core-collapse supernovae. Therefore, observations of the metal enrichment history should correspond to a measurement of the supernova rate. Distant supernovae were ignored, as it was assumed that the neutrinos they have emitted have all been redshifted to energies that are undetectable by current experiments. In order to obtain a theoretical upper bound on the SRN flux, parameters that contained uncertainty were not chosen by their central values. The parameter values used were deliberately chosen, within the allowed uncertainty, to maximize the SRN flux. As a consequence, this model seems to achieve its goal of estimating a theoretical upper bound; the SRN flux that it predicts is higher than that of any other model that has been published after SN1987A.

The total flux predictions from the various models are summarized in Table 1.1. The table also lists a prediction that includes the effects of neutrino flavor oscillation, which will be discussed in Section 1.3.3. Figure 1.5 displays the spectra calculated from each theoretical model that is evaluated in this thesis. The energy distribution of neutrinos from other sources is also shown in this figure: The dashed line below 10 MeV indicates the flux of reactor $\bar{\nu}_e$; solar neutrinos are denoted with the dotted line (*hep*) and the solid line (^{8}B); and atmospheric $\bar{\nu}_e$ are represented by the dot-dashed line. The literature often notes the existence of a "window of opportunity" for SRN detection between the solar *hep* cut-off energy of 18.77 MeV and the energy at which the atmospheric neutrino flux becomes dominant.

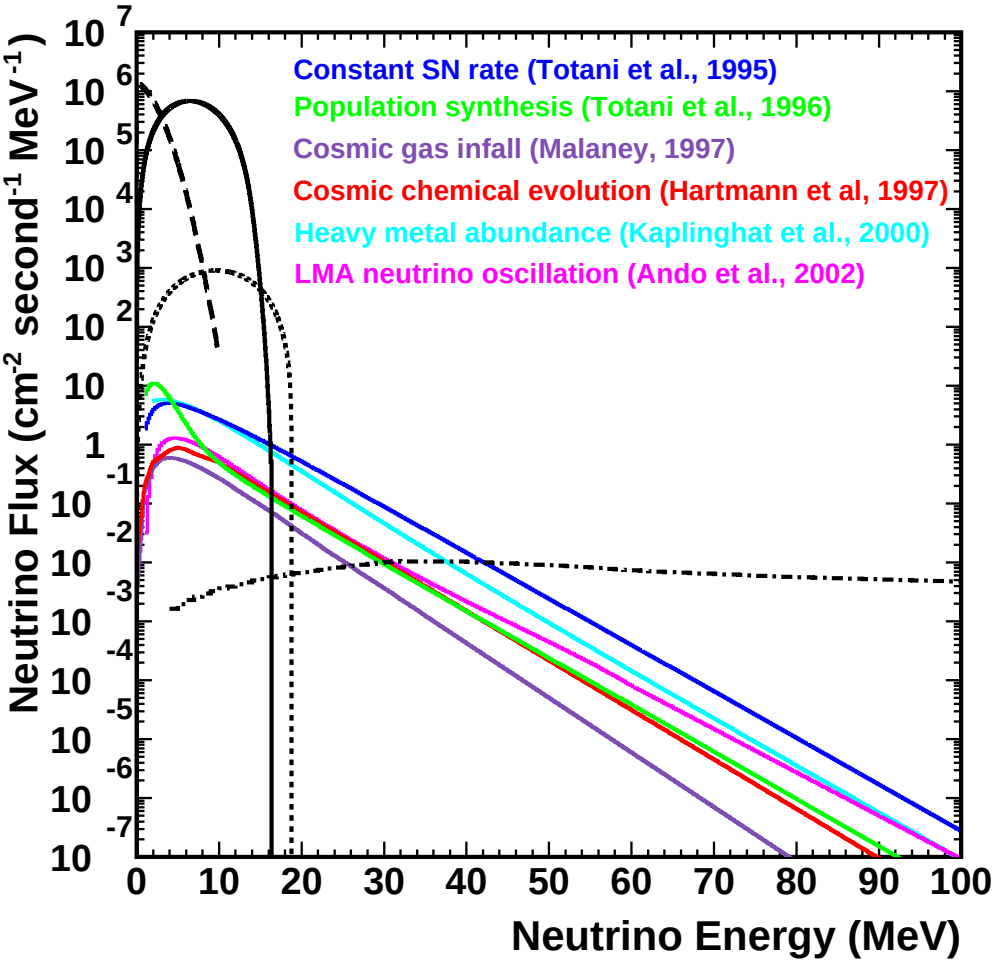

Figure 1.5: The expected SRN flux, calculated from six theoretical models, is presented. The SRN flux predictions are compared to the fluxes from the reactor $\bar{\nu}_e$ (dashed line), the ^{8}B solar ν_e (solid line), the *hep* solar ν_e (dotted line), and the atmospheric $\bar{\nu}_e$ (dot-dashed line).

1.3.3 Neutrino Oscillation

The most recent SRN predictions have also considered the effects of neutrino oscillation [24]. Neutrino flavor oscillation was first proposed as a potential solution to the observed deficit of solar neutrinos. Initially, only oscillation in vacuum was considered, which required the distance between the Sun and the Earth to be, by chance, a multiple of the oscillation length for neutrinos with energies characteristic of those being produced in the Sun. Eventually, more complicated mixing scenarios were postulated, in which neutrinos propagating in matter acquire additional potential energy by their amplitude for forward scattering. These matter effects were first published by Wolfenstein [25]; Mikheyev and Smirnov later applied the matter effects to solar neutrinos and hypothesized that a resonance could enhance neutrino oscillation within the dense matter of the Sun [26]. Thus, the effects of matter on neutrino mixing are often referred to as the MSW effect, after Mikheyev, Smirnov, and Wolfenstein. Until 2000, a global analysis of the existing solar neutrino data allowed three regions of parameter space in which MSW oscillation effects would be noticable; these regions were termed LMA (for large mixing angle), SMA (for small mixing angle), and LOW (for large mixing angle, with a low mass-squared difference).

In 1998, the first statistically significant evidence for neutrino oscillation was published, based on studies of atmospheric neutrinos performed at the Super-Kamiokande experiment [27]. This evidence was based on the zenith angle distribution of the atmospheric ν_μ to ν_e ratio. The inclusion of matter effects was not necessary to obtain this result, and only ν_μ were seen undergoing oscillation. In 2001, the first direct evidence of ν_e oscillation was obtained by comparing solar neutrino measurements made by Super-Kamiokande and the Sudbury Neutrino Observatory (SNO) [28, 29]. At Super-Kamiokande, solar neutrinos are detected by elastic scattering, which has a large charged current (CC) component and a smaller neutral current (NC) contribution. At SNO, the following reaction was used to measure only CC interactions:

$$\nu_e + d \rightarrow p + p + e^-$$

Only ν_e are produced in the Sun. Therefore, differences in the solar neutrino flux calculated from elastic scattering measurements and from CC-only measurements indicate the presence of ν_x originating from the Sun, which is evidence of ν_e oscillation.

In recent years, the effects of flavor oscillation on the production, transport, and emission of neutrinos from a core-collapse supernova have been studied [30, 31]. Furthermore, the availability of new solar neutrino data from

Super-Kamiokande and SNO has made a much more powerful global analysis possible. Super-Kamiokande data alone favor a large neutrino mixing angle, thereby ruling out the SMA MSW parameter space [32]; combining data from all solar neutrino experiments permits only the LMA solution at the 95% confidence level (C.L.) [33, 34]. The KamLAND experiment has measured the flux of $\bar{\nu}_e$ originating from nuclear reactors; this work has confirmed that only a large neutrino mixing angle is allowed [35]. The KamLAND results have also provided the first direct evidence for the oscillation of anti-electron neutrinos, which is particularly relevant to the detection of SRN.

Although neutrino oscillation effects are briefly mentioned in some of the previous SRN papers [23], they were not handled in a rigorous or quantitative manner. The first paper to produce an SRN model in which neutrino oscillation is fully considered was published quite recently [24]. Oscillation parameters obtained from solar and atmospheric neutrino studies were used to modify the energy spectrum of neutrinos emitted from a single supernova burst. Altering the emission from a single supernova also results in a modification of the SRN spectrum. LMA and SMA MSW solutions were both considered in this paper; however, the SMA parameters have little effect on the SRN spectrum, and they are disfavored by experimental results. Therefore, in this thesis, only an LMA solution is considered. Since the $\bar{\nu}_x$ are emitted from deeper in the stellar interior than the $\bar{\nu}_e$, the average energy of these flavors is higher. As a result, neutrino mixing hardens the $\bar{\nu}_e$ energy spectrum, as shown in Figure 1.5. The cross section for inverse β decay increases as the square of the $\bar{\nu}_e$ energy (see Section 6.1.1); thus, oscillation enhances the SRN signal in a water Cherenkov detector.

1.3.4 Results from Previous SRN Searches

The SRN have not yet been detected. The best previous search results were obtained by the Kamiokande-II experiment, which set upper bounds on the SRN flux. In 1988, the Kamiokande collaboration published limits on the SRN flux in the energy interval of $E_\nu = 19$ MeV to 35 MeV [36]. Using 357 days of data, Kamiokande-II was able to set a 90% C.L. upper bound of 226 $\bar{\nu}_e$ cm^{-2} s^{-1} on the SRN flux in this energy range. This limit is model-independent and it is not compared to specific predictions in the publication.

Additional SRN flux limits were obtained by Kamiokande-II, but not published. In a Ph.D. thesis from 1991, limits on the total SRN flux, obtained from 1040 days of data, were presented [37]. Positrons created by the SRN were searched for in the energy window $E_e = 19$ MeV to 50 MeV. By choosing a particular SRN model, the analysis in this energy range can be extrapolated

to obtain an upper bound on the full SRN spectrum. For the Kamiokande-II analysis, the chosen model assumed a supernova rate that was constant with time and a neutrino temperature of 4 MeV. With these assumptions, the 90% C.L. upper bound set on the total SRN flux was 780 $\bar{\nu}_e$ cm^{-2} s^{-1}. The constant model used in the Kamiokande-II thesis predicted a total SRN flux of 50 $\bar{\nu}_e$ cm^{-2} s^{-1}, which is an order of magnitude lower than the Kamiokande upper bound.

A preliminary SRN search was conducted at Super-Kamiokande during 2000 and culminated in a Masters thesis in 2001 [38]. It is somewhat inaccurate to consider that work to be a previous search, as it benefited from techniques developed for the analysis presented herein, which was conducted concurrently. Only the population synthesis model was evaluated in the Masters thesis; for this spectral prediction, an upper bound of 231 $\bar{\nu}_e$ cm^{-2} s^{-1} was placed on the total SRN flux.

Chapter 2

The Super-Kamiokande-I Detector

The Super-Kamiokande (SK) experiment is a water Cherenkov detector. This chapter describes the principles of neutrino detection in SK and the various components of the detector. The first phase of data accumulation, which began on 1 April 1996 and ended on 15 July 2001, is known as Super-Kamiokande-I (SK-I).

2.1 The Neutrino Detection Method

A charged particle that travels through a medium with an index of refraction n will emit Cherenkov light if its velocity v exceeds the speed of light in the medium, i.e. if $v > c/n$, where c is the speed of light in vacuum. SK contains ultra-pure water, which has a refraction index of $n = 1.33$; therefore, electrons (or positrons) in SK will produce Cherenkov radiation if their total energy exceeds 0.772 MeV.

Cherenkov photons are emitted as a cone with an opening angle θ_C; the axis of the cone is the direction of the particle's motion. The opening angle is determined by:

$$\cos\theta_C \;=\; \frac{1}{n\beta} \tag{2.1}$$

where $\beta = v/c$.

In pure water, an ultra-relativistic particle ($\beta \approx 1$) will emit light with an opening angle of $\theta_C \approx 42°$. The number of Cherenkov photons (dN) radiated in the frequency interval ($d\nu$) per unit of distance traveled (dx) is a constant [39, 40] described by:

$$\frac{d^2N}{dxd\nu} \;=\; \frac{2\pi\alpha}{c}\,\sin^2\theta_C \tag{2.2}$$

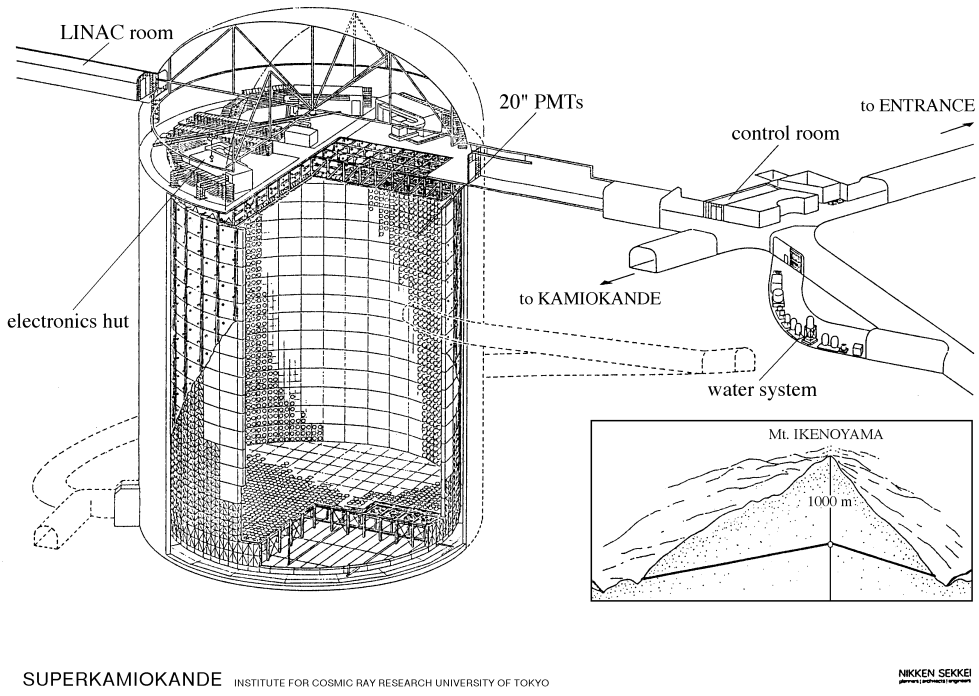

Figure 2.1: An overview of the SK detector and its surrounding area. The cut-away view shows the inner and outer detector regions and the inset shows the detector's location within Mt. Ikenoyama.

where α is the fine structure contant. For an ultra-relativistic particle with unit charge, about 390 Cherenkov photons are emitted per cm traveled. In the SK detector, charged particles are observed through the detection of these Cherenkov photons.

2.2 A General Detector Description

The Super-Kamiokande detector is located in a mine beneath Mt. Ikenoyama, in the Kamioka township of the Gifu prefecture of Japan. More precisely, the detector is located at coordinates of 36°25'N in latitude, 137°18'E in longitude, and 1000 meters underground (equivalent to 2700 meters of water). The overburden of rock reduces the rate at which cosmic ray muons enter the detector by about five orders of magnitude; in SK, this rate is $\sim$2.5 Hz.

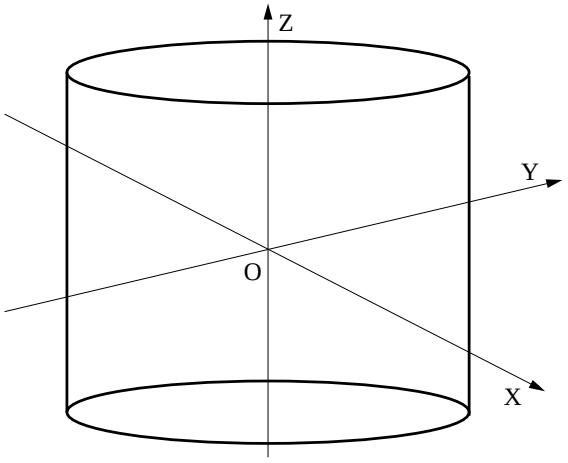

Figure 2.2: Local coordinates of the SK detector.

SK consists of a cylindrical tank with a height of 41.4 m and a diameter of 39.3 m. The tank is constructed from stainless steel plates that are welded together and backed by concrete. 50,000 metric tons of ultra-pure water are contained within the tank. A stainless steel frame divides SK into two regions – an inner detector (ID) and an outer detector (OD). Tyvek and black polyethylene sheets keep the two regions of the detector optically separated; however, water is able to flow between the regions. An overview of the SK detector and its surrounding area is shown in Figure 2.1. Positions within the detector are described by a local Cartesian coordinate system that has its origin at the center of the tank, as shown in Figure 2.2.

There is a dome-shaped hollow space directly above the SK tank. The detector's data acquisition systems and calibration equipment are located in this area. The walls of the dome are coated in a polyurethane material called "Mineguard." This covering prevents radon, which is emitted by the surrounding rock, from entering the detector. The air in the dome is supplied by pumps that are outside of the mine; this reduces radon levels in the area directly above the SK tank.

Within the detector, Cherenkov photons are collected using light-sensitive elements called photomultiplier tubes (PMTs, see section 2.3). The PMTs are mounted on the same framework that separates the ID from the OD. Figure 2.3 shows the details of the mounting system.

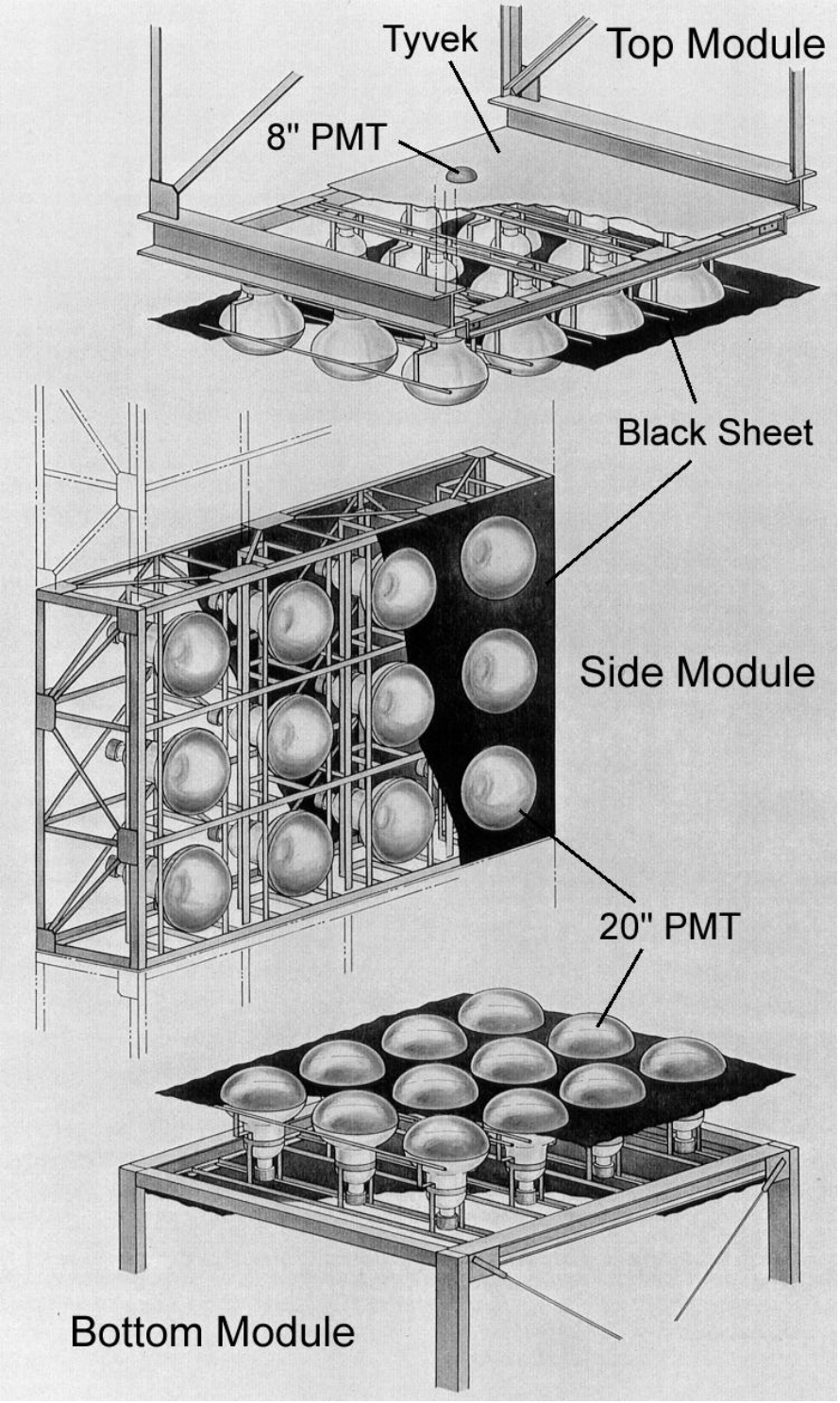

Figure 2.3: The layout of the PMT mounting structure. PMTs are mounted in frames called "super-modules." Each super-module holds twelve ID PMTs and two OD PMTs.

2.2.1 The ID and the OD

The ID is a cylinder that is 36.2 m high, 33.8 m in diameter, and encloses 32,481 metric tons of ultra-pure water. Cherenkov light in the ID is detected with 11,146 inward-facing PMTs that are 50 cm in diameter. PMTs in the ID are mounted on the points of a 70 cm grid. The PMTs cover $\sim$40% of the ID surface area; the remaining 60% is covered with black polyethylene sheets that reduce the amount of light that is reflected within the ID. The fiducial volume, which is the portion of the detector that is used for the SRN search, begins 2 m inward from the walls of the ID, and contains 22,500 metric tons of water.

The OD is a cylindrical shell that surrounds the ID. The thickness of the OD is 2.05 m at the top and at the bottom of SK; on the barrel region, it is 2.2 m thick. This volume acts as a passive shield for neutrons and γ-rays emitted by the surrounding rock; the OD thickness is equivalent to $\sim$7.5 radiation lengths and $\sim$4.5 nuclear interaction lengths. Additionally, the OD is used as an active veto for incoming particles such as cosmic ray muons. To that end, 1885 outward-facing PMTs, each 20 cm in diameter, view the OD. To enhance light collection within the OD, all of the surfaces are covered with white Tyvek sheets, which have a reflectivity of $> 80\%$ for Cherenkov photons.

2.3 Photomultiplier Tubes (PMTs)

When a PMT is struck by a photon, it outputs an electrical pulse, which is sent to SK's data acquisition (DAQ) systems. If the PMT generates a pulse that is large enough to be observed by the DAQ, that PMT is said to have been "hit." The details of the SK PMTs, and their functioning within the detector, are described below.

PMTs are composed of a thin borosilicate glass. The surface of the glass is coated with a thin bi-alkali photocathode, which makes it sensitive to light. When a photon strikes the photocathode, the photon is absorbed and the photocathode emits a single electron, dubbed a "photo-electron," (p.e.) in response. A $\sim$2 kV potential is applied between the photocathode and the anode through a series of dynodes within the PMT. This potential generates an electric field that accelerates the photo-electron towards the dynodes. When an electron hits one of the dynodes, approximately three to five more electrons are released, which then travel towards the next dynode. This process is repeated multiple times, until a cascade of roughly 10^7 electrons has been generated from the initial photo-electron. These electrons are collected at the anode of

the PMT, where they become the electrical pulse that is sent to the DAQ system.

Magnetic fields reduce the electron collection efficiency of the PMTs by deflecting photo-electrons between the photocathode and the first dynode. The large size of the 50 cm PMTs used in the SK ID makes them susceptible to even the Earth's magnetic field of 450 mG. Thus, to obtain a uniform response from these PMTs, the residual magnetic field must be reduced to less than 100 mG. To accomplish this, SK is surrounded by twenty-six Helmholtz coils, which reduce the net magnetic field in SK to $\sim$50 mG at all positions within the detector.

2.3.1 The ID 50 cm PMTs

Initially, 50 cm PMTs were developed by the Hamamatsu Photonics Company for use in the Kamiokande experiment. The PMTs used in the SK ID are Hamamatsu model R3600, which include some improvements over the original design:

- At the expected energies for the SRN, most PMTs will only be hit by a single photo-electron. The Hamamatsu R3600 separates the 1 p.e. peak from dark noise more clearly than previous models. This was accomplished by optimizing the structure of the dynode. Figure 2.4 shows the clear separation between the 1 p.e. peak and dark noise.

- A larger dynode area has reduced the effect of residual magnetic fields. This results in an improvement of the PMT timing resolution by about a factor of two. Figure 2.5 shows the timing resolution for a 1 p.e. signal.

Figure 2.6 shows a diagram of a typical ID PMT. The characteristics of these PMTs are summarized in Table 2.1.

The probability that a photon will generate a photo-electron upon striking the photocathode is called the quantum efficiency (QE), and it is a function of wavelength. For the SK ID PMTs, the QE reaches a maximum of 27% at a 390 nm wavelength, as shown in Figure 2.7. This is ideal for the detection of Cherenkov light, which peaks near 390 nm after traveling several meters through water.

2.3.2 The OD 20 cm PMTs

The OD volume is viewed by 1885 outward-facing 20 cm PMTs. The PMTs used in the SK OD are Hamamatsu model R1408, which are mounted

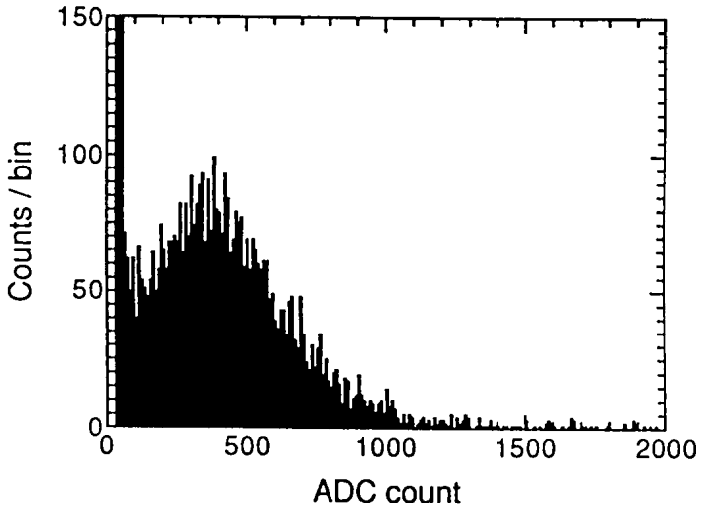

Figure 2.4: The separation of the single photo-electron (p.e.) peak from dark noise in the 50 cm PMTs used in the SK ID [41]. The clear peak centered around 400 counts is the 1 p.e. peak and the dark noise hits are all located around the 0 count bin.

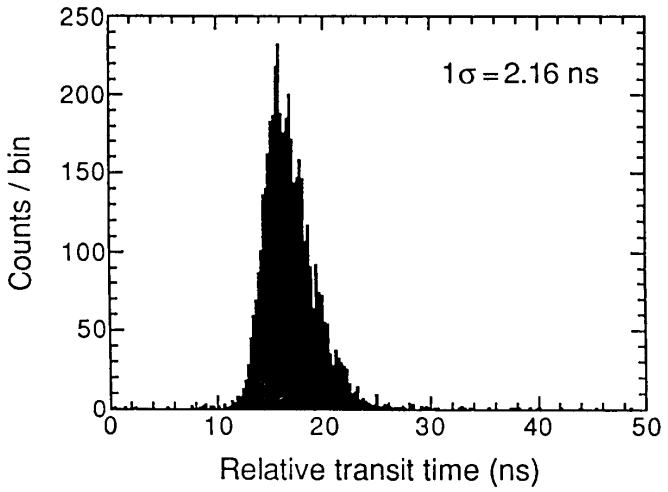

Figure 2.5: The transit time distribution for a typical ID PMT subjected to an intensity of 1 p.e [41]. The timing resolution is the one sigma spread in transit time.

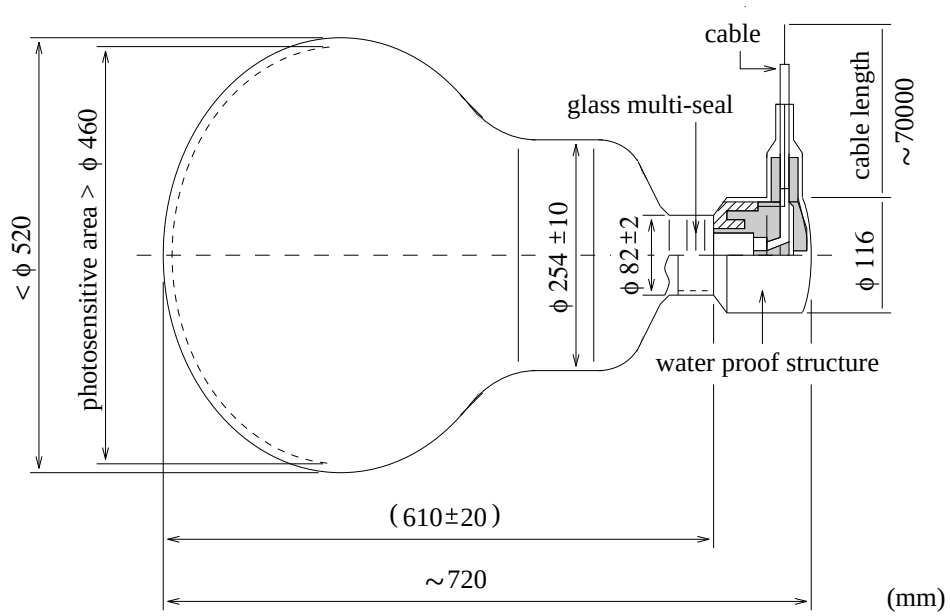

Figure 2.6: An overview of the 50 cm PMT used in the SK ID.

Table 2.1: General characteristics of the Hamamatsu R3600 PMTs

Photocathode area	50.8 cm diameter
Shape	Hemispherical
Window material	4 - 5 mm thick Pyrex glass
Photocathode material	Bialkali (Sb-K-Cs)
Dynodes	11 stages, Venetian blind design
Pressure tolerance	6 kg/cm^2 water pressure
Quantum efficiency	22% at λ = 390 nm (peak)
Gain	10^7 at ~2 kV
Dark current	200 nA
Dark noise rate	3 kHz
Cathode non-uniformity	< 10%
Anode non-uniformity	< 40%
Transit time	100 ns
Transit time spread	2.2 ns RMS at 1 p.e. levels

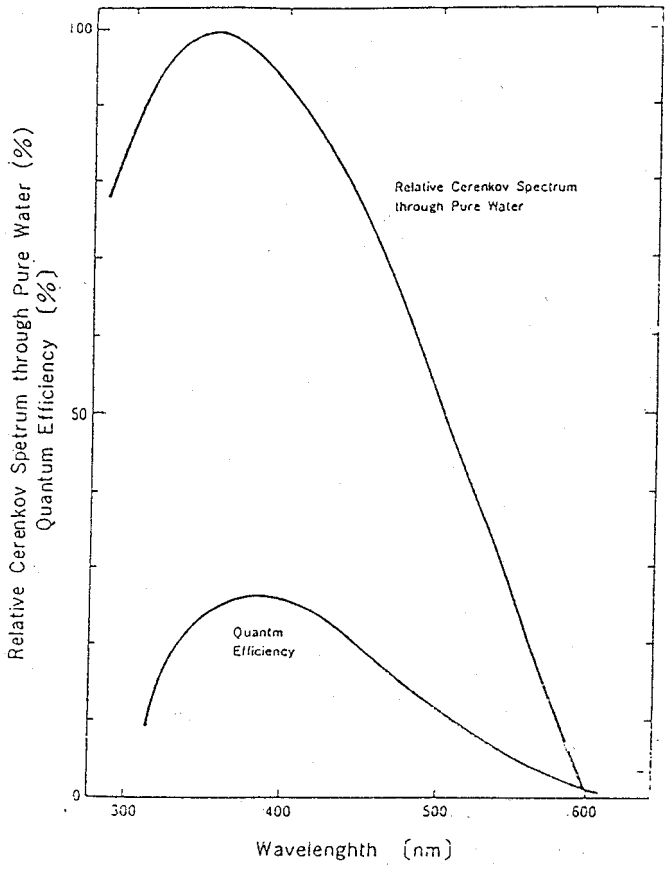

Figure 2.7: The quantum efficiency, as a function of photon wavelength, of the ID PMTs. The spectrum shape of Cherenkov light after traveling several meters through pure water is also shown.

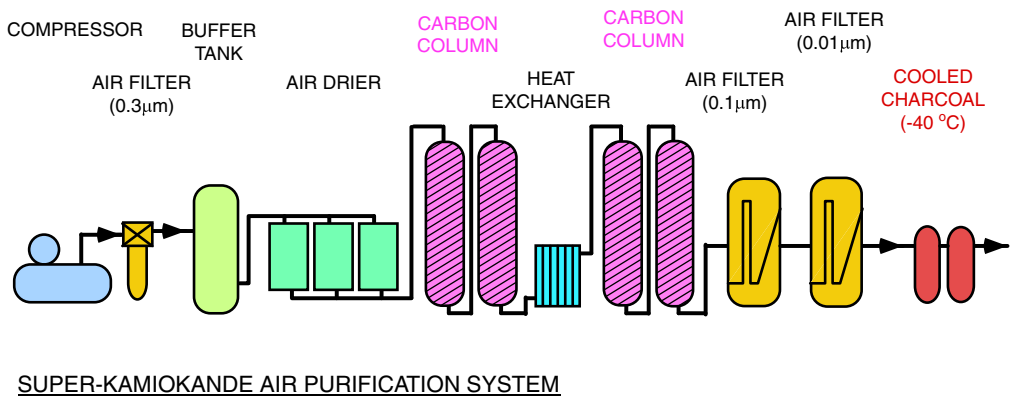

Figure 2.8: A schematic view of the radon-reducing air system.

in waterproof housings. Before being installed into SK, these PMTs were used in the IMB experiment. Light collection in the OD is enhanced by acrylic plates that are attached to the face of each OD PMT. The plates are square panels, measuring 60 cm on each side, that are 1.3 cm thick. Each plate contains the wavelength-shifting additive bis-MSB in a concentration of 50 mg/l. These plates absorb ultraviolet light and re-emit the light at blue wavelengths, where the PMTs are at peak sensitivity. Use of these wavelength-shifting plates increases the light collection of the PMT by a factor of $\sim$1.5.

2.4 The Radon-Reducing Air System

The air flow in the mine experiences seasonal changes: During the summer, cool air passes out of the mine; in the winter, cold air streams into the mine. Thus, the air in the vicinity of the SK site has radon concentration levels that range from 2,000 - 3,000 Bq/m^3 in the summer, when radon-rich mine air is flowing outward, and from 100 - 300 Bq/m^3 in the winter, when fresh air is flowing inward. In the SK dome, the radon levels are kept below 100 Bq/m^3 by pumping fresh air in from outside of the mine. Figure 2.8 shows a schematic diagram of the radon-reducing air system.

The radon-reduced air is generated by the following process: supply air from outside the mine is compressed to a pressure of $\sim$8 atm. This pressurized air is then dried and passed through charcoal columns. The carbon in the charcoal absorbs the radon gas, removing it from the air. The air then flows though a series of filters before passing though cooled charcoal (-40°C), which traps remaining radon. Finally, the resulting air is pumped into the SK dome

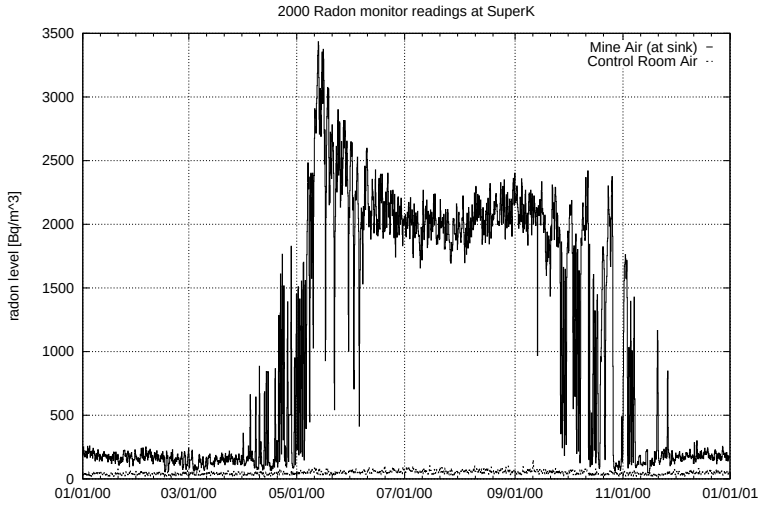

Figure 2.9: The upper, solid curve shows one year of measured radon concentration levels in the mine air [41]. The lower, dashed curve shows the corresponding radon levels in the SK dome. Strong seasonal variations in the flow of mine air affect the radon level in the vicinity of the detector.

at a flow rate of 10 m^3/min.

The supply air has radon levels from 100 to 300 Bq/m^3. The radon-reducing air system removes ∼99.98% of the radon, so that the air injected into the detector area has a radon concentration of ∼10 mBq/m^3. Typical radon concentrations in the dome are measured to be ∼40 Bq/m^3. Figure 2.9 shows one year of measured radon concentrations in the mine air and in the SK dome air.

Double doors at the entrance to the SK area reduce the amount of radon-rich mine air that directly enters the dome. Positive air pressure is maintained in the dome to further prevent mine air from entering.

2.5 The Water Purification System

Clean water is crucial to SK's ability to make precision measurements. Inpurities in the water cause light to be absorbed and scattered, which limits the transmission of Cherenkov photons. Additionally, radioactive impurities such as ^{222}Rn gas are a background source for solar and supernova neutrino studies. To minimize these effects, a water purification facility was constructed to manufacture and maintain pure water for the detector.

The effort to improve the purity of the SK water has been continuous throughout the operation of the detector. As a result, the water purification system has been modified and improved several times during the operation of SK-I [42, 43, 41]. Figure 2.10 shows a schematic view of the water purification system as of the end of Super-Kamiokande-I in July 2001.

A natural underground aquifier in the Kamioka mine serves as the initial source of the SK water. Once the detector is filled, the water is continuously recirculated through the purification system at a flow rate of 30 $\sim$ 70 metric tons per hour. The various stages of the purification system are described as follows:

- **1 μm mesh filter:**
  Removes large contaminants such as dust.
- **Heat exchanger:**
  Cools water that is heated by the pumps of the purification system. Low water temperatures decrease the PMT dark noise rate and suppress the growth of bacteria. Typical water temperatures are 14.2°C before the first heat exchanger and 12.9°C after the second heat exchanger.
- **Cartridge polisher:**
  A high performance ion exchanger that removes metal ions from the water.
- **UV sterilizer:**
  Kills any bacteria that might have survived in the cool water.
- **Radon-free air dissolving tank:**
  Dissolves air from the radon-free system into the water to improve the radon removal capabilities of the vacuum degasifier.
- **Reverse osmosis filter:**
  A high-performance membrane that removes dissolved gases and contaminants down to masses of 100 molecular weight.
- **Vacuum degasifier:**
  Further removes dissolved gases from the water, including $\sim$96% of the dissolved radon gas.
- **Ultra filter:**
  Removes small contaminants down to sizes of 10 nm.

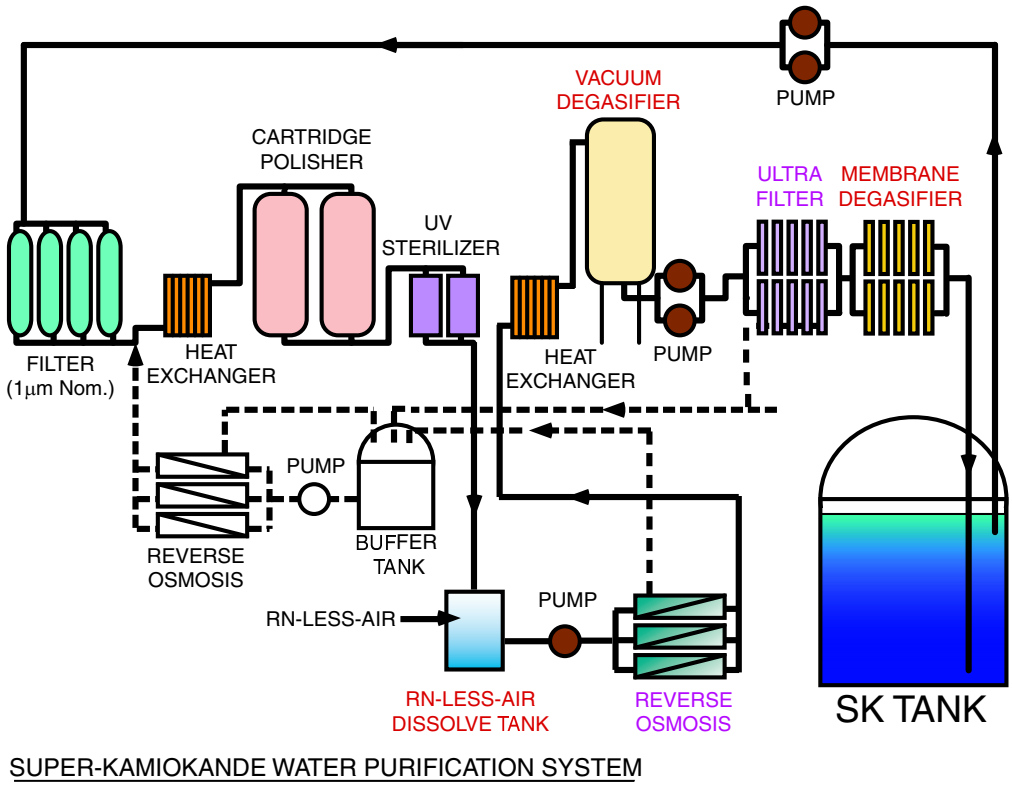

Figure 2.10: A schematic view of the water purification system.

- **Membrane degasifier:**
  Further removes dissolved radon gases with a removal efficiency of 83%.

The typical resistivity of water entering the purification system from SK is 11 MΩ·cm. After purification, the water has an average resistivity of 18.20 MΩ·cm, which is very close to the chemical limit of 18.24 MΩ·cm. Once processed by the purification system, the water is returned to the detector.

2.6 The Data Acquisition Systems (DAQ)

The data acquisition system (DAQ) monitors the output pulses from every PMT and records the time and amplitude of each hit. The DAQ is also responsible for differentiating collections of dark noise hits (which can be discarded) from data that should be saved for analysis. In the latter case, the DAQ must send a "trigger" indicating that the collection of hits, called an

"event," should be stored.

The ID and OD DAQ systems were designed by different groups for different purposes; therefore, their structure is different. When the DAQ is reading out existing data, it is unable to receive new data, which results in dead time. The ID was built to make precision measurements, and so the ID DAQ was designed to minimize dead time in the data collection process. To that end, only ID PMTs that contain hits for the current event are read out. Additionally, each PMT channel is equipped with dual signal-processing electronics hardware, so the channel can continue to collect data from new hits on one sub-channel while information from the current hit is being read out on the other.

The OD was built to detect particles entering the detector from outside, such as comic ray muons. Therefore, for any given event, the OD DAQ is designed to accumulate information from the PMTs for a longer period of time than the ID DAQ; OD hits are collected from before and after the time window in which ID hits are recorded. OD hits preceding or following ID activity can determine, respectively, whether a particle entered or exited the ID. In the search for SRN, the OD is used as a veto: any event with a signal in the OD is not considered to be an SRN candidate.

2.6.1 The ID DAQ

A schematic diagram of the ID DAQ system is shown in Figure 2.11.

Each of the 11,146 ID PMTs has a signal cable that is connected to a single channel of a front-end electronics unit. This electronics unit is called an Analog Timing Module (ATM). The ATM serves as both an analog-to-digital converter (ADC) and a time-to-digital converter (TDC); it digitizes the output time and charge information of each hit PMT. Each ATM channel is self-enabling: a threshold of $\sim \frac{1}{4}$ p.e. required for a signal to be recorded. After a channel enables, its hit information is stored for 1.3 μsec, after which this information is discarded if no global trigger (see section 2.6.3) has been issued.

When a global detector trigger does occur, all of the channels that have been enabled are digitized. During this process, all hit channels are switched to their other sub-channel to prevent dead time in the data taking. The ATM outputs a twelve bit signal, which is sent to a Super Memory Partner (SMP) module.

The ATM channels have a 450 pC dynamic range, with a 0.2 pC charge resolution, and a 1,300 ns dynamic range, with a 0.4 ns timing resolution. The ATM has a temperature variation of about 0.6 pC/°C and 0.8 ns/°C.

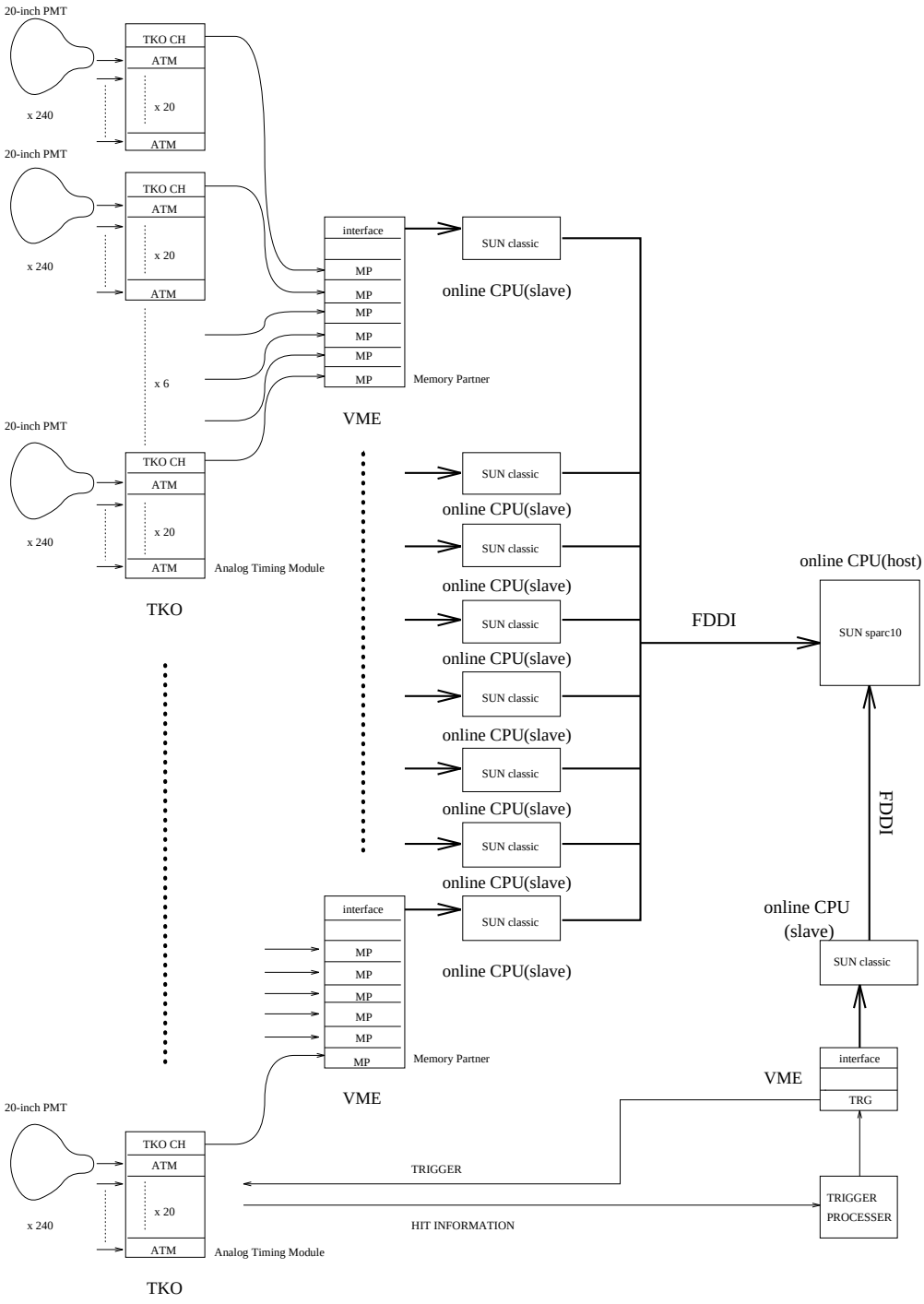

Figure 2.11: A schematic diagram of the ID DAQ

To correct for fluctuations in temperature, pedestal data are taken every 30 minutes. Each ATM accepts twelve input channels. There are 948 ATM cards, which are housed in a Tristan-KEK-Online (TKO) crate. There are 48 such TKO crates, typically holding 20 ATM cards each [44], and they are stored in the four electronics huts that are located in the SK dome area.

Every TKO crate also contains a GO-NoGo (GONG) module and a Super Control Header (SCH). The GONG modules distribute the global trigger signals and event identification numbers to each ATM. The SCH transfers the digitized ATM data to the SMPs, which are housed in a Versa Module Europe (VME) crate, for temporary storage. Each electronics hut contains two VME crates that, in turn, hold six SMP modules.

A Bit-3 VME-SBUS interface card is used to transfer the data from the SMP modules to a Sun workstation. Eight workstations are used to collect data from all of the ID PMTs; the data is then sent, via a dedicated Fiber Distributed Data Interface (FDDI) optical network, to the on-line host computer. This computer assembles all of the compiled data into one coherent event and then sends it to the off-line system described in section 2.7.

There are two time stamps associated with each SK event. The relative timing between events is measured with a 48 bit counter that is driven with a 50 MHz clock. This clock allows the event separation to be measured with a resolution of $\sim$20 ns. The absolute time of each event is provided by a GPS receiver. In this way, a UTC time stamp is obtained that is accurate to $\sim$200 ns.

Further information about the ID DAQ can be found in reference [41].

2.6.2 The OD DAQ

Unlike the ID PMTs, photomultipliers in the OD do not have a dedicated signal cable. Instead, a high-voltage capacitor network, located on a custom-built "paddle card," is used to extract the analog PMT signal from the high-voltage power supply cable; twelve PMTs are connected to each paddle card. After the extraction, the PMT signal is sent to a custom-built charge-to-time conversion (QTC) module via coaxial ribbon cables. Similar to the ID ATM channels, the QTCs are self-enabling: if the amplitude of the pulse exceeds a 25 mV threshold, corresponding to $\sim$0.5 p.e., the QTC module generates an Emitter-Coupled-Logic (ECL) pulse. The leading edge of the ECL pulse represents the hit arrival time, and the width of the pulse is proportional to the log of the charge in the hit channel.

The ECL pulses are digitized by a LeCroy 1877 Pipeline TDC. The TDC module records both the leading and trailing edge of the pulse, from which the

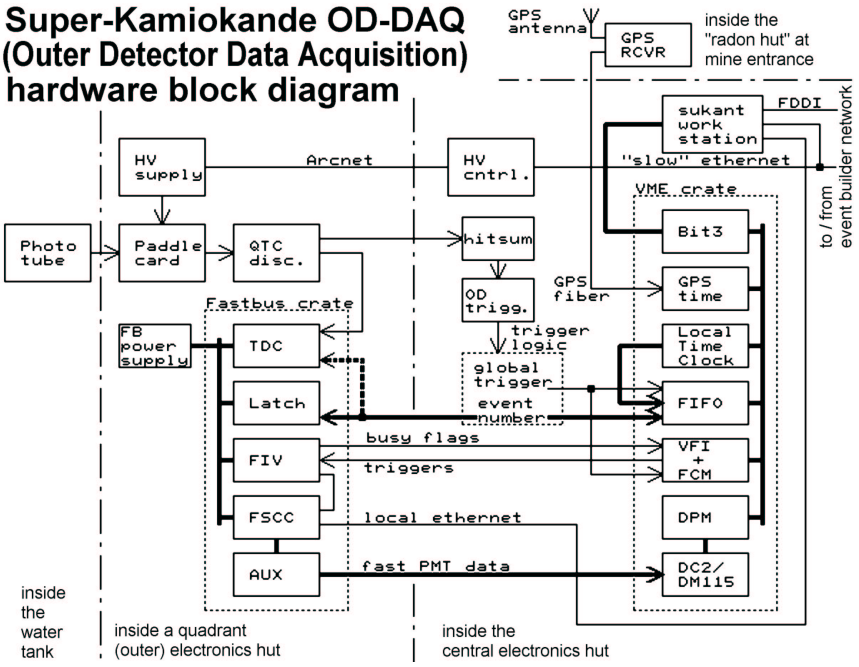

Figure 2.12: A schematic diagram of the OD DAQ

charge and timing information are obtained. Each TDC module has 96 input channels, one for each PMT. There are five TDC modules in each of the four electronics huts.

Each TDC channel works as a buffer that can store up to eight QTC pulses for up to 32 μsec. If a global trigger is issued, all TDC channels are digitized and read out simultaneously. OD data are saved in a window that begins 10 μsec before the trigger and ends 6 μsec afterwards. During the digitization process, the OD DAQ experiences a dead time of about $2 - 15$ μsec. If another global trigger is received during the OD dead time, a flag bit is put into the data stream to note this conditon.

After digitization, the TDC signals are collected by a Fastbus Smart Crate Controller (FSCC) module, and then transmitted via ethernet to an on-line Sun workstation. This computer collects the OD PMT data, sorts them, formats them, and then sends them to the on-line host machine. The host machine then adds the OD information to the ID event data to form one completed event.

A schematic diagram of this system is shown in Figure 2.12. Further information about the OD DAQ can be found in reference [41].

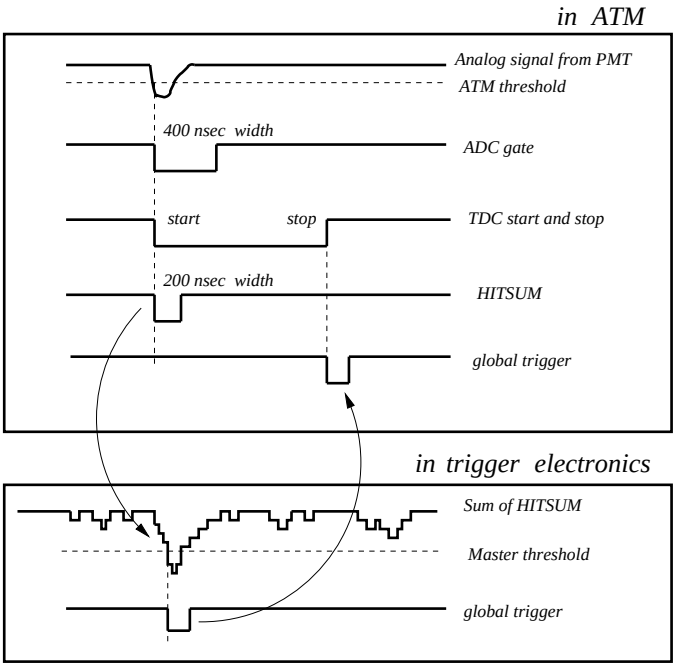

Figure 2.13: Overview of the ID trigger generation scheme for SK

2.6.3 Triggering the DAQ

There are several ways that a global trigger can be issued during data collection at SK. The most common triggers are generated by the ID DAQ system. When an ID PMT signal exceeds the theshold level of its ATM channel, it generates a "hitsum" pulse. This pulse has an amplitude of -11 mV and a width of 200 ns. The hitsum signals from all of the ATMs are summed, first in the individual electronics huts and then combined in the central hut. To reduce the effects of dark noise hits, the summed signal is AC coupled into several discriminators, each of which generates a specific ID trigger. There are three types of ID triggers: high energy (HE), low energy (LE), and super-low energy (SLE). Figure 2.13 shows an overview of the ID trigger generation.

The LE trigger is the primary trigger used in the SRN analysis. The threshold for the LE trigger is -320 mV, which corresponds to $\sim$29 hit ID PMTs within a 200 ns window, after subtracting the average dark noise hit rate. The efficiency of the LE trigger is evaluated by using the DT generator (see Section 3.8); above 6.5 MeV, the efficiency is 100%. The LE trigger rate is $\sim$16 Hz.

The SLE trigger was implented in May 1997 for the purpose of obtaining

Table 2.2: Information about the threshold and rates for the primary SK triggers.

Type	Start Date	End Date	Threshold	Rate
OD	May 1996	July 2001	19 OD hits	3 Hz
HE	May 1996	July 2001	-340 mV (31 ID hits)	6 Hz
LE	May 1996	July 2001	-320 mV (29 ID hits)	16 Hz
SLE1	May 1997	May 1999	-260 mV (24 ID hits)	100 Hz
SLE2	May 1999	September 1999	-250 mV (23 ID hits)	160 Hz
SLE3	September 1999	September 2000	-222 mV (20 ID hits)	530 Hz
SLE4	September 2000	July 2001	-186 mV (17 ID hits)	1600 Hz

a lower energy threshold for SK. The rate of background events increases exponentially as the trigger threshold drops. Therefore, to collect data at lower energies, this high background must be reduced to a level that can be handled by the on-line system. The lowest energy events, which have only triggered the SLE, are sent to on-line filtering software called the "intelligent trigger." Most of these super-low energy background events originate from the walls of the detector, e.g. γ-rays from the surrounding rock or radioactive decay in the PMT glass. The intelligent trigger removes these events by performing two separate vertex fits on-line. Only events that appear to originate more than 2 m from the walls of the SK ID are processed for further analysis; all other events are discarded. During SK-I, the SLE threshold was lowered several times as additional CPUs were added to the intelligent trigger system.

A similar procedure is used to generate the OD trigger, except that the output from the QTC modules is used. Each QTC module generates a 200 ns wide pulse for triggering; this pulse is proportional in height to the number of hit channels in the module. When an OD trigger occurs, there is a 100 ns delay before issuing the global trigger. The purpose of the delay is to see if a coincident ID trigger will occur. If no ID trigger happens in this interval, the OD signal will issue a global trigger. The OD DAQ is only read out in the case of an OD or HE trigger.

A summary of information about each of the ID and OD triggers can be found in Table 2.2.

In addition to the self-generating triggers, SK has external triggers that are available for special runs (e.g. calibration) and for to obtain special types of events (e.g. unbiased periodic trigger). When a global trigger is issued, eight

Table 2.3: The eight SK trigger types and their corresponding trigger bits.

Trigger Bit	Type of Trigger
0	Low Energy (LE)
1	High Energy (HE)
2	Super-Low Energy (SLE)
3	Outer Detector (OD)
4	Periodic trigger
5	Calibration trigger
6	Global trigger veto start
7	Global trigger veto stop

bits of data are written to record the trigger types that were asserted for that event. The trigger type corresponding to each bit is summarized in Table 2.3.

2.7 Off-line Data Processing

After the host machine has assembled all of the information about a particular event, this information is sent to another workstation, called the "reformatter." The reformatting processes take the raw data files output by the on-line host and convert them to the platform-independent ZEBRA Bank System (ZBS) format. The ZEBRA format was developed at CERN [45]; by using it at SK, it is possible to analyze SK data on computers with different architectures. As the energy theshold of SK was lowered, the detector's trigger rate increased, even with on-line filtering by the intelligent trigger. At the start of SK-I, the reformatting was handled by a single CPU; by the end of SK-I, three CPUs were necessary to handle the higher data rate.

The reformatted data are sent out of the mine via a 4 km FDDI optical fiber. After leaving the mine, the data are stored to a magnetic tape library (MTL). Originally, SK-I used a 12 Tbyte MTL system. However, in order to keep up with the increased data flow generated by a lower energy threshold, the MTL system was upgraded twice. By the end of SK-I, a 200 Tbyte MTL was being used for data storage, and the rate at which data were written to MTL was $\sim$40 Gbytes/day.

When storing events to the MTL, the information about hit PMTs is stored as the raw number of ADC and TDC counts because storing the actual physi-

cal quantities of the data would increase tape consumption by a factor of three. Therefore, the analysis software that reads the data from tape includes subroutines that perform this conversion. The conversion from ADC and TDC counts to charge (pC) and time (ns), respectively, is done using calibration tables that will be discussed in Section 3.1.

Until August 2000, the reformatter sent a second copy of the data to a dedicated workstation, which operated two Digital Linear Tape (DLT) drives. The data were stored on DLTs, which hold 20 Gbytes each, that were shipped to Stony Brook and used for the U.S. Super-Kamiokande analysis. In 1998, after results from both the U.S. and Japanese SK groups had been published, the two independent analyses were merged into a single unified analysis. At this point, the DLTs served only as a backup of the data in Kamioka. After August 2000, the DLT system was discontinued.

Chapter 3

Detector Calibration

Super-Kamiokande was designed to be a simple and elegant detector. Nevertheless, there are many components of SK that require extensive calibration. The charge and timing response of each PMT must be calibrated so that the output TDC and ADC values can be properly translated into pico-Coulombs and nanoseconds. The detector water must be continually monitored for changes in its capacity for light transmission. Such changes must be corrected for, as they directly affect the light-gathering ability of the detector. For events with low energy, such as those expected from SRN interactions, the amount of collected light corresponds to the energy of the event. Substantial calibration is necessary to understanding the correlation between the number of hit PMTs in an event and the energy of the event. These calibrations include the use of naturally occuring events like cosmic ray muons, as well as external equipment such as an electron linear accelerator (LINAC), a radioactive Ni-Cf source, and a deuterium-tritium neutron generator (DTG). Besides its central role in the primary energy calibration of the detector, the LINAC is also responsible for determining the vertex and angular resolution of the reconstruction algorithms.

3.1 PMT Calibration

PMT calibrations for the ID are performed so that their raw charge and timing outputs can be properly interpreted during the event reconstruction (see Chapter 4). Additionally, it is important to adjust the charge response from individual PMTs in order to obtain near-uniformity throughout the detector. Although PMT calibrations are also performed for the OD [46], they are significantly less important for the SRN search and are therefore not discussed here.

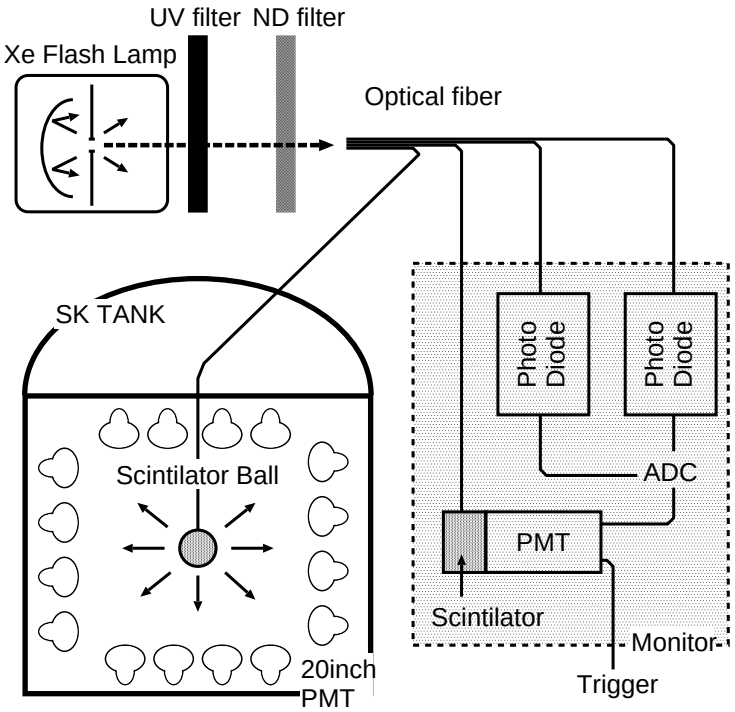

Figure 3.1: An overview of the Xe calibration system. Two photodiodes and a 5 cm PMT monitor the output of the Xe lamp that is sent into the ID.

3.1.1 Relative Gain

The gain (G) of a PMT is the factor by which the original photo-electron is multiplied before leaving the PMT. For instance, a single photo-electron in an SK ID PMT results in a cascade of $\sim 10^7$ electrons; therefore, the gain is $\sim 10^7$. Mathematically, the gain is approximated by:

$$G = aV^b \tag{3.1}$$

In this equation, a and b are constants and V is the voltage that is applied to the PMT. For each PMT the values of a and b differ slightly; in order to obtain a uniform detector response, the voltage must be adjusted so that the gain of all ID PMTs is roughly equal. To this end, a xenon flash lamp is used to measure the relative gain of the ID PMTs and to determine what voltage adjustments are necessary.

A diagram of the Xe calibration system is shown in Figure 3.1. The Xe lamp produces a flash of light with less than 5% variation in the intensity of the

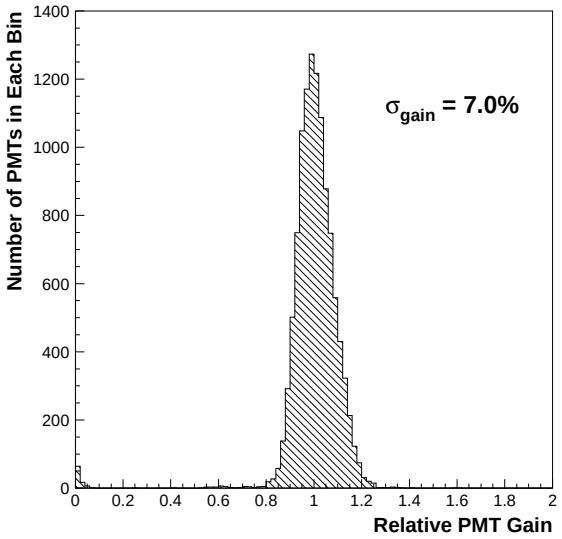

Figure 3.2: Results from the Xe calibration [41]. The spread in the gain distribution is found to be 7%.

individual pulses. This light is then passed through two filters: an ultra-violet (UV) filter only allows UV light to be transmitted, and a neutral density filter is used to control the intensity of the light. After it is filtered, the light beam is split and sent along two separate paths. One beam is sent to a monitoring system and the other goes via optical fiber to a scintillator ball that has been lowered into the SK tank. The scintillator ball is made of acrylic with BBOT and powdered MgO additives. BBOT is a wavelength-shifting scintillator that absorbs the UV Xe light and re-emits it with a peak wavelength of 440 nm, which is similar to the wavelength of Cherenkov light. MgO is a diffusing agent that causes the light to be emitted uniformly.

For every Xe flash, the light level recorded by each PMT is corrected for attenuation in water, angular acceptance of the PMT, and small deformities in the scintillator ball. The corrected charge output is then normalized to the intensity of the Xe flash, as recorded by the monitoring system. This result is the relative gain of the PMT. At the start of SK-I, Xe calibration data were taken with the scintillator ball placed at various positions within the SK tank. The results of this calibration were used to determine the supply voltage applied to each PMT; these voltages were adjusted to minimize the spread in the relative gain.

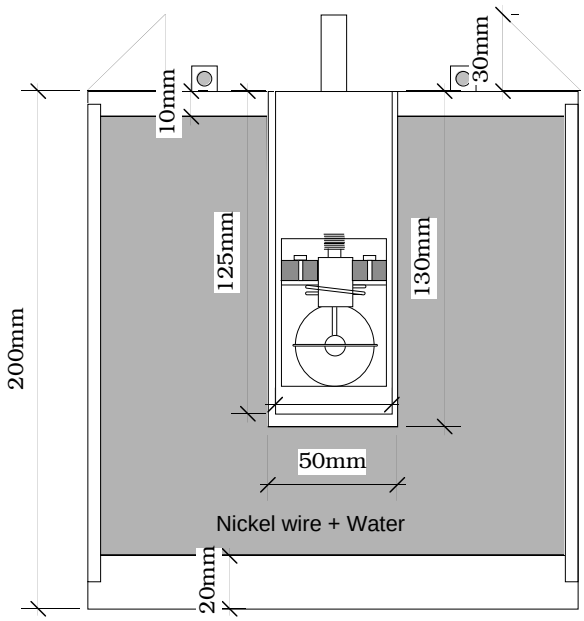

Figure 3.3: An overview of the Ni-Cf calibration system. Note that this is a cross section of a cylindrical container.

Figure 3.2 shows the spread in the relative gain after the PMT supply voltages were adjusted. The horizontal axis is the relative gain normalized by its mean value. The r.m.s. spread in the relative gain distribution is 7%. This is corrected for in the reconstruction software.

3.1.2 Absolute Gain

The light intensity from the Xe lamp is quite large, with about 100 – 200 p.e. per PMT, compared to the single p.e. hits expected for SRN events. Therefore, the absolute gain of each PMT must be checked at the single p.e. level; this is done by using a Ni-Cf source.

Figure 3.3 shows a diagram of the Ni-Cf calibration source. At the core of the polyethylene container, there is a ^{252}Cf radioactive source with an intensity of 6.3 $\times 10^4$ Bq. The Cf undergoes spontaneous fission and emits fast neutrons, which are then thermalized in the surrounding water within the container. The Ni wire captures these thermalized neutrons and emits γ-rays in response, via the reaction Ni(n,γ)Ni. The γ-rays, which have a maximum energy of 9.0 MeV, undergo Compton scattering on the electrons in the SK water, and

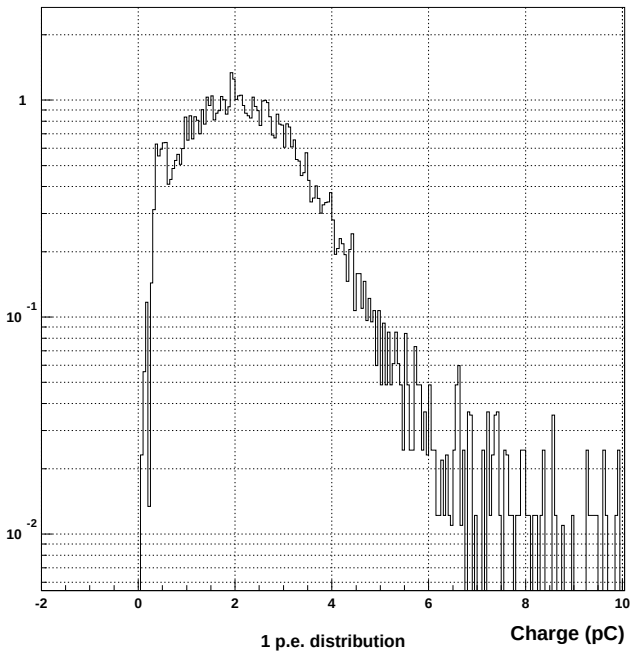

Figure 3.4: The charge distribution for single photo-electrons from the Ni-Cf calibration

the Compton electrons produce Cherenkov photons.

Due to the low energy of the γ-rays, it is safe to assume that each PMT hit during the Ni-Cf calibration has only a single p.e. The single p.e. distribution for a typical PMT in the Ni-Cf calibration is shown in Figure 3.4. The peak charge for each PMT is used as the conversion factor to translate charge into p.e. for that tube. The mean value of this conversion factor is 2.06 pC/p.e.

3.1.3 Timing

Accurate timing information is essential for reconstructing the vertex and direction of events. Corrections must be made to account for individual differences in the time, relative to the global trigger, that each hit PMT records. Such differences originate from variations in the length of the PMT signal cables and from the response time of the electronics. The relative timing is also a function of the measured charge; PMTs that are exposed to a greater level of light exceed their ATM discriminator threshold sooner. This effect is known

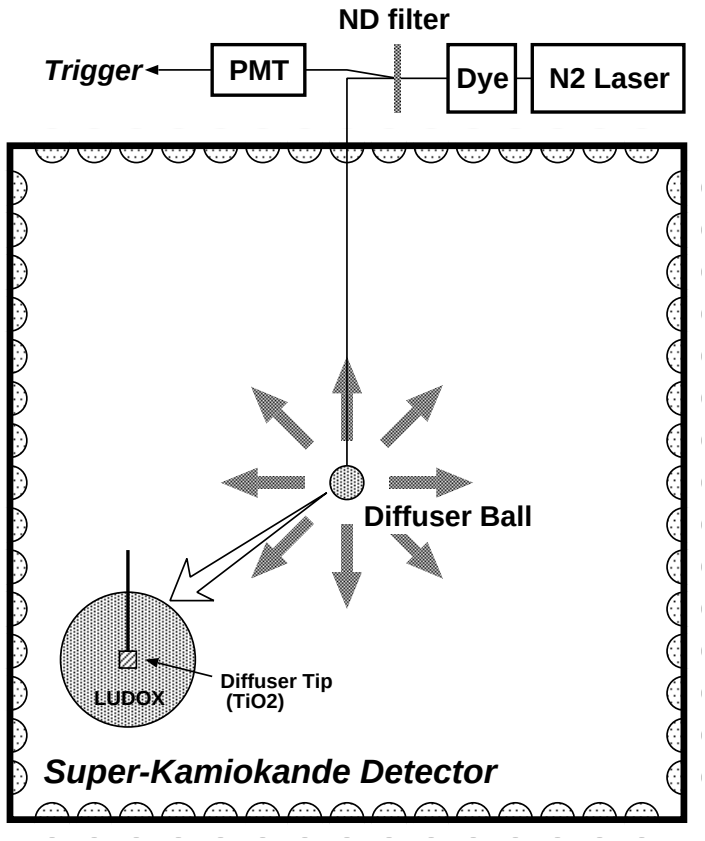

Figure 3.5: The laser system used for calibrating the ID PMTs. The inset shows a close-up view of the light-diffusing ball.

as slewing.

A laser calibration system, shown in Figure 3.5, is used to measure the relative PMT timing. Pulses of light, each lasting for 3 ns, are generated by a N_2 laser. The light, generated with a wavelength of 337 nm, is sent to a dye laser that shifts this wavelength to 384 nm, which is similar to that of Cherenkov light. This light is passed through a variable attenuation filter and then split along two separate paths: one path leads to a monitoring system and the other goes via optical fiber to a light-diffusing ball that has been lowered into the SK tank.

The ball has two components, TiO_2 and LUDOX, both of which serve to diffuse light. The TiO_2 forms a 3 mm cap on the optical fiber. This cap is embedded in a ball of LUDOX, which is a silica gel composed of 20 nm glass fragments. This combination produces diffuse light, but it does not introduce

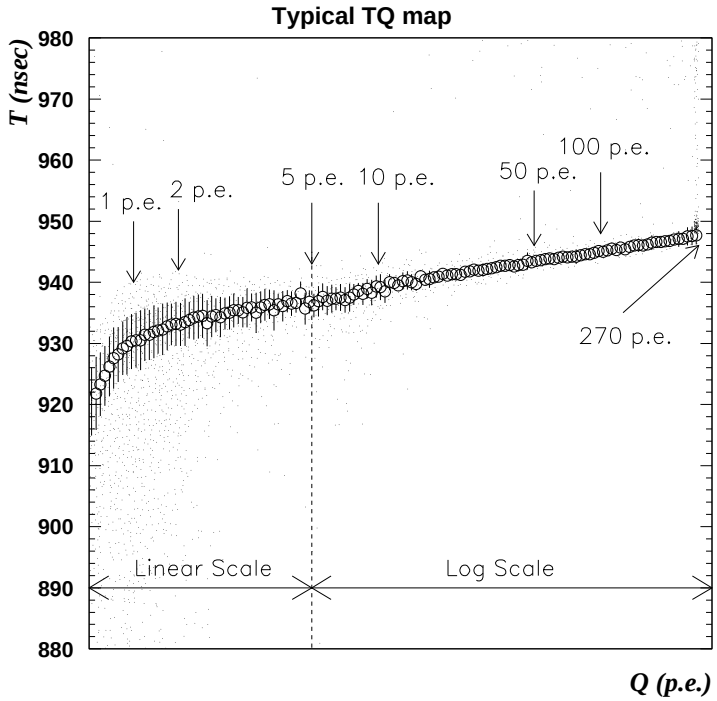

Figure 3.6: The timing response of one PMT as a function of charge, known as the "TQ map" for that PMT [41].

a significant timing spread.

By using the variable attenuation filter to change the intensity of the output light, the PMT time response can be studied at p.e. levels ranging from 1 p.e. to several hundreds of p.e. The results of the laser calibration for one PMT are shown in Figure 3.6. The small points correspond to a measured value for one event and the open circles show the mean value. These mean values are used to create a look-up table, called a "TQ map," of the timing response as a function of charge. A TQ map is made for every ID PMT, and these maps are referred to by the event reconstruction software. The 1 σ error bars on the mean values give the timing resolution. Typically, the timing resolution for a 1 p.e. signal is 3 ns.

3.1.4 Stability of the PMT Calibrations

At the beginning of SK-I, extensive PMT calibrations were carried out using the Xe, Ni-Cf, and laser systems at various positions within the detector.

These initial calibrations were used to adjust the PMT supply voltages and generate the initial TQ maps. During SK-I, these calibrations were repeated periodically and corrections were made for any observed deviations from the previous calibrations.

In October 1999, an automated calibration system was installed in the SK tank to provide continuous monitoring of the relative gain and relative timing of the PMTs. A scintillator ball for the Xe system was placed at detector coordinates (x,y,z) = (+353.5 cm, -70.7 cm, 0.0 cm) and the Xe lamp was set to flash once every 216 seconds. Xe calibration events were collected each day and automatically checked for PMTs whose relative gain had shifted by more than 1%.

Similarly, a light-diffusing ball for the laser calibration was placed at detector coordinates (x,y,z) = (-141.4 cm, -70.7 cm, 0.0 cm). The laser was flashed once every 360 seconds. Laser calibration events were collected each day and then checked for PMTs that had deviated by more than 1 ns from the mean timing value. When the number of PMTs with such deviation accumulated to greater than 100, the TQ map was updated; this occured about every six months.

3.2 Water Transparency Measurement

Due to the detector geometry, Cherenkov photons can travel up to 50 m in SK before reaching a PMT. Light attenuation and scattering in water directly affect the number of photons that are detected by the PMTs. Since the energy of an event is mainly determined from the number of hit PMTs, the water transparency must be precisely determined for an accurate energy measurement.

There are two important goals for the water transparency measurement: to understand the wavelength dependence of light attenuation in water, and to monitor the time variation of the attenuation parameter. A different measurement technique is used to achieve each goal.

3.2.1 Wavelength Dependence

The wavelength dependence of the water transparency is measured by using a tunable laser and a CCD camera. Figure 3.7 shows a diagram of this system. A Nd:YAG laser pumps a titanium-sapphire laser, which produces monochromatic light with a wavelength that can be tuned between 337 nm and 600 nm. The light is split into two paths; one path leads to a monitoring

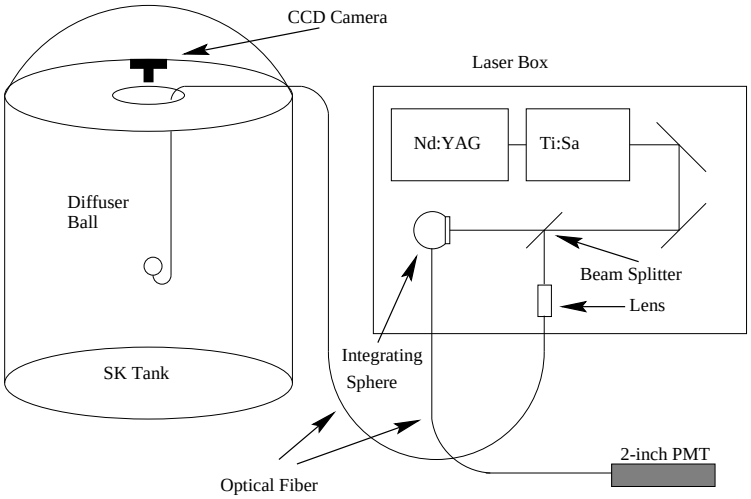

Figure 3.7: An overview of the system used to measure the wavelength dependence of light attenuation in water.

system and the other goes via optical fiber to a light-diffusing ball that has been lowered into the SK tank. The light-diffusing ball is composed of acrylic with powdered MgO added. A CCD camera at the top of the tank measures the intensity of the light emerging from the ball. The monitoring system consists of an integrating sphere and a 2 inch PMT. The pulse height of the signal from this reference PMT is used to normalize the measurement taken with the CCD camera. CCD measurements are taken with the light-diffusing ball at several different depths, and the results are fit with the following function:

$$I(d) = I_0 \times \frac{exp(-d/\lambda)}{d^2} \tag{3.2}$$

where $I(d)$ is the normalized light intensity measured by the CCD camera, I_0 is the intensity of the light source, d is the depth of the light-diffusing ball, and λ is the water transparency. Figure 3.8 shows the intensity of the CCD signal as a function of distance, obtained using 400 nm light. At this wavelength, the best fit to the data gives a water transparency of 72.1 m $\pm$ 3.2 m. Figure 3.9 shows the results from measurements taken at several other wavelengths. The wavelength dependence of the water transparency obtained by this method is used to tune the detector simulation software (see Section 6.2).

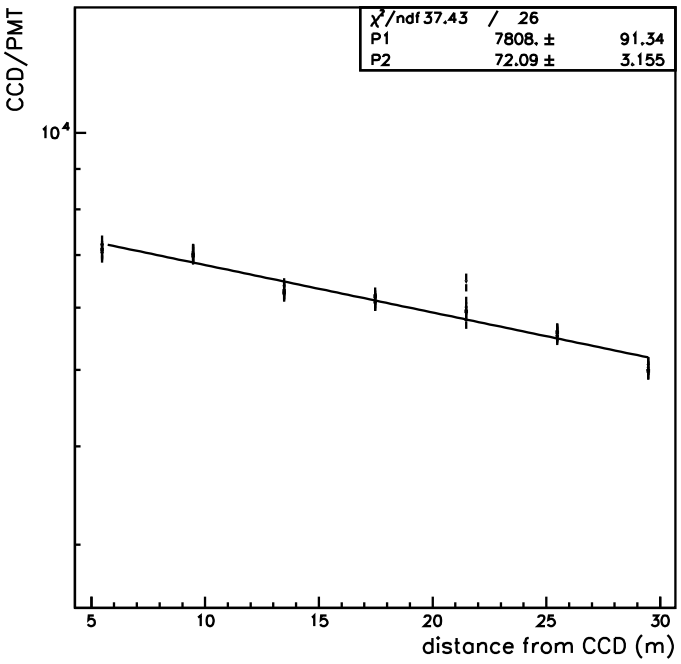

Figure 3.8: Intensity of the normalized CCD measurement as a function of the depth of the light-diffusing ball. The inverse of the fit slope is the water transparency, in this case 72.1 m ± 3.2 m

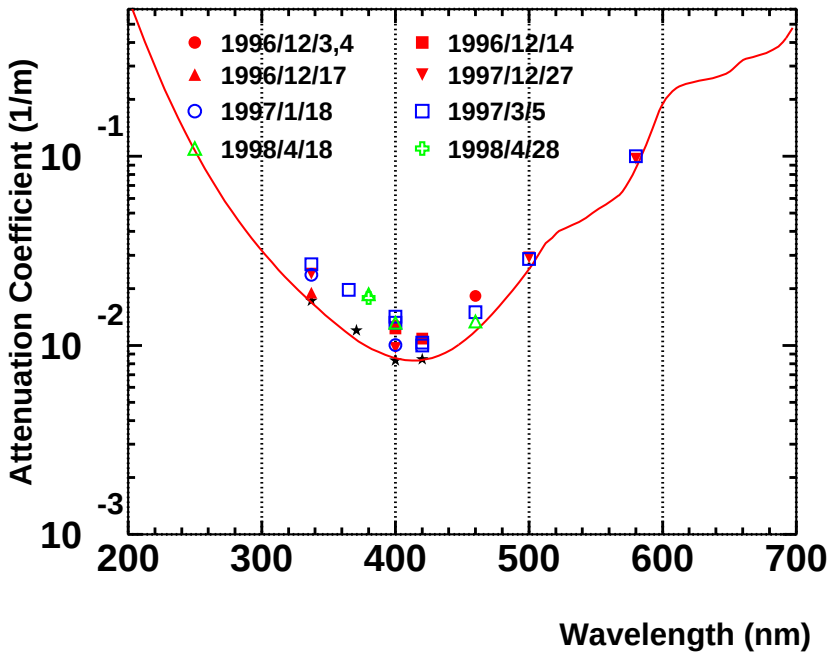

Figure 3.9: Water tranparency as a function of wavelength [41]. The solid line shows the value used in the detector simulation software.

3.2.2 Time Variation

The water transparency in SK is monitored continuously by using the decay electrons (and positrons) from cosmic ray μ (CRM) events that stop in the detector:

$$\mu^- \rightarrow e^- + \bar{\nu}_e + \nu_\mu$$

and

$$\mu^+ \rightarrow e^+ + \nu_e + \bar{\nu}_\mu$$

At SK's underground depth (2700 meters water equivalent), CRMs reach the detector at a rate of $\sim$2.5 Hz. Approximately six thousand muons per day stop in the inner detector and produce a decay electron (or positron).

To monitor the water transparency effectively, it is important to have a pure sample of μ-e decay events. Several criteria are applied to select these events:

- The time difference (ΔT) between the stopping μ event and the μ-e decay candidate must satisfy: 2.0 μsec $< \Delta T <$ 8.0 μsec.
- The reconstructed vertex of the μ-e decay candidate must be contained within the 22.5 kton fiducial volume.
- The effective number of hit PMTs must be at least 50. Hit PMTs are counted in this number if their timing lies within a 50 nsec window after time-of-flight (TOF) subtraction.

These criteria select $\sim$1500 μ-e decay events daily, which provide sufficient statistics to search for variations in the water transparency on the time scale of about one week.

Figure 3.10 shows how the individual μ-e decay events are used to obtain the water transparency. To remove the effects of scattered and reflected light, PMTs are selected using the following criteria:

1. PMTs must have timing that falls within the 50 nsec timing window after the TOF subtraction.
2. PMTs must be within a cone of opening angle $32^\circ \sim 52^\circ$ with respect to the direction of the decay electron.

The selected PMTs are projected onto an imaginary sphere of radius R that is centered on the event's vertex position. On this sphere, these PMTs lie in

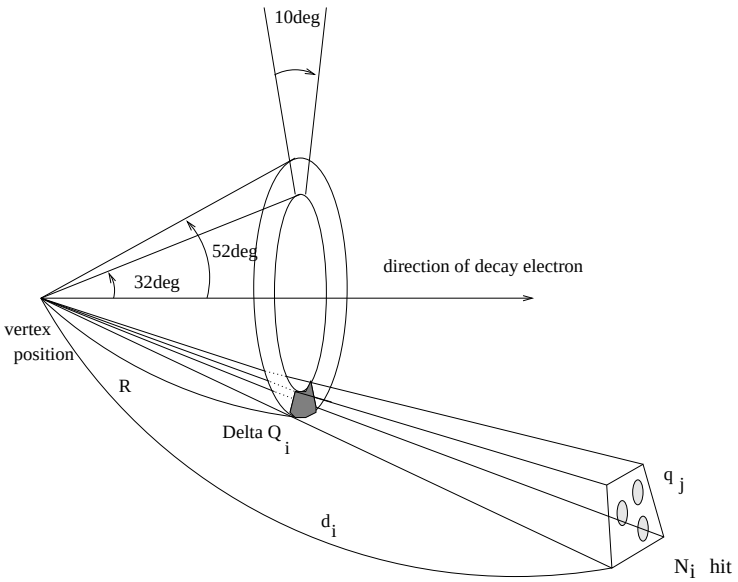

Figure 3.10: How to calculate water transparency from μ-e decay events.

a ring, which is divided into 36 equal sections. The effective number of hit PMTs (ΔN_i) in the i-th section of the ring is determined by:

$$\Delta N_i = \sum_{j=1}^{N_i} \exp\left(\frac{d_j - R}{\lambda_e}\right) \cdot 1 \tag{3.3}$$

where N_i is the number of hit PMTs in the i-th section of the ring, d_j is the distance from the event's vertex position to the j-th PMT position, and λ is the water transparency.

In principle, all ΔN_i (for $i = 1, 36$) should be equal. Therefore, since each ring segment is small, equation (3.3) can be re-written as:

$$\Delta N = \exp\left(\frac{r}{\lambda}\right) N(r) \tag{3.4}$$

where $r \equiv \sum_{j=1}^{N_i} d_j/N_i$ is the mean distance to PMTs in the i-th section, $N(r)$ is the number of hit PMTs per section as a function of distance, and R is set to zero.

The μ-e decay events have energies that are distributed according to the Michel spectrum (see equation 3.7); thus, each event has a different ΔN value. Inverting equation (3.4) and averaging over the Michel spectrum yields the following relations:

$$\overline{N(r)} = \exp\left(-\frac{r}{\lambda}\right)\overline{\Delta N} \quad (3.5)$$

$$\log(\overline{N(r)}) = -\frac{r}{\lambda} + \log(\overline{\Delta N}) \quad (3.6)$$

Log($N(r)$) distributions are made after accumulating one week of μ-e decay events. A typical distribution can be seen in Figure 3.11. These distributions are fit with a linear function; the inverse of the slope gives the water transparency value. In Figure 3.11, the slope corresponds to a water transparency of 9238 cm.

Figure 3.12 shows the SK water transparency as a function of time. Each point on the plot represents the water transparency measurement for one week. In order to reduce the effects of statistical fluctuations on the weekly measurement, the water transparency value for a given week is defined as a running average over five weeks of data that are centered on the given week. Variations in the water transparency are often caused by changes in the water purification system (see Section 2.5), such as cleaning the ultra-filters or altering the water circulation pattern.

3.3 Absolute Energy Scale

The effective number of hit PMTs in an event (N_{eff}, see Section 4.3) is used to determine the energy of the event. The absolute energy scale calibration provides a conversion factor for translating N_{eff} into an energy value. For the SRN search, two methods are used for the energy scale calibration; one involves an electron linear accelerator (LINAC) and the other uses μ-e decay events from stopping CRMs.

3.3.1 LINAC Energy Calibration

The LINAC is used to inject single mono-energetic electrons into the SK tank. The properties of these electrons are well known: the position of the injection point within the tank has an uncertainty of only a few mm, the direction of the LINAC events in the tank is always downward, the timing of these events is provided by a triggering mechanism within the LINAC, and the energy of the LINAC events is precisely determined, to within $\pm$20 kev, with a germanium detector. Therefore, the LINAC data can be used to calibrate multiple aspects of the detector response: absolute energy scale, energy reso-

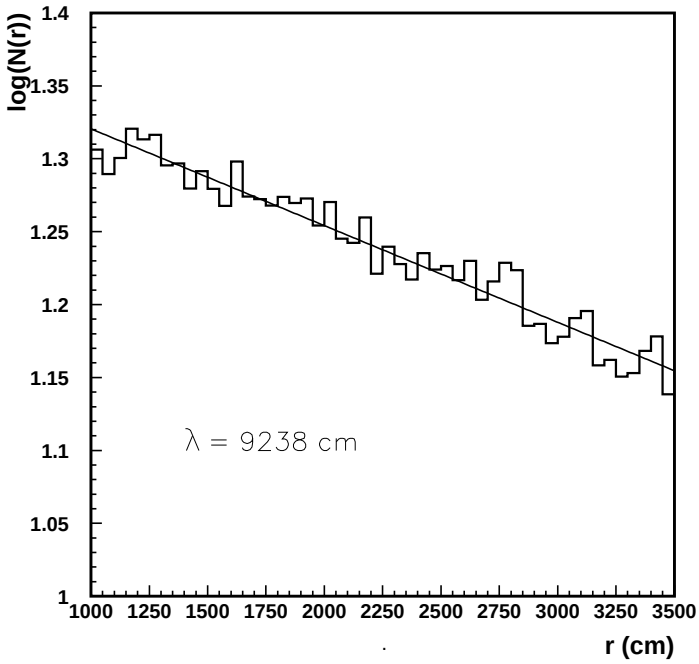

Figure 3.11: The $\log(N(r))$ distribution for a typical week of μ-e decay events. The slope measures the inverse of λ.

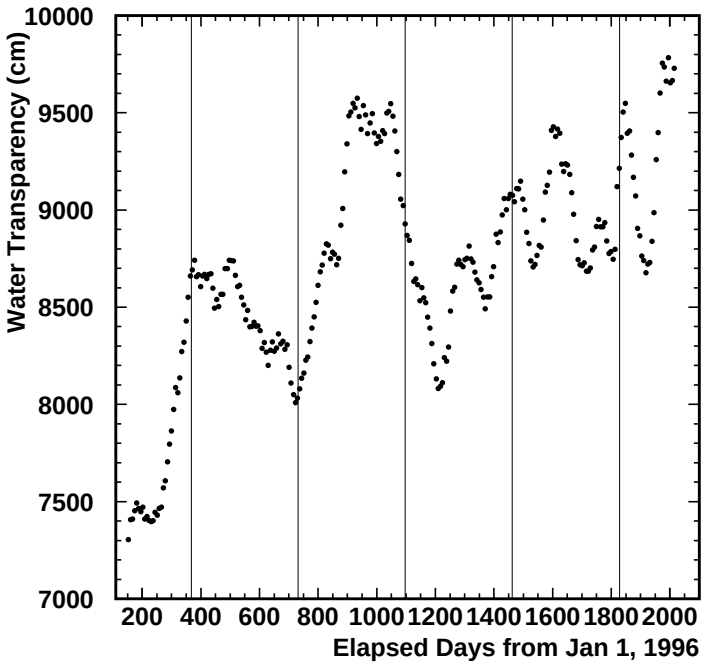

Figure 3.12: The time variation of the measured water transparency during Super-Kamiokande-I. Calendar years are separated by vertical lines.

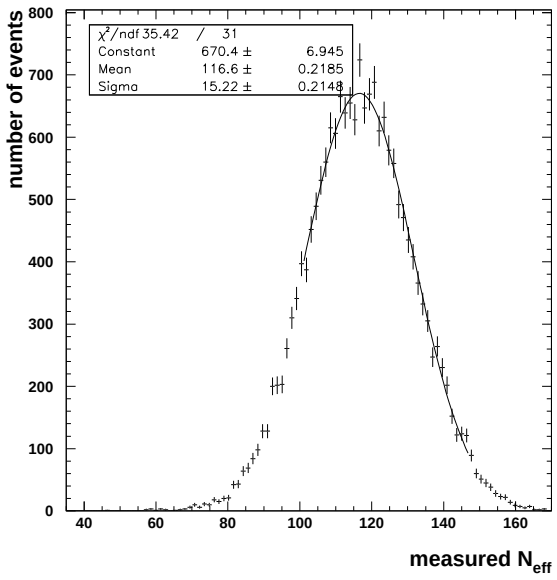

Figure 3.13: The N_{eff} distribution for a set of LINAC data with a beam momentum of 16.31 MeV.

lution, angular resolution, and vertex resolution. A more detailed description of the LINAC system can be found in Appendix A.

A LINAC data set consists of all the data taken at a particular position and beam momentum at one time. Each set of LINAC calibration data is reconstructed with the same software used for reconstructing regular data. The N_{eff} distribution of all the events in one LINAC run is fit with a Gaussian function, as shown in Figure 3.13. The mean value of the Gaussian fit is taken to be the N_{eff} value for the data set.

There is a $\sim$1% non-uniformity of N_{eff} within the fiducial volume, and LINAC data are only taken at nine positions. Therefore, a direct correlation cannot be made between the N_{eff} value and the total electron energy. To obtain the absolute energy scale, a Monte Carlo (MC) is used to simulate a set of LINAC events, which is then analyzed in the same way as the data. The simulated LINAC events are used to tune various parameters of the MC, such as scattering and absorption of light in water. The MC parameters that cause the simulated events to have an N_{eff} value closely matching that of the LINAC data are retained for future use in detector simulation. Figure 3.14 shows the reconstructed energy distributions for LINAC data and for the MC

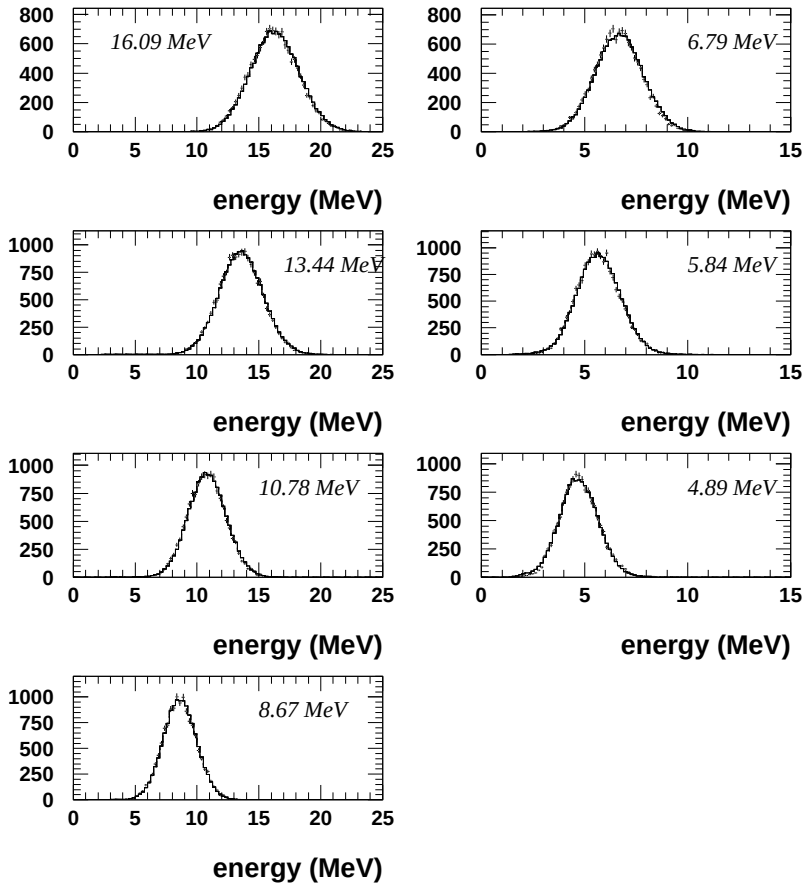

Figure 3.14: Reconstructed energy distributions for LINAC data and MC at the beam position (x,z) = (-12 m, +12 m) [47]. Cross marks represent LINAC data, while the histograms represent the MC.

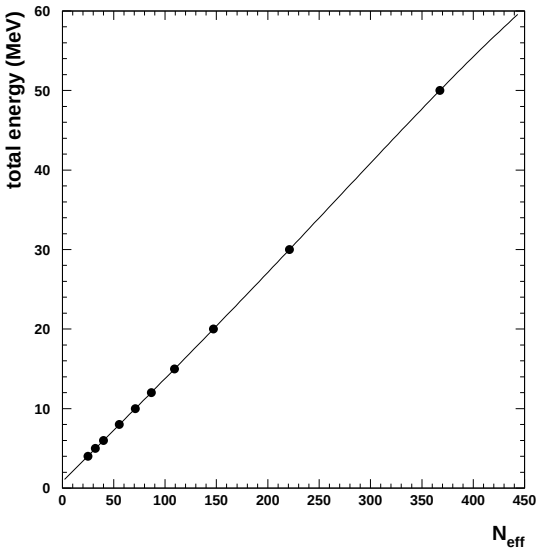

Figure 3.15: The correlation between the effective number of hits (N_{eff}) and the energy. Points represent mean N_{eff} values for MC generated at the given energies. The line shows the best 4-th order polynomial fit to these points, and it is used as the absolute energy scale.

after the parameter tuning has been completed.

Once the MC parameters have been selected, sets of simulated data are generated throughout the entire fiducial volume with energies of 4, 5, 6, 7, 10, 15, 30, and 50 MeV. The N_{eff} distribution for each of these simulated data sets is fit with a Gaussian to obtain the mean value, as shown by the points on Figure 3.15. A 4-th order polynomial function is used to interpolate the correlation between energy and N_{eff} to all energies, thereby setting the absolute energy scale of the detector.

The LINAC calibration is also used to determine the systematic uncertainty in the energy scale by evaluating the remaining differences between the LINAC data and the tuned MC. Figure 3.16 shows the deviation in the energy scale, defined as $(\frac{MC-Data}{Data})$, for each set of LINAC data. The error bars in this figure are statistical. The data taken at each position are averaged to get the energy dependence of the uncertainty in the absolute energy scale; these results are shown in Figure 3.17(a) with statistical and systematic error bars included. Similarly, the data taken at each beam momentum can be averaged to obtain the position dependence of the absolute energy scale; these results are shown

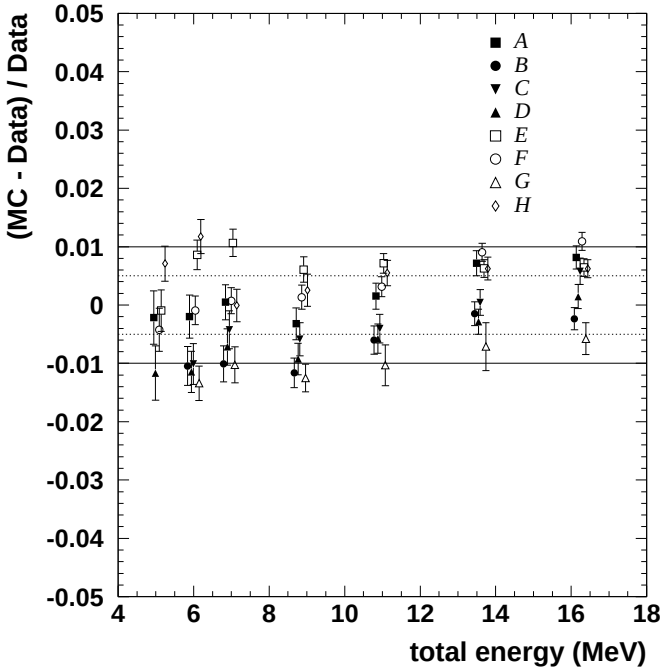

Figure 3.16: The relative difference between the reconstructed energy of LINAC data and the corresponding MC. The results are shown for all positions and beam momenta. The position tags match those shown in Figure A.1

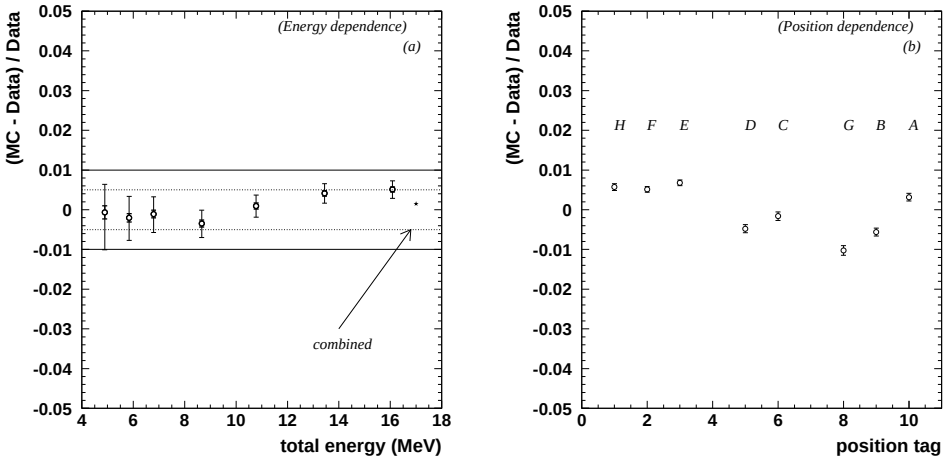

Figure 3.17: The relative difference between the reconstucted energy of LINAC data and the corresponding MC. (a) shows the energy dependence averaged over all positions. (b) shows the position dependence averaged over all energies.

in Figure 3.17(b), with statistical errors only.

At lower beam momenta, a larger fraction of the Cherenkov photons strikes the LINAC hardware, especially the end-cap. Uncertainties in the reflectivity of these surfaces increase the systematic error at those momenta. However, as seen in Figure 3.17, the deviation of the data from the MC is below $\pm 1.0\%$ at all positions and momenta.

3.3.2 Decay Electrons from Stopping Cosmic Ray Muons

The energy scale defined by the LINAC calibration is very precise. However, LINAC data only extend up to $\sim$16 MeV. The energy region of interest to the SRN search extends to higher energies (see Section 7.1) where the absolute energy scale has only been extrapolated from the LINAC measurements. In order to evaluate the consistency of the energy scale at these higher energies, decay electrons (and positrons) from stopping cosmic ray muons are used.

As discussed in Section 3.2.2, about 6000 CRMs stop in the SK ID each day and produce a decay electron. To obtain a high purity sample of μ-e decay events, the same criteria used to select events for the water transparency measurement are applied.

In a vacuum, the muon lifetime is 2.20 μsec. In water, 18.4% of the μ^- are captured by oxygen nuclei through the following process:

$$\mu^- \ + \ {}^{16}\mathrm{O} \ \rightarrow \ \nu_\mu \ + \ {}^{16}\mathrm{N}$$

This capture process reduces the effective lifetime of the μ^- to 1.80 μsec [48]; the average lifetime of a stopping muon in SK becomes 2.08 μsec.

The energy distribution of the μ-e decay events is called the Michel spectrum, and it is expressed by the following equation:

$$\frac{dN}{dE_e} \ = \ \frac{G_F^2}{12\pi^3} \, m_\mu^2 E_e^2 \left(3 - \frac{4E_e}{m_\mu}\right) \quad \left(E_e < \frac{m_\mu}{2}\right) \tag{3.7}$$

The spectrum shape of the μ^+ decay positrons follows this equation. However, the energy spectrum of the μ^- decay electrons is distorted by interactions with oxygen nuclei. Nearly all of the μ^- get trapped and enter a K-shell orbit around an oxygen nucleus. When the μ^- decays, its daughter electron is then influenced both by the orbital motion of the parent μ^- and by the electric potential of the oxygen nucleus.

Figure 3.18 shows the calculated energy spectra of the decay positrons and electrons. The positron spectrum is represented by the solid line histogram, while the electron spectrum is indicated by the dashed line histogram.

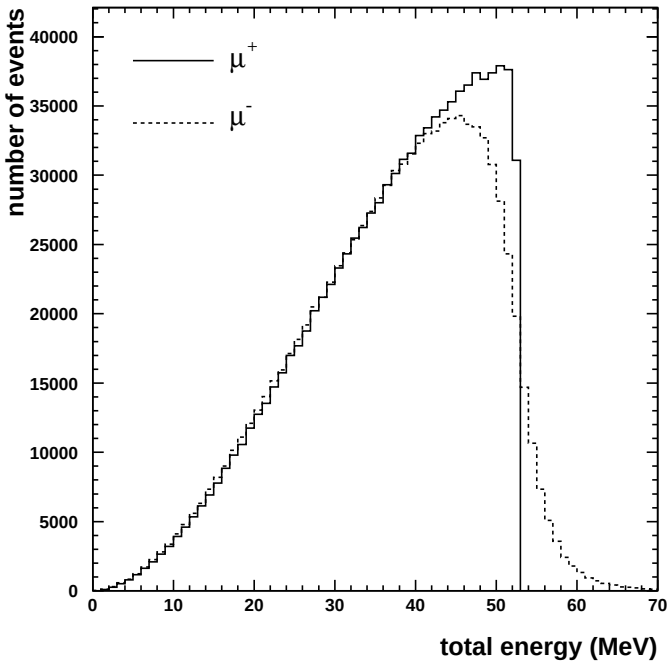

Figure 3.18: The calculated energy spectra of μ-e decay events in water. The solid line represents the positron spectrum, while the dashed line represents the electron spectrum.

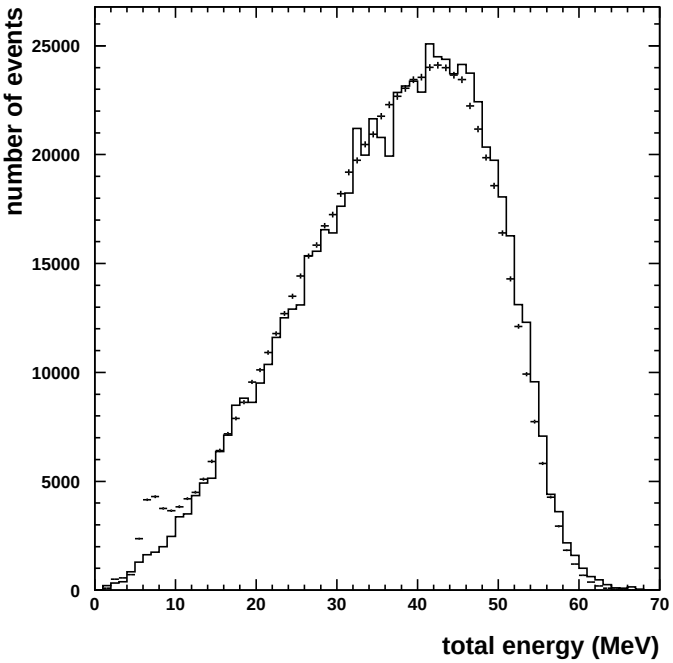

Figure 3.19: The observed energy spectrum of the μ-e decay events in the SK detector is compared with a Monte Carlo simulation. The data are shown with cross marks and the MC is indicated by a solid line histogram.

For the μ^- decay electrons, the spectrum peaks at a lower energy because of the attractive electric force of the oxygen nuclei. The decay electron spectrum also has a tail that extends to higher energies than an undistorted Michel spectrum. This tail arises from a Doppler shift that is induced by the orbital motion of the parent μ^-.

Figure 3.19 shows the observed spectrum of μ-e decay events in SK (cross marks) and compares it with the expectation from a Monte Carlo simulation (solid line histogram). The simulation takes into account the effect of μ^- capture on oxygen. Besides the features previously discussed, the data show a small peak at $\sim$6 MeV, which is caused by the emission of γ-rays from the excited ^{16}N nuclei that were produced by the μ^- capture on oxygen.

The average energy of the μ-e decay events is $\sim$37 MeV, which is much larger than the highest energy LINAC data. By comparing the energy distribution of the μ-e decay events to the MC simulated events, it is possible to evaluate the absolute energy scale in the energy region that is important for the SRN search. From the difference between data and the MC, the systematic uncertainty in the energy scale is found to be $1.23\% \pm 0.24\%$.

3.4 Time Variation of the Absolute Energy Scale

Once the absolute energy scale is set from the LINAC data, it must be monitored for stability. To some extent, this is accomplished by taking additional LINAC data at a rate of about once per year. The energy scale can be continuously monitored for time variation by using μ-e decay events and spallation events.

3.4.1 μ-e Decay Events

Although each μ-e decay event has a different energy, the average energy of these events should be constant. The μ-e events are collected into time bins that are twenty-eight days wide. For all the events in one bin, the mean N_{eff} value is calculated.

Figure 3.20 plots the mean N_{eff} value for μ-e decay events over the entirety of the SK-I period. Each point on the plot represents a single twenty-eight day bin. The solid line on the plot represents the average N_{eff} for all μ-e events during SK-I, the dashed line represents a $\pm 0.5\%$ deviation from the average, and the dotted line represents a $\pm 1.0\%$ deviation. From this figure, it can be

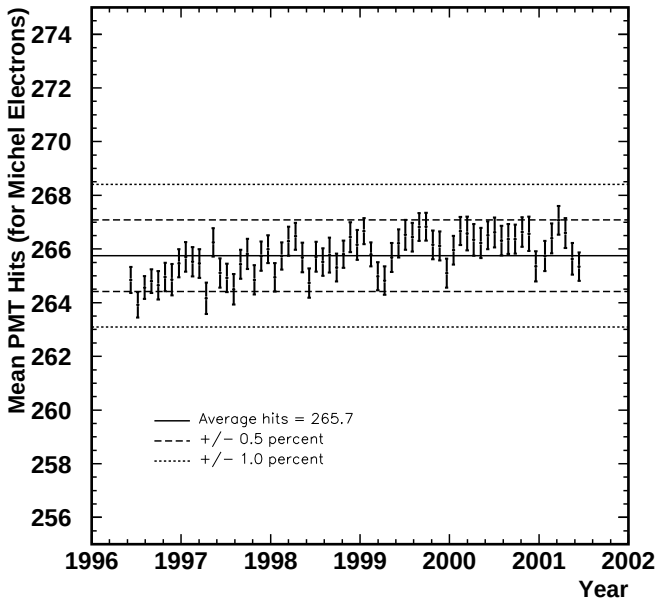

Figure 3.20: Stability of the SK-I energy scale measured with μ-e decay events. Each point represents the mean N_{eff} value for 28 days of data. The solid line represents the average N_{eff} for all μ-e events in SK-I; the dashed and dotted lined represent, respectively, $\pm 0.5\%$ and $\pm 1.0\%$ deviations from the average.

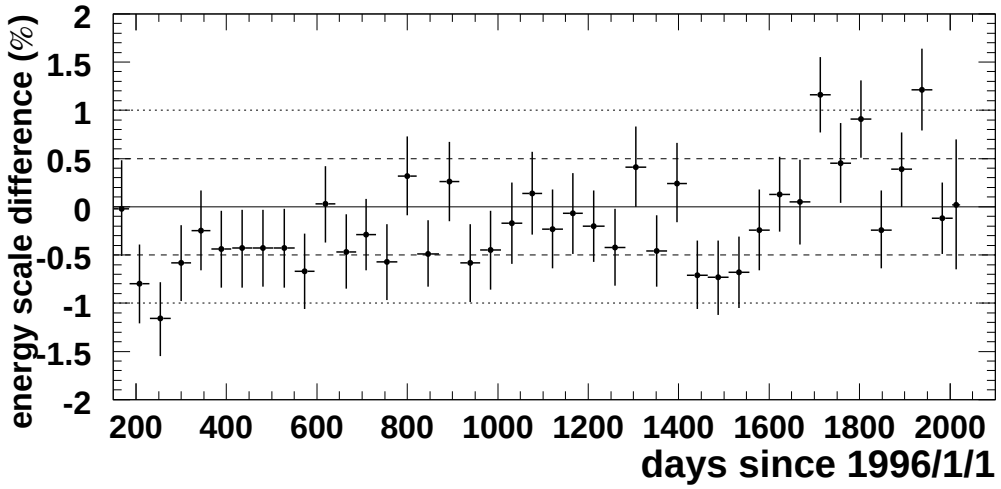

Figure 3.21: Stability of the SK-I energy scale measured with spallation events.

seen that the energy scale has remained stable to within ±0.5% during the operation of SK-I.

3.4.2 Spallation Events

Cosmic ray muons spall oxygen nuclei as they pass through the detector. The resulting nuclei are unstable and undergo radioactive decay, emitting electrons and γ-rays with energies ranging from ∼3-21 MeV. Since spallation events are produced uniformly in time, position, and direction, they can be used to study both the time variation and the direction dependence of the energy scale. A more detailed explanation of spallation events will be provided in Section 5.3.

The criteria used to select spallation events are:

- The time difference from a muon event to a spallation candidate must be less than 0.1 seconds.
- The distance from the vertex of the spallation candidate to the reconstructed track of the muon (see Section 4.5) must be less than 300 cm.
- The spallation likelihood value (described in Section 5.3.2) must be larger than 0.98.
- The spallation candidate must be contained within the fiducial volume and have an effective distance to the nearest wall greater than 450 cm.

The time variation in the mean value of the spallation energy spectrum is shown in Figure 3.21. The error bars indicate statistical uncertainty only. Although some points lie outside of the ±0.5% deviation lines, this figure generally confirms that the energy scale has been stable to within ±0.5% during SK-I.

3.5 Directional Dependence of the Energy Scale

Generally, all LINAC events are downward-going, yet the energy scale set by the LINAC calibration is extrapolated to events in all directions. To check the directional dependence of the energy scale, two methods are used: spallation events and DT generator calibration.

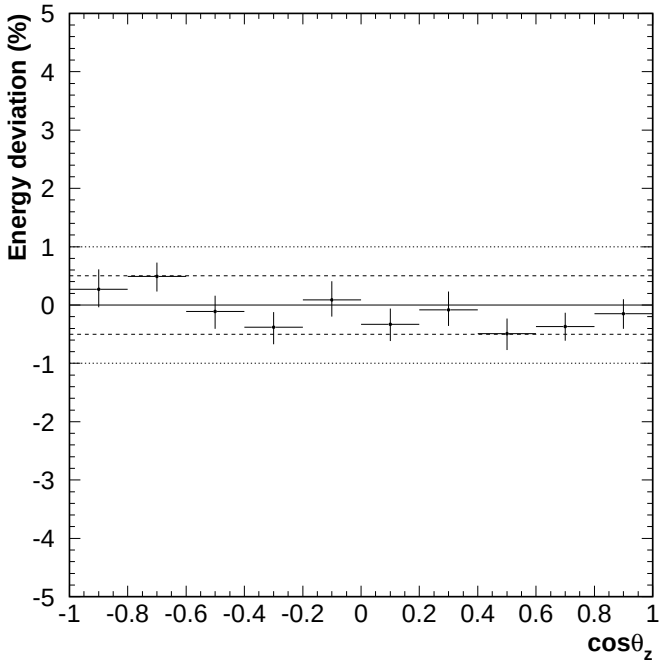

Figure 3.22: The zenith angle dependence of the energy scale as measured by spallation events.

3.5.1 Spallation Events

In addition to monitoring the time variation of the energy scale, spallation events can be used to check the directional dependence. Figure 3.22 shows the zenith angle dependence of the energy scale obtained from spallation events. From this figure, it can be seen that the zenith angle dependence of the energy scale is less than $\pm 0.5\%$.

3.5.2 DT Generator

A precise measurement of the directional dependence of the energy scale can be made from the decay of ^{16}N, which is produced by an (n,p) reaction on ^{16}O molecules in SK water. Such reactions occur naturally in small quantity, but in order to produce a large sample, a deuterium-tritium neutron generator (DTG) is used [49]. Figure 3.23 shows the layout of the DTG calibration system.

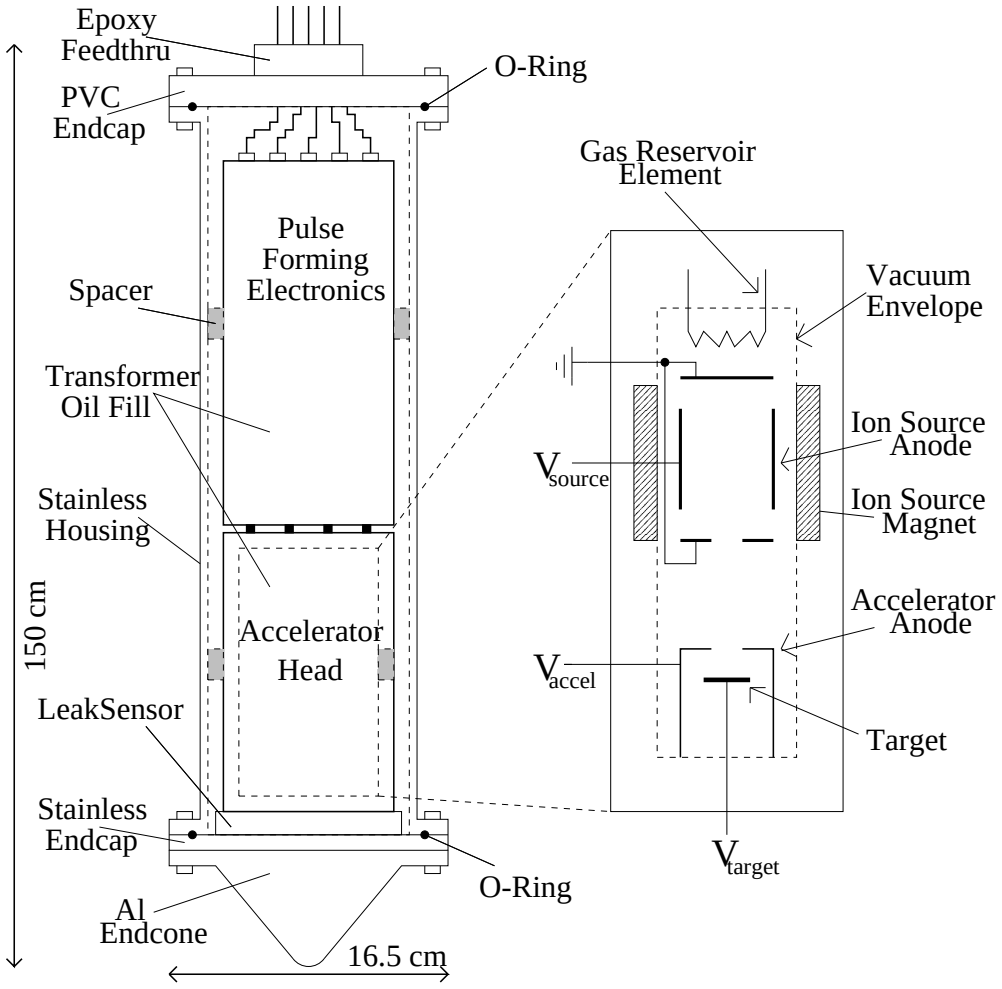

Figure 3.23: Layout of the DTG accelerator head and pulse-forming electronics, contained in a stainless steel housing. The inset shows the components of the accelerator head.

Fraction	$J_i^p \rightarrow J_f^p$	ΔI	Gamma Energy (MeV)	Type
66.2%	$2^- \rightarrow 3^-$	+1	6.129	GT allowed
28.0%	$2^- \rightarrow 0^+$	-2	none	GT 1st forbidden
4.8%	$2^- \rightarrow 1^-$	+1	7.116	GT allowed
1.06%	$2^- \rightarrow 2^-$	+0	8.872	F+GT allowed
0.012%	$2^- \rightarrow 0^+$	-2	6.049	GT 1st forbidden
0.0012%	$2^- \rightarrow 1^-$	+1	9.585	GT allowed

Table 3.1: Beta decay modes for ^{16}N. Gamma energies are also included. "GT" denotes Gamow-Teller transitions and "F" denote Fermi transitions.

The DTG is an MF Physics Model A-211 pulsed neutron generator. It can produce roughly 10^6 neutrons per pulse, with a pulse rate of up to 100 Hz. The DTG produces neutrons by the following reaction:

$$^3\mathrm{H} + {}^2\mathrm{H} \rightarrow {}^4\mathrm{He} + \mathrm{n}$$

The generated neutron has an energy of 14.2 MeV, which exceeds the 11 MeV threshold required for the production of ^{16}N via the following reaction:

$$^{16}\mathrm{O} + \mathrm{n} \rightarrow {}^{16}\mathrm{N} + \mathrm{p}$$

The ^{16}N decays with a half-life of 7.12 seconds and a Q value of 10.4 MeV. The decay products, listed in Table 3.1, are dominated by an electron, with a maximum energy of 4.3 MeV, coincident with a 6.1 MeV γ-ray:

$$^{16}\mathrm{N} \rightarrow {}^{16}\mathrm{O} + \mathrm{e}^- + \gamma + \bar{\nu}_\mathrm{e}$$

During data taking, the DTG is lowered into the detector by a crane. Once placed at the desired position, the DTG is pulsed three times and then raised 2 m before the data is collected, in order to minimize the reflection of Cherenkov light off of the stainless steel housing. Calibration data are collected from 10 - 40 seconds after the DTG is fired; data from the first ten seconds are discarded so that electrical noise generated by the crane will not contaminate the data. Normally, this cycle is repeated 25 times at a given position in the SK tank, resulting in a sample of $\sim$300,000 ^{16}N events.

Figure 3.24 shows the observed energy spectrum for a typical DTG calibration run. The data are compared with a MC simulation that includes modeling of the ^{16}N decay and of the reflection from the DTG's stainless steel housing. The energy spectra of the data and the MC are both fit with a Gaussian from

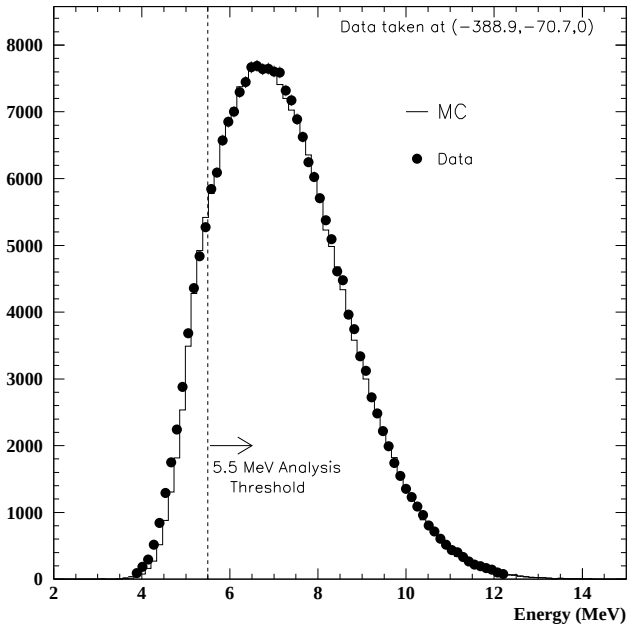

Figure 3.24: The energy spectrum of DTG calibration data and the corresponding MC [49].

5.5 MeV to 9.0 MeV. The mean energy value of the Gaussian fit for the data is compared to that of the MC.

The directional dependence of the energy scale, evaluated from DTG calibration data, is shown in Figure 3.25. These results were obtained by taking a position-weighted average at each point where DTG data were taken. The directional dependence of the energy scale is shown to be less than $\pm 0.5\%$, which is consistent with the results obtained from spallation events.

Due to the relatively high portability of the DTG system, DTG calibration data are taken at more positions than LINAC data. Therefore, the DTG events can also be used to evaluate the position dependence of the absolute energy scale as shown in Figure 3.26. The bottom figure shows the variation in the energy scale as a function of radius, while the top figure shows the variation as a function of z-position. Within the fiducial volume, the radial dependence of the energy scale is less than $\pm 0.5\%$ and the z-dependence is within $\pm 1.0\%$. This is consistent with the systematic errors for the absolute energy scale that were obtained from the LINAC calibration.

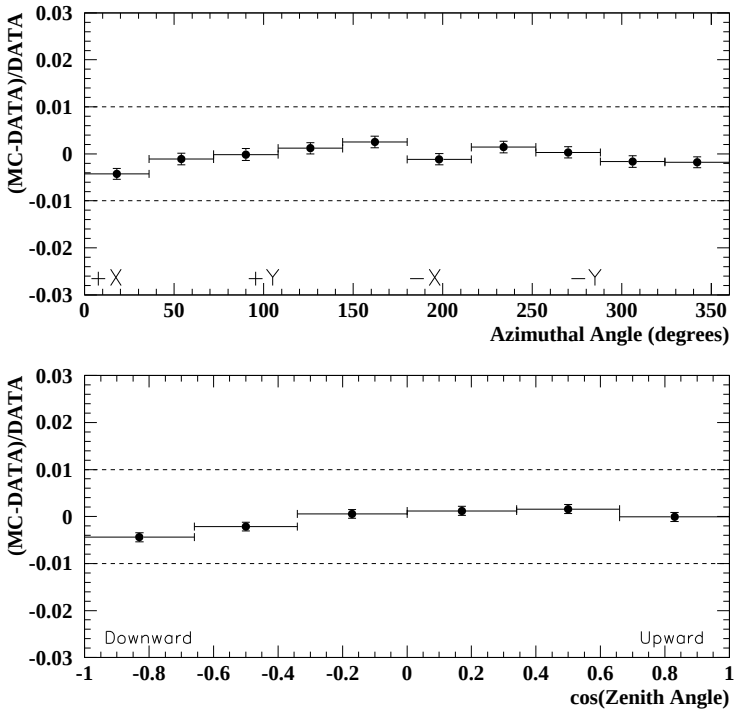

Figure 3.25: The azimuthal angle dependence (top) and zenith angle dependence (bottom) of the absolute energy scale of SK, obtained from DTG calibration data [49].

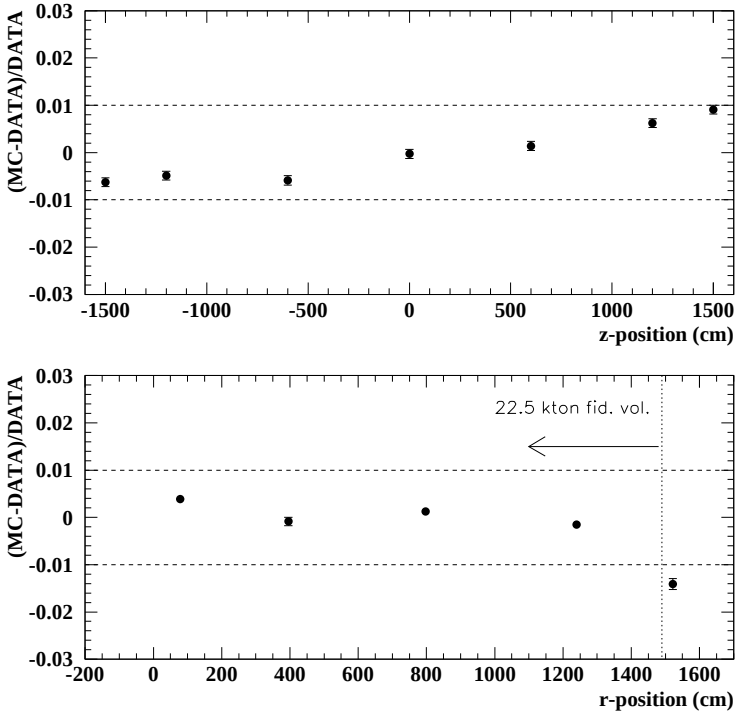

Figure 3.26: The position dependence of the absolute energy scale of SK, obtained from DTG calibration data [49]. The top plot shows the z-dependence while the bottom plot shows the radial dependence.

3.6 Detector Resolutions: Energy, Angular, and Vertex

In addition to setting the absolute energy scale of the detector, the LINAC calibration data are used to determine the energy resolution, angular resolution, and vertex resolution of SK.

3.6.1 Energy Resolution

As mentioned in Section 3.3.1, the N_{eff} distribution of LINAC data is fit with a Gaussian function, and the mean value is related to the energy. The energy resolution is defined as the 1σ width of the Gaussian fit divided by the mean value. The LINAC MC is treated the same way, and the results from the data and the MC are compared at each position and energy. Figure 3.27 shows the energy resolution as a function of the total electron energy at each position for the LINAC data (a) and the MC (b). The systematic difference between the data and the MC, averaged over all positions, is shown in (c). Although energy resolution is not a tunable parameter, the LINAC data and the MC are consistent to within $\pm 1.5\%$, with the MC having slightly better energy resolution. The energy resolution for each LINAC beam energy is summarized in Table 3.2.

3.6.2 Angular Resolution

The angular resolution is defined as the opening angle, relative to the downward-going beam of LINAC electrons, that contains 68% of the reconstructed event directions. The position-averaged angular resolution, as a function of energy, is shown in Figure 3.28. The systematic difference between the angular resolution of the data and of the MC is less than $\pm 3\%$ at the energies that are relevant to the SRN search. The angular resolution value for each LINAC beam energy is summarized in Table 3.2.

3.6.3 Vertex Resolution

The vertex resolution is defined as the size of a sphere, whose center is at the true vertex, that contains 68% of the reconstructed event vertexes. The position-averaged vertex resolution, as a function of energy, is shown in Figure 3.29. By tuning the timing resolution of the PMTs in the detector simulation, the vertex resolution of the data and of the MC can be made consistent to within the statistical uncertainty (see Section 6.2.2). The final

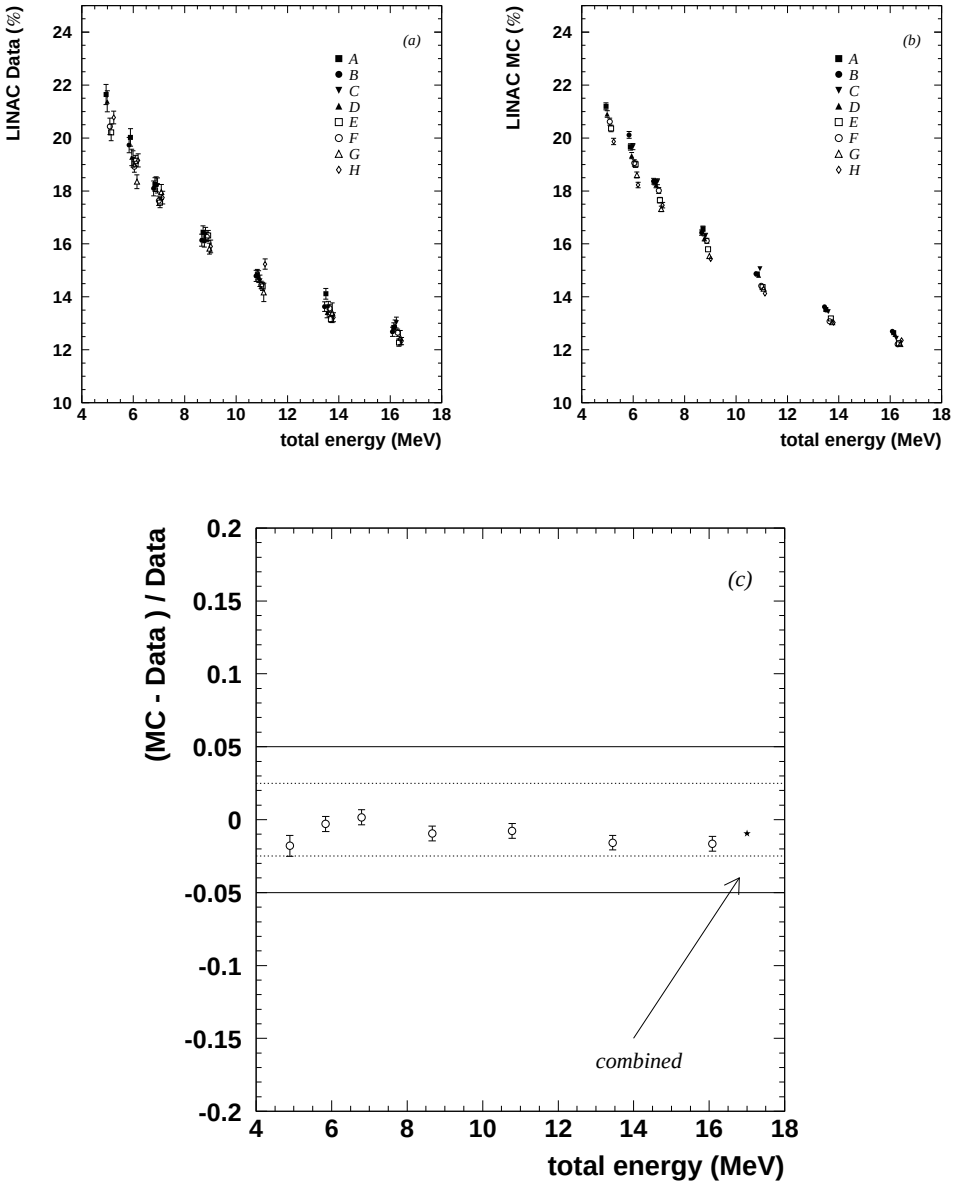

Figure 3.27: The energy resolution as a function of the total electron energy at each position for LINAC data (a) and the MC (b). The position-averaged deviation of the energy resolution is shown in (c).

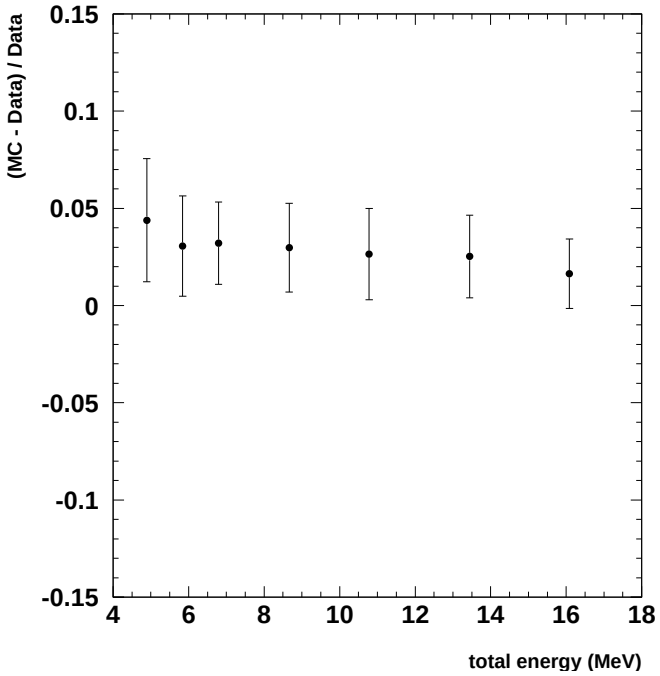

Figure 3.28: The position-averaged angular resolution deviation as a function of total electron energy [47]. Only statistical error bars are shown.

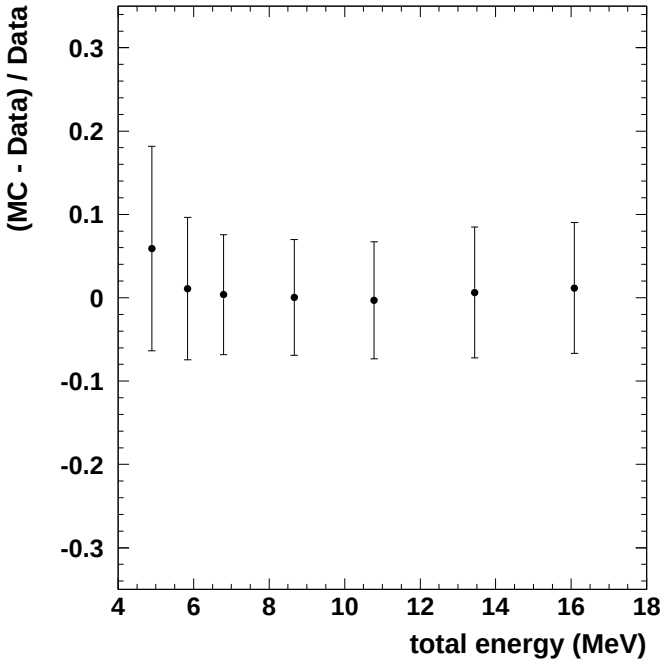

Figure 3.29: The position-averaged vertex resolution deviation as a function of total electron energy [47]. Only statistical error bars are shown.

Total Electron Energy (MeV)	Energy Resolution (%)	Angular Resolution (degrees)	Vertex Resolution (cm)
4.89	21.4 ± 0.2	36.8 ± 0.1	178.8 ± 0.5
5.84	18.5 ± 0.1	34.5 ± 0.1	132.7 ± 0.4
6.79	17.9 ± 0.1	32.0 ± 0.1	107.8 ± 0.2
8.67	16.3 ± 0.1	28.4 ± 0.1	85.2 ± 0.2
10.78	14.8 ± 0.1	25.3 ± 0.1	72.9 ± 0.1
13.44	13.7 ± 0.1	22.5 ± 0.1	64.6 ± 0.2
16.09	12.7 ± 0.1	20.5 ± 0.1	59.7 ± 0.1

Table 3.2: Detector resolutions, as measured by the LINAC calibration.

timing resolution value used in the MC is 2.4 nsec, which is consistent with the independently measured value [50]. The vertex resolution value for each LINAC beam energy is summarized in Table 3.2.

3.7 Speed of Light Measurement

It is important to accurately measure the speed of Cherenkov light in the detector, because performing the vertex reconstruction (described in Section 4.1) with an inaccurate speed can cause a systematic shift in the reconstructed vertex position. Such a vertex shift would cause a change in the effective size of the fiducial volume, and therefore alter the SRN search results.

For any given photon, the speed of light in SK water depends on the wavelength of that photon. Since there is no way of knowing the wavelength of each detected photon, the reconstuction software uses a single value for the effective speed of Cherenkov light in ultra-pure water. This effective speed can be measured by using LINAC calibration events.

The position of the LINAC endcap in the SK detector is known to a precision of $\sim$2 cm, and the LINAC trigger counter provides timing information when an electron leaves the LINAC beam pipe. Coupled with the position and timing of hit PMTs, this information allows for a direct measurement of the effective speed of Cherenkov light.

For each set of LINAC data, the peak value of the timing distribution from each PMT was obtained. This was considered to be the ΔT value for that PMT; the distance from the PMT to the LINAC position for that data set was taken to be the ΔD for the PMT. All PMTs with clear timing peaks in a

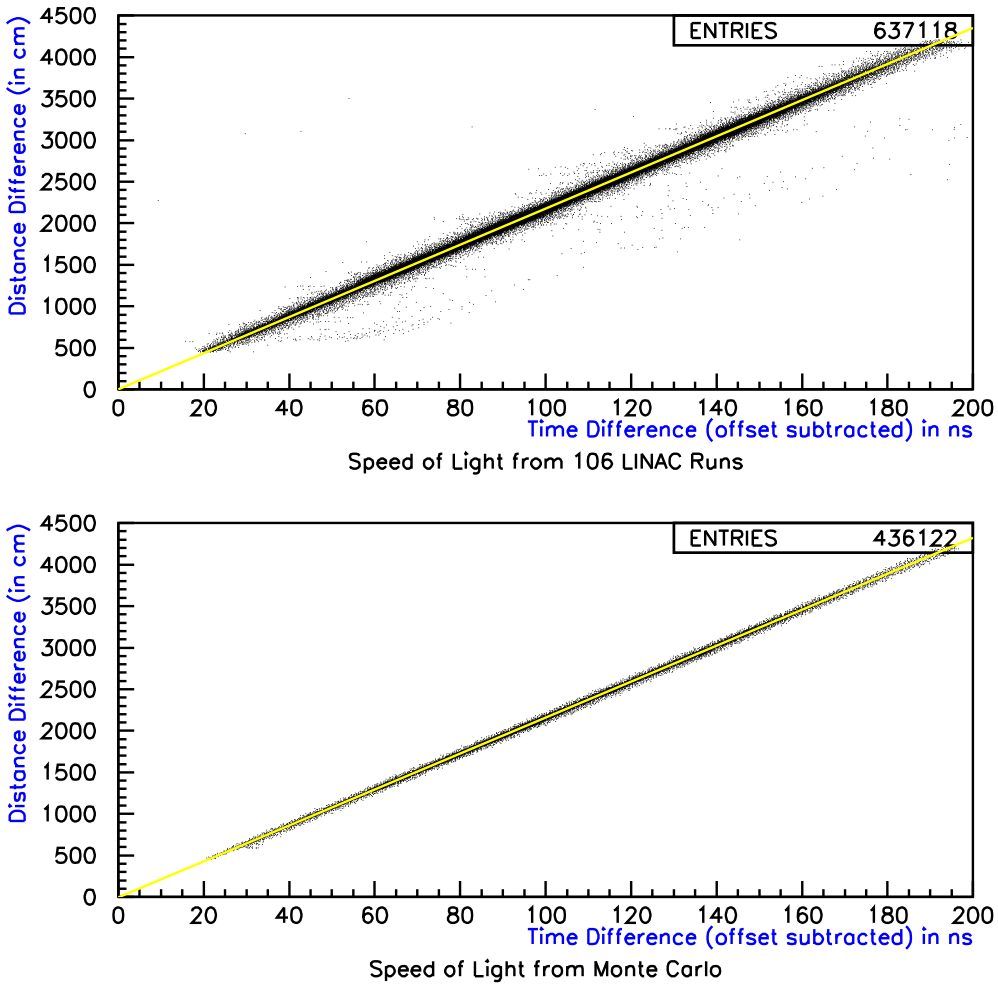

Figure 3.30: ΔD versus ΔT for PMTs hit during the LINAC calibration. The top figure represents the data and the bottom figure represents the MC. The straight lines show the best fit with a linear regression; the slope of the line is the effective speed of Cherenkov light.

given data sample were considered, and a linear regression was used to fit the resulting ΔD versus ΔT plots. The slope of each fit was considered to be the effective speed of Cherenkov light for that position and energy.

By subtracting the offset value obtained by the linear regression, all LINAC runs could be combined to get one effective speed for use in data reconstruction. The data from all LINAC runs are shown in the top plot of Figure 3.30. Each point on the plot represents one PMT from one LINAC data set. The line shows the best fit to the linear regression, and its slope represents an effective light speed of 21.738 ± 0.001 cm/ns.

The LINAC MC was treated the same way, and the result is shown in the bottom plot in Figure 3.30. The best fit to the MC speed of light is 21.633 ± 0.001 cm/ns, which indicates a systematic difference of 0.5% between the data and the MC.

3.8 Trigger Efficiency

As described in Chapter 2, data collected with the LE trigger is used in the SRN analysis. The efficiency of this trigger is evaluated with the DTG and the Ni-Cf calibration systems. When taking data to measure the trigger efficiency, a special trigger level is added at a threshold of 150 mV, which corresponds to about 14 hit PMTs ($\approx$ 2.5 MeV). This low threshold ensures that the efficiency of the special trigger will be 100% in the energy region where the LE trigger is inefficient.

LE trigger efficiency is defined by the following equation:

$$\epsilon_{LE} = \frac{N_{LE}}{N_{special}} \tag{3.8}$$

where ϵ_{LE} is the LE trigger efficiency, $N_{special}$ is the number of events that activate the special trigger, and N_{LE} is the number of events that activate both the special trigger and the LE trigger.

The closed circles in Figure 3.31 show the LE trigger efficiency as a function of energy, evaluated using DTG data. Above 6.5 MeV, the LE trigger is 100% efficient.

The trigger efficiency is measured at various positions in the ID and at various water transparency values in order to evaluate any possible dependence on position, direction, and attenuation in water. Although such dependencies are small, they must be properly modelled in the MC simulation. To accomplish this, a trigger simulator is used in which the threshold level is set to reproduce the effects seen in the trigger efficiency data. The open circles in Figure 3.31

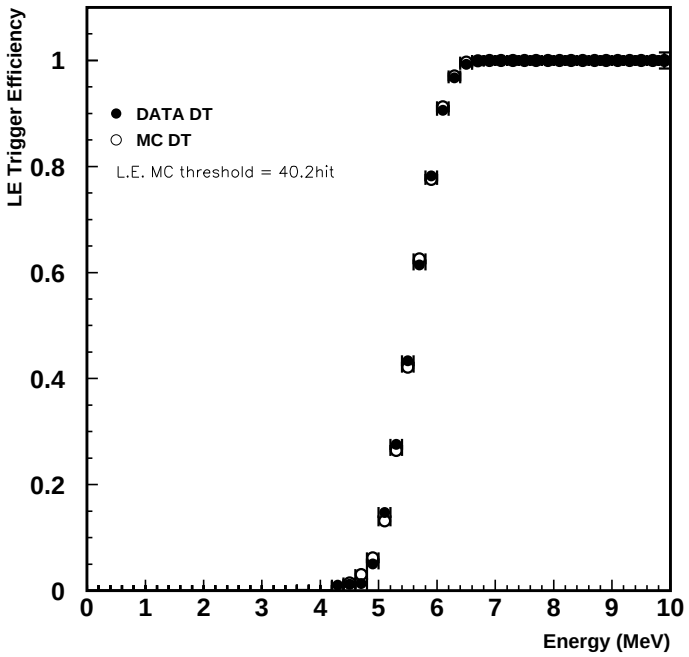

Figure 3.31: The LE trigger efficiency as a function of energy, as evaluated by DTG data taken at the center of the detector.

show the simulated trigger efficiency. The maximum deviation between the data and the MC is $^{+0.4}_{-1.7}\%$ and occurs between 6.5 MeV and 7.0 MeV. The SRN search is conducted at higher energies where the difference is essentially zero.

Chapter 4

Event Reconstruction

The data from each event that triggers the Super-Kamiokande detector is used to reconstruct information about that event. For this analysis, there are two types of events: SRN candidates and cosmic ray muons (CRMs). The total charge of the event is used to differentiate between these two categories. Events with 1000 photo-electrons or less are considered to be SRN candidates. Events with greater than 1000 photo-electrons are classified as CRMs and are used to tag spallation events as described in Section 5.3.

For each event categorized as an SRN candidate, the vertex, direction, and energy are reconstructed. The Cherenkov angle is also reconstructed for events in this sample if they meet certain selection criteria, which are described in Section 5.2.

Events classified as CRMs are reconstructed with a muon track fitter. This fitter attempts to locate the point at which the muon entered and exited the detector. The fitter can also reconstruct stopping muon events, which have no exiting point, and multiple muon events. Once reconstructed, the muon information is saved for use in the spallation cut phase of the data reduction process.

4.1 Vertex Reconstruction

The relative timing of the hit PMTs is used to reconstruct the vertex position within the SK ID. The particles that emit Cherenkov light must be in motion. However, the path length of a positron created from an SRN interaction is on the order of 10 cm, which is an order of magnitude less than the vertex resolution. Therefore, the positron's track can be neglected and the vertex can be treated as a single point for the purposes of reconstruction.

Vertex reconstruction takes place in two stages. The first stage is the "hit

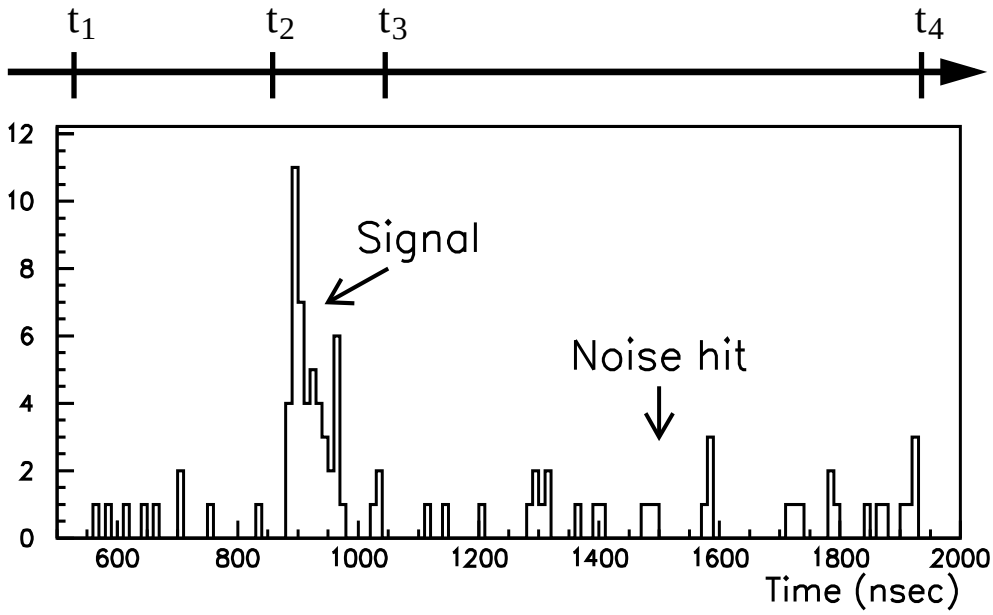

Figure 4.1: The timing distribution of hit PMTs in a typical event. The times t_x are defined in the text.

selection" process, where PMT timing information is used to remove PMT hits caused by dark noise and reflected light. Next, a grid search is performed to find the vertex position that minimizes the time-of-flight corrected timing residuals from the selected PMTs. In an ideal case, zero timing residuals will remain when the true vertex has been found.

The steps of the hit selection are as follows:

1. A sliding 200 ns window is used to select the peak in the timing distribution of the hit PMTs. An example of this is shown in Figure 4.1. Times t_1 and t_4 denote, respectively, the start and end time of the event. Times t_2 and t_3 define the 200 ns window that contains the maximum number of hits (N_{200}). The timing window is 200 ns wide because that is the maximum length of time required for a photon to traverse the ID.

2. The number of dark noise hits (N_{noise}) in this window is estimated with the relation:

$$N_{noise} \equiv \frac{t_3 - t_2}{(t_2 - t_1) + (t_4 - t_3)}[N_{hit}(t_1 < t < t_2) + N_{hit}(t_3 < t < t_4)] \quad (4.1)$$

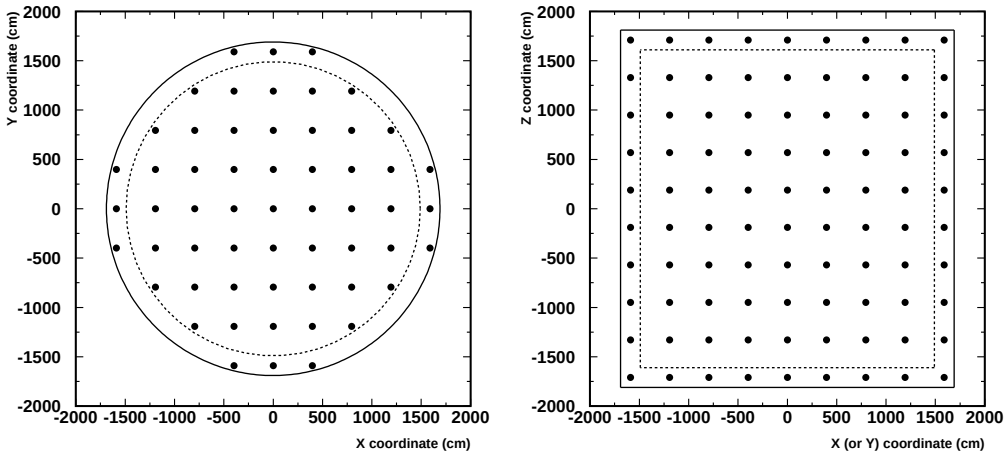

Figure 4.2: The locations of the grid points used in the vertex reconstruction software. Solid lines mark the edge of the ID; dashed lines denote the boundary of the fiducial volume.

3. The signficance ($\frac{N_{200}-N_{noise}}{\sqrt{N_{noise}}}$) is evaluated for the selected time window. The significance is also calculated for a series of eleven smaller time windows, each 19 ns shorter than the previous window (i.e. 181 ns, 162 ns, 143 ns, etc.). The hits in the time window with the maximum significance are selected to be used in the grid search.

Once the hits are selected, a grid search is used to locate the vertex position. Initially, a coarse grid, shown in Figure 4.2, is used. The spacing between points on the coarse grid is 397.5 cm. Each point in the grid is temporarily assumed to be the correct vertex and the "*goodness*" of that point is evaluated with the following equation:

$$goodness \equiv \frac{1}{N_{hits}} \sum_{i=1}^{N_{hits}} \exp\left(-\frac{\left(t_{res,i}(\boldsymbol{x_i},\, \boldsymbol{x}) - \overline{t_{res}(\boldsymbol{x})}\right)^2}{2\sigma^2} \right) \tag{4.2}$$

In this equation, N_{hits} is the number of selected PMT hits, $\boldsymbol{x_i}$ is the position of the i-th hit PMT, $\boldsymbol{x}$ is the position of the grid point being tested, and σ is the PMT timing resolution, which is taken to be 5 ns for all PMTs. The time-of-flight corrected timing residual for the i^{th} hit PMT, $t_{res,i}$, is defined as follows:

$$t_{res,i} \equiv t_i - \frac{n}{c}\sqrt{(\boldsymbol{x} - \boldsymbol{x_i})^2} \tag{4.3}$$

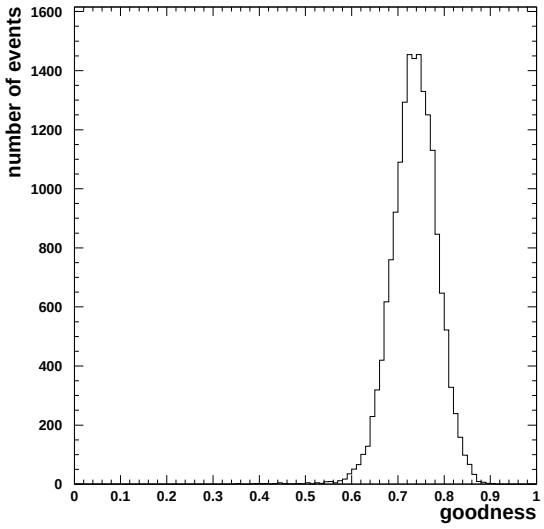

Figure 4.3: A typical *goodness* distribution as obtained from LINAC calibration events.

where t_i is the timing of the i^{th} hit PMT, n is the refractive index of ultra-pure water, and c is the speed of light in a vacuum. The mean value of the timing residuals is $\overline{t_{res}(\boldsymbol{x})}$.

After the grid point that yields the largest *goodness* value is found, a more finely-spaced grid is constructed around that point and another grid search is conducted. This procedure is repeated until the best fit point is located.

The *goodness* value of the best fit point indicates the quality of the fit. Ideally, all of the of residuals are equal and so the *goodness* will be 1. In reality, however, *goodness* values peak at about 0.7. Figure 4.3 shows a typical *goodness* distribution for LINAC calibration events.

The resolution of the vertex fits obtained from this algorithm are evaluated with LINAC calibration events and shown in Table 3.2.

4.2 Direction Reconstruction

After the location of the vertex has been determined, the event direction is reconstucted by examining the pattern of hit PMTs. Since Cherenkov light is emitted as a cone, the PMTs in an ideal event would form a clear ring on the walls of the detector. The direction of the event is reconstructed with a

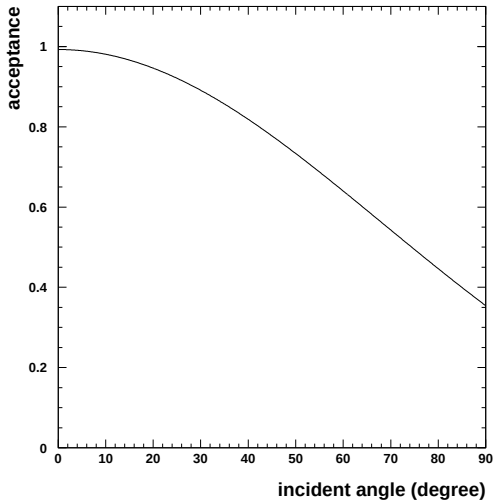

Figure 4.4: The relative acceptance of the PMT photocathode as a function of a photon's angle of incidence. This acceptance is used as a correction factor in the direction reconstruction.

maximum likelihood method; a set of sample directions, $\boldsymbol{d} = (d_x,d_y,d_z)$, are searched to find the one that maximizes the following likelihood function:

$$L(\boldsymbol{d}) = \sum_{i=1}^{N_{hits}} \log\left[f(\phi_i(\boldsymbol{d}))\right] \times \frac{\cos\theta_i}{a(\theta_i)} \tag{4.4}$$

In this equation, $\phi_i(\boldsymbol{d})$ is the opening angle between the sample direction $\boldsymbol{d}$ and the vector connecting the vertex position to the location of the i^{th} hit PMT; θ_i is the angle between a vector perpendicular to the face of the i^{th} PMT and the vector connecting the vertex position to the location of the PMT. The function $a(\theta_i)$, shown in Figure 4.4, corrects for the acceptance of the PMT as a function of the photon's incident angle. The function $f(\phi_i(\boldsymbol{d}))$ is the relative probability that a particular photon will be emitted in a given direction relative to the event direction. This distribution was obtained from MC simulated events, and it is shown in Figure 4.5. Although there is a sharp peak at 42°, the distribution differs from the ideal case by the presence of broad tails. The tails are primarily caused by multiple Coulomb scattering of the electrons (or positrons) in water.

A series of grid searches are performed to find the event direction that gives the maximum likelihood value. The grid step sizes used in these searches are

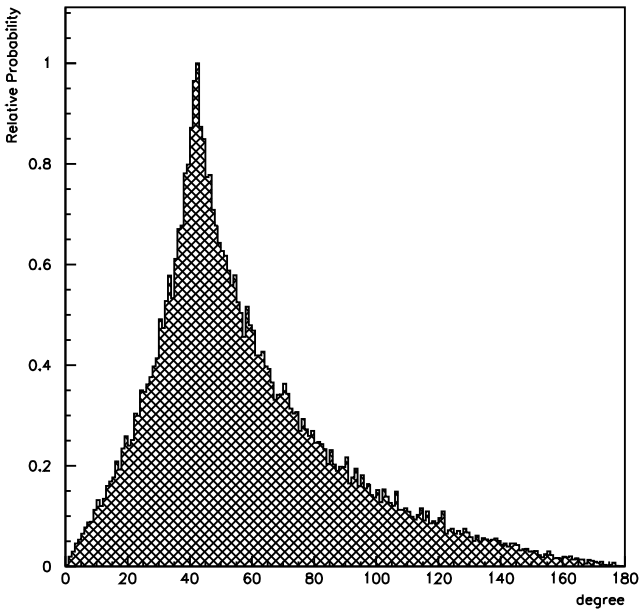

Figure 4.5: The probability density function $f(\phi_i(\boldsymbol{d}))$ for Cherenkov photon direction.

20°, 9°, 4°, and 1.6°. After these searches are completed, the direction with the maxiumum likelihood value is taken to be the direction of the event.

The angular resolution of the direction fits is obtained from LINAC calibration events (see Table 3.2). The angular resolution of SK is limited by the multiple Coulomb scattering discussed above. In the energy region of greatest importance for the SRN search (∼18 MeV), the angluar resolution is approximately 20°.

4.3 Energy Reconstruction

The energy of a charged particle can be inferred from the number of Cherenkov photons that it deposits in the SK detector. As discussed in Section 2.3.1, an SRN event is expected to generate only one photo-electron in each hit PMT. Thus, the energy of an electron (or positron) is proportional to the number of PMTs hit during the electron event. The proportionality factor is about 6 hit PMTs per MeV of particle energy. By using the number of hit PMTs instead of total charge as the means by which energy is measured, certain complications are avoided. These include:

- The charge resolution of the PMTs is poor (~50%) near the single photo-electron level.
- The charge registered by a PMT is dependent on the gain of that PMT.
- Fluctuations in the electronic noise of a PMT can significantly alter the total charge of a PMT near the single photo-electron level.

PMT hits are counted in the energy reconstruction only if their timing residuals, using the reconstructed vertex, are within a 50 ns window. This narrow window reduces the effect of noise hits on the energy reconstruction. The number of hits satisfying this criterion, N_{50}, must be corrected for various position- and detector-dependent effects, which are descibed in detail below. After applying these corrections, an effective number of hits for the event, N_{eff} is obtained:

$$N_{eff} = \sum_{i=1}^{N_{50}} \left[(X_i + \alpha_{tail} - \alpha_{dark}) \times S(\theta_i, \phi_i) \times \frac{N_{all}}{N_{alive}} \times \exp\left(\frac{r_i}{\lambda_{run}}\right) \times K_i \right] \quad (4.5)$$

The corrections in the N_{eff} calculation are:

X_i : Multiple p.e. correction

When an event occurs near the edge of the fiducial volume and is directed towards the nearest wall, the Cherenkov ring will not have much distance in which to expand. Consequently, the assumption that each PMT receives a single p.e. may not be valid for this type of event. The expected number of photo-electrons for each hit PMT, X_i, is estimated from the occupancy of the eight surrounding PMTs by using the ratio ($\varepsilon_i = \frac{n_i}{N_i}$) between the number of neighboring PMTs that are hit (n_i) to the number of neighboring PMTs that could have been hit (N_i):

$$X_i = \begin{cases} \frac{1}{\varepsilon_i} \ln\left[(1-\varepsilon_i)^{-1}\right] & \text{for } \varepsilon_i < 1 \\ 3 & \text{for } \varepsilon_i = 1 \end{cases} \quad (4.6)$$

This method of estimation assumes a Poisson distribution and uniform light over the 3×3 group of PMTs. Figure 4.6 shows the corrected number of photo-electrons assumed per PMT, as a function of ε_i.

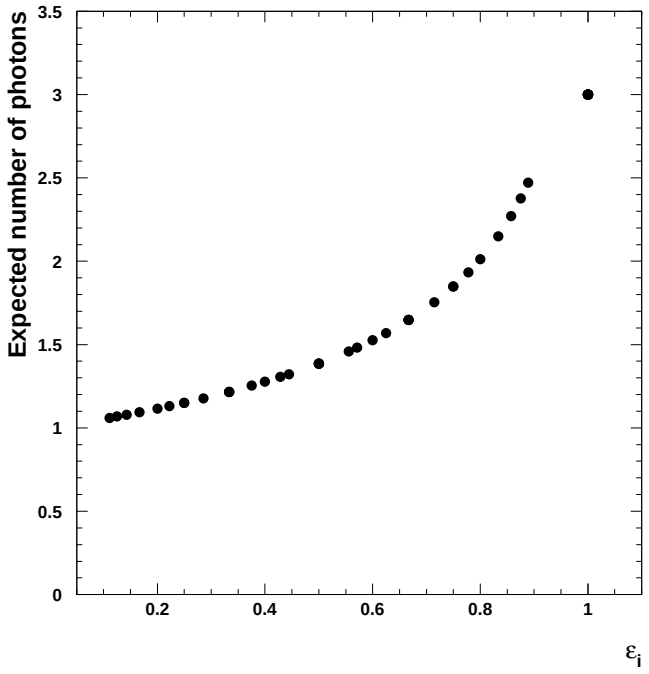

Figure 4.6: The expected number of photo-electrons received by a hit PMT as a function of ε.

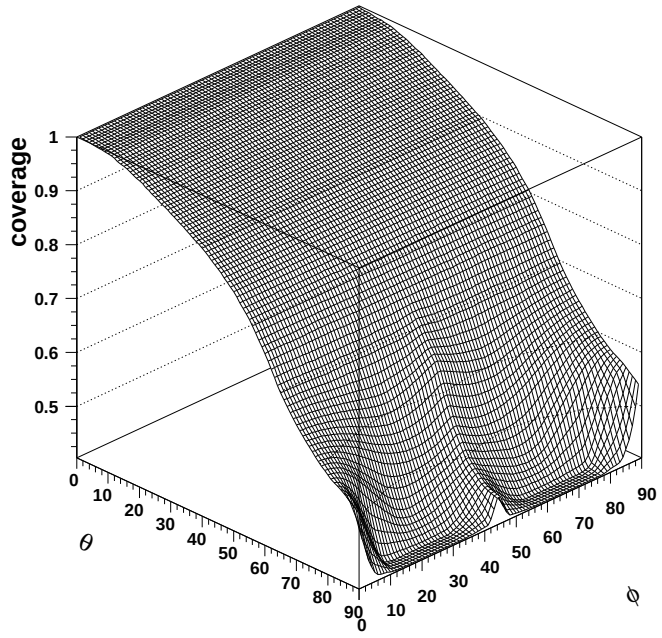

Figure 4.7: The effective photocathode area as a function of incident photon direction.

α_{tail} : Reflected light correction

A Cherenkov photon that reflects off of a PMT or the blacksheet may still hit a PMT and generate a photo-electron. However, that delayed PMT hit will usually not occur within the 50 ns timing window. To "recover" such hits for the energy calculation, a 100 ns timing window is used to calculate the correction factor α_{tail}:

$$\alpha_{tail} = \frac{N_{100} - N_{50}}{N_{50}} \tag{4.7}$$

α_{dark} : Dark noise correction

The total dark noise rate in SK-I was usually ~3.3 kHz. Thus, in a 50 ns window, about 2 dark noise hits are expected. To correct for these hits, the following factor, α_{dark}, is applied:

$$\alpha_{dark} = \frac{N_{alive} \cdot R_{dark} \cdot 50\text{ns}}{N_{50}} \tag{4.8}$$

In this equation, N_{alive} is the number of operational PMTs in the detector and R_{dark} is the mean dark noise rate measured for the run.

$S(\theta_i, \phi_i)$: Photocathode coverage correction:

The effective photocathode area of the i^{th} PMT, $S(\theta_i, \phi_i)$, is determined by the direction (θ_i,ϕ_i) from which the photons approach it. Figure 4.7 shows the effective area function; the ϕ asymmetry is a result of shadowing by neighboring PMTs, which occurs at large values of θ.

$\frac{N_{all}}{N_{alive}}$: Dead PMT correction

During SK-I, PMTs occasionally failed and were switched off. The factor $\frac{N_{all}}{N_{alive}}$ is used to compensate for this effect and to ensure that the energy scale is not changed by it. N_{all} is the total number of PMTs in the SK-I ID (i.e. 11,146).

$\exp(\frac{r_i}{\lambda_{run}})$: Water transparency correction

As discussed in Section 3.2, light attenuation in water directly affects the number of photons that are detected by the PMTs. To compensate for this attenuation, the factor $\exp(\frac{r_i}{\lambda_{run}})$ is used, where r_i is the distance from the vertex to the location of the i^{th} hit PMT and λ_{run} is the water transparency value measured on a continual basis using μ-e decay events.

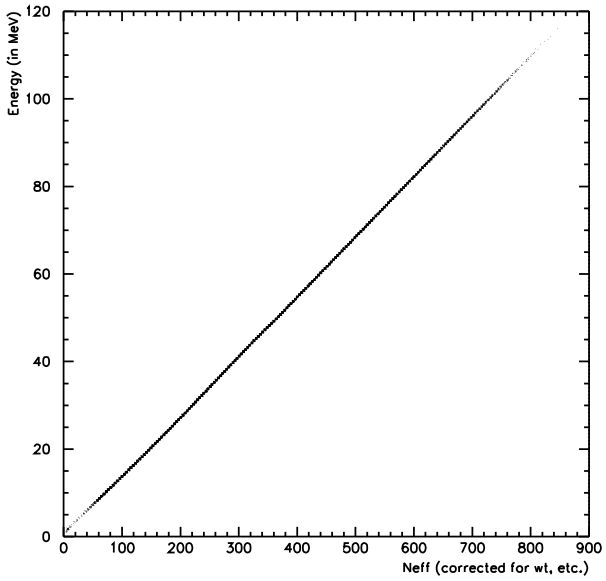

Figure 4.8: Reconstructed total energy as a function of N_{eff}.

K_i : Quantum efficiency correction

SK-I contained 375 ID PMTs that were manufactured at an earlier time than all of the other ID PMTs. During the Ni-Cf calibration, it was determined that these "pre-series" PMTs have a larger quantum efficiency than the other ID PMTs. To remove this non-uniformity, the following correction factor is used:

$$K_i = \begin{cases} 0.833 & \text{for the 375 pre-series PMTs} \\ 1.000 & \text{for all other PMTs} \end{cases} \tag{4.9}$$

After applying these corrections, the obtained N_{eff} is found through LINAC calibration to be uniform to within $\sim$1% inside of the fiducial volume. The N_{eff} value corresponds directly to the energy of the event. The conversion from N_{eff} to energy is designed to give the total energy of the event, as opposed to only the visible energy deposited in the detector. This conversion factor is explained in Section 3.3.1. Figure 4.8 shows the reconstructed total energy as a function of N_{eff} over the entire energy range relevant for the SRN search.

4.4 Cherenkov Angle Reconstruction

The Cherenkov angle is reconstructed for all events that are kept after the first round of the data reduction (see Section 5.2). The 42° opening angle used in the direction reconstruction (Section 4.2) assumes that the detected particle is ultra-relativistic (i.e. $\beta \geq 0.99$). In the energy range considered for the SRN search, heavier particles such as muons are not ultra-relativistic and would therefore have smaller opening angles determined by equation 2.1.

Hit PMTs with timing residuals within a 15 ns window (N_{15}) are considered for the Cherenkov angle reconstruction. Each set of three PMTs is evaluated separately, and all such combinations are considered. Figure 4.9 shows a reconstructed vertex and three hit PMTs within the SK inner detector. The vectors $\vec{A}$, $\vec{B}$, and $\vec{C}$ extend from the vertex to the position of the three hit PMTs. Figure 4.10 shows a unit sphere centered upon the reconstructed vertex. The unit vectors $\hat{A}$, $\hat{B}$, and $\hat{C}$ extend from the center of the sphere to its surface and point in the same relative directions as $\vec{A}$, $\vec{B}$, and $\vec{C}$. These unit vectors touch the surface of the sphere at points A, B, and C. Any three points on a sphere define a circle; the circle defined by A, B, and C is drawn in Figure 4.10 and shown more closely in Figure 4.11. This circle has radius R, which is related to the opening angle (θ_{open}) by the following equation:

$$R^2 = \sin\theta_{open} \tag{4.10}$$

Each combination of three hit PMTs is evaluated in this way to obtain a value for the opening angle. The resulting distribution of opening angles for one event is fit with a Gaussian function; the mean value of the fit is taken to be the Cherenkov angle for the event. Figure 4.12 shows the distribution of opening angles reconstructed from all of the hit combinations of a typical event, as well as the Gaussian fit. For this event, the mean value of the fit yielded a Cherenkov angle of 43.3°.

For a given value of N_{15}, there are N_{comb} such combinations, where:

$$N_{comb} = \frac{1}{3!} \times (N_{15}) \cdot (N_{15} - 1) \cdot (N_{15} - 2) \tag{4.11}$$

The number of possible combinations grows as the cube of the number of selected PMTs. Since the precision of the Cherenkov angle reconstruction depends on the number of combinations, it is possible to use a narrow 15 ns timing window for the Cherenkov angle reconstruction instead of the wider 50 ns window used for vertex reconstruction. Using this reconstruction technique, noise hits tend to form combinations that reconstruct with large opening angles, as shown by the tail in Figure 4.12. By narrowing the timing window to 15 ns, fewer dark noise hits are selected and so this effect is minimized.

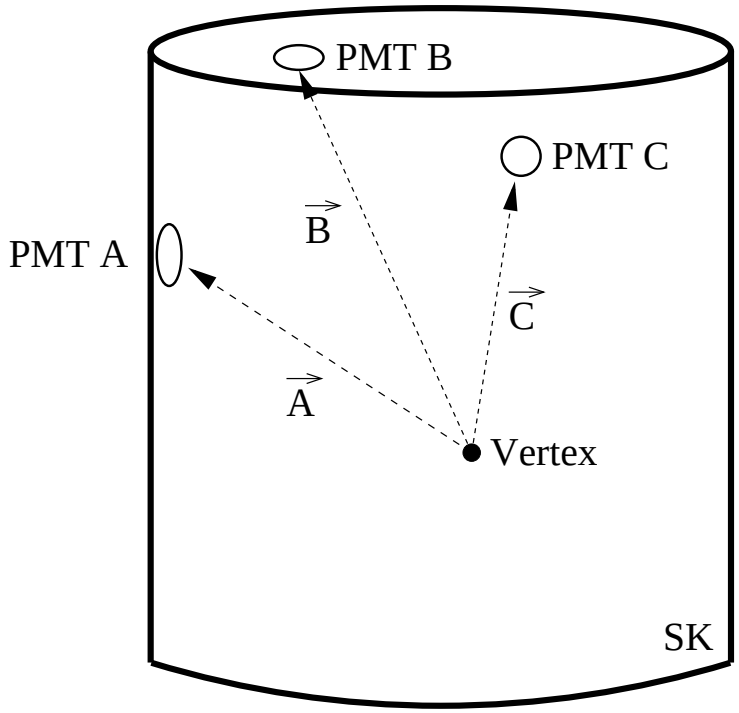

Figure 4.9: A reconstructed vertex and three hit PMTs from a hypothetical event. The vectors $\vec{A}$, $\vec{B}$, and $\vec{C}$ extend from the vertex to the hit PMTs.

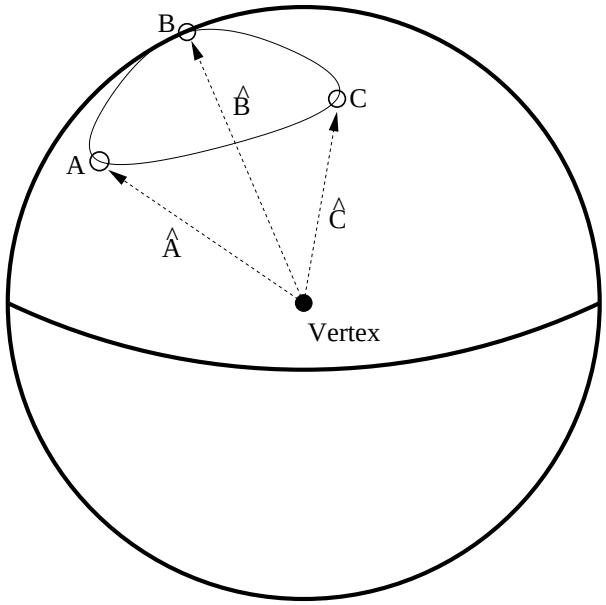

Figure 4.10: A unit sphere centered on the vertex of the same event from Figure 4.9. The unit vectors $\hat{A}$, $\hat{B}$, and $\hat{C}$ define three points on the sphere which, in turn, define a circle.

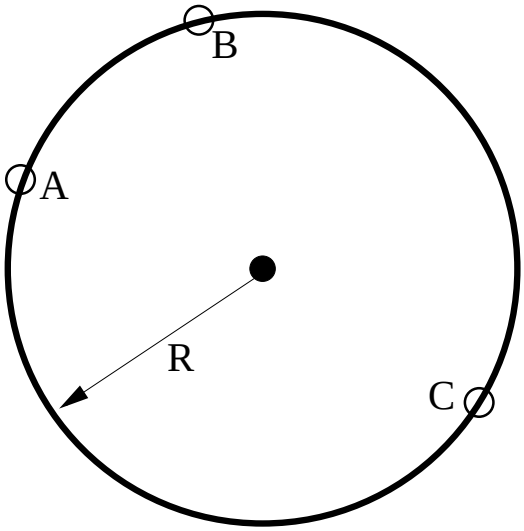

Figure 4.11: The circle defined by points A, B, and C in Figure 4.10 is shown here. The radius R of the circle defines the opening angle between the three selected PMTs.

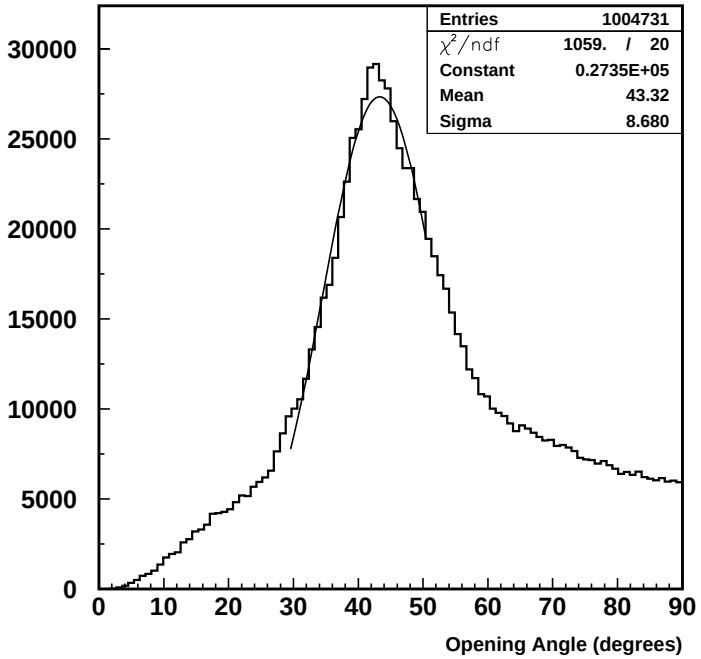

Figure 4.12: The distribution of reconstructed opening angles for a typical event. Each combination of three hit PMTs results in one value for the opening angle. After all combinations have been evaluated, the distribution is fit with a Gaussian function and the mean value of the fit is taken to be the Cherenkov angle of the event.

4.5 Muon Reconstruction

Muons created by cosmic ray interactions enter the detector at a rate of about 2.5 Hz. Spallation events induced by cosmic ray muons are one of the major sources of background for the SRN search. The spallation events have strong spatial and temporal correlations to their parent muons. These correlations can be exploited to reduce the spallation background; the spallation cuts are described in detail in Section 5.3. For these cuts to be effective, it is necessary to reconstruct the tracks of muons in the detector.

For each meter that a muon travels within the detector, about 2300 p.e. are observed. As an exiting muon approaches the wall of the ID, its Cherenkov ring cannot spread out before hitting a PMT; therefore, exiting muons cause at least one PMT to record a large number of photo-electrons. Based on this information, an event is reconstructed as a muon if a total charge (Q_{tot}) of at least 6000 p.e. is detected and at least one PMT has recorded a charge greater than 200 p.e.

Two attempts are made to reconstruct the muon track. In the first attempt, the entrance and exit points of the muon are located and the track is considered to be the path between them. The entrance point is determined by the position of the PMT that was hit earliest and has at least two adjacent PMTs hit within 5 ns. PMTs become charge-saturated when they receive more than 231 p.e. at once; the exit point is defined as the central point between the charge-saturated PMTs. Two parameters are used to check the result of this reconstruction. The minimum distance from the entrance position to a saturated PMT is called L_{ent} and the maximum distance from the exit position to a saturated PMT is called L_{exit}. If $L_{ent} > 300$ cm and $L_{exit} < 300$ cm, then the muon reconstruction is considered to be successful. Events are also considered to have failed this reconstruction if the residual charge, Q_{res} is greater than 25,000 p.e. Q_{res} is defined as:

$$Q_{res} = Q_{tot} - pL \tag{4.12}$$

where $p = 2300$ p.e./meter and L is the track length in meters. This reconstruction method works best on single muons that have enough energy to traverse the entire detector. Muons that stop inside the ID generally fail this reconstruction because L_{exit} is too large; multiple muon events tend to fail because Q_{res} is too high.

If the first reconstruction is unsuccessful, information from the TDCs is used to make a second attempt. The second reconstruction performs a fit that is similar to the vertex reconstruction described in Section 4.1; however, the track of the muon cannot be approximated by a point. Thus, the entrance

point from the first attempt is used and a grid search is conducted to find the exit point that will maximize the following *goodness* function:

$$goodness = \frac{\sum_i \frac{1}{\sigma_i^2} \exp\left\{-\frac{1}{2}\left(\frac{t_i - T}{1.5\sigma_i}\right)^2\right\}}{\sum_i \frac{1}{\sigma_i^2}} \tag{4.13}$$

where:

$$t_i = T_i(\boldsymbol{x}_i) - \frac{l_\mu(\boldsymbol{x}_{exit})}{c} - \frac{l_{photon}(\boldsymbol{x}_{exit})}{c/n} \tag{4.14}$$

$\boldsymbol{x}_{exit}$ = Muon exit position
σ_i = Timing resolution of the i-th hit PMT
T = Time when the muon enters the ID
T_i = Time when the i-th PMT is hit with a Cherenkov photon
l_μ = Flight distance of the muon, assuming exit point $\boldsymbol{x}_{exit}$
l_{photon} = Flight distance of Cherenkov photon, assuming exit point $\boldsymbol{x}_{exit}$
c = Speed of light in a vacuum
n = Refractive index of ultra-pure water

Figure 4.13 shows the variables used in the second attempt at muon reconstruction. If a value for $\boldsymbol{x}_{exit}$ can be found that results in a $goodness > 0.8$, the second muon reconstruction is considered successful; otherwise, the muon event is considered to be "un-fit."

The efficiency of the muon reconstruction was evaluated by using 1000 typical muon events from the data. The muon events were categorized as:

- Single muons: Events with a single muon track that traverses the ID
- Stopping muons: Events with a single muon track that does not traverse the ID
- Hard interactions: Events with $Q_{res} > 25,000$ p.e.
- Corner clippers: Events where the muon track length is less than 5 m
- Multiple muons: Events with more than one muon track

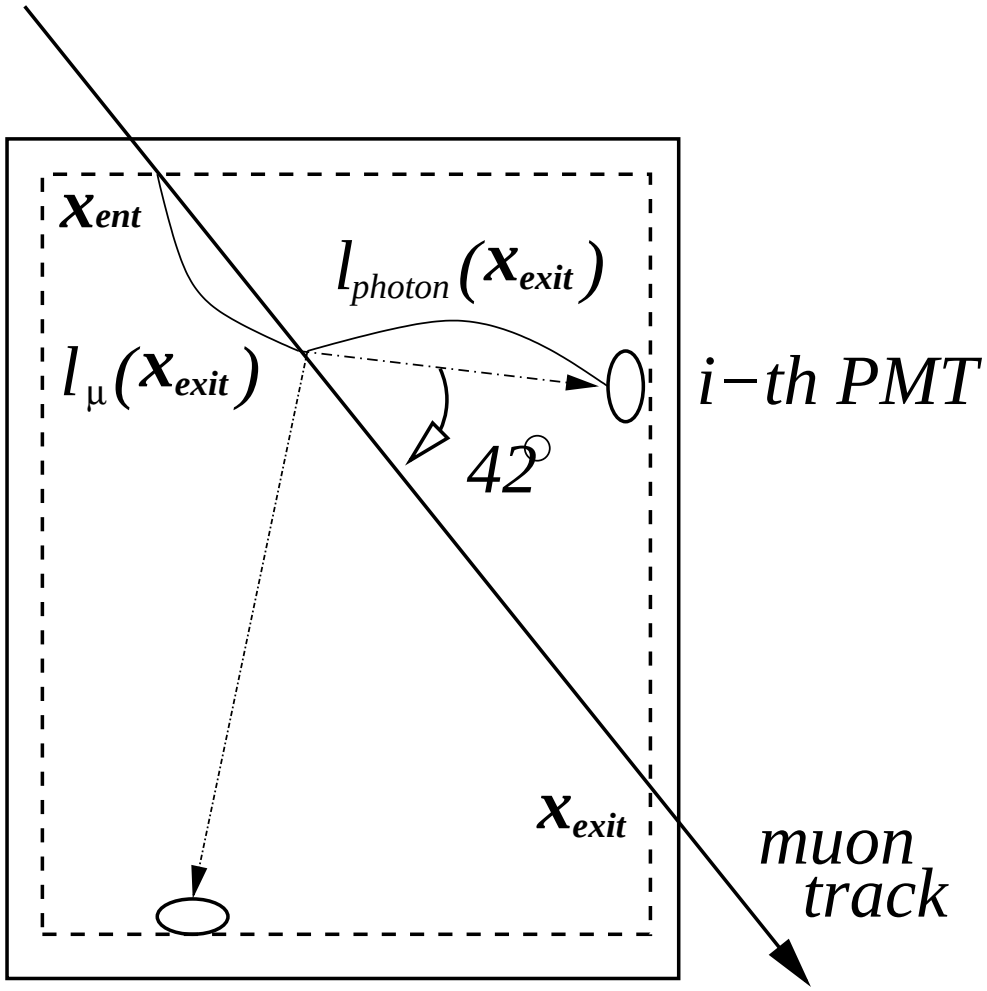

Figure 4.13: Explanation of the variables used in the second attempt at muon reconstruction.

Muon type	Number of events	Number of un-fit events
Single muons	835	5
Stopping muons	10	8
Hard interactions	41	2
Corner clippers	58	19
Multiple muons	56	28
Total	1000	62

Table 4.1: Reconstruction efficiency for various types of muons

The fitting efficiency for each type of muon is summarized in Table 4.1. Overall, the muon reconstruction is found to be 94% efficient.

The resolution of the muon track reconstruction was evaluated by using Monte Carlo simulated muon events. The reconstructed entrance and exit positions were compared to the generated positions and the 1σ resolution was found to be 67 cm for a single muon event.

Chapter 5

Data Reduction

Super-Kamiokande-I took data from 1 April 1996 until 15 July 2001. For the first two months, the water quality was insufficient for an effective SRN search. The data used in the SRN search began on 31 May 1996, and continued until the end of Super-Kamiokande-I. During this period, 1496 live days of good data were collected, corresponding to a duty cycle of 81%.

There are several backgrounds to the SRN search, including electronic noise within the detector, cosmic ray muons and the spallation products that they induce, and other neutrino sources. To reduce these backgrounds, various selection criteria are applied. The data reduction is performed in three stages: the first reduction, the spallation cut, and the second reduction. By dividing the reduction procedure into separate steps, it becomes possible to modify the selection criteria in the later stages without fully reprocessing the entire data sample. The first reduction removes events that are clearly not SRN candidates, such as events originating outside of the fiducial volume. The spallation cut rejects the decay products of the unstable nuclei created by cosmic ray muons passing through the detector. The second reduction targets several specific physics backgrounds, such as low energy muons and neutrinos from sources other than supernovae.

5.1 Runs and Subruns: Filling the Data Set

Data are collected in sets; a set of data is called a "run". Each run has a maximum duration of 24 hours. This limits the data files to a managable size. Additionally, a new run is started whenever the operating conditions of the detector are changed, so that individual runs mark periods of stable data-taking. Runs must be started manually by a shiftworker. The runs are further divided into "subruns," which last from $90 - 600$ seconds, depending

upon the trigger rate. Sub-runs are incremented automatically by the on-line data acquisition system (DAQ).

Runs and subruns are evaluated with several criteria. First amongst these is the duration of the run (or subrun). Runs that are less than 5 minutes long are generally indicative of problems with the DAQ. Such runs are removed from the data set.

Subruns are considered bad if they are less than 30 seconds long. If a subrun is very short, it can be difficult to accurately gauge the quality of the data, so these subruns are rejected. Short subruns usually occur at the end of a run.

Furthermore, runs that have serious hardware or software trouble (e.g. high voltage problems) are labeled as faulty runs, and calibration runs are specially marked as such, so that they may be easily removed from the regular data sample. The data that remain after these basic criteria are applied get processed by the first reduction steps.

5.2 First Reduction

After the initial selection described above is completed, the first reduction is performed. These criteria are highly effective, and remove the vast majority of the data while maintaining most of the signal, as evaluated using Monte Carlo simulation (Section 6.3). The main criteria for the first reduction are described below:

Total Charge Cut: Most events caused by cosmic ray muons or atmospheric neutrino events deposit more than 1 GeV of energy into the detector. In contrast, the energy distribution of the SRN is expected to peak at around 5 MeV and become negligible by about 50 MeV. Figure 5.1 shows the total distribution of photo-electrons measured per event. To eliminate the higher energy peak, only events with a total charge less than 1000 p.e. (corresponding to $\sim$130 MeV) are retained.

Time Difference Cut: Only events that occur more than 50 μsec after another event are retained in the data. This criterion removes the μ-e decay events. It also removes events caused by "ringing" noise in the DAQ electronics, which can occur after an event that has deposited very large amounts of light in the detector. Figure 5.2 shows a typical distribution of the time difference between consecutive events.

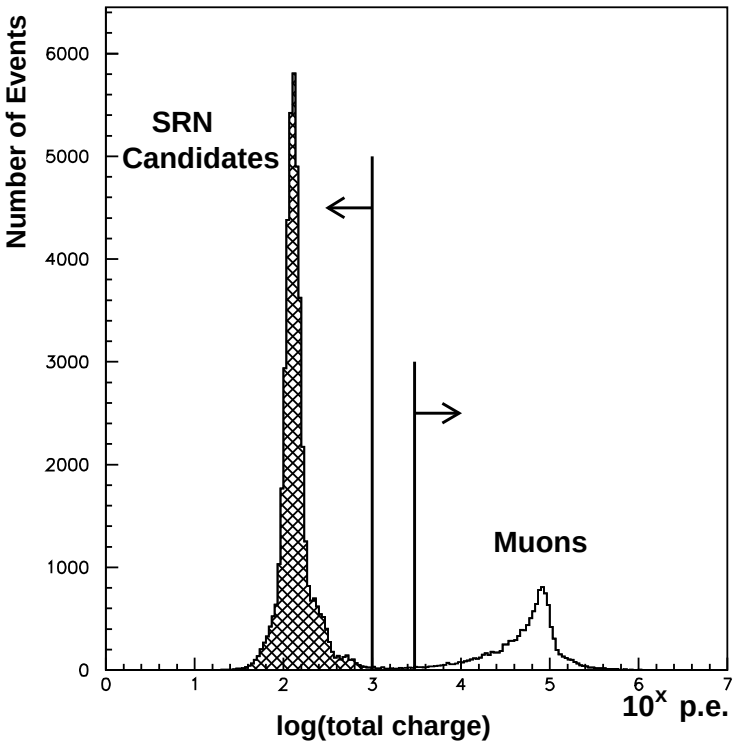

Figure 5.1: The distribution of the total charge of events. The events on the shaded side of the distribution are retained as SRN candidates. The events with more than 3000 photo-electrons are categorized as muons.

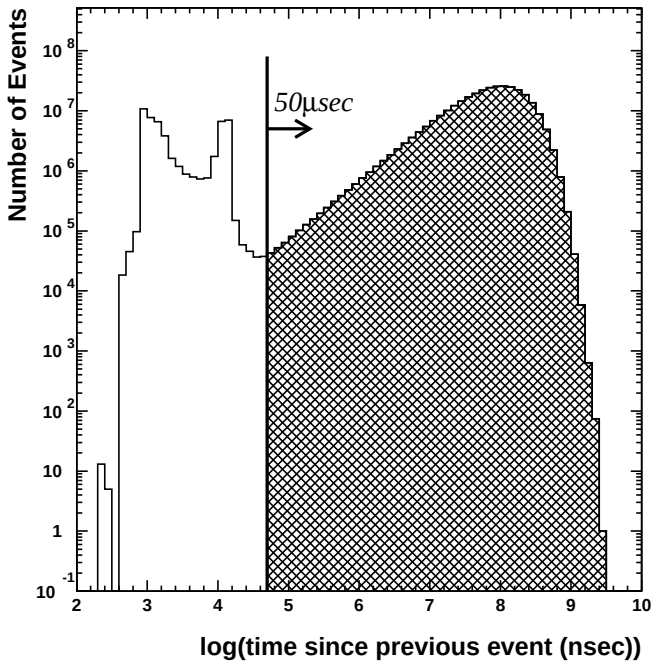

Figure 5.2: The distribution of the time difference between consecutive events. Events that occur within 50 μsec of another event are removed. The peak at ΔT $\approx$ 15 μs is caused by an after-pulse that follows energetic events: When $\geq$400 p.e. are generated in a PMT, the electrons ionize the gas in the PMT; the after-pulse occurs when the ions strike the photocathode.

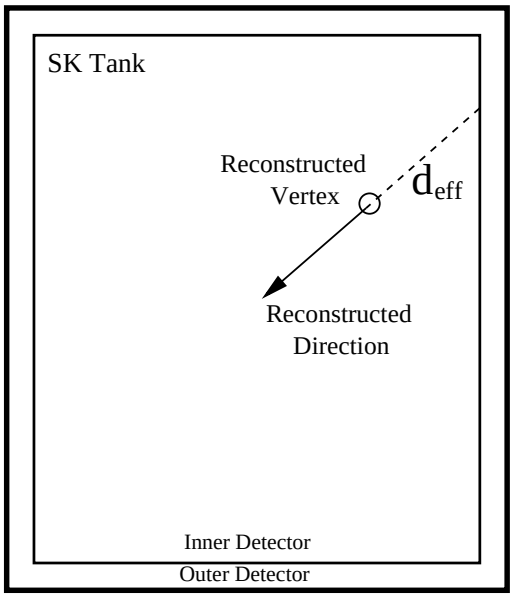

Figure 5.3: The definition of d_{eff} that is used in the secondary fiducial cut.

Primary Fiducial Volume Cut: The material of the ID wall and γ-rays from the surrounding rock induce background events with vertexes that are very close to the ID wall. To eliminate this background, a fiducial volume cut is imposed that removes any event with a vertex that is less than 200 cm from the ID wall. The 22.5 kton fiducial volume used for the SRN search is defined by this cut. Additionally, this cut removes events for which a vertex could not be found, as such events are automatically assumed to be outside of the fiducial volume.

Secondary Fiducial Volume Cut: Some events originating outside of the 22.5 kton fiducial volume may still be reconstructed with vertexes more than 200 cm from the ID walls if the direction of the event points away from the walls. To remove such events, the reconstructed direction is projected backwards from the vertex position until it reaches the ID wall. This distance between the vertex and the wall, called d_{eff} is illustrated in Figure 5.3. Events with d_{eff} greater than 450 cm are removed from the data.

Pedestal Event Cut: As mentioned in Section 2.6.1, ATM pedestal data are taken every 30 minutes. Pedestal data are acquired in eight short stages; during each stage, the ATM channels that are being adjusted cannot record data from their PMTs. Thus, events that occur during the pedestal data-taking period are rejected.

Outer Detector Event Cut: Events that originate outside of the detector must pass through the OD before reaching the ID. As mentioned in Table 2.2, the OD trigger is normally activated when more than nineteen OD PMTs are hit within a 200 nsec time window. Events that trigger the OD are removed from the data sample. Additionally, events in which more than twenty OD PMTs have been hit are also removed, regardless of whether the OD trigger has been issued. For these events, it is assumed that OD DAQ trouble was responsible for the lack of an OD trigger.

First Electronic Noise Cut: PMT hits created by electronic noise generally contain a very low amount of charge. Events that are induced by electronic noise are characterized by a large fraction of hit PMTs with low charge. Such noise events can be caused by the fluorescent lights in the electronics huts and other similar sources. To remove these events, the "noise ratio" is used: PMTs that have registered less than 0.5 photoelectrons are considered to have noise hits. The noise ratio is defined as the fraction of hits that are created by noise; events with a noise ratio greater than 0.4 are removed from the data. Figure 5.4(a) shows the noise ratio distribution for a typical run.

Second Electronic Noise Cut: If an ATM board experiences electronic noise, it can appear as if most of the channels on that board are registering hits. The "ATM ratio" for an event is defined as the fraction of channels registering as hit on the maximally hit ATM board. If any board has more than 95% of its channels hit during a particular event, then that event is removed from the data. Figure 5.4(b) shows the ATM ratio for a typical run.

First Goodness Cut: If the *goodness* of the vertex fit (see equation 4.2) is low, then the accuracy of the reconstructed vertex may be poor. Many types of background events will reconstruct with low *goodness*. LINAC events, which are essentially background-free, have a *goodness* distributions such as the one shown in Figure 4.3. For a typical run of data, the *goodness* distribution looks more like Figure 5.5. To remove background and poorly fit data, only events with *goodness* > 0.4 are kept.

Second Goodness Cut: A small fraction of events containing many noise hits reconstruct with *goodness* > 0.4. To remove such events, the stability of the *goodness* is checked. A two-dimensional virtual grid that contains the reconstructed vertex point is placed in the plane normal to the reconstructed direction. The full grid measures 10 m $\times$ 10 m.

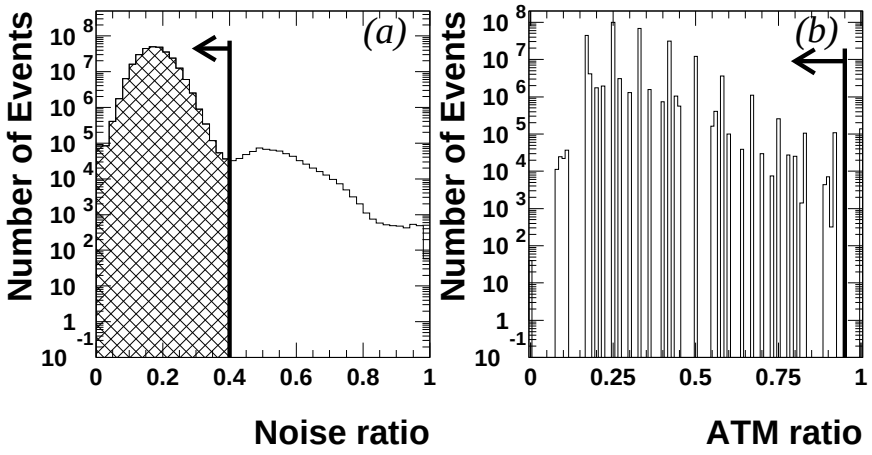

Figure 5.4: The fraction of hit PMTs registering less than 0.5 p.e. in each event is shown in (a). The fraction of hit channels from the maximally hit ATM board in a given event is shown in (b). In both cases, the events to the left of the line are retained in the data.

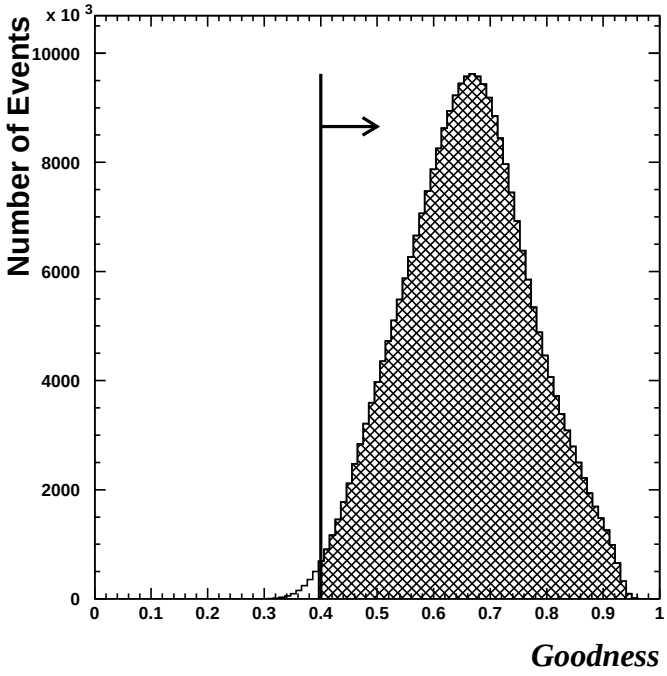

Figure 5.5: A typical *goodness* distribution for normal data. The non-shaded portion of the distribution is removed to eliminate events that were poorly reconstructed.

The vertex is then artifically shifted to each of the grid points and the *goodness* value is evaluated at that point. If more than 8% of the test vertexes have a *goodness* value that deviates significantly from the true *goodness* of the event, then the event is removed from the data sample.

5.2.1 Bad Subrun Selection

The selection criteria employed in the first reduction are used to remove individual events. If many events in a subrun fail a particular first reduction cut, it may be assumed that a hardware or software problem has occurred during that subrun. In this case, the entire subrun should be removed to prevent bad data from being processed. To account for the fact that individual subruns have different durations, the number of events removed by each first reduction cut is converted to a rate. Subruns with excessively high failure rates for a given criterion are presumed to be faulty and are discarded. All first reduction cuts are considered for the bad subrun selection except for the total charge cut, the fiducial volume cuts, and the *goodness* cuts.

Figure 5.6 shows the rate of events that failed the time difference cut in each subrun during SK-I. Each point on Figure 5.6 represents one subrun. The rate is expressed as the number of events per day, though no subrun ever lasts for more than ten minutes. Subruns with an event rate that falls between the two sets of dashed lines are retained. Similar figures can be made for each of the other first reduction criteria.

As the trigger threshold of SK-I was lowered (see Section 2.6.3), the time of each subrun decreased. The shorter subrun duration caused a larger spread in the distribution of failure rates for a normal subrun. To account for this, the cut criteria were re-evaluated each time the trigger threshold was adjusted.

5.3 Spallation Cut

As cosmic ray muons pass through Super-Kamiokande, they can spall oxygen nuclei through the following interaction:

$$\mu + {}^{16}\mathrm{O} \rightarrow \mu + \mathrm{X}$$

where the resulting nuclei, X, are unstable. These nuclei are appropriately called "spallation products" and are listed in Table 5.1 [51]. The spallation products typically undergo β and γ decay, with half-lives ranging from a few milliseconds (8.5 ms for ^{11}Li) to a few seconds (13.8 s for ^{11}Be). The energy of

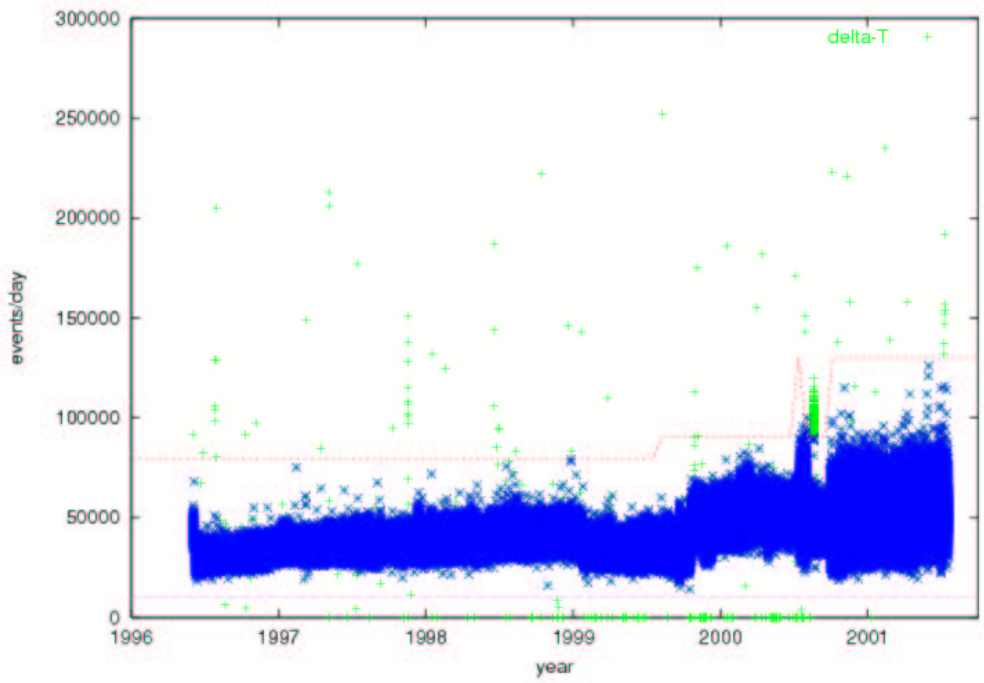

Figure 5.6: The rate of events that fail the time difference cut in the first reduction. Each point represents a single subrun. The ordinate of a given point corresponds to the number of events that failed this cut during that subrun. To account for variations in the subrun livetime, the y-axis values are expressed as a daily event rate. Subruns with failure rates outside of the dashed lines are rejected. As the trigger threshold of SK-I was lowered, the criteria for good subruns needed to be adjusted. This is reflected by the changes in the value of the dashed lines.

Isotope	$\tau_{1/2}$(sec)	Decay mode	Kinetic Energy(MeV)
$^{11}_{3}$Li	0.0085	β^- $\beta^- + n$	20.77 (31%) $\sim$16 (61%)
$^{13}_{8}$O	0.0090	$\beta^+ + p$	8$\sim$14
$^{12}_{7}$N	0.0110	β^+	16.38
$^{12}_{4}$Be	0.0114	β^-	11.66
$^{14}_{5}$B	0.0161	β^-	14.07+6.09(γ)
$^{13}_{5}$B	0.0173	β^-	13.42
$^{12}_{5}$B	0.0204	β^-	13.37
$^{8}_{2}$He	0.122	β^- $\beta^- + n$	10.56+0.99(γ) (11%)
$^{9}_{6}$C	0.127	$\beta^+ + p$	3$\sim$13
$^{9}_{3}$Li	0.178	β^- $\beta^- + n$	13.5 (75%) 11.0+2.5(γ) (25%) $\sim$ 10 (35%)
$^{16}_{6}$C	0.7478	$\beta^- + n$	$\sim$4
$^{8}_{5}$B	0.77	β^+	13.73
$^{8}_{3}$Li	0.84	β^-	12.5$\sim$13.0
$^{15}_{6}$C	2.449	β^-	9.82 (32%) 4.51+5.30(γ) (68%)
$^{16}_{7}$N	7.134	β^-	10.44(26%) 4.27+6.13(γ) (74%)
$^{11}_{4}$Be	13.8	β^-	11.48 (61%) 9.32+2.1(γ) (29%)

Table 5.1: A list of the spallation products and information about their decay modes. The list is organized by the half-life of the decay, in increasing order.

the emitted β and γ rays can be as high as 20.8 MeV; when these are detected in SK, they are referred to as "spallation events."

The spallation events are generated uniformly in space and time within the detector. About six hundred spallation events occur per day inside of the 22.5 kton fiducial volume. These events can be useful for detector calibration (see Sections 3.4.2 and 3.5.1), but they are a significant background for the SRN search. The SRN search is conducted only in the energy region where spallation events can be completely removed. Above the SK trigger threshold, all of the SRN models predict a flux that falls exponentially with increasing energy (see Figure 1.5). Therefore, a low SRN analysis threshold is desirable, and this requires an effective spallation cut.

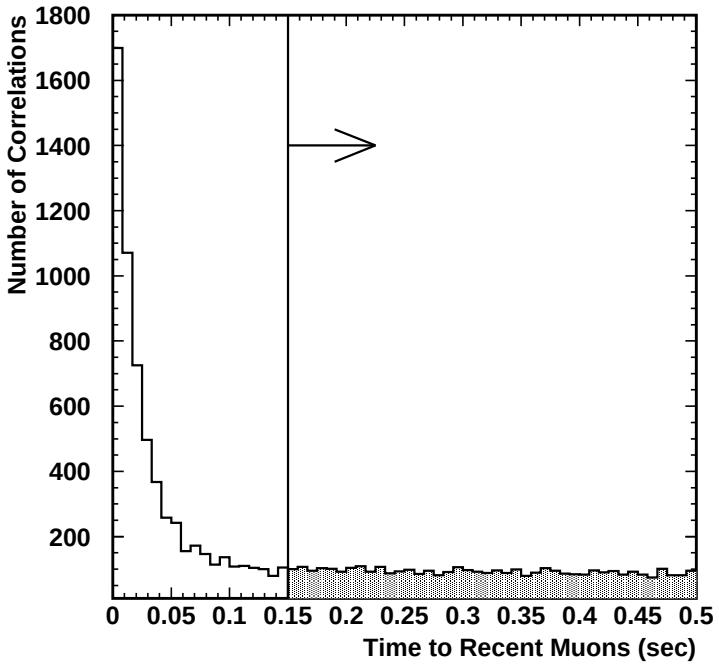

Figure 5.7: The time correlation between data events and cosmic ray muons. A clear abundance of spallation events occurs within 0.15 seconds of a muon.

Spallation events have strong spatial and temporal correlations to the cosmic ray muons that induce them. Such correlations can be exploited to remove these events from the data. The spallation cut is applied in two stages. During the first stage, timing information is used to remove the highest energy spallation events from the data. In the second stage, additional information about the CRM is used to eliminate the spallation events with longer half-lives.

5.3.1 Time Correlation Cut

As shown in Table 5.1, the spallation products with the shortest half-lives, such as ^{11}Li and ^{12}N, tend to create spallation events with the highest energies. Using only timing information, it is possible to remove most of the events caused by spallation products with half-lives less than $\sim$20 ms. These events are most likely to impede the SRN search.

Figure 5.7 shows the time correlations between SRN candidate events (with $E_e > 15$ MeV) and the muon events that preceded them. For each SRN candidate, the previous two hundred muons are considered. In Figure 5.7, the time difference, ΔT, between the muon event time and the SRN candidate

event time is shown for all correlations with $\Delta T < 0.5$ s. There is a clear excess of correlations between muon events and SRN candidate events for $\Delta T < 0.15$ s. These events are quite likely to be spallation-induced; therefore, any event that occurs less than 0.15 s after a muon is removed from the data sample. For ΔT values greater than 0.15 s, the distribution is flat, as one would expect for unrelated events.

When only the time correlation cut is applied to the data, no discernible spallation events remain in the data above 20 MeV.

5.3.2 Likelihood Function Cut

All spallation products with half-lives greater than 0.1 s decay to events with less than 14 MeV of kinetic energy. However, due to the finite energy resolution of the detector, it is possible for such events to occasionally reconstruct with higher energies. In order to permit a lower analysis for the SRN search than that made possible by the time correlation cut, a second spallation cut is applied. In addition to using the ΔT variable, the likelihood function cut uses two other types of information to search for correlations between SRN candidates and muon events. The two additional variables are:

- ΔL – The closest distance between the fitted track of the muon event and the vertex of the SRN candidate event. Spallation events are expected to have low values of ΔL.

- Q_{res} – The residual charge of the muon, as defined by equation (4.12). Positive values of Q_{res} indicate muons that are likely to have interacted within the detector and created spallation products.

There are two spallation likelihood functions; the result of the muon reconstruction determines which one is used. For muons with a track that was successfully fit, a function that considers all three variables (ΔT, ΔL, and Q_{res}) is used to calculate the likelihood value. For muons that have failed the reconstruction, a likelihood function that considers only ΔT and Q_{res} information is used. The form of the likelihood functions is described in detail in reference [52].

For each SRN candidate event, a likelihood value is evaluated for each of the two hundred muons that preceded it. The largest likelihood value, L_{max}, is assigned to the event. The solid histograms in Figure 5.8 show the distribution of likelihood values for a subset of the data. The top and bottom figures correspond, respectively, to distributions from muons with and without successful track reconstructions. The cut parameters are shown by the vertical

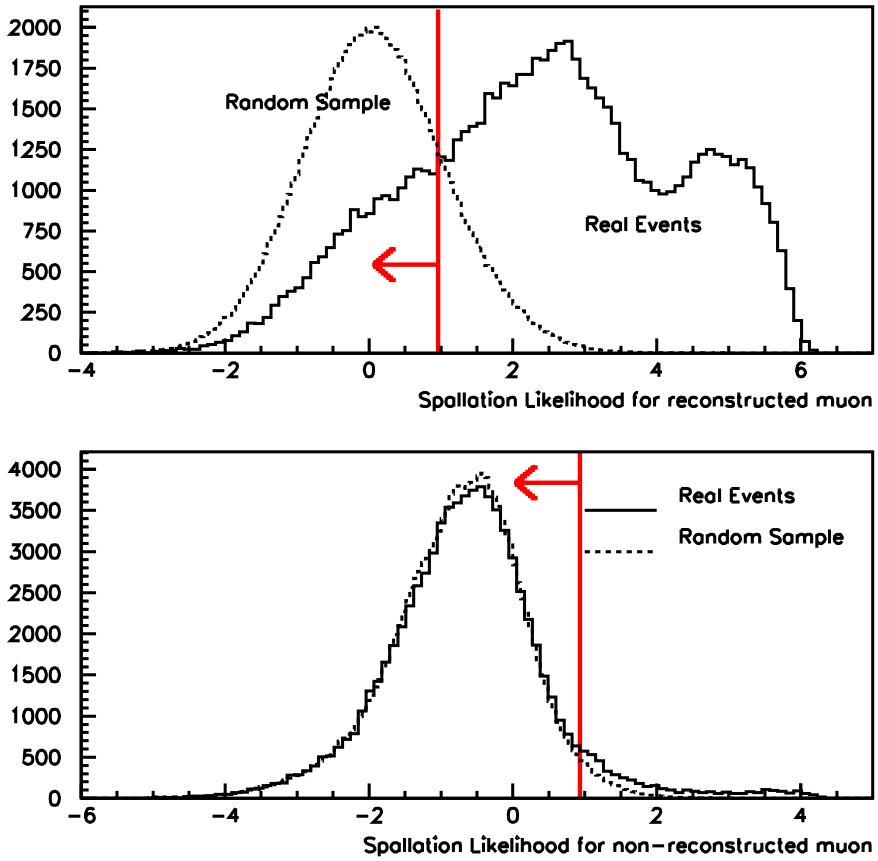

Figure 5.8: The spallation maximum likelihood distributions. The top figure shows the distribution obtained from muons with tracks that were successfully fit; the bottom figure shows the distribution obtained from muons without a fit track. The vertical lines represent the cut parameter; the data to the left of the line are retained.

lines on the figures: events with $L_{max} > 0.98$ are removed if the correlated muon reconstructed successfully, and events with $L_{max} > 0.92$ are removed if the correlated muon failed the track fit.

When both spallation cuts are applied to the data, no discernible spallation events remain with energies above 18 MeV. Hence, 18 MeV was chosen as the analysis threshold for the SRN search.

5.3.3 Applying the Spallation Cuts

As shown in Table 5.1, the highest energy of any spallation product is 20.77 MeV, which is the cut-off energy of ^{11}Li. At this energy, the 1σ energy resolution of SK-I, shown in Table 3.2, is about 2.6 MeV. To ensure that no spallation events contaminate the SRN sample, the spallation cuts are applied over an energy range that extends 5σ above the spallation cut-off energy. Thus, SRN candidate events reconstructed with energies less than 34 MeV are subjected to the spallation cut.

The efficiency loss caused by the spallation cut is estimated with a sample of Monte Carlo simulated events that are generated with random vertex positions within the fiducial volume and with random event times. The dashed histograms in Figure 5.8 represent the distribution of likelihood values for this random sample. The spallation cuts are applied to the random sample, and the fraction that remains is taken to be the efficiency of the cut for retaining signal. The time correlation cut has an efficiency of 81% for retaining SRN events, and the likelihood function cut has an efficiency of 79%. When combined, the full spallation cut has an efficiency of 64%.

5.4 Second Reduction

The second reduction is designed to remove physics backgrounds that are specific to the SRN search. The primary sources of these backgrounds are solar and atmospheric neutrinos, which have been the subject of other analyses [46, 52, 53, 54]. Thus, the properties of these backgrounds are well known and can be used to separate them from the SRN candidate event sample.

There are three second reduction cuts. The sub-event cut removes events induced by atmospheric ν_μ; the Cherenkov angle cut removes more of these events, as well as multiple γ-rays caused by nuclear de-excitations; the solar direction cut prevents contamination of the SRN sample by ^{8}B and *hep* neutrinos from the Sun. Each cut is described in detail below.

5.4.1 Sub-Event Cut

As atmospheric ν_μ pass through the detector, they can produce muons via charged current quasi-elastic scattering:

$$\nu_\mu + N \rightarrow \mu + N'$$

Most atmospheric ν_μ have large energies relative to those expected for the SRN; thus, the muons that they create will not be a concern. However, some low energy ν_μ will produce muons with $p_\mu < 350$ MeV/c. These muons become a background to the SRN search.

If $p_\mu < 120$ MeV/c, then the muon is below the threshold for emitting Cherenkov photons (see equation 2.1). Such muons are said to be "invisible" and will be discussed further in Section 5.6. Muons with 120 MeV/c $< p_\mu <$ 350 MeV/c will emit Cherenkov light and will also reconstruct in the energy range that is relevant to the SRN search. Although this search is conducted at energies less than 90 MeV, the energy reconstruction described in Section 4.3 assumes that the particle being considered is an electron (or positron). Electrons undergo electromagnetic showering and they experience multiple scattering in water; as a result, electrons lose energy in water at a faster rate than muons do. Figure 5.9 plots the actual momentum versus reconstructed energy for a set of Monte Carlo simulated muons. Muons with less than ~350 MeV/c of momentum reconstruct the same as electrons with less than 90 MeV of energy, and are therefore a background to the SRN search. Figure 5.10(A) shows the energy spectrum of the atmospheric ν_μ that can produce a muon in this momentum range. The momentum spectrum of the muons created from these ν_μ is shown by the shaded region of Figure 5.10(B). The non-shaded region of the figure represents the spectrum of the invisible muons.

As a muon moves through water, it continuously loses energy through electromagnetic interaction. The energy loss, $-dE/dx$, is given by the Bethe-Bloch equation [55]; at the relevant values of p_μ, the muon loses about 2.5 MeV per cm traveled in water. Therefore, all muons with momentum low enough to be a background for the SRN search will stop in the detector and produce a decay electron (or positron). Since the timing window for one event (1.3 μs, see Section 2.6.1) is comparable to the muon lifetime (2.2 μs), the decay electron is often found in the same event as the parent muon. When this happens, the decay electron is referred to as a "sub-event." Figure 5.11 shows the SK event display for such an event; two rings emanating from a single vertex are clearly visible. The smaller, collapsed ring was formed by the parent muon and the larger ring was created by the decay electron.

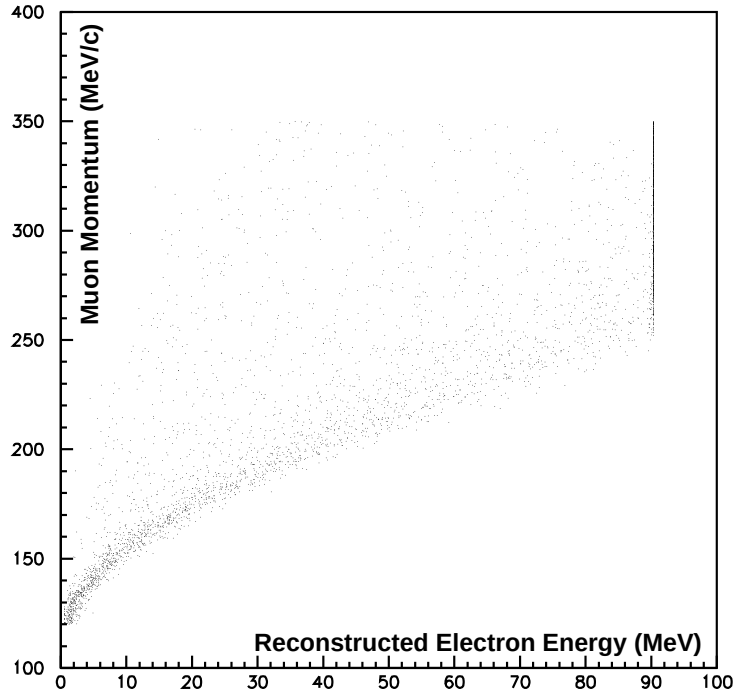

Figure 5.9: The correspondence between the actual muon momentum and the reconstructed energy is shown. The energy reconstruction assumes that the particle is an electron, so muons with $p_\mu < 350$ MeV/c appear to be electrons with $E_e < 90$ MeV.

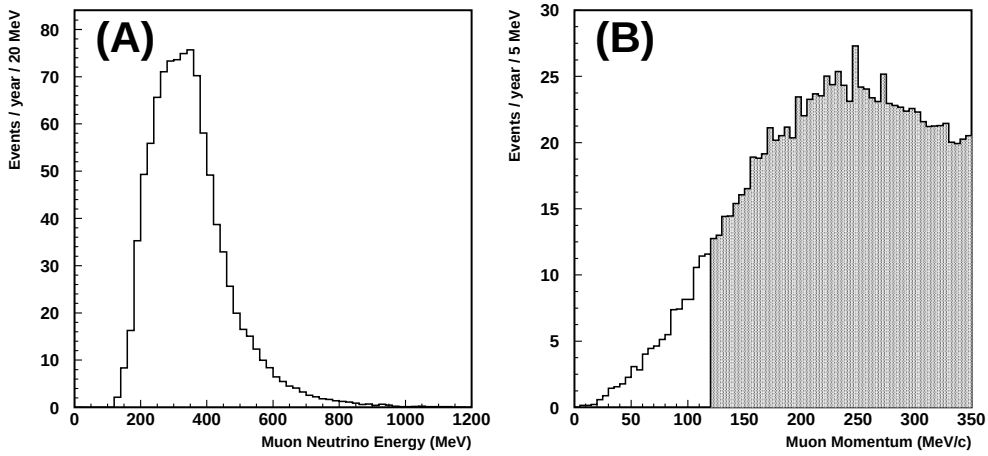

Figure 5.10: The energy spectrum of atmospheric ν_μ that produce a muon with 120 MeV/c $< p_\mu <$ 350 MeV/c is shown in (A). The momentum spectrum of the muons is shown in (B). Muons in the shaded region are a background to the SRN search; the other muons are invisible.

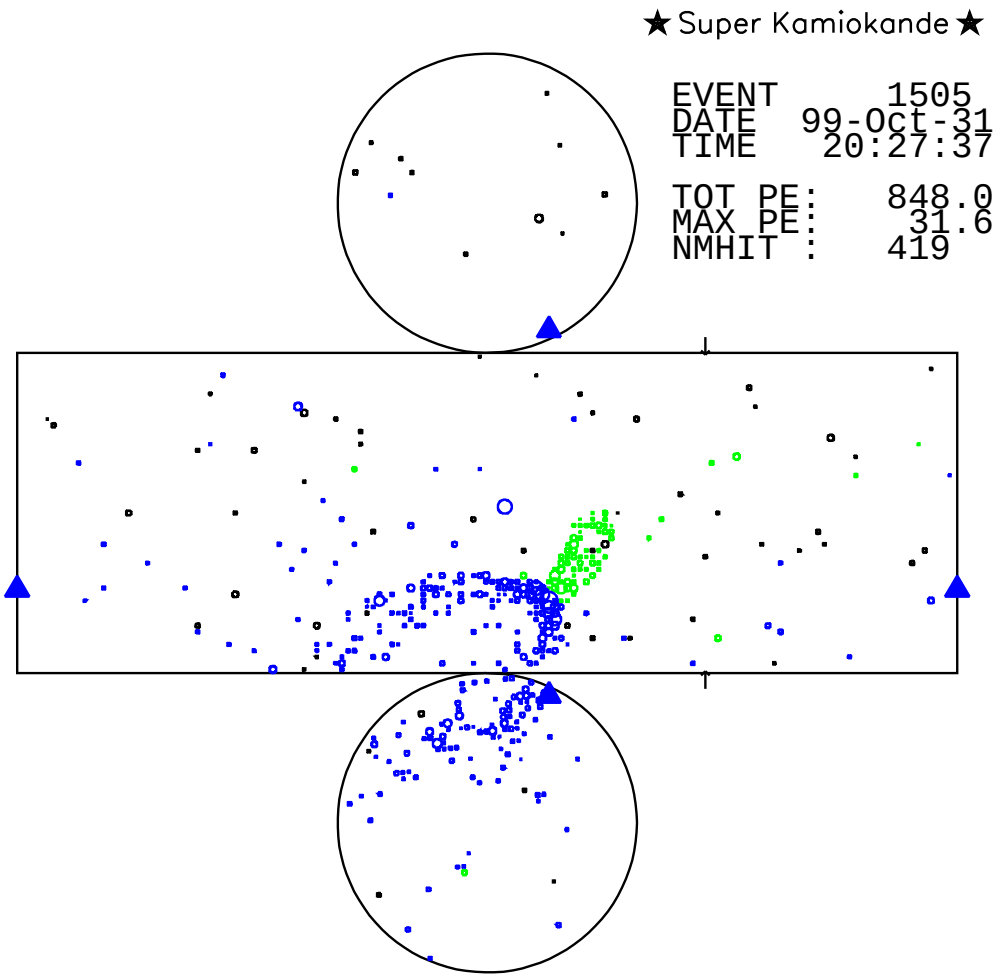

Figure 5.11: The SK event display is shown for a typical two ring μ-e decay event. The smaller ring was produced by the muon and the larger ring was formed by the decay electron.

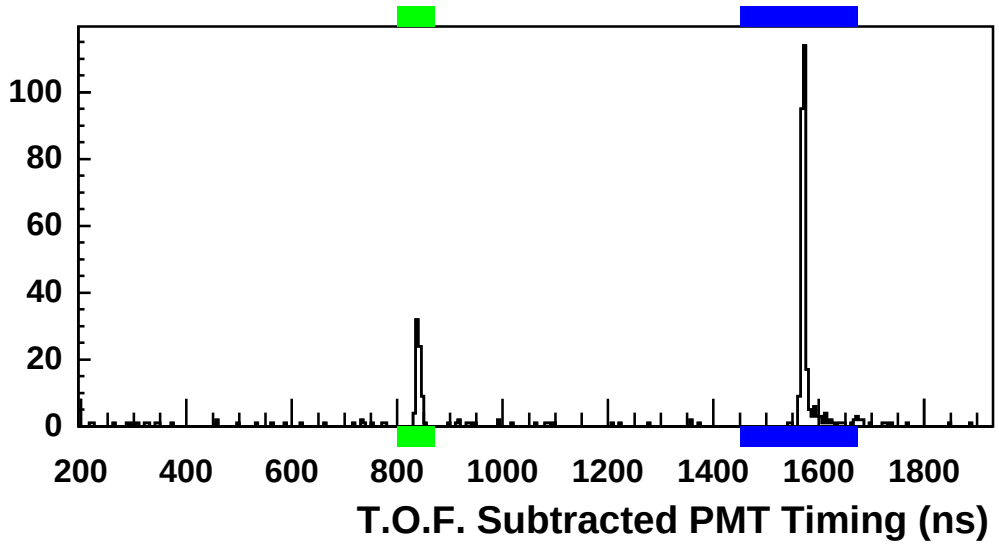

Figure 5.12: The TOF-subtracted timing distribution for the event shown in the previous figure.

When cosmic ray muons enter the detector, they are tagged by the OD and removed from the data during the first reduction. The low energy muons discussed here are produced within the ID and have no such tag. Instead, these muons can be identified by searching for a sub-event with the following method: A muon drops below the Cherenkov threshold when its momentum becomes less than 120 MeV/c, after which it only travels about 25 cm before it comes to rest and decays. This distance is less than the vertex resolution of SK (see Table 3.2); thus, the muon and its decay electron can be treated as having the same vertex. Once this common vertex has been reconstructed, it can be used to subtract the time of flight (TOF) that each Cherenkov photon traveled before encountering a PMT.

Figure 5.12 shows the TOF-subtracted timing distribution for the event displayed in Figure 5.11. Just as two distinct rings were visible in the event display, two separate peaks can be seen in the timing distribution. The earlier peak corresponds to the parent muon and the decay electron peak occurs about 750 ns later. The TOF-subtracted timing distributions for the SRN candidates were searched; any event that was found to have a second peak containing at least nine PMTs was labeled as a muon and removed from the data.

The efficiency of this criterion for removing muons with $p_\mu < 350$ MeV/c

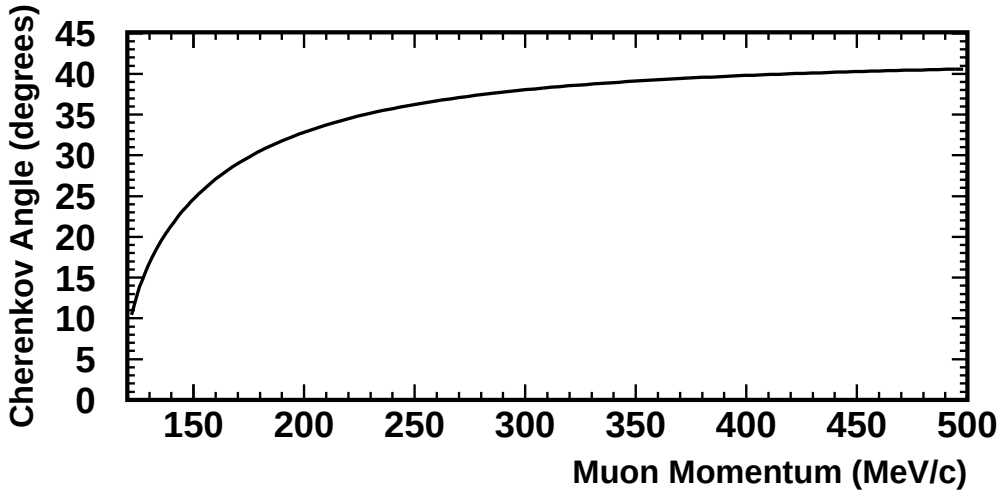

Figure 5.13: The Cherenkov angle for muons is plotted as a function of the muon momentum.

was evaluated with Monte Carlo. It was found that the sub-event cut removes 34% of the muon background while retaining more than 99% of the positron signal. The remaining 66% of the muons did not have their decay electron occur in the same event timing window; thus, they could not be tagged by this method.

5.4.2 Cherenkov Angle Cut

The Cherenkov angle of each event that passed the first reduction cuts was reconstructed using the method described in Section 4.4. Electrons (or positrons) that are energetic enough to trigger SK are all ultra-relativistic and have a Cherenkov angle of $\theta_C \approx 42^\circ$ (see Section 2.1). By rejecting events that deviate from this value, two types of backgrounds can be removed: single ring muon events and multiple γ-ray events.

Single Ring Muon Events

The Cherenkov angle cut exploits the mass difference between the muon and the positron, which results in a difference in their θ_C values. Figure 5.13 shows the Cherenkov angle for a muon as a function of its momentum. The muons that are likely to contaminate the SRN search have $p_\mu < 350$ MeV, which corresponds to a maximum θ_C value of 38°. Therefore, muons that do not have a decay electron in the same event can be still be removed from

the data by using the Cherenkov angle to distinguish them from electrons (or positrons).

The SK event display is shown for a typical electron event in Figure 5.14. This event was reconstructed with a total energy of 59 MeV. The ring of hit PMTs is fuzzy; this is normal for electron events, because they undergo changes in direction due to multiple scattering in water. The display also shows a ring that has been superimposed on the event; this represents the expected Cherenkov ring given the reconstructed vertex and direction. In this figure, the expectation is a good match for the actual ring of hit PMTs.

The SK event display is shown for a typical muon event in Figure 5.15. This event was reconstructed with a total energy of 68 MeV. However, it is important to recall that the energy reconstruction algorithm implicity assumes that the particle is an electron. The ring of hit PMTs is sharp, because the muon is not subjected to multiple scattering. Again, the ring expected from the reconstructed vertex and direction is superimposed on the event. Unlike the expectation shown in Figure 5.14, this ring is a poor match for the actual hit PMTs. The discrepancy arises because the likelihood function used in the direction reconstruction (equation 4.4) assumes that the Cherenkov light is emitted at an angle of 42° relative to the event direction. This assumption is contained within the probability density function $f(\phi_i(\boldsymbol{d}))$, shown in Figure 4.5.

Figure 5.16 shows the distribution of opening angles, obtained from combinations of three hit PMTs, for the electron event (A) and the muon event (B). For each distribution, the peak was roughly located by finding the histogram bin with the largest number of entries. A Gaussian function was then used to fit the distribution around this peak value; the mean of the Gaussian was taken to be the Cherenkov angle of the event. A clear difference can be seen between the electron and the muon distributions. To remove muons from the sample of SRN candidates, any events that reconstruct with $\theta_C < 38°$ are rejected.

The efficiency of the Cherenkov angle cut for retaining the SRN signal can be seen from Figure 5.17. The points on this figure represent the distribution of reconstructed Cherenkov angles for a sample of 5000 Monte Carlo simulated positrons. By rejecting events with $\theta_C < 38°$, only $\sim$2% of the positrons are eliminated. Therefore, the Cherenkov angle cut is highly efficient at retaining the SRN signal. The MC distribution is normalized so that it can be directly compared to the actual data, which has an order of magnitude fewer events. The solid histogram in this figure represents the normalized distribution of Cherenkov angles obtained from the actual data. In addition to the electron-like peak, a peak of muon events is visible with smaller values of θ_C. The

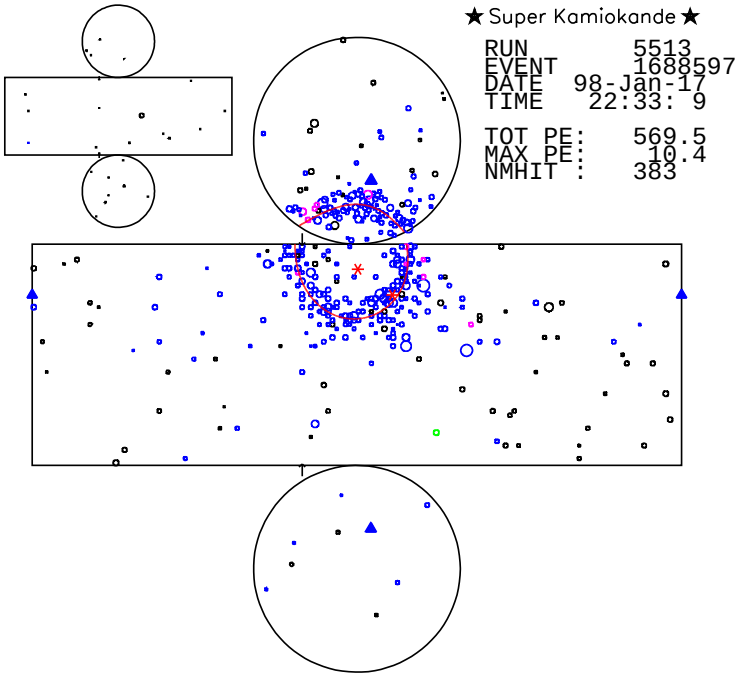

Figure 5.14: The SK event display is shown for an electron that reconstructed with 59 MeV of energy. The fit Cherenkov ring, which assumes a 42° opening angle, is shown.

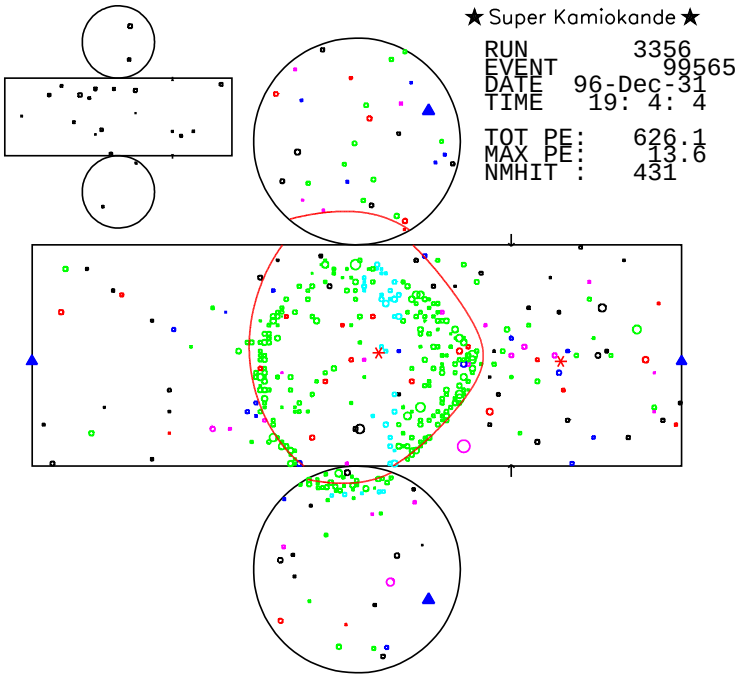

Figure 5.15: The SK event display is shown for a muon that reconstructed with 68 MeV of energy. The fit Cherenkov ring, which assumes a 42° opening angle, is shown.

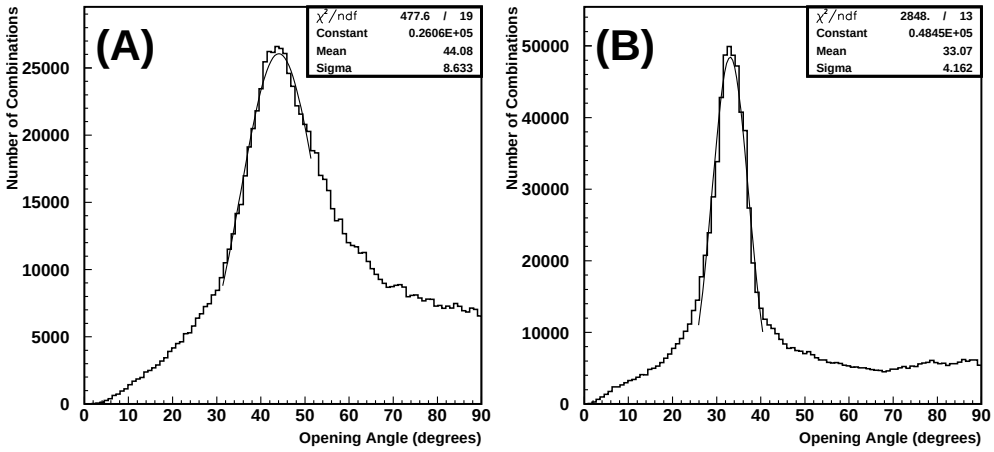

Figure 5.16: The distribution of opening angles, obtained from combinations of three hit PMTs, is shown for the events displayed in the previous two figures. Fitting the distribution for the electron event (A) gives $\theta_C = 44°$; for the muon event (B), the distribution peaks at $\theta_C = 33°$.

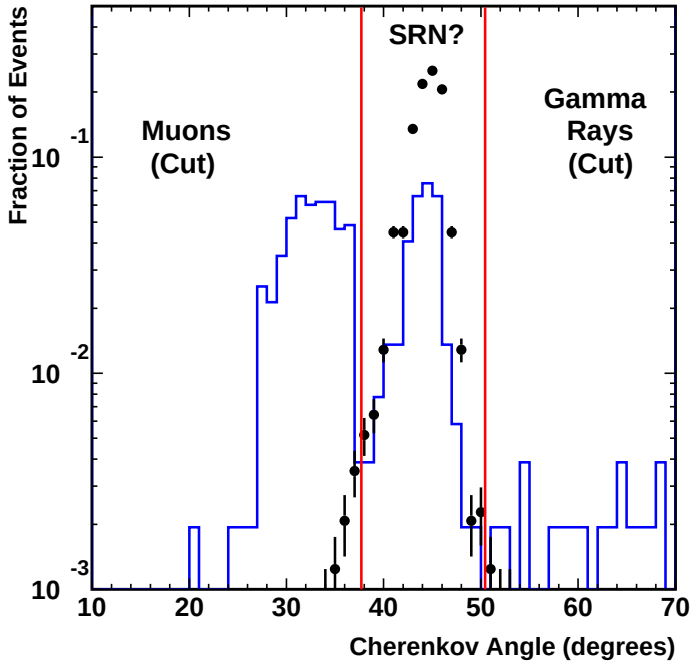

Figure 5.17: The Cherenkov angle distribution is shown for actual data (solid histogram) and positron MC (circles). The vertical lines represent the cut parameters; events between the two lines are retained.

requirement that the reconstructed event energy be less than 90 MeV causes the the muon peak to drop sharply at $\theta_C = 38°$, thereby creating a clear separation between the two peaks.

It is worth noting that there are particles other than muons that can cause an event with a Cherenkov angle less than 42°. Some of these events may actually be protons that are marginally above the Cherenkov threshold. The value of studying such proton events has been written about elsewhere [56]. However, for the purposes of this study, it is clear that those events are not SRN candidates and it is sufficient to simply reject them.

Multiple γ-Ray Events

It is possible for low energy muons in the detector to be captured by the neutrons in ^{16}O. This capture can elevate the neutron to an excited nuclear state. Upon de-excitation, the neutron releases a cascade of γ-rays. Although the energy of each individual γ-ray will be significantly less than 18 MeV, the combined energy of the cascade can exceed this threshold. The maximum energy of such an event is $\sim$25 MeV. Since these events appear in the energy range where SRN detection is most likely, they can mimic the expected signal. Therefore, it is very important to remove this type of event from the data.

If the captured muon had sufficient momentum to exceed the Cherenkov threshold, then the resulting multiple γ-ray event is likely to be rejected by the spallation cut because it will have a strong correlation to a tagged muon. If, however, the muon is invisible, then the resulting nuclear cascade will not be correlated with any previous event.

Figure 5.18 shows the event display for a typical multiple γ-ray event. Despite 20 MeV of visible energy being deposited in the detector, there is no clear evidence of a Cherenkov ring in this display. The event appears to consist of random noise hits, and the best fit to the vertex and direction yields a ring that bears no resemblence to the distribution of hit PMTs. From the display, such an event looks as if it should have been rejected as electronic noise; however, there is a clear peak in the TOF-subtracted timing distribution, shown in Figure 5.19. The unambiguous timing peak makes it clear that the event is not simply made up of noise hits. The timing peak, coupled with the lack of a Cherenkov ring, is evidence that multiple particles, each with very low energy, were emitted simultaneously. This signature is used to identify and reject these multiple γ-ray events.

As mentioned in Section 4.4, noise hits tend to form combinations that reconstruct with large opening angles. For events caused by multiple γ-ray emission, the spatial distribution of hit PMTs resembles that of random noise;

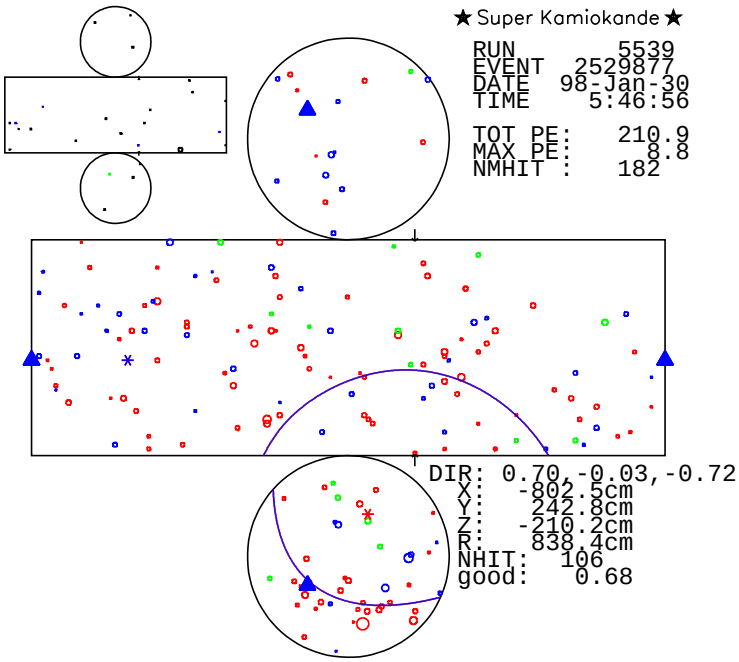

Figure 5.18: The SK event display is shown for a multiple γ-ray event that reconstructed with 20 MeV of energy. The reconstructed vertex is listed, along with the *goodness* of the fit. The fit Cherenkov ring is superimposed, though it bears little resemblence to the actual event.

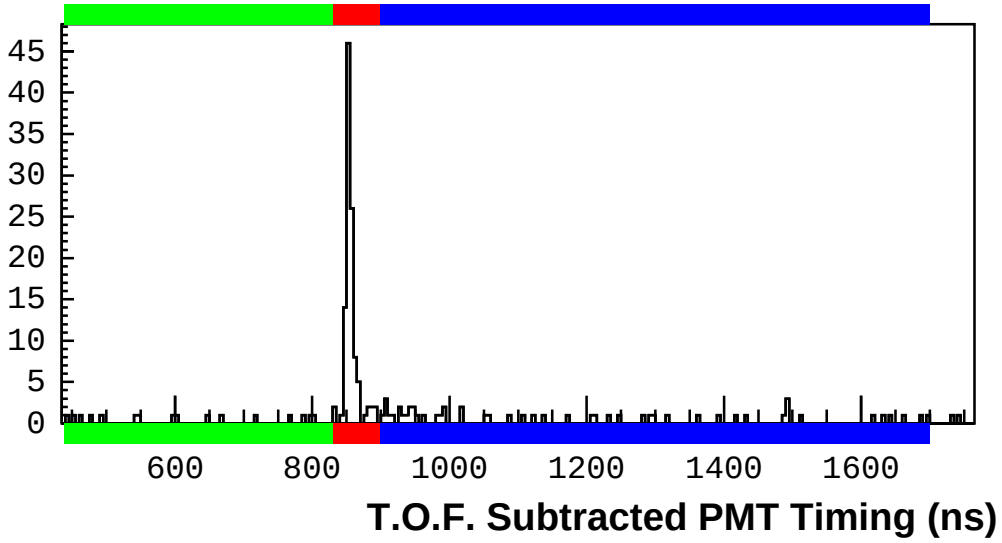

Figure 5.19: The TOF-subtracted timing distribution is shown for the event displayed in the previous figure. A clear timing peak reveals that this event is not simply random noise.

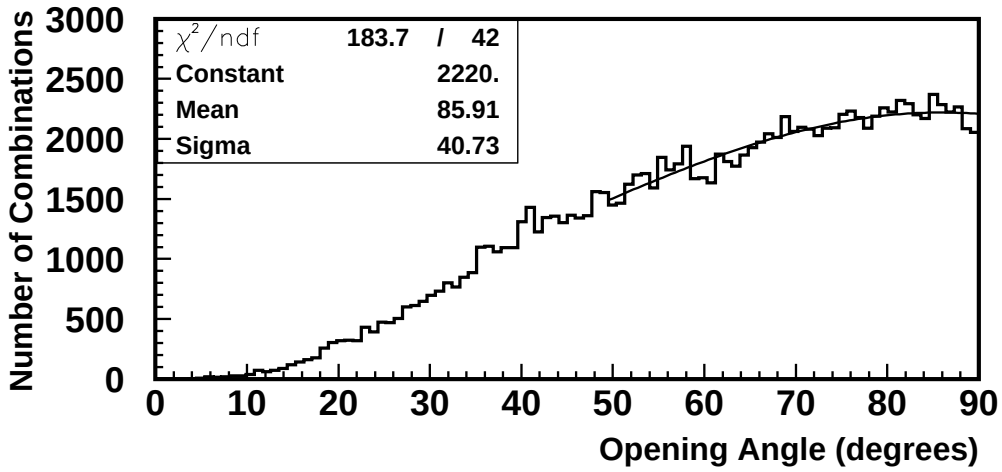

Figure 5.20: The distribution of opening angles, obtained from combinations of three hit PMTs, is shown for the event displayed in Figure 5.18. No Cherenkov ring is visible in the display, and the reconstructed Cherenkov angle value is $\theta_C = 86°$.

thus, the reconstructed Cherenkov angle is expected to approach $\theta_C = 90°$. Figure 5.20 shows the distribution of opening angles for all combinations of three hit PMTs from the multiple γ-ray event displayed in Figure 5.18. The mean value of the Gaussian fit yielded a Cherenkov angle of 86°. To remove multiple γ-ray events from the SRN sample, any event that reconstructs with $\theta_C > 50°$ is rejected. From the reconstructed θ_C distribution of the MC positrons, shown in Figure 5.17, it can be seen that a negligible fraction of the SRN signal is lost as a result of this selection criterion.

5.4.3 Solar Direction Cut

The 18 MeV analysis threshold is low enough to allow for potential contamination from ^{8}B and *hep* solar neutrinos. These neutrinos are produced in the Sun via the following nuclear reactions:

$$^8\mathrm{B} \rightarrow {}^8\mathrm{Be} + \mathrm{e}^+ + \nu_\mathrm{e}$$

and

$$^3\mathrm{He} + \mathrm{p} \rightarrow {}^4\mathrm{He} + \mathrm{e}^+ + \nu_\mathrm{e}$$

The cut-off energy for these reactions is about 15 MeV for ^{8}B neutrinos and 18.77 MeV for *hep* neutrinos.

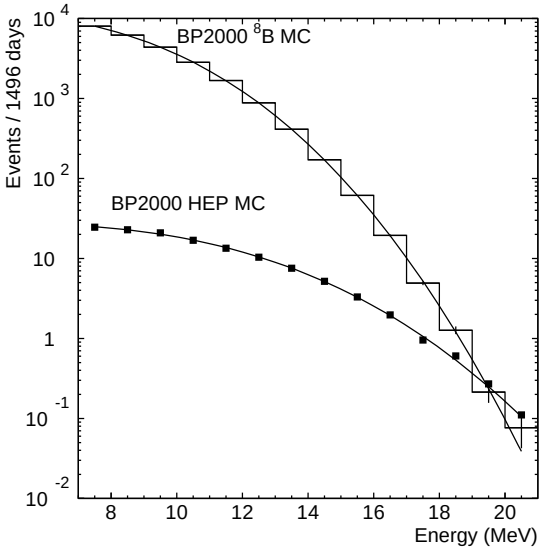

Figure 5.21: The expected contamination of recoil electrons from ^{8}B and *hep* solar neutrinos is shown. The prediction is based on the BP2000 standard solar model [57], and detector resolutions have been considered.

Figure 5.21 shows the expected number of ^{8}B and *hep* solar neutrino events in SK as a function of energy. To obtain these expectations, Monte Carlo simulated events were generated according to the flux and spectra predicted by the BP2000 standard solar model [57]. The MC events were processed with the detector simulating software (described in Chapter 6) and fit with the standard reconstruction tools. Thus, detector resolution effects are accounted for in this figure. Due to the energy resolution of SK, it is possible to detect both types of solar neutrinos with reconstructed energies greater than 20 MeV.

Solar neutrinos are detected in SK via the recoil electrons from elastic scattering ($\nu_e + e \rightarrow \nu_e + e$) interactions. Above a total recoil electron energy of 18 MeV, the expected number of *hep* solar neutrinos in the SK-I data is 1.06 events. Using this energy threshold, the total number of observed solar neutrinos in SK-I, from either type, is 4.9 ± 2.7 events. This value is comparable to the number of SRN events expected in the SK-I data; therefore, the solar neutrino events represent a non-trivial background that must be eliminated.

Fortunately, solar neutrino events are easy to remove because the position of their source, the Sun, is well known. The variable θ_{sun} is defined as the angle between the direction of a particular event and the vector that points from the

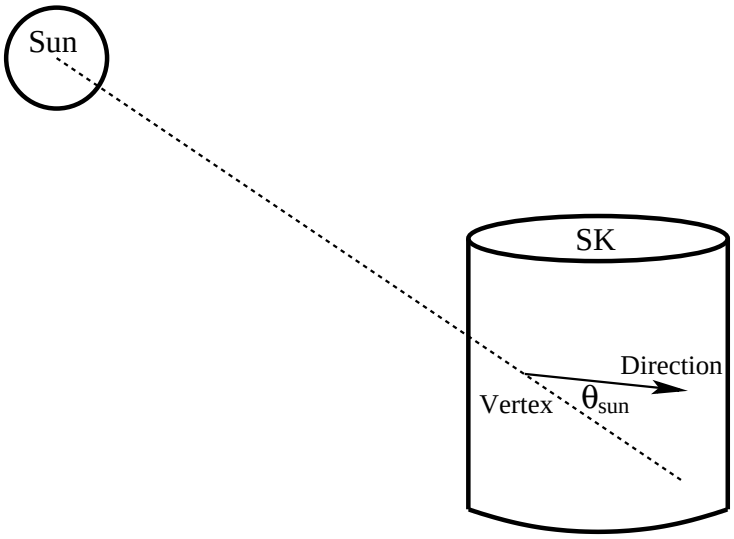

Figure 5.22: The variable θ_{sun} is defined as the angular separation between the reconstructed direction of an event and the vector that connects the Sun and the Earth at the time of the event.

Sun to the event vertex; this definition is shown graphically in Figure 5.22. Ideally, solar neutrinos events have $\theta_{sun} = 0°$. In actuality, the recoil electron does not point back to the Sun perfectly, especially at lower energies ($E_e <$ 6 MeV) where scattering effects are large. Above 18 MeV, these effects are small. In this energy region, the limiting effect is the angular resolution of the direction reconstruction (see Table 3.2), which is about 20°.

Figure 5.23 shows the $\cos(\theta_{sun})$ distribution for SRN candidate events with a reconstructed energy less than 34 MeV. This energy value was chosen very conservatively; it is highly unlikely that there will be any solar neutrino events reconstructed so poorly as to appear to have an energy greater than 34 MeV. In order to remove potential contamination from solar neutrinos, all events with reconstructed energy less than 34 MeV were rejected if they pointed back to within 30° of the Sun. This corresponds to removing the rightmost bin in Figure 5.23, which contains events with $\cos(\theta_{sun}) > 0.866$.

With an analysis threshold of 18 MeV, the requirement that events must have $\cos(\theta_{sun}) < 0.866$ should eliminate all of the solar neutrino events from the SRN sample. The efficiency of this cut for retaining signal can be evaluated from simple geometric considerations. SRN events are expected to be isotropic. Thus, 93.3% of the signal should point back to a direction that is more than 30° away from the Sun.

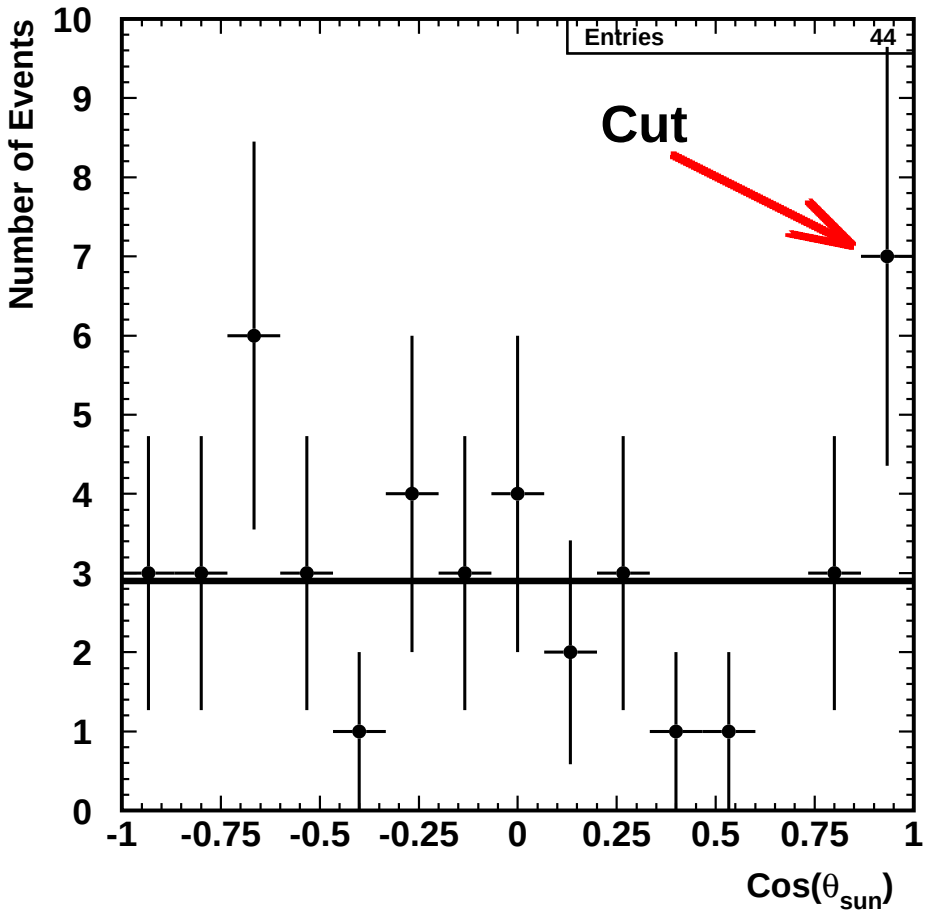

Figure 5.23: The $\cos(\theta_{sun})$ distribution for SRN candidates with E < 34 MeV. The horizontal line shows the average number of events per bin. To prevent contamination from solar neutrinos, the bin corresponding to $\cos(\theta_{sun}) > 0.866$ is removed.

Reduction Step	Number of Events Remaining After	Efficiency of the Cut
No cuts applied (18 – 82 MeV)	8066	100%
First reduction	1602	81%
Spallation cut (E < 34 MeV)	992	64%
Sub-event cut	828	99%
Cherenkov angle cut	278	98%
Solar direction cut (E < 34 MeV)	271	93%
Final Sample – all cuts applied	271	47%

Table 5.2: The steps of the reduction are summarized. The number of events remaining after each stage of the reduction is listed. The efficiency for retaining signal is quoted for each individual cut and is not cumulative.

5.5 Reduction Summary

The number of events remaining at each stage of the reduction process is listed in Table 5.2. The reconstructed energy range selected for the SRN search is 18 – 82 MeV. The lower threshold was set as the lowest energy above which no spallation appeared to remain in the data. The choice of the upper threshold is less important, since the expected SRN signal is negligible at higher energies; the selection of 82 MeV as the upper threshold value will be discussed in Section 7.1.

Table 5.2 also shows the signal-retaining efficiency for each of the reduction steps. Note that the values listed are for each specific cut and do not include efficiencies from the previous cuts. The total efficiency, when all cuts are applied, is 47% ± 0.4%. Above 34 MeV, the spallation cut and the solar direction cut are not applied. In this energy region, the efficiency is 79% ± 0.5%.

Figure 5.24 plots the SK-I energy spectrum after each stage of the data reduction. In this figure, all of the cuts have been applied across the entire energy range. The solid lines represent the event rate predictions obtained from each of the six theoretical models described in Chapter 1. The signal detection efficiency of 47% has been considered in these predictions.

The systematic uncertainty in the data reduction was determined by applying the selection criteria to a sample of 1.2×10^6 μ-e decay events. The fraction of remaining μ-e decay events, as a function of energy, was compared to the fraction of MC simulated events that remained after the cuts were applied. The difference was about 3% at all energies; this value was taken as the systematic error inherent in the reduction.

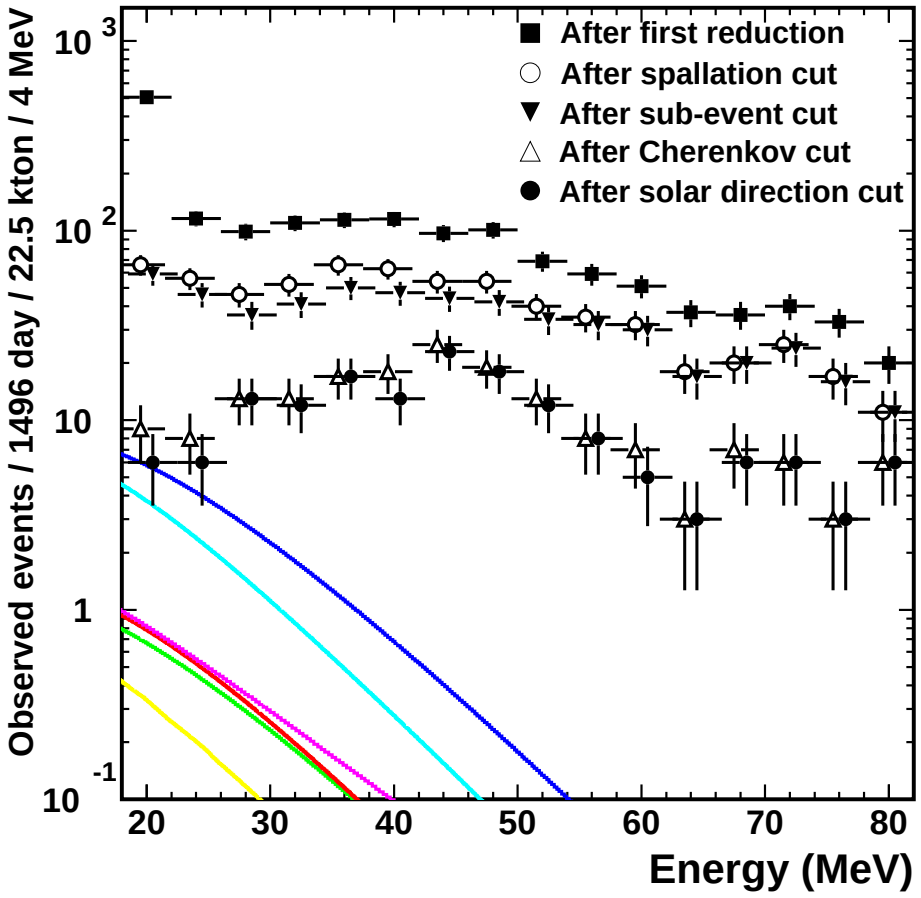

Figure 5.24: The energy spectrum is shown at each stage of the data reduction. In the final data set, the spallation cut and the solar direction cut will only be applied to the first four bins. The solid lines represent various theoretical predictions for the SRN, with detection efficiencies considered.

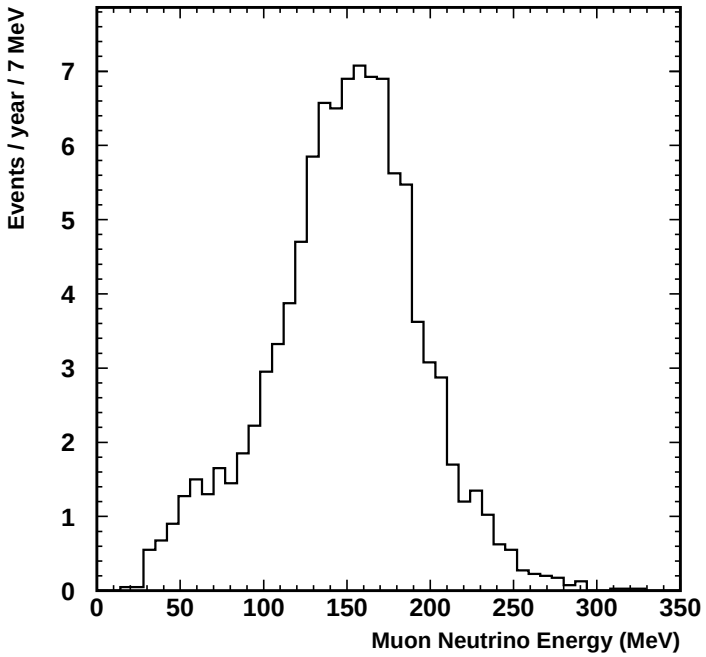

Figure 5.25: The energy spectrum of atmospheric ν_μ that produce muons with $p_\mu < 120$ MeV/c. Such muons are below the threshold for emitting Cherenkov light; thus, they are said to be invisible.

5.6 Remaining Backgrounds

After the full reduction has been applied, two known sources of background remain in the data. Both of these sources orginate from atmospheric neutrino interactions.

When ultra-low energy atmospheric ν_μ undergo charged current quasi-elastic scattering, they produce muons that have $p_\mu < 120$ MeV/c. Figure 5.25 shows the energy spectrum of the atmospheric ν_μ that can create a muon in this momentum range. As mentioned in Section 5.4.1, these muons are invisible; they do not emit Cherenkov photons. Thus, when an invisible muon decays there is no way to tag the resulting electron (or positron) as a μ-e decay event. Decay electrons from invisible muons are one of the two irreducible backgrounds to the SRN search.

The other irreducible background comes from low energy atmospheric ν_e and $\bar{\nu}_e$ with $E_\nu < 200$ MeV. Although these neutrinos originate from cosmic

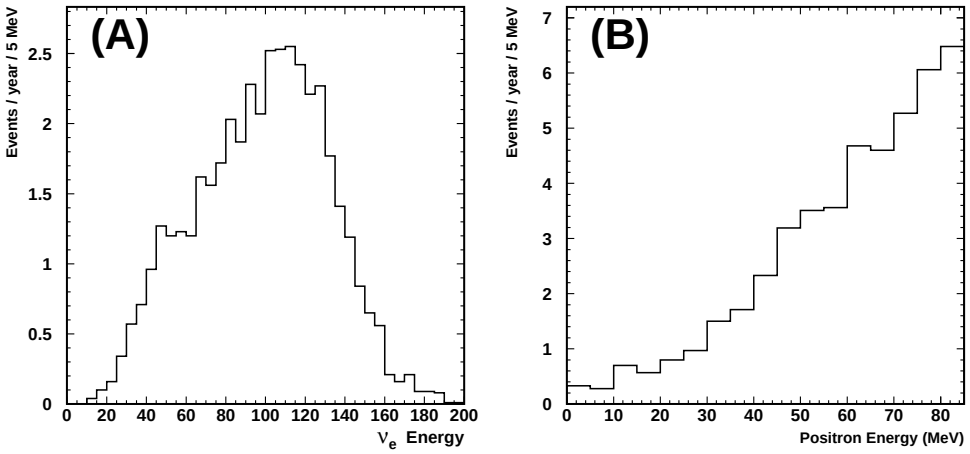

Figure 5.26: The energy spectrum of atmospheric $\bar{\nu}_e$ (and ν_e) that produce positrons (and electrons) with $E_e < 82$ MeV is shown in (A). The spectrum of the positrons is shown in (B).

ray interactions in the Earth's atmosphere, the events that they produce in SK are identical to those produced by the SRN. For most of the energy range relevant to the SRN search, the dominant atmospheric neutrino interaction is $\bar{\nu}_e$ undergoing inverse β decay. At higher energies, $E_\nu \approx 90$ MeV, the ν_e interactions must also be considered. The ν_e primarily react with the neutrons in ^{16}O via:

$$\nu_e + n \rightarrow e^- + p$$

Events created by these interactions are produced isotropically and are not correlated with other events. Therefore, individual atmospheric ν_e and $\bar{\nu}_e$ events cannot be tagged and removed from the data. Figure 5.26 shows the energy spectrum of the parent $\bar{\nu}_e$ (and ν_e) distribution (A), and the spectrum of the positrons (and electrons) that they produce (B).

Simulation of the irreducible backgrounds is discussed in Section 6.1. The procedure for extracting an SRN signal from these remaining backgrounds is explained in Section 7.1.

Chapter 6

Event Simulation

Simulated Super-Kamiokande data are used to evaluate the efficiency of the reduction processes, and to understand the energy spectrum of SRN events that are expected in SK. To simulate SRN events, the predicted spectra are obtained from various theoretical models and combined with the cross section for the inverse β decay reaction. The simulated positrons that are created from this interaction are processed by the SK detector simulation software. This software produces a set of simulated data, which is subjected to the same reconstruction and reduction algorithms as the actual data. The effects of the analysis programs on the simulated data are studied to understand the efficiency and systematic uncertainty inherent in these tools. Additionally, the fully reduced SRN simulations provide an expectation for the spectrum of SRN events that should be searched for in the data.

As mentioned in Section 5.6, two irreducible backgrounds remain in the data after all of the reduction cuts have been applied. In addition to simulating the expected signal from the SRN, each of these backgrounds is also simulated and subjected to the full reduction. A thorough understanding of the expected backgrounds, especially their spectrum shapes, is necessary for the attempt to extract an SRN signal.

6.1 Neutrino Interaction Simulation

Neutrino interactions are modeled for the SRN and for the irreducible background sources. The theoretical flux and spectra for the signal and for the backgrounds are considered, as are the cross sections for the interactions being simulated. The output of the neutrino interaction simulation is then processed by the detector simulator described in Section 6.2.

6.1.1 Supernova Relic Neutrinos

The precise flux and spectral shape of the SRN are still unknown. This analysis considers predictions from six theoretical models of the SRN [19, 20, 21, 22, 23, 24]. There is a strong model dependence in the flux predictions; the most divergent models differ from each other by about an order of magnitude. Table 1.1 lists the total flux predicted by each model. The spectral shape of the SRN has a weaker model dependence that mainly derives from uncertainties about the supernova rate in the early universe. Figure 1.5 shows the energy spectra of the SRN predicted by the different models.

Neutrino interaction is mediated by the weak force; thus, the cross sections for these interactions are typically quite small. The supernova relic neutrinos searched for in Super-Kamiokande are $\bar{\nu}_e$ that have undergone the inverse β reaction:

$$\bar{\nu}_e \; + \; p \; \rightarrow \; e^+ \; + \; n$$

The cross section $\sigma(E_\nu)$ for quasi-elastic anti-neutrino/proton scattering has been precisely calculated in reference [58]. In general, however, theoretical predictions for the number of SRN events expected in a water Cherenkov detector have used the following approximation for the cross section:

$$\sigma(E_\nu) \; = \; 9.52 \times 10^{-44} \; E_e \; p_e \tag{6.1}$$

where:

$$E_e \; = \; E_\nu \; - 1.3 \text{ MeV} \tag{6.2}$$

This approximation has been used to obtain results in previous SRN searches [36, 37]. The SRN analysis presented here also adopts this form for the cross section.

For a given theoretical model, the energy spectrum of SRN events expected within a water Cherenkov detector can be obtained by the following calculation:

$$\frac{dN_{SRN}}{dE_e} = (N_p \times \tau) \; F(E_\nu) \; \sigma(E_\nu) \; dE_\nu \tag{6.3}$$

where N_{SRN} is the number of SRN-induced events, N_p is the number of free protons available as targets for the SRN, τ is the detector livetime, and $F(E_\nu)$ is the SRN flux for the model being considered.

The quantity $(N_p \times \tau)$ is known as the "exposure." One kton of water contains 6.7×10^{31} free protons, so the exposure can be expressed in terms of kton years. In Figure 6.1, the flux of the population synthesis model [20] is compared to the energy spectrum of events expected for an exposure of 1 kton year.

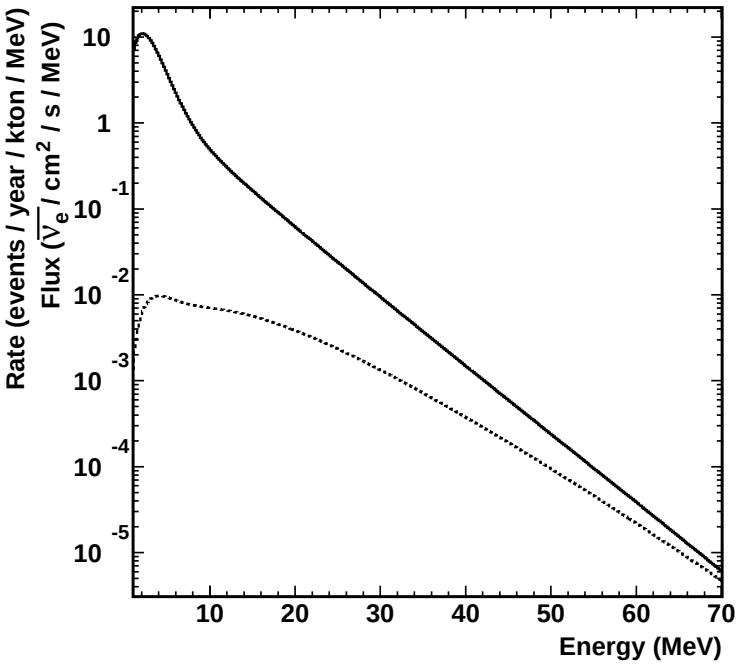

Figure 6.1: The solid line represents the SRN flux predicted for the population synthesis model. The dotted line shows the expected energy spectrum of SRN events for a 1 kton year exposure that would be induced by this flux. Note that the flux and the rate are expressed in different units.

Figure 6.2 shows the spectra of SRN events expected annually at SK for each of the theoretical models being considered. The normalized shape of each spectrum in Figure 6.2 was used to generate simulated SRN events. For each of the models, twenty thousand SRN-induced positron events were generated. All of the simulated positrons were produced with at least 10 MeV of total energy. Although the SRN analysis threshold is 18 MeV, the energy resolution of the detector could cause some SRN events with less energy to reconstruct above this threshold. Events with energies less than 10 MeV were not simulated because the possibility of those events being reconstructed with energy above 18 MeV was considered to be negligible.

6.1.2 Atmospheric ν_e and $\bar{\nu}_e$

There have been several detailed calculations of the atmospheric neutrino flux. This analysis uses the results of the Honda group [59]. Figure 6.3 shows the flux and spectrum of atmospheric neutrinos. The Honda fluxes are indicated by the solid line. The results of another calculation, by the Bartol group [60], are indicated by the dotted line.

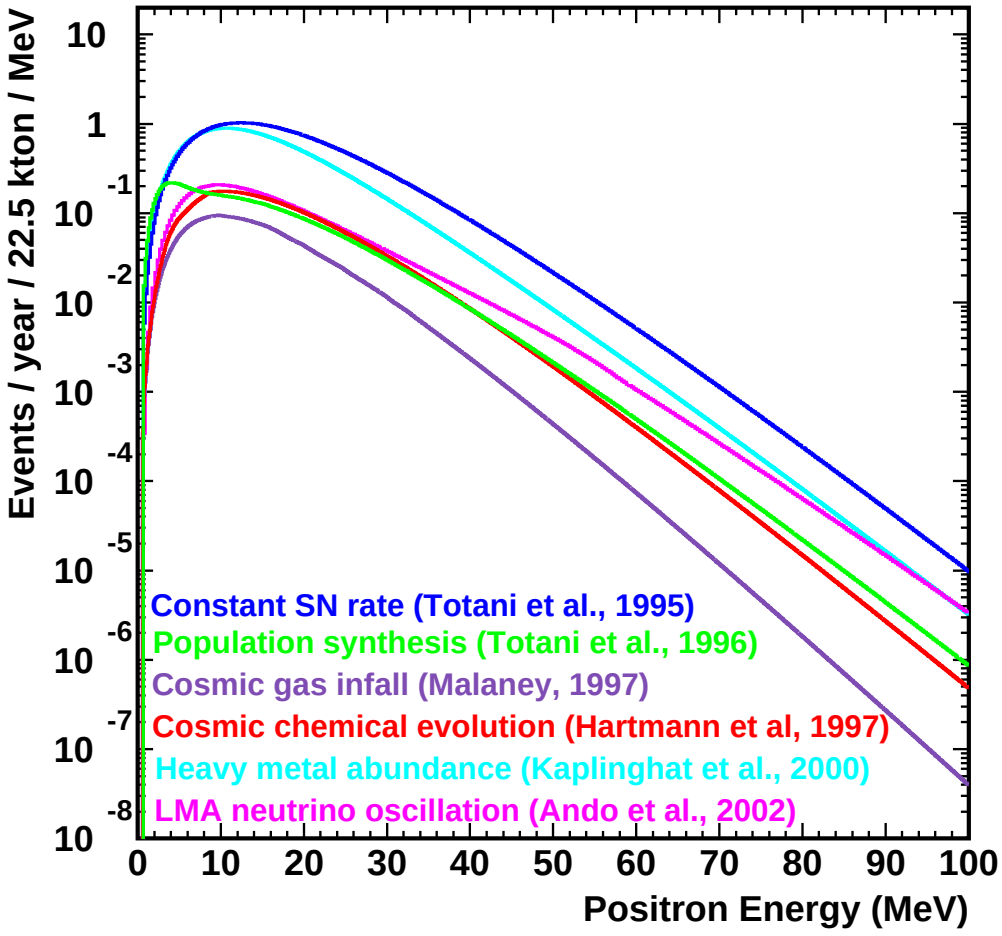

Figure 6.2: The energy spectra of SRN events are presented for six theoretical models. Note that the ordinate is expressed in terms of the annual event rate expected at Super-Kamiokande.

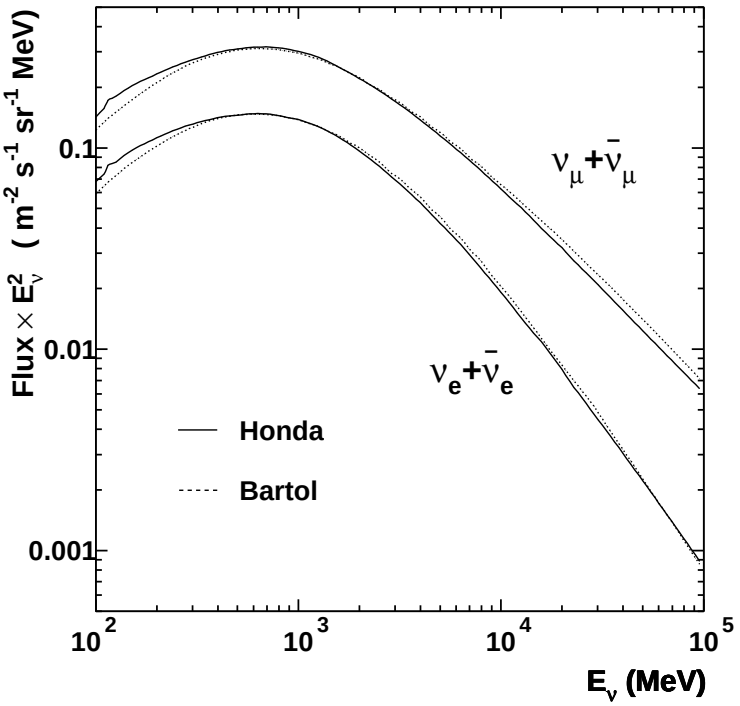

Figure 6.3: The calculated fluxes and spectra of atmospheric neutrinos expected at Kamioka is shown. The solid line denotes the results of the Honda group, and the dotted line represents the results of the Bartol group.

There is a large systematic error associated with the atmospheric neutrino flux. The two dominant contributions to this error are: uncertainty in the absolute flux of the primary cosmic rays that create atmospheric neutrinos, and uncertainty in the cross section for the hadronic interactions that produce atmospheric neutrinos. The error in the atmospheric neutrino flux is estimated to be about 20% over most of the spectrum. From Figure 6.3, it can be seen that the different flux calculations deviate most at low energies. This is significant for the SRN search, as the lowest energy atmospheric neutrinos are the ones that create an irreducible background in the relevant energy window. Below 100 MeV, the systematic error in the atmospheric neutrino flux is estimated to be about 30%.

The cross sections used in the simulation of atmospheric neutrino events are described in detail in reference [54]. Using the flux results from the Honda group, the number of events induced by atmospheric $\bar{\nu}_e$ and ν_e over a two hundred year period was simulated. No lower bound was placed on the energy of the simulated events. An artifical upper limit was set at 100 MeV, as it is unlikely that events with greater energy would reconstruct below the 82 MeV

upper threshold of the SRN search. With this restriction on the energy, 7334 atmospheric $\bar{\nu}_e$ (and ν_e) events were generated. Figure 5.26 shows the spectra of these simulated neutrinos (A) and of the positrons (and electrons) that they produce (B).

6.1.3 Decay Electrons from Invisible Muons

Ultra-low energy atmospheric ν_μ (and $\bar{\nu}_\mu$) can undergo quasi-elastic charged current interactions and form invisible muons. The μ-e decay events created by invisble muons are an irreducible background to the SRN search and must be simulated.

Figure 5.25 shows the spectrum of atmospheric ν_μ that produce invisible muons. Since the muons are never seen, precise spectral information about the atmospheric ν_μ is not required to simulate this background. Instead, these μ-e decay events are modeled by the Michel spectrum, which is described by equation (3.7). The effects of μ^- capture, shown in Figure 3.18, must also be considered. Each day, several hundred cosmic ray muons penetrate SK, then stop and decay in the detector. During SK-I, a large number ($\sim 10^6$) of μ-e decay events were accumulated into a very pure sample by using the selection criteria outlined in Section 3.2.2. Figure 3.19 shows the measured shape of the μ-e decay spectrum; this modified Michel spectrum shape was used to simulate the μ-e decay background.

The uncertainty in the modified Michel spectrum is quite low as a result of the high statistics event sample used to measure the spectral shape. Some systematic uncertainty arises from the ratio of μ^+ to μ^- events. Cosmic ray muons have a different μ^+/μ^- ratio than the muons produced by atmospheric neutrino interactions. To evaluate the magnitude of this uncertainty, pure samples of μ^+ and μ^- were simulated. The difference in the μ^+/μ^- ratio for CRMs and atmospheric neutrinos is $\sim$10%. Once simulated, the pure muon samples were mixed with different μ^+/μ^- ratios ranging from 0.75 to 1.25. The resulting spectral shapes were considered, and it was determined that the systematic uncertainty in the modified Michel spectrum was about 2%

The rate of μ-e decay events induced by invisible muons was obtained from the calculations of the Honda group [59]. A sample of 20,666 such events was generated, which corresponds to the number expected in SK during a two hundred year period.

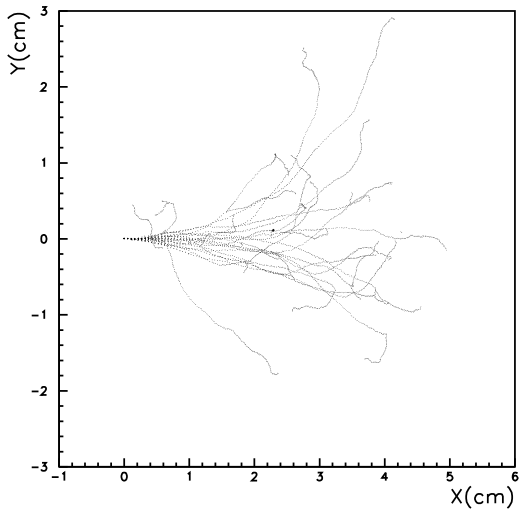

Figure 6.4: The path through water is shown for twenty simulated electrons that were generated at the origin and initially travelling in the +X direction. The initial electron momentum is 10 MeV/c.

6.2 Detector Simulation

The detector simulation software is executed in three stages. The first stage models the path of a particle through the SK water, including secondary interactions that the particle may experience, and the emission of Cherenkov light. The second stage models the transmission of Cherenkov photons through water. The final stage models the detection of these photons by the PMTs, and includes the effects of the SK electronics.

6.2.1 Simulation Software

The programs that simulate the SK detector are based on GEANT 3.21, a particle interaction software package produced by particle physicists working at CERN [61]. GEANT is capable of simulating electromagnetic interactions that occur at energies between 10 keV and 10 TeV. For electrons and positrons, the simulation software models many processes, including multiple Coulomb scattering, energy loss due to ionization, Cherenkov light emission, particle annihilation, and Bremsstrahlung radiation. For photons, Rayleigh scattering and absorption are modeled, as well as Compton scattering and pair production effects. Figure 6.4 shows the tracks of twenty simulated electrons moving through water. All twenty electrons were generated with the same position,

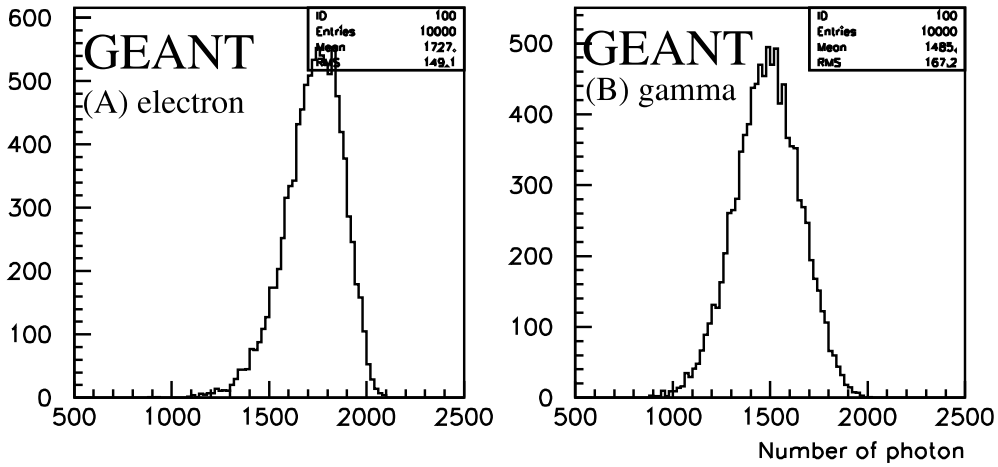

Figure 6.5: The distribution of the total number of Cherenkov photons emitted by a 9 MeV electron (A) and a 9 MeV γ-ray (B). The number of photons generated has an approximately linear correlation with the energy of the particle.

momentum, and direction; divergences in the tracks arose as a result of the effects mentioned above.

Figure 6.5 shows distributions for the total number of Cherenkov photons produced by 9 MeV electron events (A), and 9 MeV γ-rays (B). The total number of Cherenkov photons produced by an electron is approximately proportional to the energy of the electron; this explains the nearly linear correlation between N_{eff} and energy shown in Figure 3.15. The number of Cherenkov photons emitted at each wavelength is determined by using equation (2.2). Simulated Cherenkov photons are generated with wavelengths in the range of 300 nm to 700 nm; beyond this range, the quantum efficiency of the PMTs is negligible, as shown in Figure 2.7.

The speed of light in water is dependent on the wavelength of the propagating photon. A photon of wavelength λ will travel with a group velocity v_g, which is defined by:

$$v_g = \frac{c}{n(\lambda) - \lambda \frac{dn(\lambda)}{d\lambda}} \tag{6.4}$$

In this equation, $n(\lambda)$ is the index of refraction as a function of wavelength,

parameter	value
λ_a^2	0.018085
a_1	5.743534×10^{-3}
a_2	1.769238
a_3	-2.797222×10^{-2}
a_4	8.715348×10^{-3}
a_5	-1.413942×10^{-3}

Table 6.1: The values of the parameters used in equation (6.5). These values assume that the wavelength, λ, is given in units of μm.

and it has the following functional form:

$$n(\lambda) = \sqrt{\frac{a_1}{\lambda^2 - \lambda_a^2} + a_2 + a_3\lambda^2 + a_4\lambda^4 + a_5\lambda^6} \tag{6.5}$$

Table 6.1 shows the values of λ_a^2 and a_x that were used in equation (6.5); these values are the result of a fit to a set of measurements. The denominator of equation (6.4) is termed the "effective index of refraction" and it is compared with the actual refractive index in Figure 6.6.

While travelling in water, Cherenkov photons can be scattered or absorbed. The attenuation factor caused by Rayleigh scattering is proportional to λ^{-4}, which makes it the dominant effect for photons with short wavelengths. For photons with wavelengths longer than about 400 nm, the attenuation is dominated by absorption, which is modeled using the data provided by reference [62]. The ratio of scattering to absorption was left as a tunable parameter, and is discussed further in Section 6.2.2.

When a Cherenkov photon reaches the wall of the ID, it can be reflected by the surface of a PMT or by the black sheet. The probability that a given photon will be reflected depends upon the incident angle of that photon. The reflectivity of both types of surfaces was calculated; the result is shown in Figure 6.7 for the black sheet (A) and for the PMTs (B). Polarization effects are considered in this calculation; the average of the p-wave and s-wave polarization curves is used in the detector simulator. These curves agree well with reflectivity values obtained by direct measurement [63].

Once a Cherenkov photon has reached a PMT and avoided reflection, the detector response is simulated. The quantum efficiency of the PMTs is considered by the simulation software when determining whether a given photon registers as a hit. The SK electronics are also simulated by considering the

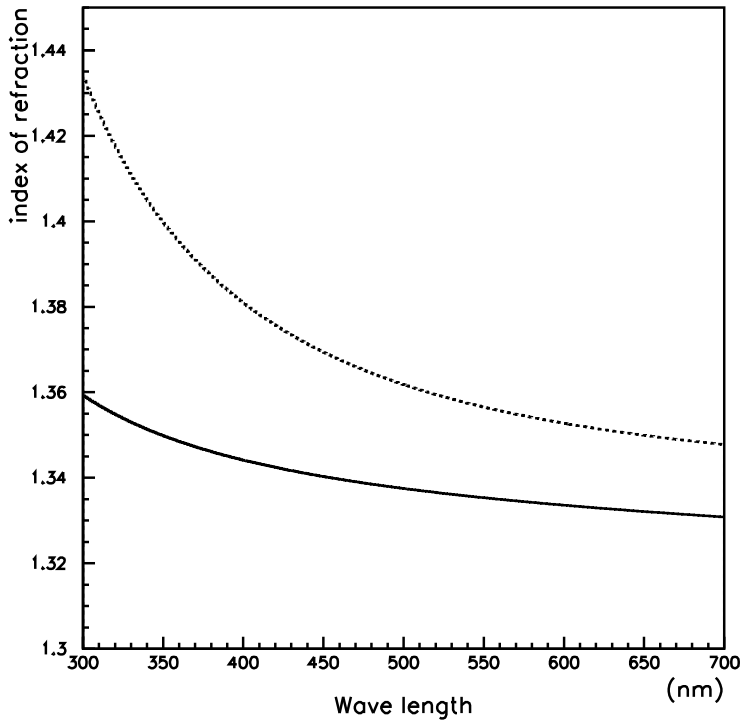

Figure 6.6: The solid line represents the refractive index of water, as a function of wavelength. The dotted line is the effective index obtained from the denominator of equation (6.4).

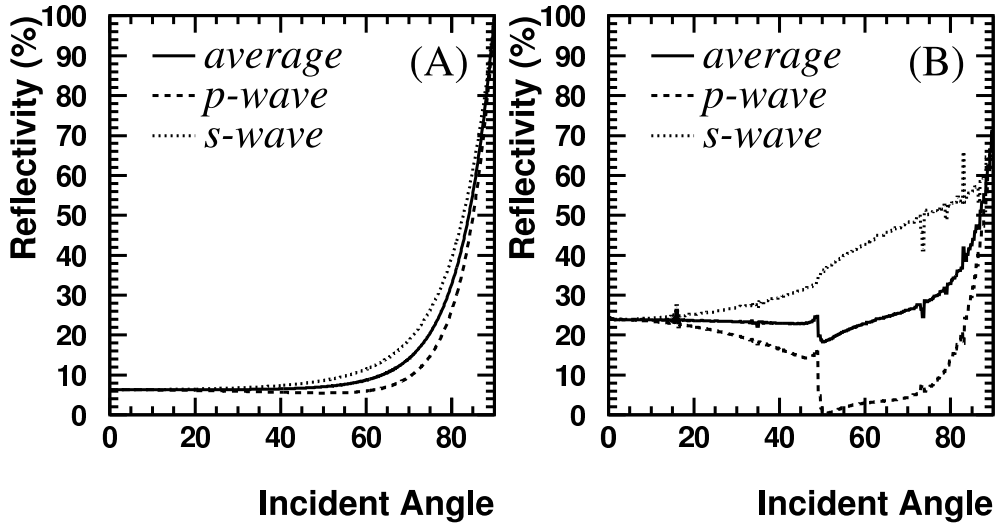

Figure 6.7: The surface reflectivity for the black sheet (A) and the PMTs (B) is shown as a function of the photon incident angle.

resolution of the ADCs and the TDCs. The charge distribution from a single photo-electron is shown in Figure 3.4; when a simulated Cherenkov photon hits a PMT, the charge output for that PMT is determined according to this distribution, by use of a random number generator. The TDCs experience a slewing effect, described in Section 3.1.3. To simulate slewing, the time of the PMT hit is offset by a Gaussian-distributed random variable with a 1σ width as shown in Figure 3.6.

After the time and charge information has been gathered for all PMTs that were hit by simulated Cherenkov photons, PMT dark noise effects must be added. The dark noise simulation is implemented by distributing random hits throughout the detector, according to the measured dark noise rate of the ID PMTs. A PMT that is simulating dark noise is recorded as if it were a single photo-electron hit.

For each simulated event, the trigger simulator is used to determine whether the global trigger is issued. The procedure by which the trigger simulator was tuned is described in Section 3.8.

Simulated events are generated to match the livetime distribution of the detector. In order to generate simulated data that closely matches the actual data, the number of dead PMTs and the relative water transparency are used by the detector simulation.

6.2.2 Monte Carlo Tuning

Most of the parameters in the detector simulation are determined independently by direct measurement or by theoretical expectation. However, some parameters remain that need to be tuned with the SK calibration data. The ratio of scattering to absorption in water, the PMT timing resolution, and the PMT collection efficiency are all adjusted to make the simulated calibration data replicate the actual data.

The ratio of scattering to absorption for Cherenkov photons was tuned by using data from the LINAC and from the Ni-Cf calibration system. The pattern of the hit PMTs was studied and the ratio was adjusted until the simulated events matched the real data. Once this ratio was fixed, the light attenuation used in the detector simulator was compared to the direct measurements made with the laser and CCD camera (see Section 3.2.1); the light attenuation values obtained by these two methods were found to be consistent. Figure 3.9 shows the attenuation coefficient, as a function of wavelength, that was used for the detector simulator.

The PMT timing resolution for single photo-electron hits is tuned by studying the vertex resolution of LINAC calibration events. The timing resolution

of the simulated PMTs is adjusted so that the vertex resolution of the simulated data matches that of the LINAC data (see Section 3.6.3). Although the PMT timing resolution is manually set in this manner, the resulting values used in the detector simulator are in agreement with the directly measured values [50].

The PMT collection efficiency is the final parameter to be adjusted. This parameter is used to fix the energy scale of the Monte Carlo. The collection efficiency is set to the value that causes the reconstructed energy of the simulated LINAC events to match that of the actual LINAC data. The value selected for this parameter is 78%, which is in rough agreement with the mean collection efficiency of 70% that was directly measured by Hamamatsu Photonics [50].

6.3 Reconstruction and Reduction

The SK detector simulator outputs data in the same ZBS format that is used for storing the actual data. Thus, the reconstruction software (see Chapter 4) and reduction algorithms (see Chapter 5) can be applied directly to the simulated data sets.

Figure 6.8 shows a spectrum of simulated SRN events; this spectrum was obtained by using the population synthesis model. The solid histogram represents the generated event spectrum; the points show the spectrum of events after the detector simulation, reconstruction and reduction have all been applied. The same information is presented on both a linear and a logarithmic scale so that the points at higher energies are visible. Although 20,000 SRN events were generated with energies above 10 MeV, only 9391 events reconstruct with energies above the 18 MeV analysis threshold. The processed data shows a discontinuity at 34 MeV that is caused by applying the selection criteria in an energy-dependent manner; above 34 MeV, the spallation cut and the solar direction cut are not implemented. The effects of the energy resolution can be clearly seen: Although no SRN events were generated with energy greater than 62 MeV, a few events were reconstructed with higher energy. By applying the reduction tools to the simulated SRN data, the efficiency of these tools for retaining signal can be evaluated; the values in Table 5.2 were obtained in this manner. The SK event displays and TOF-subtracted timing distributions are shown for some typical simulated SRN events in Section B.1.

The energy spectrum of the simulated atmospheric $\bar{\nu}_e$ (and ν_e) events is shown in Figure 6.9(A), and the simulated spectrum of μ-e decay events is shown in Figure 6.9(B). The spectral shapes of the reduced background simulations will be used in the attempt to extract an SRN signal (see Chapter 7).

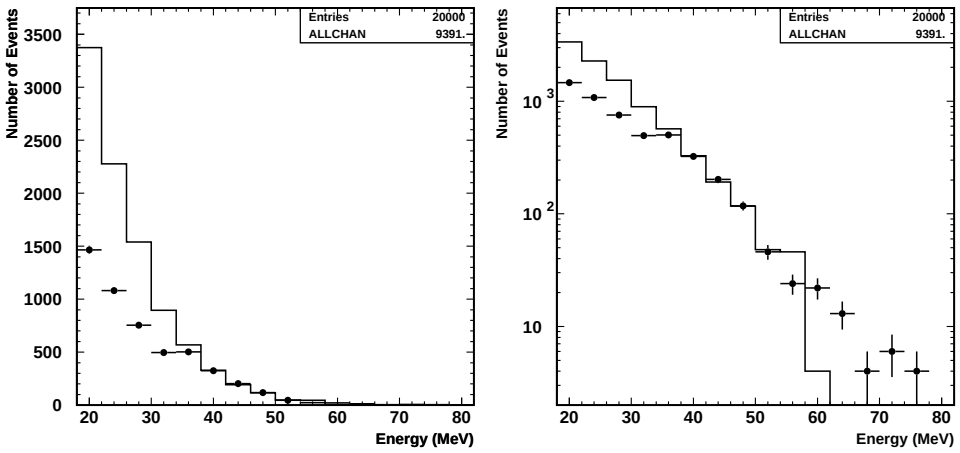

Figure 6.8: The energy spectrum is shown for a sample of simulated SRN events based on the population synthesis model. The solid histogram represents the generated event spectrum; the points indicate the spectrum of events after the detector simulation and analysis tools have been applied. The same information is presented on a linear and a logarithmic scale.

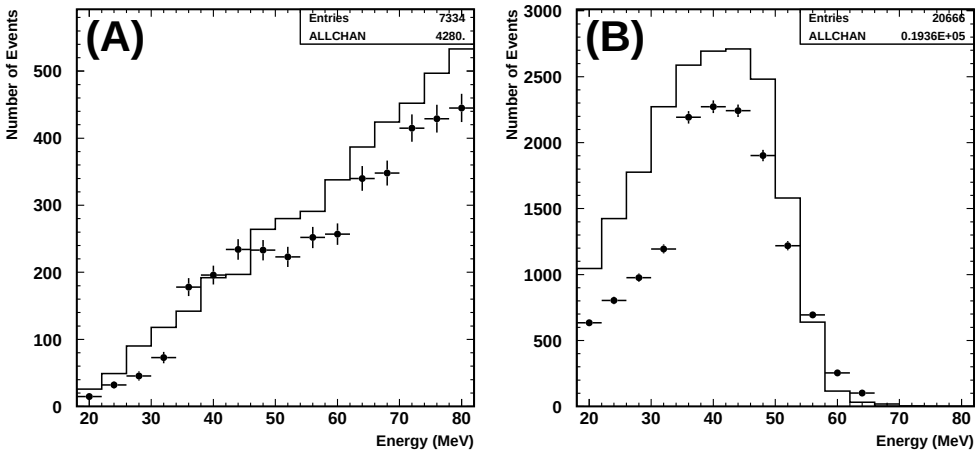

Figure 6.9: The energy spectrum of simulated atmospheric ν_e events is shown in (A). The spectrum of simulated μ-e decay events is shown in (B). In both cases, the solid histogram denotes the generated event spectrum and the points represent the spectrum after the detector simulation, event reconstruction, and data reduction have all been applied.

Chapter 7

Analysis, Results, and Discussion

After applying all of the selection criteria to the Super-Kamiokande-I data (see Chapter 5), a final sample of SRN candidate events is produced. Ideally, this sample would only contain events produced by supernova relic neutrino interactions. In practice, however, two sources of background events are known to be present (see Section 5.6). Although individual SRN events cannot be identified, statistical methods can be used to extract a potential SRN signal from these backgrounds.

Two outcomes are possible for the SRN search. Evidence for the SRN can be concluded if there is a statistically significant excess of events beyond the expected backgrounds. If no such excess is discovered, then an upper limit on the number of SRN events in the SK-I data can be derived.

Using the SRN spectra predicted by the various theoretical models, the number of SRN-induced events that are detected (or the limit on that number) can determine the total SRN flux (or place an upper bound on that flux) for each model. Additionally, the flux above the energy threshold of this analysis can be measured (or bounded) in a manner that is insensitive to the choice of theoretical model.

7.1 Analysis Method

The expected energy distribution of events produced from SRN interactions, calculated for six theoretical models, was shown in Figure 6.2. Although each model predicts a slightly different spectral shape, all models predict that above the analysis threshold of $E_e = 18$ MeV, the number of SRN events should decrease exponentially with increasing energy. In contrast, the event rate from each of the two remaining backgrounds, shown in Figure 6.9, is expected to rise with increasing energy. Since the spectral shape of the backgrounds is

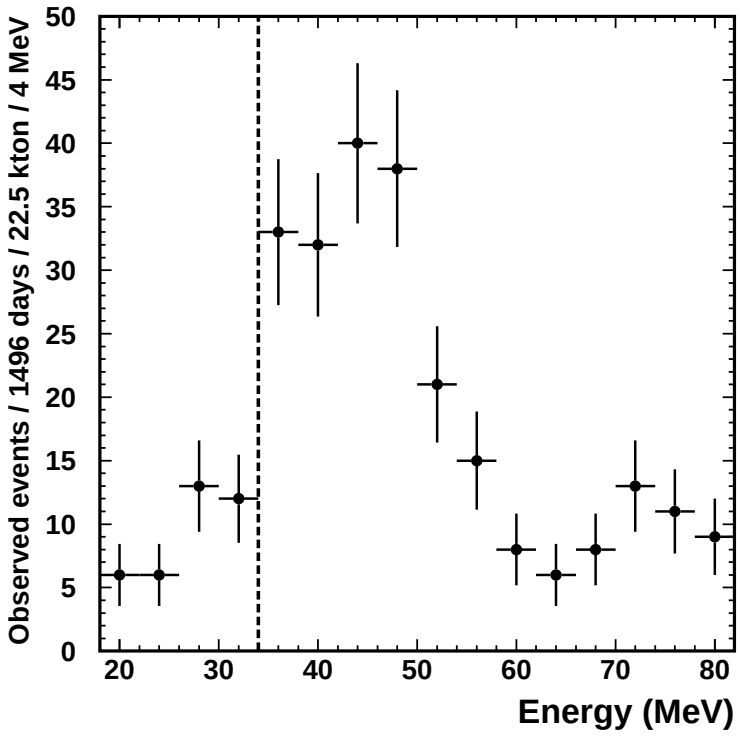

Figure 7.1: The energy distribution is shown for the final sample of SRN candidate events. The vertical line at 34 MeV marks the change in the data reduction process.

quite different from that of the expected SRN signal, a shape fit can be used to statistically extract the signal from the data.

The solid histogram in Figure 6.8 shows the spectrum of SRN-induced events expected for the population synthesis model [20]; the points in this figure represent the distribution after the data reduction has been applied. Similarly, the points in Figure 6.9 represent the reduced spectra that are expected from atmospheric $\bar{\nu}_e$ (and ν_e) events (A) and from μ-e decay events (B). These reduced spectra were normalized by the number of events in each Monte Carlo sample, and the three spectral shapes were used to fit the final data set. The fitting procedure was then repeated for each of the other SRN models being tested.

Figure 7.1 shows the energy distribution of the events in the final SRN candidate sample. The points in this figure correspond to the bottom set of points in Figure 5.24, except that the spallation cut and the solar direction cut were not applied to events with reconstructed energy greater than 34 MeV.

The dashed vertical line in Figure 7.1 separates the regions with different selection criteria. To extract SRN-induced events from the data, the energy distribution in this figure is fit with the spectral shapes defined by the points in Figure 6.8 and Figure 6.9.

From Figure 6.8, it is clear that a negligible fraction of SRN events are expected to be reconstructed with energies above 50 MeV. Therefore, the choice of 82 MeV as the upper threshold for this analysis must be explained. Furthermore, most of the SRN signal should reconstruct with energies less than 34 MeV; from Figure 6.9, it is evident that the irreducible background in this energy range is dominated by μ-e decay events. Thus, the decision to analyze the data with a three-parameter fit must also be justified. Although μ-e decay events form the dominant background in the energy region where the SRN are most likely to be detected, atmospheric $\bar{\nu}_e$ (and ν_e) events distort the Michel spectrum at higher energies; understanding this distortion is essential for properly fitting the data with a reduced Michel distribution. To evaluate the contribution of the atmospheric $\bar{\nu}_e$ events, the upper analysis threshold must be extended to energies where only the atmospheric neutrino background is present. From kinematic considerations, decay positrons have a maximum energy of 53 MeV. Decay electrons can have slightly higher energies due to the Doppler shift produced by the orbital motion of the parent μ^- when it is captured by an oxygen nucleus (see Section 3.3.2). The energy resolution of SK makes it possible to reconstruct μ-e decay events with energies as high as $\sim$65 MeV, as shown in Figure 6.9(B). At energies greater than 65 MeV, only atmospheric $\bar{\nu}_e$ and ν_e events occur; data in this energy region are used to characterize the amount of distortion expected from these events. Thus, the upper analysis threshold was set to 82 MeV, and the data were analyzed with a three-parameter fit.

For the fitting, the data were divided into sixteen energy bins, each 4 MeV wide (see Figure 7.1), and the following χ^2 function was minimized with respect to α, β, and γ:

$$\chi^2 = \sum_{l=1}^{16} \frac{[(\alpha \cdot A_l) + (\beta \cdot B_l) + (\gamma \cdot C_l) - N_l]^2}{\sigma_{data}^2 + \sigma_{MC}^2 + \sigma_{sys}^2} \tag{7.1}$$

In this equation, the sum l is taken over all energy bins, and N_l is the number of events in the l-th bin. A_l is the fraction of the SRN event spectrum expected in the l-th bin. Similarly, B_l and C_l represent, respectively, the fractions of the modified Michel spectrum and the atmospheric ν_e event spectrum that are in the l-th energy bin. The free parameters α, β, and γ represent the total number of SRN events, decay electrons, and atmospheric ν_e events in the

final data sample. These parameters are constrained to the physical region by requiring that they be non-negative.

The total number of events in the data sample is small, so the statistical error of the data, σ_{data}, is the dominant term in the denominator. The statistical uncertainty in the spectral shapes of the simulated signal and background is given by:

$$\sigma_{MC}^2 \;=\; (\alpha \cdot \sigma_{SRN})^2 \;+\; (\beta \cdot \sigma_{\mu-e})^2 \;+\; (\gamma \cdot \sigma_{atm})^2 \tag{7.2}$$

Due to the large number of MC-generated events, σ_{MC} is negligibly small. The systematic error term, σ_{sys}, considers the effects that uncertainties in the spectral shapes have on the SRN search result. This term contains the 3% uncertainty in the data reduction that was discussed in Section 5.5. Other sources of systematic error included in this term are uncertainties in the SK energy resolution and the error in the theoretical shape of the atmospheric $\bar{\nu}_e$ (and ν_e) spectrum. For all of the energy bins, the systematic error is approximately 6%, which is always much smaller than the statistical uncertainty of the data.

7.2 Results

Minimizing the χ^2 function (equation 7.1) with respect to the three free parameters yields best-fit values for the number of SRN events and background events in the SK-I data set. If there is no SRN signal (i.e. $\alpha = 0$), then an upper limit can be set for the number of SRN events that could be present in the data. This limit is determined by examining the behavior of the χ^2 function for deviations from the best-fit parameter values.

Once the number of SRN events has been determined for a particular theoretical model, the spectral shape of that model can be used to calculate the total SRN flux. If no SRN events are detected, then the limit on the number of signal events can be used to place a model-dependent upper bound on the SRN flux.

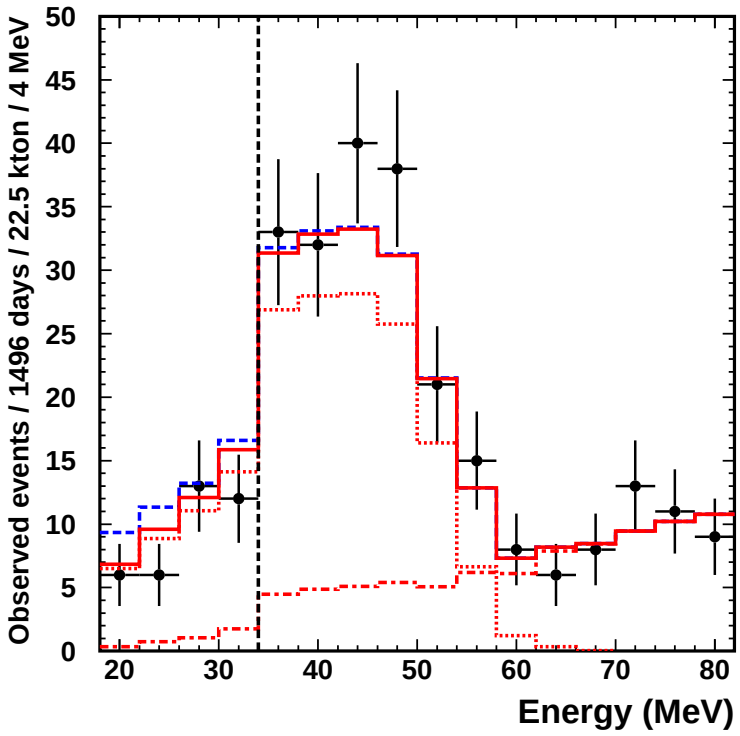

Figure 7.2: The results from the χ^2 fit to the distribution of SRN candidate events are shown. The data points are the same as those in the previous figure. The dotted and dot-dashed lines are the fitted backgrounds from invisible muons and atmospheric ν_e, respectively. The solid histogram is the sum of these two backgrounds and the best fit to the data. The dashed line shows the sum of the total background and the 90% C.L. upper limit on the SRN signal.

7.2.1 Fitting Results

Figure 7.2 shows the energy distribution of the final SRN data sample. Overlaid on the data points, which are the same as those shown in Figure 7.1, are lines indicating the results of the χ^2 fit. The best fits to β and γ are marked, respectively, by the dotted and dot-dashed lines. These lines represent the number of μ-e decay events and atmospheric $\bar{\nu}_e + \nu_e$ events in the data. The solid histogram shows the sum of these two lines, and represents the best fit to the total background. For all six theoretical models, the best fit to α was zero; no SRN events were detected in the SK-I data. Therefore, the solid line also represents the best fit to the entire data sample. The minimum χ^2 value was 8.1 with 13 degrees of freedom for all of the models that were considered.

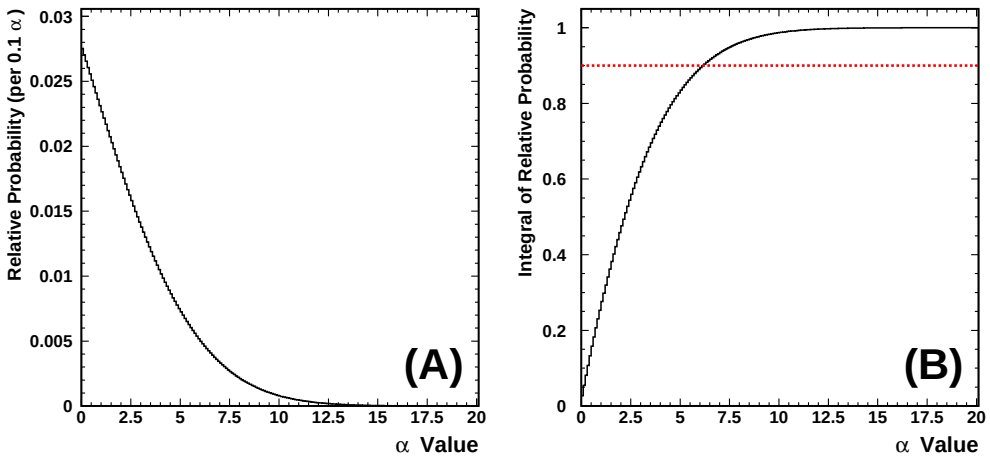

Figure 7.3: The relative probability that a given number of SRN-induced events are present in the SK-I data is shown in (A). The integral of the relative probability is shown in (B); the dotted line indicates the 90% C.L.

7.2.2 SRN Event Limits

In the absence of an SRN signal, a 90% confidence level limit was set on α for each theoretical model. This limit was determined by artificially increasing the value of α in increments of 0.1 events and re-evaluating the χ^2 function using only β and γ as free parameters. The minimum χ^2 value obtained for each value of α corresponds to a relative probability via the following relation:

$$Probability \;=\; K \cdot \exp(-\chi^2_\alpha) \tag{7.3}$$

where χ^2_α is the minimum χ^2 value for a particular fixed value of α, and K is a normalizing constant defined by:

$$\sum_{\alpha=0}^{\infty} K \cdot \exp(-\chi^2_\alpha) \;=\; 1 \tag{7.4}$$

Figure 7.3(A) shows the relative probability for each value of α as calculated by equation (7.3). Figure 7.3(B) displays the relative probability integrated from $\alpha = 0$ to 20. For any particular value of α, the function in this figure gives the probability that the number of SRN-induced events in the SK-I data is less than that value. The dotted line in Figure 7.3(B) corresponds to the 90% confidence level. The 90% C.L. upper limit on the number of SRN events

Theoretical Model	α limit (90% C.L.)
Constant supernova rate [19]	< 7.0 events
Population synthesis [20]	< 6.5 events
Cosmic gas infall [21]	< 5.7 events
Cosmic chemical evolution [22]	< 6.7 events
Heavy metal abundance [23]	< 6.1 events
Large mixing angle oscillation [24]	< 7.1 events

Table 7.1: The 90% C.L. limits on α, the number of SRN events in the SK-I data sample, are summarized for six theoretical models.

in the SK-I data, called α_{90}, is indicated by the value of α for which the integrated probability crosses this line. The functions in Figure 7.3 are the results of a fit to the heavy metal abundance prediction [23]; for this model, the α_{90} value is 6.1 events. Similar figures were made for each of the other SRN predictions; the model-dependent α_{90} values are listed in Table 7.1.

The dashed line in Figure 7.2 represents the sum of the background and the 90% C.L. upper bound on α for the population synthesis model [20]. This line shows the distortion in the Michel spectrum that would indicate an SRN signal in Super-Kamiokande.

The first two data points in Figure 7.2 are lower than the best fit to the background. Since these two bins are most sensitive to the SRN, it appears as if the best fit to α should be slightly negative. Such an unphysical result is prevented by requiring the fitting parameters to be non-negative. A negative best-fit value of α would shift the relative probability function, and decrease the upper bound on the number of SRN events. Therefore, the constraint on α was implemented in order to avoid the circumstance where a downward statistical fluctuation in the data led to a result that would overstate the power of this analysis.

7.2.3 Background Event Rates

Figure 7.2 shows that the expected backgrounds fit the data well. In this analysis, no normalization was chosen for the background event rates; β and γ were allowed to vary as free parameters. There are large uncertainties ($\sim$30%) in the atmospheric neutrino fluxes at the low energies where the SRN search is conducted (see Section 6.1.2); avoiding flux constraints prevents these uncertainties from affecting the analysis results. As a consistency check, the fit

Background Source	Predicted # of events	Observed # of events
Atmospheric $\bar{\nu}_e + \nu_e$	75 ± 23	88 ± 12
Invisible μ decay	145 ± 43	174 ± 16

Table 7.2: The number of events predicted for each of the irreducible backgrounds is compared to the results of the χ^2 fit.

results for the number of background events were compared to the predictions. Atmospheric neutrino flux calculations made by the Honda group [59] were used to determine the background event rate in SK (see Section 6.1). The equivalent of two hundred years of SK data was simulated for each background, and processed by the event reconstruction and data reduction algorithms. The predicted number of background events expected in SK-I was determined by the number of MC events that passed the reduction cuts, normalized to the SK-I livetime.

Table 7.2 lists the predicted and observed number of events for each of the irreducible backgrounds to the SRN search. For 1496 days of SK-I data, the expected number of atmospheric $\bar{\nu}_e$ and ν_e events was 75 ± 23, which is consistent with the best fit to the free parameter γ: 88 ± 12 events. Neutrino oscillation affects the number of decay electrons (and positrons) expected to be produced by invisible muon decay. The invisible muons are created by ultra-low energy atmospheric ν_μ (see Section 5.6), and it has been shown that atmospheric ν_μ oscillate into ν_τ [27, 64]. The oscillation probability depends on both the distance traveled by the neutrino, L, and the neutrino energy:

$$P(\nu_\mu \rightarrow \nu_\tau) \;=\; \sin^2 2\theta \;\cdot\; \sin^2\left(\frac{1.27\ \Delta m^2(\mathrm{eV}^2)\ L(\mathrm{km})}{E_\nu(\mathrm{GeV})}\right) \qquad (7.5)$$

In this equation, θ is the mixing angle between the neutrino flavor eigenstates and mass eigenstates, and $\Delta\mathrm{m}^2$ is the difference in the squares of the neutrino masses. According to Figure 5.25, the atmospheric ν_μ that produce invisible muons have $E_\nu < 300$ MeV; for such low neutrino energies, it is reasonable to assume that half of the ν_μ have oscillated into ν_τ. Using this assumption, the predicted number of background events created from invisible muon decay is 145 ± 43, which is consistent with the best fit to the free parameter β: 174 ± 16 events.

As a second consistency check, the double ratio R was evaluated, where R is defined as follows:

$$R \equiv \frac{(\nu_\mu + \bar{\nu}_\mu)/(\nu_e + \bar{\nu}_e)_{DATA}}{(\nu_\mu + \bar{\nu}_\mu)/(\nu_e + \bar{\nu}_e)_{MC}} \tag{7.6}$$

Both types of irreducible background events originate from atmospheric neutrinos. After accounting for neutrino oscillation, the number of decay electrons (and positrons) from invisible muons provides a measurement of the low energy atmospheric $\nu_\mu + \bar{\nu}_\mu$ flux. The events produced by atmospheric $\nu_e + \bar{\nu}_e$ interactions are fit directly from the data. By taking the ratio of data to Monte Carlo, the large uncertainties in the neutrino flux and cross sections cancel out. The expected value for R is unity if all of the remaining background events originate from atmospheric neutrino interactions. Using the data and MC values listed in Table 7.2, the value of the double ratio is $R = 1.02 \pm 0.17(\text{stat})$. Although the small size of the data sample results in a large statistical uncertainty, the value of R is in very good agreement with unity.

It is worth noting that the error on the observed number of background events is less than the theoretical uncertainty in the atmospheric neutrino flux predictions. Most previously published measurements of the atmospheric neutrino fluxes studied neutrinos with higher momentum values: $p_e > 100$ MeV/c and $p_\mu > 200$ MeV/c (e.g. reference [65]). Perhaps, with further work, the measurements presented here could be of value to studies of the atmospheric neutrino fluxes.

7.2.4 Efficiency-Corrected SRN Event Rate Limits

Due to the energy-dependent application of the reduction cuts, the spectrum of the final SRN candidate events contains a discontinuity at 34 MeV. The efficiency for retaining signal is either 47% or 79%, depending on the event energy relative to 34 MeV. (see Section 5.5). This discontinuity makes it difficult to directly compare the 90% C.L. limits on the number of SRN events in the SK-I data (shown in Table 7.1) to the theoretical predictions.

The data and the results of the χ^2 fit can be presented without discontinuity by converting them to an efficiency-corrected annual event rate [66]. This is accomplished by scaling N_l, the number of events in each bin of the energy spectrum, as follows:

$$N_l' \equiv \frac{N_l}{\epsilon(E_l)} \times \frac{365 \text{ days}}{\tau} \tag{7.7}$$

Theoretical Model	Efficiency-corrected event rate limit (90% C.L.)	Theoretical prediction ($E_e > 18$ MeV)
Constant supernova rate [19]	< 3.4 events/year	8.6 events/year
Population synthesis [20]	< 3.2 events/year	0.96 events/year
Cosmic gas infall [21]	< 2.8 events/year	0.41 events/year
Cosmic chemical evolution [22]	< 3.3 events/year	1.1 events/year
Heavy metal abundance [23]	< 3.0 events/year	< 5.0 events/year
Large mixing angle osc. [24]	< 3.5 events/year	1.2 events/year

Table 7.3: The SK-I efficiency-corrected annual SRN event rate limits are compared to predictions from six theoretical models. Only SRN that would produce positrons with $E_e > 18$ MeV are considered in the predictions.

where τ is the detector livetime of 1496 days, and ϵ(E) is the signal detection efficiency. The fraction of signal and background events expected in each energy bin, A_l, B_l, and C_l, can be similarly converted, although the spectral shapes must be re-normalized after applying the efficiency correction. By using the converted data and spectral shapes, the information presented in Figure 7.2 can be displayed without a discontinuity; Figure 7.4 shows continuous distributions for the SRN data and fit results.

The 90% C.L. limit on the number of SRN events in the SK-I data, α_{90}, can be efficiency-corrected in a similar manner:

$$\alpha_{90}^{'} \equiv \frac{365 \text{ days}}{\tau} \times \sum_{l=1}^{16} \left(\frac{\alpha_{90}}{\epsilon(E_l)} \cdot A_l \right) \tag{7.8}$$

The middle column of Table 7.3 lists $\alpha_{90}^{'}$ for each of the theoretical models. These values are the maximum number (at 90% C.L.) of SRN events, with positron energy greater than 18 MeV, that would be observed annually at a 100% efficient Super-Kamiokande detector. Expressed in this form, the limits can be directly compared to the theoretical predictions for the annual SRN event rate in SK; the predictions are shown in the third column of Table 7.3. For the heavy metal abundance model [23], the prediction in the table is a theoretical upper bound.

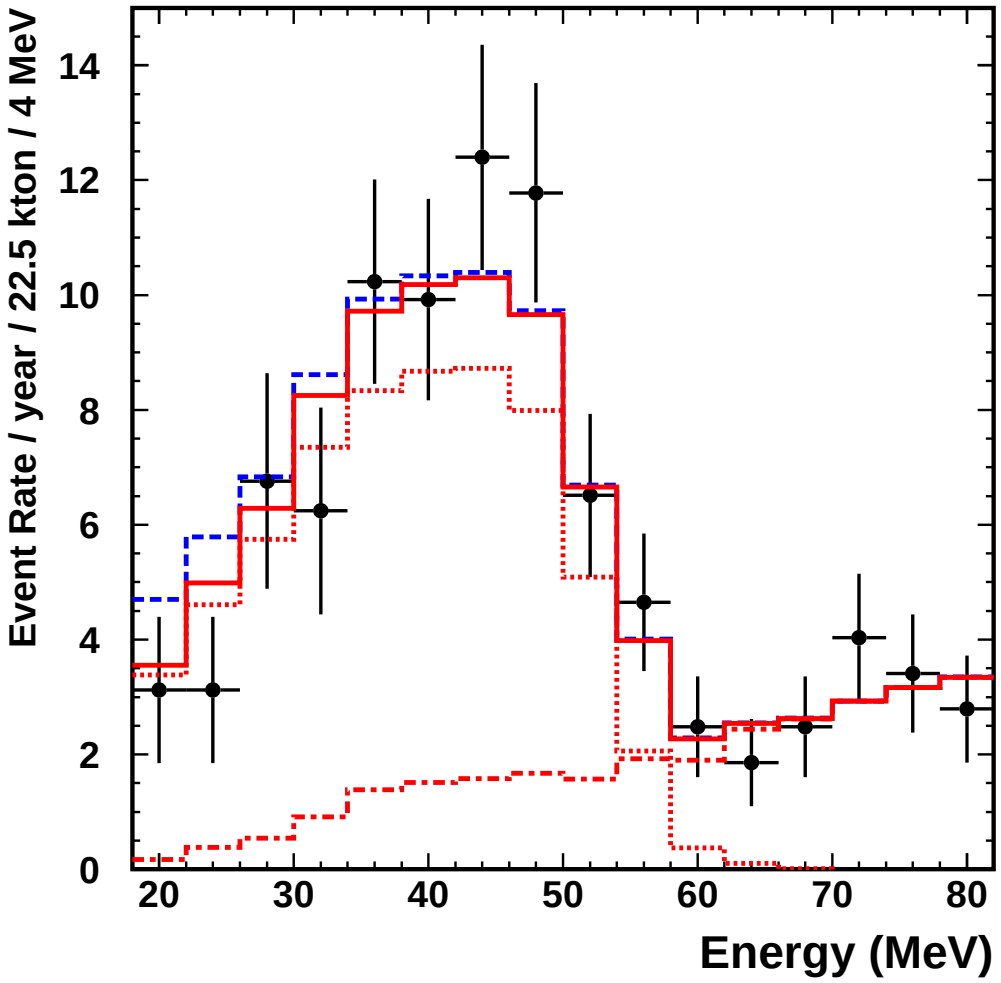

Figure 7.4: The energy distribution of the SRN candidate events is presented as an efficiency-corrected annual event rate. The various lines are defined the same as in Figure 7.2.

7.2.5 Flux Limits

The limit on α can be used to derive a 90% C.L. limit on the SRN flux for each of the theoretical models. The predicted number of SRN-induced events for a given flux and spectrum is obtained by integrating equation (6.3):

$$\alpha = (N_p \times \tau) \int_{E=19.3\ \mathrm{MeV}}^{83.3\ \mathrm{MeV}} F(E_\nu)\, \sigma(E_\nu)\, \epsilon(E_\nu)\, dE_\nu \tag{7.9}$$

where:

$$\begin{aligned}
\alpha &\equiv N_{SRN} = \text{Number of SRN-induced events} \\
N_p &= \text{Number of free protons in SK} = 1.5 \times 10^{33} \\
\tau &= \text{Detector livetime} = 1496\,\text{days} = 1.29 \times 10^{8}\,\text{seconds} \\
F(E_\nu) &= \text{Theoretical spectrum of the SRN flux} \\
\sigma(E_\nu) &= \text{Cross section for inverse } \beta \text{ decay} = 9.52 \times 10^{-44}\, E_e\, p_e \\
\epsilon(E_\nu) &= \text{Signal detection efficiency} = \begin{cases} 47\% & \text{for } E_e < 34\ \text{MeV} \\ 79\% & \text{for } E_e > 34\ \text{MeV} \end{cases}
\end{aligned}$$

The energy of the positron, E_e, created by an SRN of energy E_ν, is given by equation (6.2); the integral in equation (7.9) spans the range of $\bar{\nu}_e$ that produce positrons within the thresholds of the SRN analysis (18 MeV $< E_e <$ 82 MeV).

The function $F(E)$ contains information about both the spectrum shape and the total number flux of the SRN. This function can be split into two components: $F(E) = F \times f(E)$, where $f(E)$ is the normalized SRN spectrum shape, and F is the total flux of the SRN intergrated over the entire spectrum. Since F does not depend on energy, it can be removed from the integral in equation (7.9), which can then be inverted to express the total flux as a function of α. Using the α_{90} values from Table 7.1, an upper bound on the SRN flux, F_{90}, can be obtained for each model:

$$F_{90} = \frac{\alpha_{90}}{(N_p \times \tau) \int_{19.3\,\mathrm{MeV}}^{83.3\,\mathrm{MeV}} f(E_\nu)\, \sigma(E_\nu)\, \epsilon(E_\nu)\, dE_\nu} \tag{7.10}$$

Table 7.4 lists the SK-I flux limits for the various SRN models, and compares them to the total SRN flux predictions. Figure 7.5 shows this information graphically. Each SRN model displays two bars on the graph: the bar on the left represents the upper bound on the SRN flux obtained from this analysis, the bar on the right represents the total flux predicted by the model. SK-I is sensitive to signals from the theories for which the upper bound is lower than the flux prediction.

Theoretical model	SRN flux limit (90% C.L.)	Predicted flux
Constant supernova rate [19]	$< 20\ \bar{\nu}_e\ \mathrm{cm}^{-2}\ \mathrm{s}^{-1}$	$52\ \bar{\nu}_e\ \mathrm{cm}^{-2}\ \mathrm{s}^{-1}$
Population synthesis [20]	$< 130\ \bar{\nu}_e\ \mathrm{cm}^{-2}\ \mathrm{s}^{-1}$	$44\ \bar{\nu}_e\ \mathrm{cm}^{-2}\ \mathrm{s}^{-1}$
Cosmic gas infall [21]	$< 32\ \bar{\nu}_e\ \mathrm{cm}^{-2}\ \mathrm{s}^{-1}$	$5.4\ \bar{\nu}_e\ \mathrm{cm}^{-2}\ \mathrm{s}^{-1}$
Cosmic chemical evolution [22]	$< 25\ \bar{\nu}_e\ \mathrm{cm}^{-2}\ \mathrm{s}^{-1}$	$8.3\ \bar{\nu}_e\ \mathrm{cm}^{-2}\ \mathrm{s}^{-1}$
Heavy metal abundance [23]	$< 29\ \bar{\nu}_e\ \mathrm{cm}^{-2}\ \mathrm{s}^{-1}$	$< 54\ \bar{\nu}_e\ \mathrm{cm}^{-2}\ \mathrm{s}^{-1}$
Large mixing angle osc. [24]	$< 31\ \bar{\nu}_e\ \mathrm{cm}^{-2}\ \mathrm{s}^{-1}$	$11\ \bar{\nu}_e\ \mathrm{cm}^{-2}\ \mathrm{s}^{-1}$

Table 7.4: The SRN flux limits are presented for six theoretical models. These limits are compared to the theoretical flux predictions from the corresponding models. Note that the heavy metal abundance calculation only sets a theoretical upper bound on the SRN flux [23].

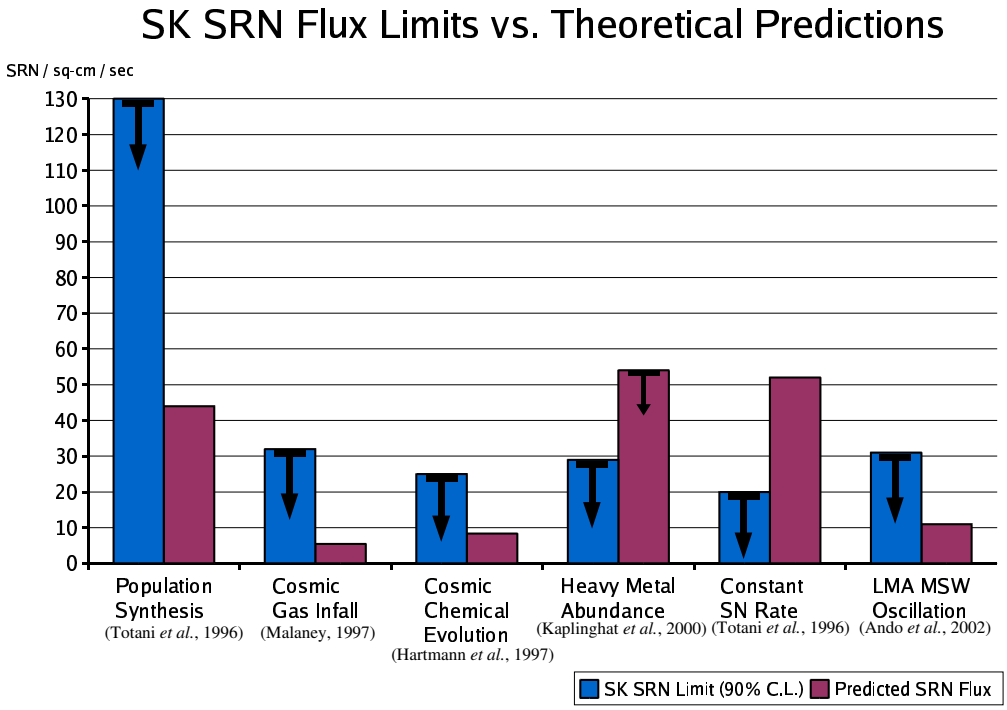

Figure 7.5: The information from Table 7.4 is presented graphically. For each model considered, two bars are shown. The bar on the left represents the model-dependent upper bound on the SRN flux. The bar on the right represents the total flux predicted by that model.

7.3 Discussion

Table 7.4 and Figure 7.5 summarize the model-dependent upper bounds on the SRN flux obtained by this analysis and compare these limits to the theoretical predictions. Of the six models that were tested, the SRN search produced four flux limits that are greater than the corresponding model predictions, and two limits that are below the predictions.

For the population synthesis model [20], the SK-I flux limit is higher than the prediction by a factor of $\sim$3. The population synthesis method uses a supernova rate that peaked and then dropped sharply within the initial 1 Gyr after galaxy formation occurred in the universe. According to the calculations of this model, more than 50% of the total number of core-collapse supernovae exploded during this initial period. Relic neutrinos from these early supernovae were strongly redshifted before reaching the Earth. As a result, this method predicts that the SRN flux is dominated by neutrinos with energies shifted below the analysis threshold; this explains why the current analysis is not sensitive to the population synthesis model. Additionally, the SRN flux limit for this spectrum is significantly higher than the limits set on the other five theories. The spectrum of SRN calculated by this method is shown in Figure 1.5; a distinct peak is visible for $E_\nu < 10$ MeV, containing the large SRN flux from the early universe to which SK-I is not sensitive. This peak is not present in the other theoretical predictions, which explains why the upper bound on the population synthesis flux is larger than all of the other limits.

The upper bound on the cosmic chemical evolution model [22] is also higher than the prediction by about a factor of three. In the energy region $E_\nu > 19.3$ MeV, where the SRN can produce positrons that are above the analysis threshold, the spectral shape and flux predicted by this theory are very similar to the those of the population synthesis method (see Figure 1.5). Thus, the α_{90} values for these two models are nearly identical, as are the ratios of the flux limits to the flux predictions. Although the dominant contribution to the SRN flux still comes from supernovae in the early universe, the cosmic chemical evolution model does not contain a strong peak at very low energies. Therefore, the total flux predicted from this method is smaller than the population synthesis expectation, as is the absolute upper bound on the flux.

The spectral shape predicted by the cosmic gas infall calculations [21] has the most sharply decreasing slope of all the theories considered here. This soft spectrum means that the SRN signal shape for this model differs most from the spectral shapes of the backgrounds. Thus, the minimum χ^2 function is deeper, i.e. the χ^2 value increases more quickly for deviations from the best-fit parameters. A deeper χ^2 minimum results in a lower limit on α for

this model (see Table 7.1 and Table 7.3). However, with a softer spectrum, a smaller fraction of the SRN flux produces positrons that are above the 18 MeV analysis threshold. As a consequence, this analysis is even less sensitive to the cosmic gas infall model than it is to the population synthesis or cosmic chemical evolution theories; the upper bound on this flux is greater than the prediction by nearly a factor of six.

The hardest SRN energy spectrum considered here arose from the inclusion of LMA neutrino oscillation effects [24]. The average energy of the $\bar{\nu}_\mu$ and the $\bar{\nu}_\tau$ is higher than that of the $\bar{\nu}_e$ (see Section 1.2.1). Thus, neutrino mixing hardens the spectrum of the relic $\bar{\nu}_e$, which are the most detectable species of supernova relic neutrinos. This hardened spectrum influences the search results for the LMA model with effects that are opposite to those described for the soft spectrum of the cosmic gas infall model. Although it is still distinct, the oscillated SRN signal shape is closest to the spectral shape of the backgrounds. Therefore, the minimum χ^2 value increases more slowly for deviations from the best-fit parameters, resulting in a higher upper bound on α. However, since the cross section for inverse β decay increases as the square of the energy, the harder spectrum means that SK is sensitive to a larger fraction of the SRN flux. These two competing effects largely negate each other. Due to the relatively small total flux expected for this model, the upper bound on the flux is still larger than the prediction by about a factor of three.

Supernovae at redshifts $z < 1$ make the dominant contributions to the SRN flux in the heavy metal abundance model [23]. Neutrinos from these supernovae do not experience a strong decrease in energy from the Doppler effect; therefore, SK is sensitive to a large fraction of the SRN flux. For this model, the SK-I flux limit is smaller than the calculated total flux. However, this prediction was designed to be conservative; parameters that contained uncertainty were assigned the allowed value that would maximize the SRN flux. Thus, this calculation essentially places a theoretical upper bound on the flux. Since the experimental upper bound on the SRN flux is lower than this theoretical limit, the results of this analysis can constrain this model, but they cannot completely eliminate it. By adjusting some of the uncertain parameters, a lower flux prediction could be calculated using the same methodology.

The total SRN flux predicted by the constant model scales with the rate of core-collapse supernovae [67], so the SRN flux limit directly corresponds to a 90% C.L. upper bound on the constant supernova rate. The SRN flux prediction for this model, listed in Table 7.4, is based on a constant supernova rate of 1.6×10^3 SN year^{-1} Mpc^{-3}. This supernova rate was chosen to be consistent with the nucleosynthesis requirement (see Section 1.3.2). The

observed SRN flux limit (20 $\bar{\nu}_e$ cm^{-2} s^{-1}) corresponds to a supernova rate limit of 6.2×10^2 SN year^{-1} Mpc^{-3}. Therefore, the constant model can be ruled out because this limit on the supernova rate is too low to be consistent with the observed abundance of oxygen [68, 20], which is synthesized in the massive stars that become core-collapse supernovae. At Kamiokande-II, a flux limit of 780 $\bar{\nu}_e$ cm^{-2} s^{-1} was set with the assumption of a constant supernova model [37]. In comparison, the SK-I limit obtained from the current analysis is 39 times more stringent. The exposure ($N_p \times \tau$) of the SRN search at SK-I is 47 times greater than that of Kamiokande-II. Since the SRN search is background-limited, the upper bound on the SRN flux should improve as the square root of the exposure. Considering only the ratio of the exposures in SK-I and Kamiokande-II, the limit on the SRN flux would be expected to decrease by about a factor of seven; the results presented here are improved over the Kamiokande-II limits by a significantly greater factor. The additional improvement is a consequence of the more powerful analysis method described in Section 7.1.

7.4 Model-Insensitive Approach

The flux limits presented in Section 7.2.5 have a strong model dependence. The upper bound on the SRN flux is largely determined by the shape of the theoretical spectrum at energies that are below the analysis threshold. These limits are useful for evaluating the validity of individual theories; however, the extrapolation to energies beyond what SK can directly observe introduces ambiguity into these results.

Perhaps a more important quantity to measure is the limit on the SRN flux above the SK-I analysis threshold of $E_e = 18$ MeV. A limit set in this energy range is based only on actual data; no extrapolation is necessary and the result should be unambiguous. Furthermore, in the region $E_\nu > 19.3$ MeV, all six models have similar spectral shapes; no sharp peaks or dips are present. Thus, the upper bound for this region should be insensitive to the choice of model. A model-insensitive flux limit, F_{ins}, can be obtained from any of the model-dependent results (see Table 7.4) by dividing out the model dependence as follows:

$$F_{ins} = F_{90} \times \frac{\int_{19.3\,\mathrm{MeV}}^{83.3\,\mathrm{MeV}} f(E_\nu)\, dE_\nu}{\int_0^\infty f(E_\nu)\, dE_\nu} \tag{7.11}$$

This equation was evaluated multiple times, using F_{90} from each of the six theoretical models. As expected, the flux limits were the same for all of the

Theoretical model	Predicted flux ($E_\nu > 19.3$ MeV)
Constant supernova rate [19]	3.1 $\bar{\nu}_e$ cm^{-2} s^{-1}
Population synthesis [20]	0.41 $\bar{\nu}_e$ cm^{-2} s^{-1}
Cosmic gas infall [21]	0.20 $\bar{\nu}_e$ cm^{-2} s^{-1}
Cosmic chemical evolution [22]	0.39 $\bar{\nu}_e$ cm^{-2} s^{-1}
Heavy metal abundance [23]	< 2.2 $\bar{\nu}_e$ cm^{-2} s^{-1}
Large mixing angle osc. [24]	0.43 $\bar{\nu}_e$ cm^{-2} s^{-1}

Table 7.5: The predicted SRN flux above a neutrino energy of 19.3 MeV is presented for six theoretical models. The SRN with greater energy can produce positrons that are above the analysis threshold. These predictions can be compared to the model-insensitive limit of 1.2 $\bar{\nu}_e$ cm^{-2} s^{-1}.

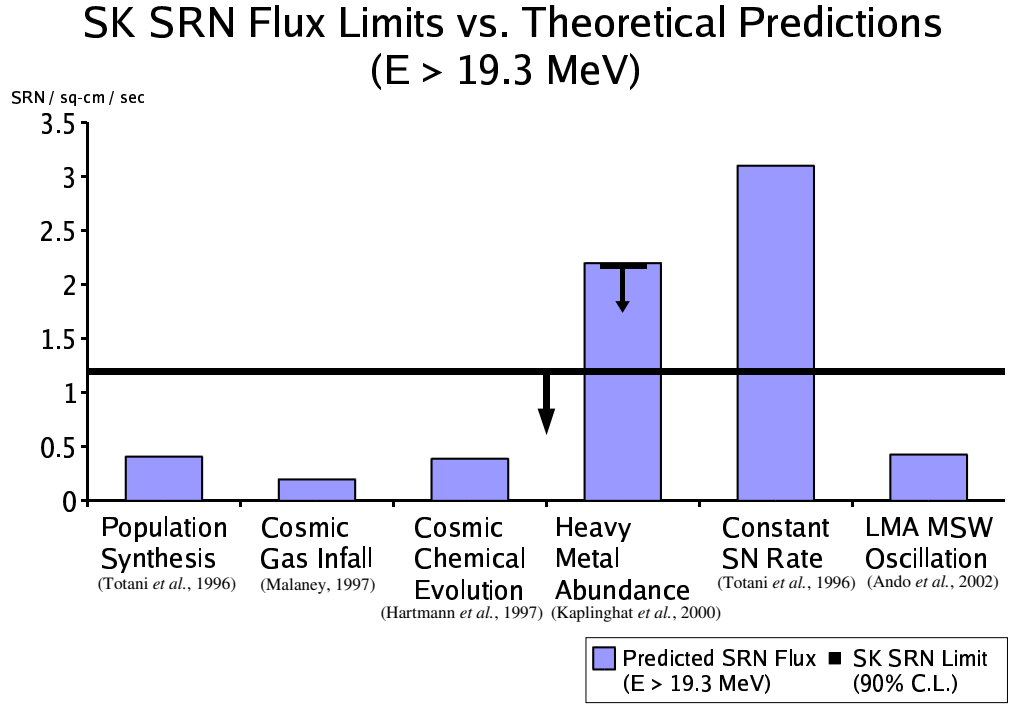

Figure 7.6: The information from Table 7.5 is displayed graphically. For each theoretical model, a bar is shown to represent the SRN flux predicted by that model above a neutrino energy of 19.3 MeV. The upper bound on the SRN flux in this energy range is insensitive to the choice of model, and is indicated by the horizontal line.

models that were considered. The 90% C.L. upper bound on the SRN flux is 1.2 $\bar{\nu}_e$ cm^{-2} s^{-1} for $E_\nu > 19.3$ MeV. This model-insensitive limit can be compared to the predictions for the SRN flux above this energy, which are listed in Table 7.5. Figure 7.6 makes this comparison graphically: The flux predicted by each method is represented by a bar; the model-insensitive upper bound is indicated with a horizontal line.

Even though each theoretical model has a slightly different α_{90} value (see Table 7.1), the flux limit above this energy threshold is the same. The flux limit is determined by using both α_{90} and the integral of the theoretically expected event rate, i.e. the predicted flux times the cross section. The limit on α is determined by a shape fit, so the falling shape of a harder (softer) SRN spectrum is slightly more (less) difficult to distinguish from the rising shape of the Michel spectrum. As a consequence, the limit on α becomes slightly worse (better). The cross section increases quadratically with energy; thus, SK is sensitive to a larger (smaller) fraction of the SRN flux for models with a harder (softer) spectrum. This effect tends to lower (raise) the upper bound on the SRN flux. Both effects are considered in equation (7.11); since they affect the $E_\nu > 19.3$ MeV SRN flux limit in opposite ways, these effects tend to cancel each other out. Thus, this limit is not sensitive to the small differences that do exist in the theoretical spectral shapes at energies greater than the analysis threshold.

Previously, the best upper bound on the SRN flux in this energy region was set using 357 days of data at Kamiokande-II [36]. The Kamiokande-II flux limit was 226 $\bar{\nu}_e$ cm^{-2} s^{-1}. Comparing 1496 days of SK-I data to 357 days of Kamiokande-II data results in an exposure ratio of 138. As a background-limited measurement, the statistical improvement expected in the SK-I analysis is a factor of $\sqrt{138}$, or about twelve. The SK-I limit of 1.2 $\bar{\nu}_e$ cm^{-2} s^{-1} is more stringent than the Kamiokande-II result by a factor of 188, which is more than two orders of magnitude.

Chapter 8

Conclusions and Future

8.1 Conclusions from Super-Kamiokande-I

A search was conducted at Super-Kamiokande-I to detect the diffuse signal of $\bar{\nu}_e$ from all previous core-collapse supernovae. Signal events cannot be individually tagged in SK-I. Thus, in order to extract an SRN signal statistically, effective background reduction tools were developed to create an energy region that was nearly free of background contamination. The reduction algorithms were able to reduce the background by an order of magnitude and create such a minimally contaminated region above an energy threshold of 18 MeV. Two sources of irreducible background remained, the primary source being the decay electrons that are formed when invisible muons decay in the detector.

In the presence of the irreducible backgrounds, a shape fit was used to attempt to identify SRN-induced events in the SK-I data. A positive SRN signal would appear as a distortion in the expected shape of the Michel spectrum. No such distortion was found in the 1496 days of SK-I data. In the absence of a positive signal, upper bounds on the number of SRN events were set at the 90% confidence level. The upper bound on the number of SRN events was then used to place 90% confidence level limits on the flux of the supernova relic neutrinos. These limits are model-dependent and strongly influenced by the shape of the SRN spectrum at energies below the 18 MeV analysis threshold. Of the six models that were examined, two could be either eliminated or constrained by the SK-I results. To adequately probe the other four predictions, the sensitivity needs to be increased by a factor of about three to six. Potential methods of obtaining such an increase are discussed in Section 8.2 and Section 8.3.

Previous SRN flux limits of 780 $\bar{\nu}_e$ cm^{-2} s^{-1} were obtained from searches at the Kamiokande-II detector [37] with the assumption that the supernova rate

has been constant with time. This assumption formed the basis of one of the models that were tested in this thesis; the SK-I flux limit for this model was 20 $\bar{\nu}_e$ cm^{-2} s^{-1}. The improvement in the SK-I upper bound is substantially greater than that expected from the increased exposure alone.

By dividing out the model-dependence in the calculation of the upper bound, a model-insensitive limit was obtained for the energy region that could be directly observed in this analysis. Above a neutrino energy threshold of $E_\nu > 19.3$ MeV, an upper limit of 1.2 $\bar{\nu}_e$ cm^{-2} s^{-1} was placed on the flux of the supernova relic neutrinos.

8.2 The Near Future

A decade ago, the best limits on the SRN flux were greater than the expectations by two orders of magnitude. In contrast, the results from this analysis are able to exclude or constrain some of the theoretical models. If the experimental sensitivity to the SRN could be improved by approximately another factor of three, it seems likely that the SRN could finally be detected.

Given the proximity of the current results to the expectations, there is a growing interest in the topic of supernova relic neutrinos. Although it seems likely that the large detectors discussed in Section 8.3 will be sensitive to the SRN flux, several ideas on how to discover the SRN in the next few years are now being considered.

8.2.1 Contemporary Experiments

In Super-Kamiokande-I, the signature of an SRN event was a single positron event; the SRN flux is also expected to be isotropic. Therefore, these positrons are not correlated in either time, space, or direction to a source. Furthermore, SK-I lacks the ability to distinguish positrons from electrons, so an SRN event is simply an electron-like single ring. This signature is hardly unique to the SRN; thus, there was no way to tag individual events as signal. This was the greatest weakness in the SK-I search for the SRN: there was no way to reliably distinguish individual signal events from background events.

There are other experiments currently operational that do not suffer from this inability to separate electrons from positrons. The KamLAND experiment [35] is a liquid scintillator detector designed to observe electron antineutrinos. The $\bar{\nu}_e$ that undergo inverse β decay are detected if the resulting positron is above the detector threshold of 1.8 MeV. During the inverse β reaction, a neutron is also produced (see Section 1.2.2). In both Super-Kamiokande

and KamLAND, that neutron is captured on a free proton via the following reaction:

$$n + p \rightarrow d + \gamma \quad (E_\gamma = 2.2 \text{ MeV})$$

At Super-Kamiokande, the energy of the γ-ray is too low to trigger the detector efficiently (see Section 2.6.3); however, KamLAND has a very low threshold and so the γ-ray is easily detectable. Thus, a delayed coincidence between the detection of an electron-like event and the detection of a 2.2 MeV γ-ray is used to identify $\bar{\nu}_e$ events efficiently in KamLAND.

Most of the backgrounds to the SRN search do not have a delayed coincidence signature and can be easily rejected from the KamLAND data. Approximately 80% of the invisible muons do not occur in coincidence with a neutron [69]. Thus, the dominant irreducible background can be greatly reduced, increasing the sensitivity of an SRN search at KamLAND. Additionally, the spallation background can be entirely removed, which permits the SRN analysis threshold to be lowered. Since the SRN flux is expected to decrease exponentially with increasing energy (see Figure 1.5), it is desirable to have a low analysis threshold when searching for the SRN. Reactor anti-neutrinos have a cut-off energy of about 10 MeV. At this energy, the flux of reactor $\bar{\nu}_e$ is $\sim$60 times higher than the SRN flux predicted by the models for which SK-I is not sensitive [70]. Since events caused by the reactor $\bar{\nu}_e$ have the same signature as the SRN-induced events, the cut-off energy of the reactor anti-neutrinos determines the lower threshold of the SRN search at KamLAND. By lowering the analysis threshold from 18 MeV to $\sim$10 MeV, the fraction of the SRN spectrum that is directly observable increases by roughly a factor of two.

Since KamLAND has the ability to detect neutrons that have been captured by free protons, it gains sensitivity to the SRN flux via more a powerful background reduction and a lower threshold. However, there are only 3.46×10^{31} free protons in the 408 tons of liquid scintillator that comprises the KamLAND fiducial mass; the Super-Kamiokande fiducial volume contains more free protons by a factor of 43 ($N_p = 1.5 \times 10^{33}$). Free protons are the interaction targets for the $\bar{\nu}_e$; due to the relatively small number of targets in KamLAND, the rate of SRN-induced events is predicted to be quite low. For instance, the model that includes LMA oscillation effects [24] predicts an SRN event rate in KamLAND of 0.1 events per year above a threshold of 10 MeV (compared to 1.2 events per year above 18 MeV expected at SK). This tiny event rate rules out the possibility of discovering the SRN signal at the KamLAND experiment.

The situation for the Sudbury Neutrino Observatory (SNO) is very similar to that of KamLAND. SNO contains heavy water (D_2O) into which two tons of salt (NaCl) have been dissolved [71]. The SRN, and other $\bar{\nu}_e$, interact in SNO through the following reaction:

$$\bar{\nu}_e + d \rightarrow e^+ + n + n$$

The resulting neutrons can then interact with deuterons and also with the nuclei of ^{35}Cl, which have a particularly large cross section for neutron capture. The neutrons are absorbed via the interactions:

$$n + d \rightarrow {}^3\mathrm{H} + \gamma \quad (E_\gamma = 6.3 \text{ MeV})$$

$$n + {}^{35}\mathrm{Cl} \rightarrow {}^{36}\mathrm{Cl} + \gamma \quad (E_\gamma = 8.6 \text{ MeV})$$

As with KamLAND, SNO possesses the ability to eliminate most of the backgrounds by searching for a delayed coincidence signal. However, SNO is also too small to discover the SRN. Above a threshold energy of 10 MeV, the LMA model predicts an SRN rate at SNO of 0.03 events per year.

It is clear that the ability to observe coincident neutrons greatly enhances a neutrino detector's sensitivity to the SRN flux. Current experiments with this capability are not large enough to discover the SRN; however, in the future, it may be possible to apply this principle to a larger detector.

8.2.2 Super-Kamiokande-II

In July 2001, the first phase of Super-Kamiokande came to a close so that the detector could be drained for the replacement of failed PMTs. On 12 November 2001, while SK was being refilled with water, one of the PMTs at the bottom of the ID imploded. The implosion triggered a chain reaction that destroyed 6,777 of the 11,146 ID PMTs and nearly 1100 of the 1885 OD PMTs. During 2002, Super-Kamiokande was partially rebuilt. The OD was fully restored and, to prevent a recurrence of the implosion accident, the ID PMTs were removed and encased within a shell of fiberglass and acrylic. After being protected thusly, 5182 PMTs were installed in the ID and distributed within the detector so as to obtain a nearly-uniform 18% photocathode coverage. In December 2002, Super-Kamiokande began taking data again; the new configuration of the detector is referred to as Super-Kamiokande-II (SK-II).

There are several consequences of the reduced population of ID PMTs in SK-II. The most significant effect for the SRN search is probably the change in the energy resolution. Since the energy calculation is based on the number of

hit PMTs, the resolution essentially follows counting statistics. With less than half the number of PMTs currently available, the energy resolution is degraded by a factor of $\sim \sqrt{2}$. As a result, a larger number of spallation events will be reconstructed above 18 MeV, possibly affecting the threshold of the SRN analysis in SK-II.

SK-II is accumulating more data that will be used to increase the exposure of the SRN search. However, in a normal water Cherenkov detector, the SRN search results are background-limited, and so the sensitivity will only increase as the square root of the exposure. To probe most of the remaining SRN predictions, the analysis sensitivity must be increased by a factor of three; to obtain this factor from additional statistics alone, the total exposure must increase by a factor of nine. Presently, SK-II is scheduled to run until October 2005; therefore, combining the SK-I and SK-II data will only result in an exposure increase of $\sim$50%, which should lower the flux limits by about $\sim$18%.

As noted in Section 8.1, it is possible to increase the sensitivity by improving the power of the analysis. In an attempt to detect the SRN using only SK-I and SK-II data, new ideas are being discussed for a re-analysis of existing and newly accumulated data. Two types of improvements are being considered: enhanced spallation cuts that would allow the analysis threshold to be lowered, and methods for tagging the decay electrons from invisible muons. Table 8.1 summarizes the expected SRN event rate in SK for different values of the analysis threshold energy. The current goal is to lower the threshold from 18 MeV to 15 MeV, which would increase the expected event rate by about 50%. However, preliminary studies aimed at improving the spallation cut have not yet proven effective. The invisible muon identification scheme targets muons that have been captured by oxygen nuclei, thereby raising the nucleus to an excited state. When the nucleus de-excites, a γ-ray is emitted with a few MeV of energy. The SK trigger is not 100% efficient for these ultra-low energy (i.e. E $\leq$ 4 MeV) γ-ray events; nevertheless, some of these events might have been recorded in the existing data. Searching for γ-rays that are coincident with SRN candidate events may eliminate part of the invisible muon background. Although these re-analysis techniques will undoubtably lead to some improvement in the SRN limits, it seems ambitious to attempt SRN discovery in this manner. The current SK-I analysis already contains significantly more power than previous analyses, and it is uncertain whether an additional sensitivity factor of three can be gained from either existing or newly accumulated data.

8.2.3 Super-Kamiokande-III

In October 2005, the second phase of Super-Kamiokande is scheduled to end. The detector will be drained and the full complement of 11,146 ID PMTs will be restored. By June 2006, Super-Kamiokande is expected to begin taking data again; the third phase of detector operation will be referred to as Super-Kamiokande-III (SK-III). The SK-III configuration will not be identical to that of SK-I; significant alterations, such as protection for the PMTs, will still be in place as a result of the implosion accident. Nevertheless, SK-III is expected to have similar resolutions to SK-I.

If SK-III is an ordinary water Cherenkov detector, it will gather additional data that can be used to improve the SRN flux limits. As discussed in Section 8.2.2, this background-limited search must accumulate significantly more data in order to yield a discovery. Thus, ideas for altering Super-Kamiokande are now being considered that, if implemented, may lead to the discovery of SRN at SK-III. In Section 8.2.1, neutrino experiments with neutron detection capabilities were discussed. Although a delayed coincidence neutron signal is a powerful tool for increasing sensitivity to the SRN flux, current experiments with this ability are too small to expect a noticable rate of SRN events. If Super-Kamiokande could be enhanced to detect the coincident neutrons efficiently, then SRN detection is likely, due to the large fiducial mass of SK.

The 2.2 MeV γ-ray emitted when thermalized neutrons are captured by free protons cannot be efficiently detected by SK; the energy is too low. In SNO, ^{35}Cl is used for neutron capture, since ^{35}CL has a large absorption cross section for thermal neutrons. A similar idea has been proposed for SK-III, except that gadolinium trichloride ($GdCl_3$) would be used instead of ordinary salt [69, 72, 73]. Gadolinium has a larger cross section for thermal neutron absorption than any other known nucleus; therefore, a relatively small concentration of $GdCl_3$ in SK could still capture most of the coincident neutrons. Adding approximately 9 tons of $GdCl_3$ to the 50,000 tons of SK water would result in 50% of neutrons being captured by the gadolinium instead of by the free protons in the water. About 100 tons of $GdCl_3$, which is only a 0.2% concentration, would be required to capture $\sim$90% of the neutrons on gadolinium. When the gadolinium absorbs a neutron, it releases a cascade of γ-rays; the total energy of the cascade is 8.0 MeV. The trigger threshold in SK-III is expected to be the same as in SK-I; all events with energy greater than 5.0 MeV will trigger the detector. Thus, the γ-ray cascade could be efficiently detected. Since $GdCl_3$ is water soluble, it could be easily added to SK. Toxicology studies have discovered no known dangers presented by $GdCl_3$, and the purchase price has dropped three orders of magnitude in the past two decades,

so this suggestion for improving SK is being taken very seriously. Currently, the optical properties of a $GdCl_3$ solution are being studied. There are also plans to examine several other effects of adding $GdCl_3$ to SK (e.g. corrosive properties, conduction properties).

It is too soon to decide whether gadolinium can be safely introduced into SK; it is not too soon to estimate the increase in sensitivity to the SRN that would occur if SK gains the ability to detect coincident neutrons. As with KamLAND and SNO, a gadolinium-enriched SK-III would be able to reject $\sim$80% of the invisible muon background and virtually all of the spallation events. With no spallation contamination, the SRN threshold could be lowered considerably. Lowering the threshold would allow a larger fraction of the SRN spectrum to be directly observed; additionally, the remaining background from invisible muons decreases at lower energies. If the spallation can be entirely rejected, then the background that will determine the lower analysis threshold will be the reactor anti-neutrinos. Japan has many nuclear reactors, so the total flux of reactor $\bar{\nu}_e$ is quite high at Kamioka. Although it has not yet been measured, the reactor $\bar{\nu}_e$ flux through SK is expected to be about $\sim$30 $\bar{\nu}_e$ cm^{-2} s^{-1} at the cut-off energy of 10 MeV [70]. According to Figure 1.5, this flux is about sixty times higher than the four flux predictions that are not ruled out by the current analysis; therefore, the reactor $\bar{\nu}_e$ are ultimately the limiting factor for the SRN analysis threshold. When a reactor $\bar{\nu}_e$ with an energy of 10 MeV undergoes inverse β decay, a positron with about 9 MeV of total energy is created. If SK had perfect energy resolution, then the SRN search threshold could be lowered to $\sim$9 MeV in a gadolinium-enriched SK-III. The number of SRN events expected annually in SK, assuming a 9 MeV threshold, is listed in the last column of Table 8.1. Realistically, the energy resolution of SK-III is expected to be about the same as in SK-I: at 9 MeV, the 1σ resolution width is $\sim$1.5 MeV (see Table 3.2). Thus, the SRN analysis threshold will need to be higher. At 12 MeV, about 2σ from the reactor $\bar{\nu}_e$ cut-off energy, the predicted rate of SRN-induced events is expected to be slightly higher than the rate of events produced by reactor $\bar{\nu}_e$. Although the source of individual events could not be identified at this energy, it should be possible to discover the SRN through statistical methods. The calculated SRN event rate above a 12 MeV analysis threshold is listed in Table 8.1; for most predictions that are not excluded by the current analysis, approximately 2 SRN events per year are expected.

Although it is possible to estimate the analysis threshold of a gadolinium-enriched SK-III, the actual threshold will not be known until (and unless) SK is modified and SK-III begins taking data. Figure 8.1 generalizes the dependency of the event rate on the analysis threshold for the SRN model that includes

Theoretical Model	Analysis Threshold Energy			
	18 MeV	15 MeV	12 MeV	9 MeV
Constant supernova rate [19]	8.6	11	14	17
Heavy metal abundance [23]	5.0	7.0	9.4	12
Large mixing angle osc. [24]	1.2	1.6	2.2	2.8
Cosmic chemical evolution [22]	1.1	1.5	2.0	2.5
Population synthesis [20]	0.96	1.3	1.7	2.2
Cosmic gas infall [21]	0.41	0.60	0.85	1.1

Table 8.1: The expected SRN event rate in SK is summarized for several analysis threshold energies. The table entries have units of events per year, and the energies values are for the positron. The theoretical models are listed in order of decreasing expectation; the first two sets of predictions are already ruled out by the SK-I data.

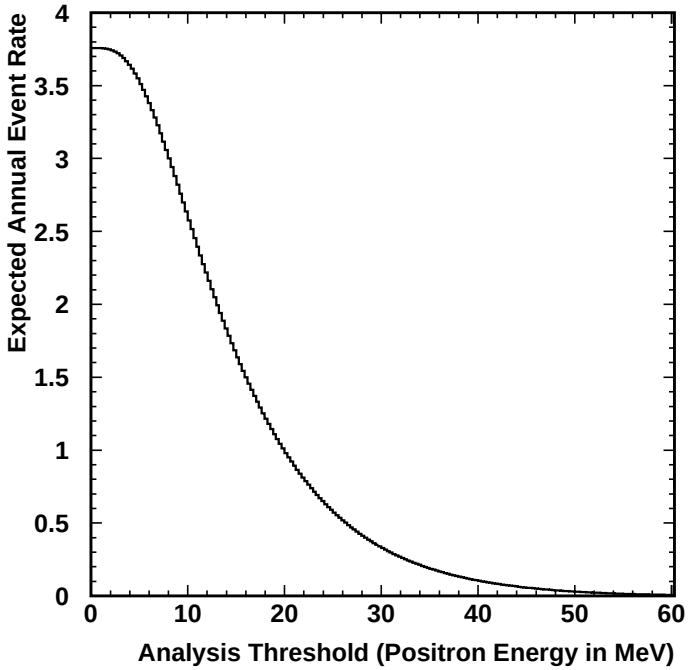

Figure 8.1: The expected SRN event rate in SK is plotted as a function of threshold energy for the LMA oscillation model [24]. The abscissa indicates the energy of the positron produced by the SRN.

LMA oscillation. The abscissa corresponds to the analysis threshold energy; the ordinate indicates the prediction from this model for the rate of SRN events produced in SK with energy above that threshold.

The results from studies that will occur during the next two years will be used to determine whether $GdCl_3$ will be added to SK-III. If SK-III is to be enriched with gadolinium, then it seems likely that the first discovery and measurement of the SRN will occur there. No other ideas are currently being discussed that would enable the detection of SRN within the next five years.

8.3 The Distant Future

Of all the current ideas for detecting the SRN in the near future (see Section 8.2), only an SK-III enhanced with neutron detection capabilities seems likely to succeed. However, it is far from certain that SK will be modified in this manner; many tests remain to be completed before the decision can be made. In the event that SK-III is an ordinary water Cherenkov detector, discovery of the SRN may eventually be accomplished from increased exposure. Two larger water Cherenkov detectors are presently being proposed, with data-taking to begin around 2020. If these experiments are built, they might gather sufficient data to detect the SRN within a few years of operation.

8.3.1 UNO and Hyper-Kamiokande

The first generation of water Cherenkov detectors was comprised of one Japanese experiment, Kamiokande [3], and one experiment based in the United States, IMB [4]. Super-Kamiokande, a second-generation water Cherenkov experiment, is based in Japan and the collaboration is predominantly comprised of institutions from Japan and the United States. Essentially, it is a unification of the two prior experiments. For the next generation of water Cherenkov detectors, two proposals are currently being considered: one of these proposals is for a detector in the United States, the other is for a detector in Japan.

The proposed detector in the United States is called the Underground Nucleon decay and Neutrino Observatory (UNO). The current plan is for a total volume of 650 kton, with a fiducal volume of 440 kton. The conceptual design [74, 75] envisions three adjacent cubic modules, each 60 m on a side. The middle module would have the same 40% photocathode coverage enjoyed by SK-I; the outer modules would only have 10% coverage. To first approximation, the sensitivity of UNO for detecting SRN events can be estimated from the ratio of the fiducial volumes. Of the SRN predictions that are not ruled

out by the SK-I analysis, most expect a flux that is below the current upper bound by a factor of three. If all other things are equal, the sensitivity is expected to increase with the square root of the exposure. Thus, an exposure nine times greater than the SK-I data is required to probe these models. SK-I operated for five years, and the UNO fiducial volume will be ∼20 times larger than that of SK. Therefore, the exposure necessary to be sensitive to these models could be obtained with less than three years of UNO data.

It may be necessary to make corrections to the sensitivity estimation to account for the regions of UNO that will only contain 10% photocathode coverage. Although the detector efficiency would be 100% at the 18 MeV analysis threshold, a smaller photocathode coverage area would result in a degraded energy resolution thereby allowing more spallation background to be reconstructed with higher energy. The analysis threshold in these regions may have to be raised, which would lower the sensitivity to the SRN and increase the time required to probe the theoretical models. The spallation problem could be somewhat ameliorated by building UNO at a location that has a thicker rock overburden than Super-Kamiokande. At a depth of 2700 meters water equivalent (m.w.e.), cosmic ray muons penetrate SK at a rate of ∼2.5 Hz. Some of the sites being considered for UNO are considerably deeper than 2700 m.w.e. If UNO is constructed at one of these deep sites, the relative rate of CRMs, and the spallation products that they create, would be smaller, thereby permitting a lower analysis threshold. Besides a lower threshold, there is a second advantage to a detector with fewer spallation products; in SK, cuts to remove the spallation events incur a 36% loss in signal detection efficiency. If UNO is located in a deeper cavern, it could have a higher efficiency for SRN than SK.

The Japanese have proposed the next experiment in the Kamiokande series: Hyper-Kamiokande (Hyper-K). The Hyper-K proposal calls for a 1,000 kton detector with a fiducial volume of 540 kton. From volume considerations alone, Hyper-K could be expected to be sensitive to several SRN models within two years of operation, since it will have a fiducial volume that is 24 times larger than that of SK. Initially, Hyper-K was to be constructed under Mt. Ikenoyama. Unfortunately, geological considerations prohibit the excavation of a cavity that is large enough to contain Hyper-K in the dense rock region where SK is located. At the SK site, the rock overburden is composed of gneiss, which is a high-grade metamorphic rock. At the proposed Hyper-K site, the rock overburden is made up of limestone. Due to metamorphic processes, gneiss is more dense than limestone, and so the effective rock overburden at the proposed Hyper-K site is considerably less. If Hyper-K is eventually erected at this location, the high rate of spallation events is likely to make an SRN search at Hyper-K infeasible. Other locations for Hyper-K have been suggested, such

as the Tochibora mine, which is 8 km away from the SK site. However, this alternate Hyper-K site is still quite shallow: only 1400 – 1900 m.w.e [76]. The location of Hyper-K is constrained to be close to SK because the detector needs to be situated in the neutrino beam from the J-PARC 50 GeV proton synchrotron. Thus, depth considerations may make it impossible to conduct an SRN search at Hyper-Kamiokande.

8.3.2 Measuring the SRN Spectrum

In Section 8.3.1, the sensitivity for observing the SRN was estimated for very large water Cherenkov detectors. These estimates implicitly assumed that both Hyper-Kamiokande and UNO will be ordinary water Cherenkov detectors. If, however, SK-III is gadolinium-enriched, it may discover the SRN before either of these third-generation water Cherenkov detectors can be built. If that happens, the possibility of enriching Hyper-K and UNO with $GdCl_3$ should be considered.

Spallation backgrounds should be easily eliminated in a gadolinium-enriched UNO or Hyper-K. Therefore, concerns about the depth of the detector are much less important if $GdCl_3$ can be added to UNO or Hyper-K. This is especially important to Hyper-K, which may be at a location that is too shallow to detect the SRN if it does not contain gadolinium. Since the reactor $\bar{\nu}_e$ flux determines the analysis threshold in such a detector, Hyper-K would probably have the same threshold as SK-III. The lower threshold for UNO is less certain, as a detector site has not yet been chosen; for the purposes of this section, it is assumed that UNO would have the same threshold as the Kamioka detectors.

As discussed in Section 8.2.3, a gadolinium-enriched SK-III could conceivable detect two SRN-induced events per year. The discovery of the SRN would be a noteworthy result. The SK event rate could be used to measure the SRN flux; however, most of the event rate predictions that were not ruled out by SK-I are quite similar to each other. Therefore, to distinguish between theoretical models, the energy spectrum of the SRN should be measured. Even if SK-III ran for fifteen years before UNO and Hyper-K were completed, it would still only observe $\sim$30 events. The error bars on the energy spectrum would be large and it is doubtful whether such an uncertain spectrum could differentiate between different models.

In contrast, if SK-III detects two SRN events per year, then it is reasonable to expect an annual rate of forty events to be observed in UNO and fifty events in Hyper-K. After several years of statistics have been accumulated, it might be possible to measure the SRN spectrum with sufficient precision to make cosmological statements. The spectrum of the SRN is directly determined by

the supernova rate as a function of time. Therefore, a precisely measured SRN spectrum would provide information on the supernova rate and related quantities, such as nucleosynthesis and the star formation history of the universe. Although the detection of the SRN would be interesting in its own right, such "neutrino cosmology" is the primary motivation for studying the SRN.

8.4 Concluding Remarks

The analysis presented in this thesis began in 1999. At that time, supernova relic neutrinos were an obscure topic in physics. The most recent journal publication of an experimental SRN result was over a decade old [36], and the number of theoretical papers produced in the same time interval was on the order of unity. Such a situation is hardly surprising, as the best upper bound on the SRN flux was two to three orders of magnitude higher than the few existing predictions.

The results presented in this thesis show that there is finally an operational experiment that is sensitive to certain SRN models. In response, interest in and awareness of the SRN is growing within the physics community [73]. New theoretical papers are being produced; some of these papers contain refined SRN models, while others place new constraints on the star formation rate that are based on the limits from this analysis [77]. Perhaps more importantly, new experimental techniques are being considered that may allow the remaining models to be probed within the next few years. Although this analysis did not detect supernova relic neutrinos, it may provide guidance for detectors that are capable of doing so.

The discussion in Section 8.3 is largely speculative. Neither UNO nor Hyper-Kamiokande have been approved for funding yet, nor have methods of enhancing them with neutron detection capabilities been proven. However, now that the means for detecting the SRN and measuring their energy spectrum are being actively considered, other ideas are likely to follow – hopefully one of them will be successful.

In the absence of a galactic supernova burst occurring in the near future, which no one can predict, the discovery of the SRN would only mark the second time that neutrinos from outside of this solar system have been detected, and the first such detection in approximately two decades. Furthermore, neutrino astronomy has recently gained recognition as a valuable method for probing the stars [78]. Precise measurements of the SRN energy spectrum would take neutrino science one step further, with neutrino cosmology being established as a tool for exploring the universe itself.

Appendix A

The LINAC Calibration System

A.1 Overview

An electron linear accelerator (LINAC) is used for various calibration purposes in Super-Kamiokande [47]. Such purposes include determining the absolute energy scale, measuring the effective velocity of Cherenkov photons, and obtaining the resolution of the detector for reconstructing energy, direction, and position.

The LINAC injects downward-going electrons of known energy into the SK tank. The momentum of these electrons is tunable, with a range of 5 MeV to 16 MeV. This range corresponds to the energy region of interest to solar neutrino studies; it also covers the lower energy range that is relevant to the SRN search.

LINAC data are collected at nine different positions in the SK tank, as shown in Figure A.1. These data are then used to set the detector response, which is compared to that of a Monte Carlo (MC) detector simulation. The MC is adjusted until its absolute energy scale agrees well with the calibration data. Once adjusted to the positions, energies, and single direction of the LINAC data, this MC is extrapolated to cover events in all directions throughout the entire detector. Remaining differences between LINAC data and the MC are used to determine systematic errors.

A.2 Hardware

The LINAC hardware is shown in Figures A.2 through A.5, The beam pipe at the right edge (or bottom) of each figure is connected to the beam pipe at the left edge (or top) of the following figure. Figure A.1 shows the location of this hardware relative to SK.

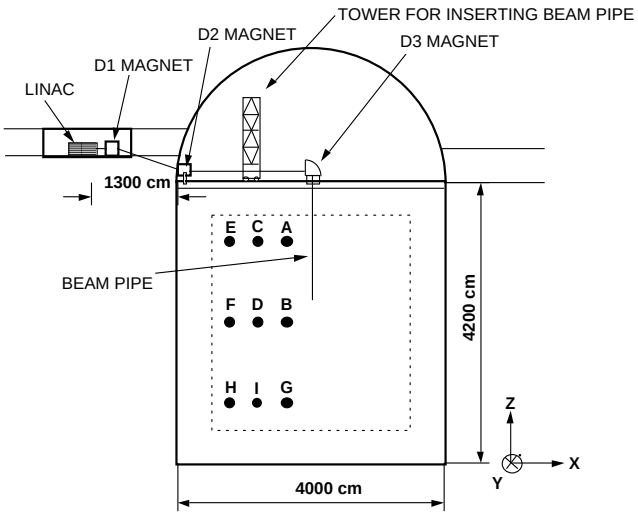

Figure A.1: The LINAC system at SK. The dashed line represents the fiducial volume of the detector and the black dots indicate the positions where LINAC data were taken.

The LINAC is a Mitsubishi model ML-15MIII that was originally used for medical purposes. At SK, a low-current electron gun was installed to control the electron flux entering the acceleration tube; for SK calibration, single electron levels are required.

Microwave pulses with a width of $\sim$2 μs are generated in a klystron; the pulse rate can be adjusted between 10 Hz and 66 Hz. Electrons from the electron gun are accelerated as they travel with the microwave in the accelerating tube. Once generated, the electron beam is sent into a magnetically shielded beam pipe that has been evacuated to $\sim 10^{-4}$ torr.

The average beam momentum is adjusted by changing the input power and frequency of the microwaves. A bending magnet (D1) is used to transform the spread in beam momentum into a spread in beam direction; a set of collimators around the D1 magnet are used to select mono-energetic electrons. After bending, the beam pipe passes through 9 m of rock, which shields the detector from radiation emitted by the electrons that have been filtered out. A second bending magnet (D2) restores the horizontal direction of the beam.

To enter the SK tank, the beam is bent 90° by the D3 magnet. The beam then enters the detector inside of a vertical beam pipe that has been inserted into the tank with a crane. Quadrupole magnets (Q1 and Q2) on either side of D3 focus the beam onto the end-cap of the beam pipe, which is shown in

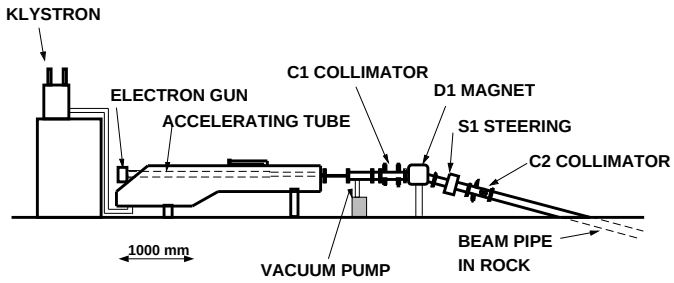

Figure A.2: The first bending magnet (D1) defines the beam momentum.

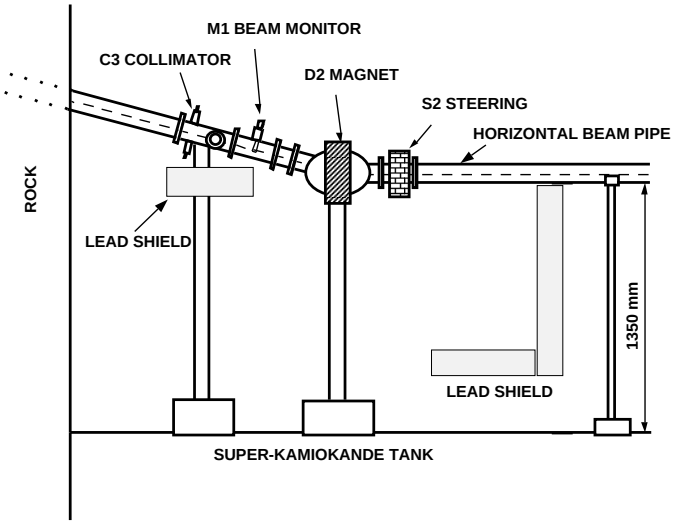

Figure A.3: The second bending magnet (D2) returns the beam to a horiztonal direction over the SK tank.

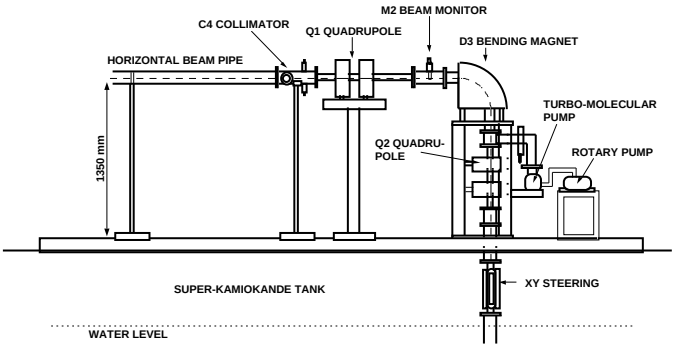

Figure A.4: The beam is focused (Q1, Q2 magnets), bent 90° (D3 magnet) and injected into the SK tank, where it is steered (X, Y magnets) to the center of the end-cap.

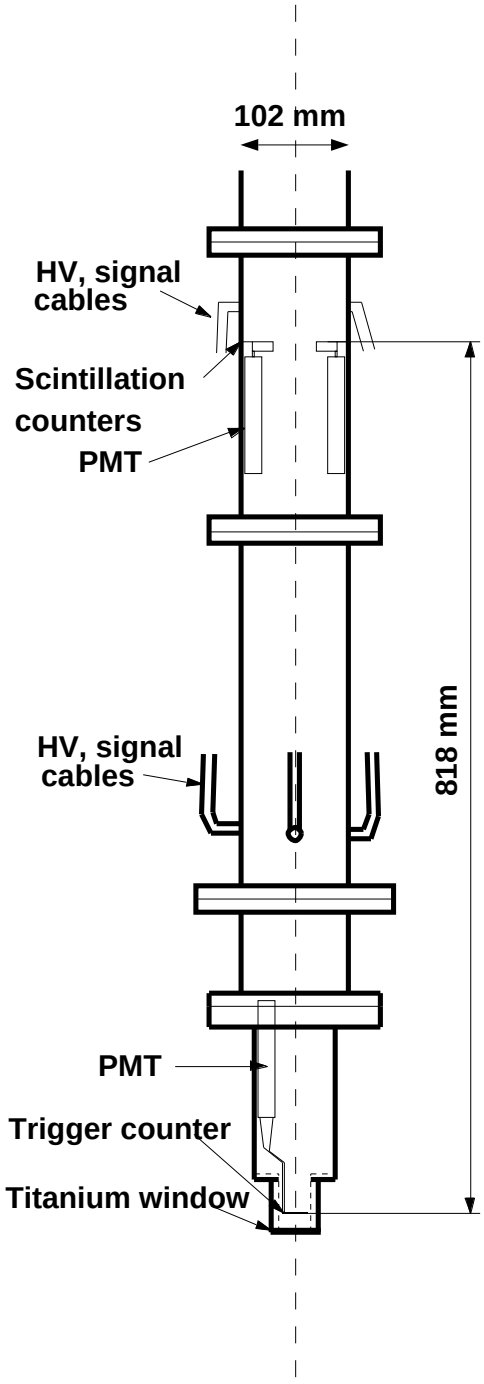

Figure A.5: The end-cap for the LINAC beam line. A scintillation counter located directly above the titanium window is used for triggering SK on LINAC events. Four additional scintillation counters assist in centering the beam within the pipe.

Figure A.5. Two steering magnets (X and Y) enable the beam to be manually steered to the center of the end-cap.

The LINAC end-cap is closed by a 100 μm thick titanium window, which allows electrons to pass through without significant momentum loss but prevents water from entering the beam pipe. The end-cap is composed of cylinders of decreasing radius in order to reduce shadowing by the beam pipe. Inside of the end-cap is a scintillation counter that serves to trigger SK when a LINAC electron leaves the beam pipe. In addition to the primary scintillation counter, four secondary counters are positioned 80 cm above the exit window. These register off-center electrons and are used to provide feedback that is useful for steering the LINAC beam.

A.3 Beam Energy Measurement

The energy of the electrons in the LINAC beam is measured with a germanium detector. The germanium detector is placed in front of a second titanium window that covers a horizontal segment of the beam pipe on top of the SK tank. After all of the LINAC data at a particular position has been accumulated, the current in the D3 magnet is turned off. Instead of entering the SK tank, the LINAC electrons enter the germanium detector.

The germanium in the detector is a coaxial ultra-pure crystal with a diameter of 57.5 mm and a length of 66.4 mm. To enter the detector, electrons must pass through a 500 μm beryllium window. The output from the germanium detector is digitized by a Seiko EG&G Multi-Channel Analyzer 7700 (MCA).

The germanium detector is calibrated with various γ-ray sources. The correlation between the peak MCA channel number and the γ-ray energy is linear to better than 99.98%. The energy resolution of the germanium detector is 1.92 keV, as measured with the 1.33 MeV γ-rays of ^{60}Co. To understand the response of the germanium detector to charged particles, a second calibration is performed using mono-energetic electrons produced by ^{207}Bi through an internal conversion process.

Monte Carlo simulations are made to model the beam energy loss in the titanium window, the beryllium window, and the 41 μm inactive region of the germanium detector. The LINAC beam momenta, as measured by the germanium detector, are shown in Figure A.6 and compared with the MC. The uncertainty in the beam energy is evaluated by comparing measurements at different x positions on top of the SK tank and found to be $\pm$20 keV. Table A.1 shows the D1 current values used in the LINAC calibration (first column), along with the corresponding beam energy measured in the germanium detec-

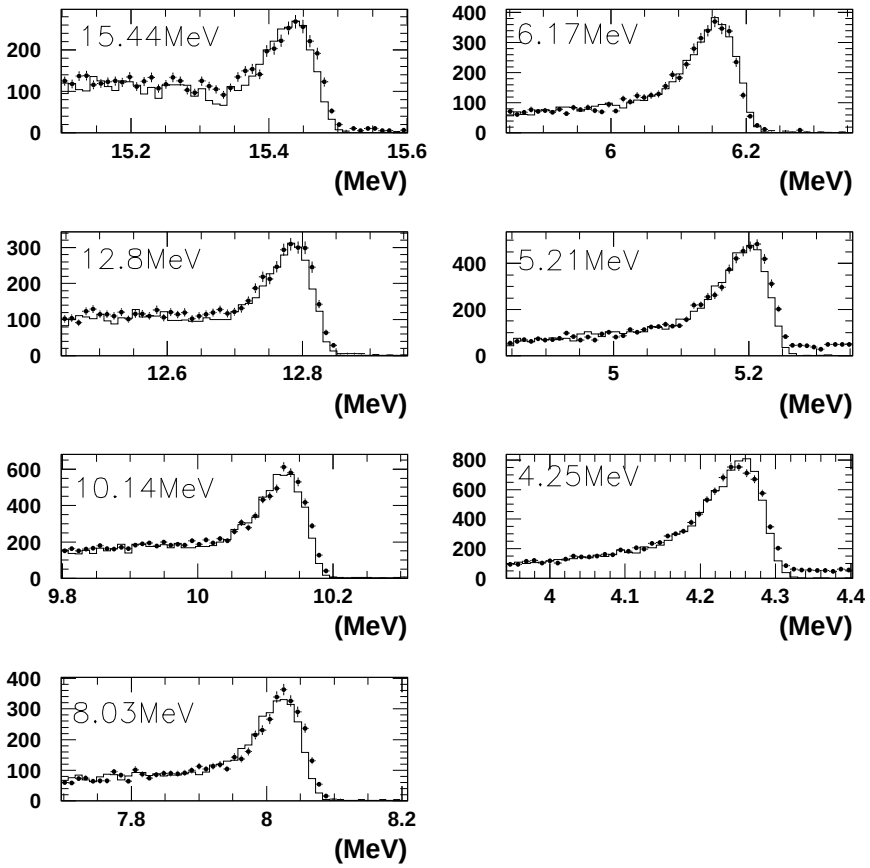

Figure A.6: The LINAC beam momenta, as measured by the Ge detector. The solid circles show the data, with statistical error bars, and the histograms represent the MC simulation [47].

D1 current (A)	Ge energy (MeV)	beam momentum (MeV/c)	SK tank energy (MeV)
1.8	4.25	5.08	4.89
2.15	5.21	6.03	5.84
2.5	6.17	7.00	6.79
3.2	8.03	8.86	8.67
4.0	10.14	10.99	10.78
5.0	12.80	13.65	13.44
6.0	15.44	16.31	16.09

Table A.1: D1 settings and associated beam momenta. The second column shows the energy measured in the Ge calibration system. The third and fourth columns, respectively, show the electron energy in the beam pipe and in the SK tank, both of which have been evaluated with the MC.

tor (second column). This measurement is used by the MC simulation to get a value for the energy of the electrons within the beam pipe (third column) and inside of the SK tank (fourth column).

A.4 Data Taking

LINAC data are taken at each of the nine positions shown in Figure A.1. For every position, data are taken at the seven momenta listed in Table A.1.

During LINAC calibration, beam spills occur at a rate of 60 Hz. The average occupancy at the beam pipe end-cap is set, by adjusting the voltage of the electron gun, to about 0.1 electrons/spill. This low occupancy minimizes the number of spills that contain multiple electrons. If a multiple electron event does occur, it is removed by the following cut: Using the position of the LINAC end-cap as the vertex, the time of flight is subtracted from each of the hit PMT times. The result is put into a histogram and checked for the number of peaks. Only events with single peaks are used for calibration. Figure A.7 shows timing distributions for single, double, and triple electron events.

The single-electron LINAC events are reconstructed with the same software as regular data. This software performs a vertex fit, a direction fit, and obtains an energy for the event, as described in Chapter 4. Figure A.8 is a two-dimensional scatterplot of the reconstructed vertexes for all of the LINAC events accumulated during one data taking session; the LINAC end-cap position is clearly visible.

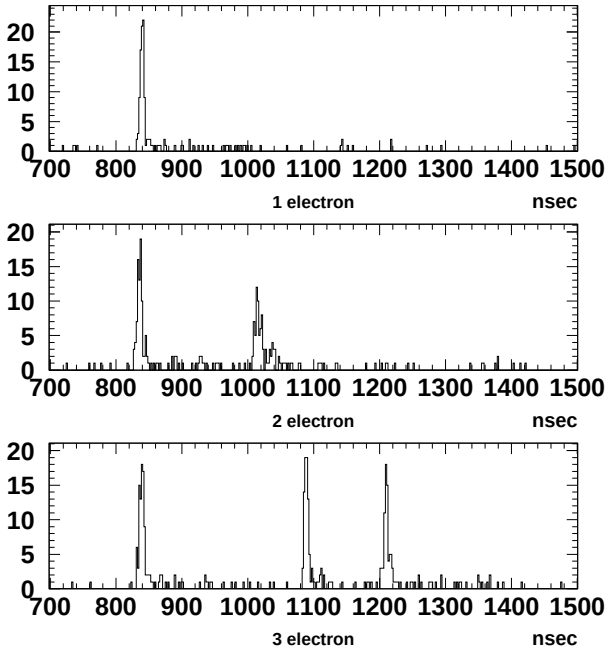

Figure A.7: The time-of-flight subtracted timing information for LINAC events containing one, two, and three electrons [47].

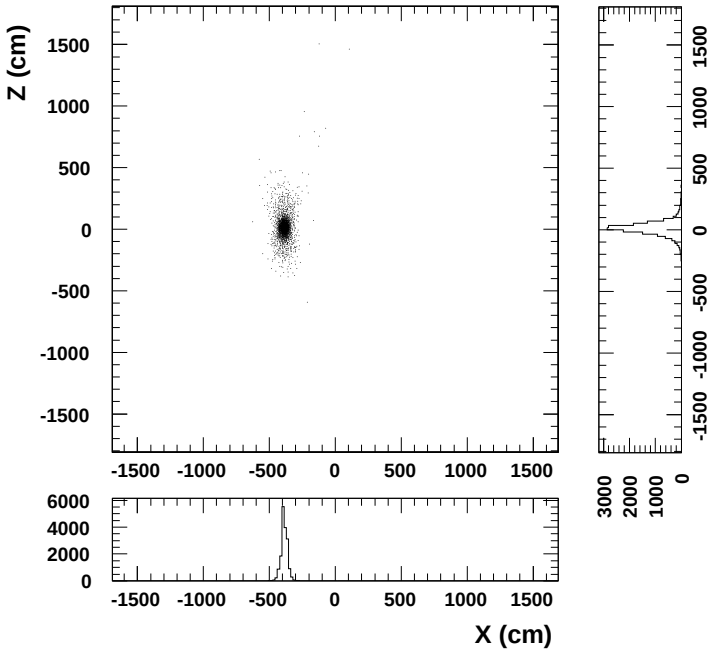

Figure A.8: A distribution of the reconstructed position of LINAC events. The LINAC end-cap was positioned at (x,z) = (-4 m, 0 m). Projections of the scatterplot to the x and z axis are shown [47].

Appendix B

Event Displays

In Chapter 5, event displays and TOF-subtracted timing distributions were shown for typical background events that had been removed by the data reduction process. It is also important to show what an actual SRN-induced event would look like in Super-Kamiokande; since no such events were detected, this can only be done by using SRN simulations. The simulated SRN events can be compared to the actual SRN candidates from the data, which are shown in Section B.2.

B.1 Simulated Events

The SK event display and the TOF-subtracted timing distributions from two Monte Carlo simulated SRN events are shown on the following two pages. In this analysis, the energy bin that is most likely to contain SRN-induced events extends from 18 MeV to 22 MeV. Thus, the two simulated events that were chosen have energies that bracket this range. Figure B.1 and Figure B.2 are for an 18.2 MeV SRN event; Figure B.3 and Figure B.4 are for a 21.9 MeV SRN event.

B.2 Data Events

As shown in Figure 7.1, the final data sample contains six events in the 18 – 22 MeV energy bin. The irreducible background shape fits the energy spectrum well, so none of these events appear to have been created by SRN interactions. Nevertheless, for the purpose of comparison, the SK event displays and TOF-subtracted timing distributions are shown for all six of these SRN candidates (see Figure B.5 through Figure B.16).

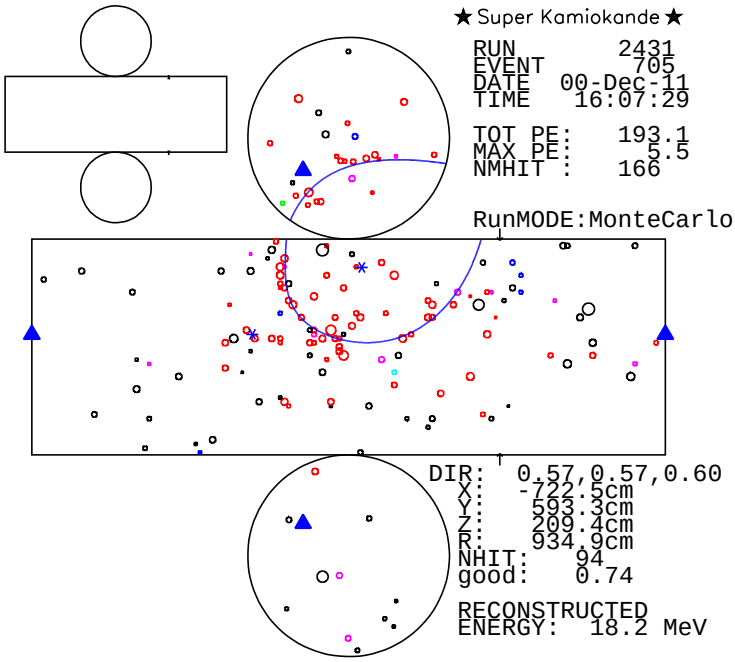

Figure B.1: The SK event display is shown for a simulated SRN event that reconstructed with 18.2 MeV of energy. The reconstructed vertex is listed, and the fit Cherenkov ring is superimposed on the event display.

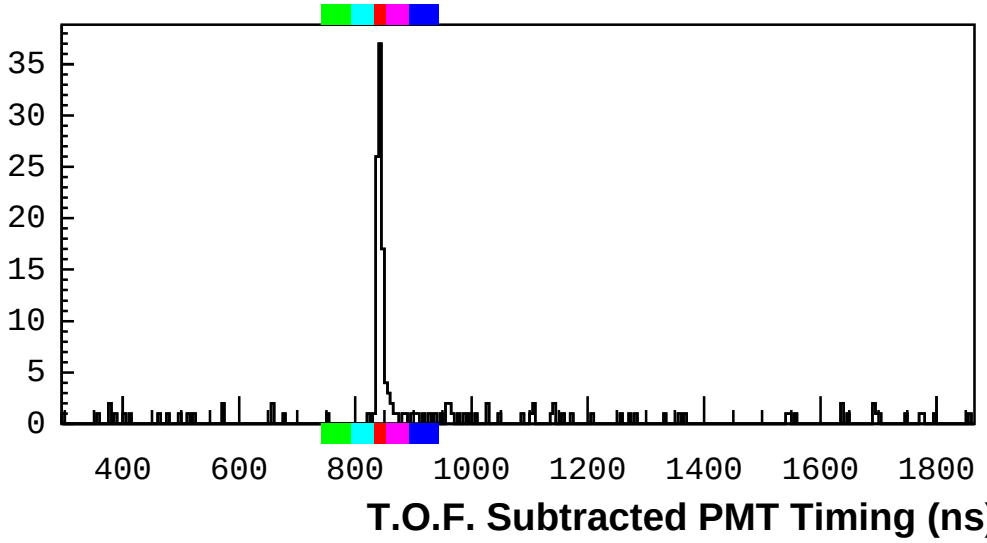

Figure B.2: The TOF-subtracted timing distribution is shown for the event displayed in the previous figure.

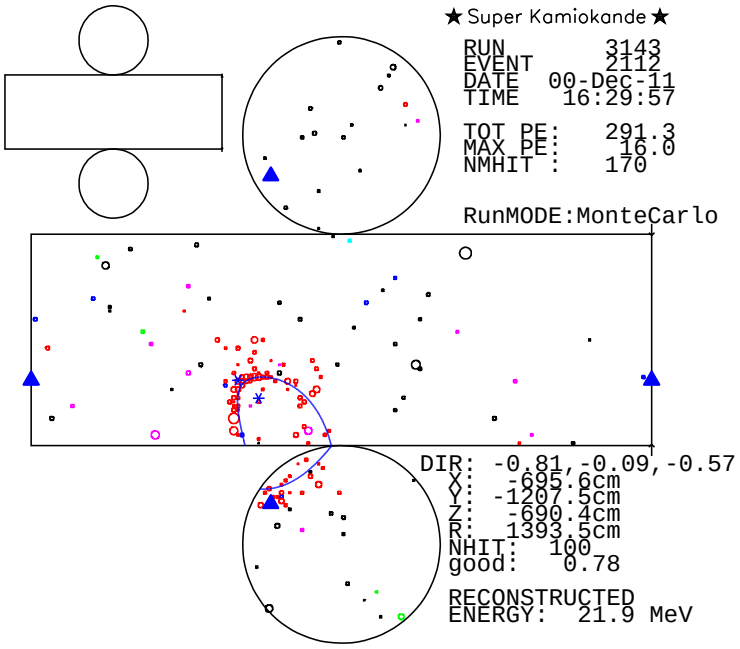

Figure B.3: The SK event display is shown for a simulated SRN event that reconstructed with 21.9 MeV of energy. The reconstructed vertex is listed, and the fit Cherenkov ring is superimposed on the event display.

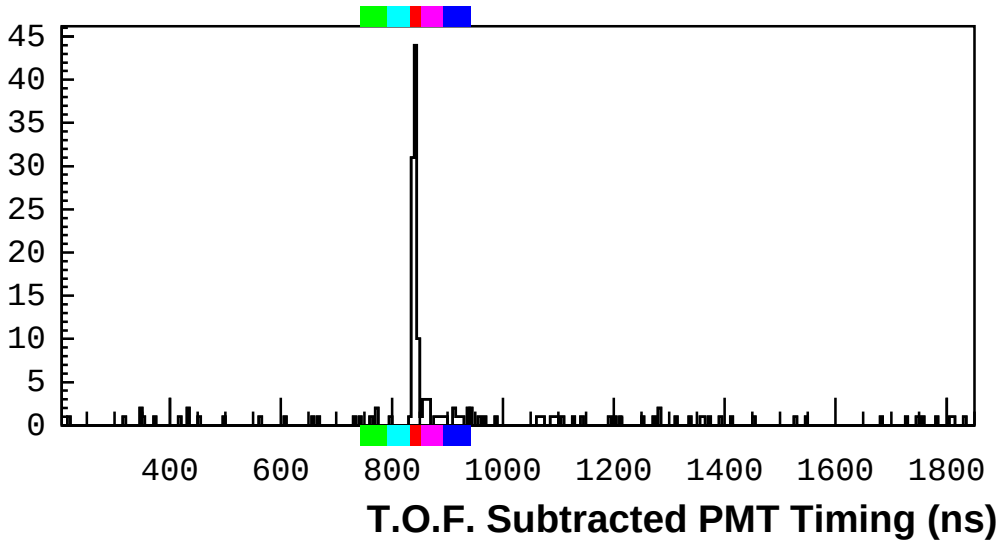

Figure B.4: The TOF-subtracted timing distribution is shown for the event displayed in the previous figure.

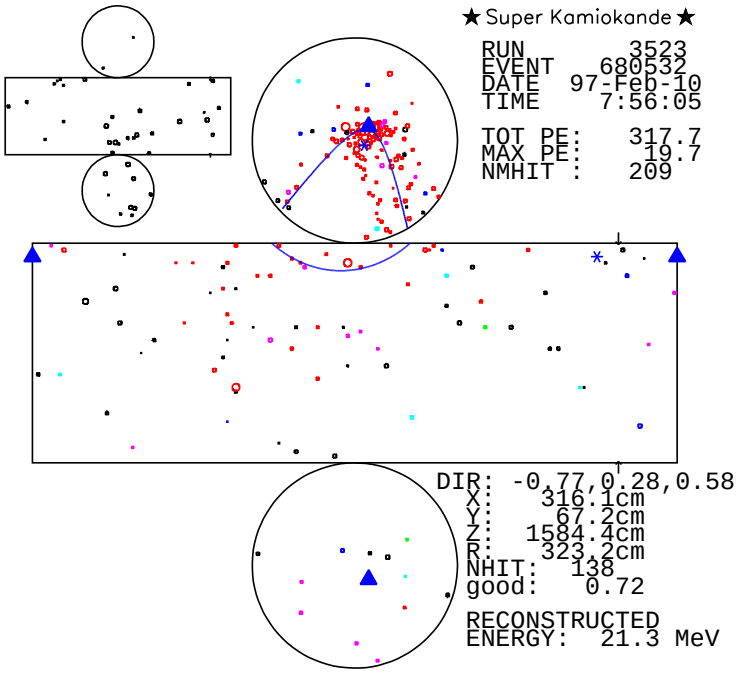

Figure B.5: The SK event display is shown for an SRN candidate event that reconstructed with 21.3 MeV of energy. The reconstructed vertex is listed, and the fit Cherenkov ring is superimposed on the event display.

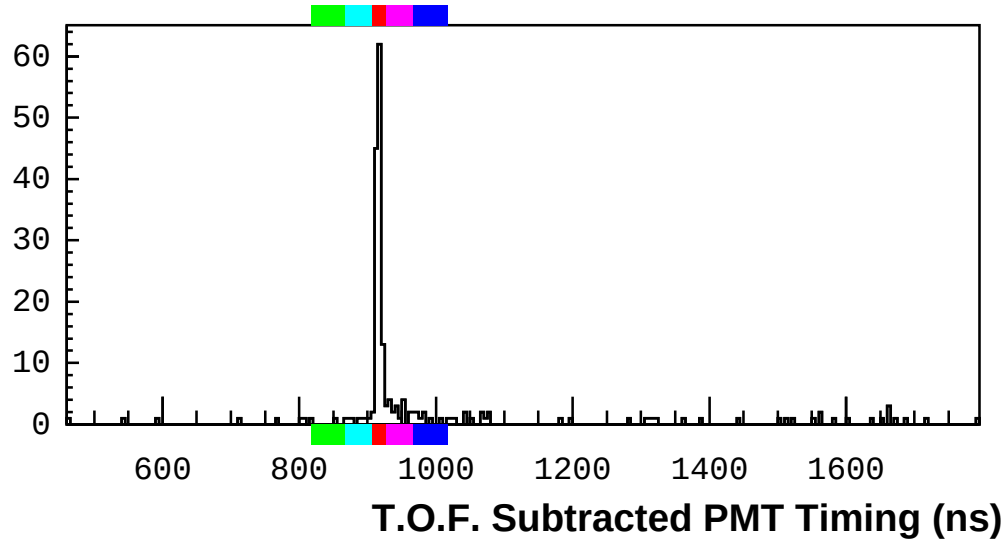

Figure B.6: The TOF-subtracted timing distribution is shown for the event displayed in the previous figure.

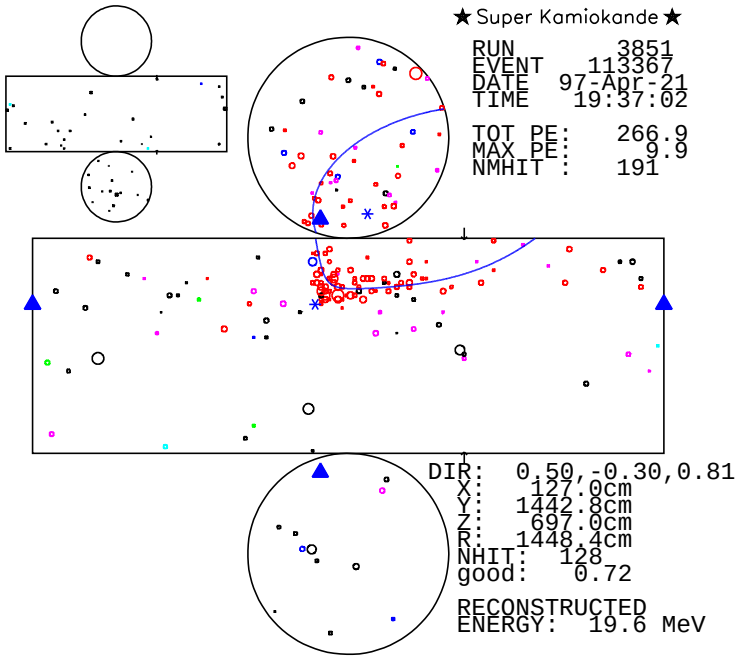

Figure B.7: The SK event display is shown for an SRN candidate event that reconstructed with 19.6 MeV of energy. The reconstructed vertex is listed, and the fit Cherenkov ring is superimposed on the event display.

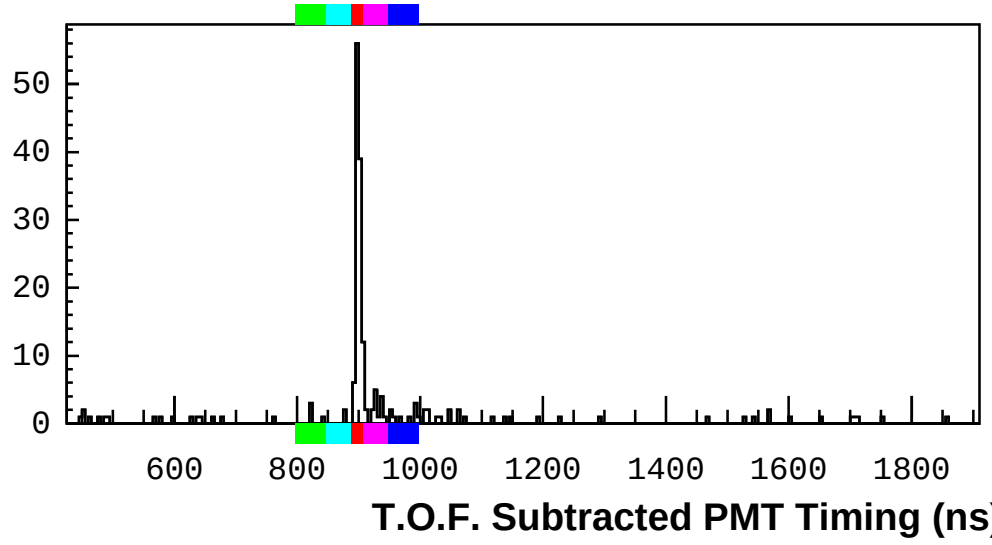

Figure B.8: The TOF-subtracted timing distribution is shown for the event displayed in the previous figure.

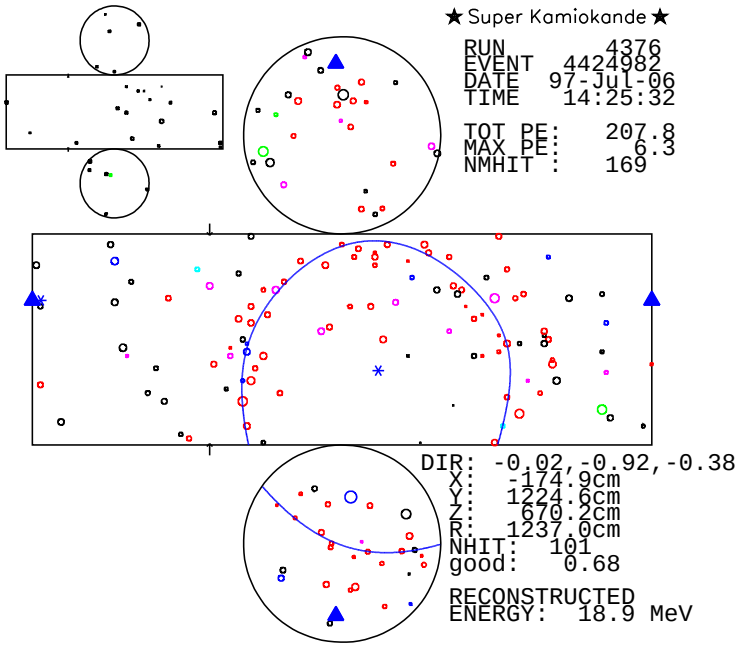

Figure B.9: The SK event display is shown for an SRN candidate event that reconstructed with 18.9 MeV of energy. The reconstructed vertex is listed, and the fit Cherenkov ring is superimposed on the event display.

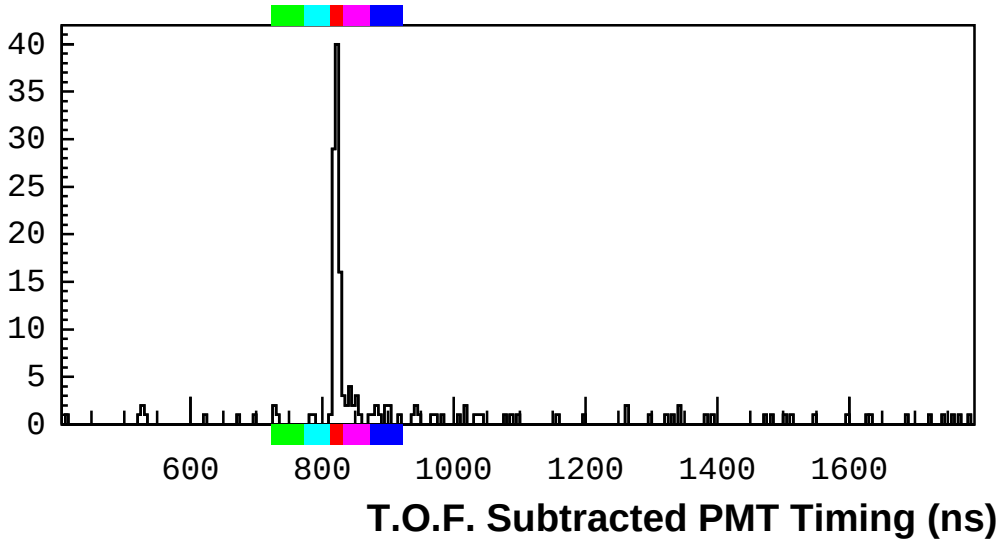

Figure B.10: The TOF-subtracted timing distribution is shown for the event displayed in the previous figure.

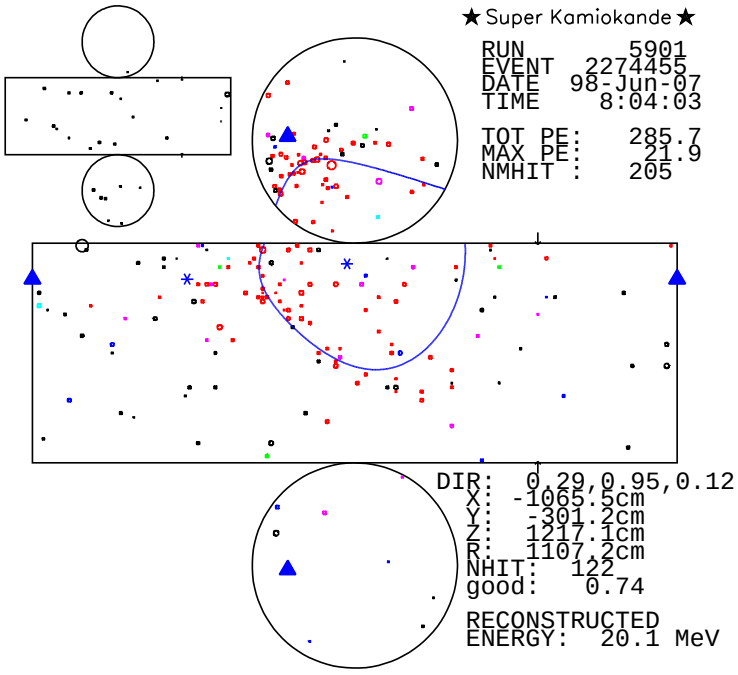

Figure B.11: The SK event display is shown for an SRN candidate event that reconstructed with 20.1 MeV of energy. The reconstructed vertex is listed, and the fit Cherenkov ring is superimposed on the event display.

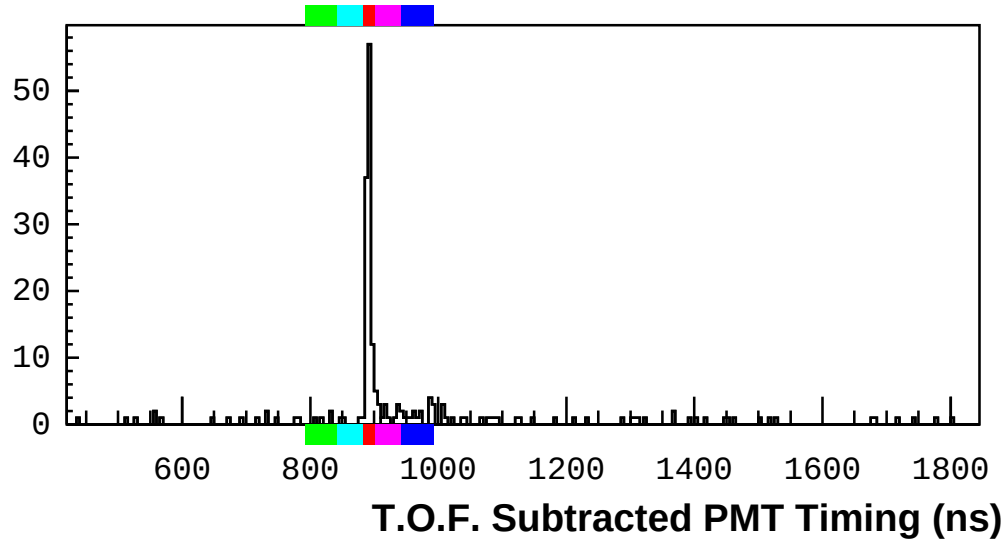

Figure B.12: The TOF-subtracted timing distribution is shown for the event displayed in the previous figure.

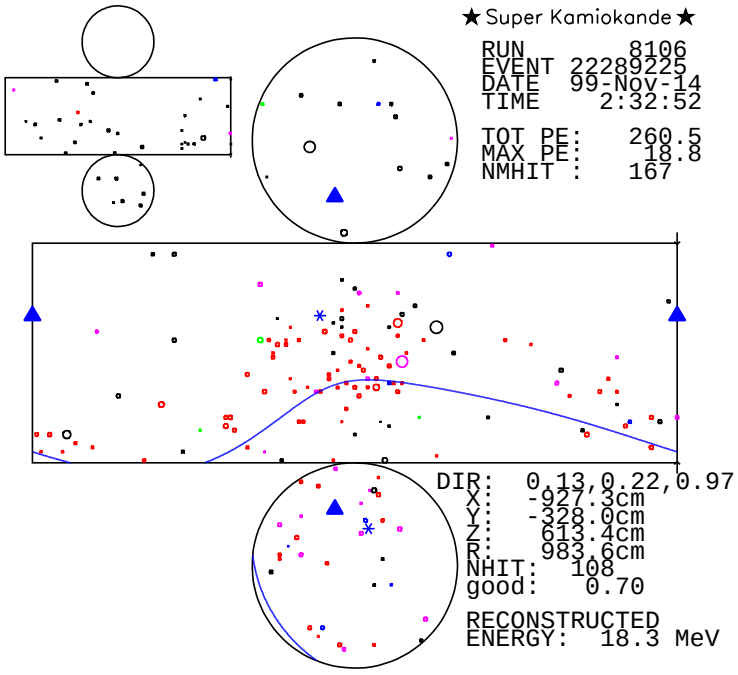

Figure B.13: The SK event display is shown for an SRN candidate event that reconstructed with 18.3 MeV of energy. The reconstructed vertex is listed, and the fit Cherenkov ring is superimposed on the event display.

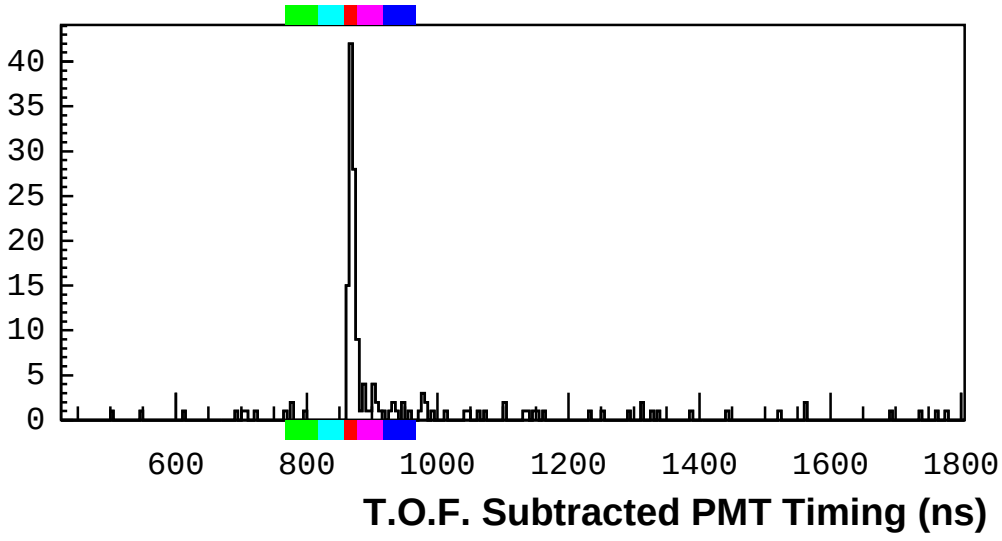

Figure B.14: The TOF-subtracted timing distribution is shown for the event displayed in the previous figure.

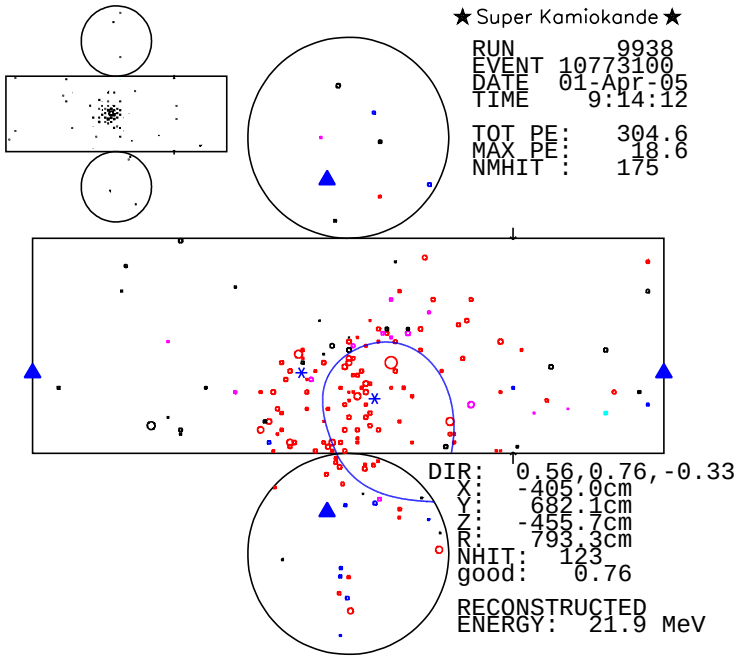

Figure B.15: The SK event display is shown for an SRN candidate event that reconstructed with 21.9 MeV of energy. The reconstructed vertex is listed, and the fit Cherenkov ring is superimposed on the event display.

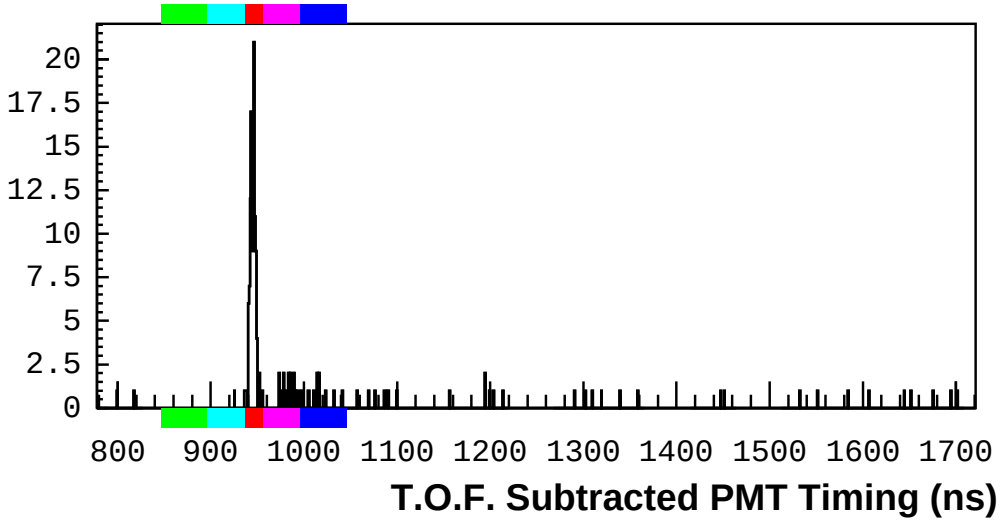

Figure B.16: The TOF-subtracted timing distribution is shown for the event displayed in the previous figure.

Bibliography

[1] K.S. Hirata *et al.* [The Kamiokande Collaboration], Phys. Rev. Lett. **58**, 1490 (1987).

[2] R.M. Bionta *et al.* [The IMB Collaboration], Phys. Rev. Lett. **58**, 1494 (1987).

[3] K.S. Hirata *et al.* [The Kamiokande Collaboration], Phys. Rev. D **38**, 448 (1988).

[4] C.B. Bratton *et al.* [The IMB Collaboration], Phys. Rev. D **37**, 3361 (1988).

[5] D. Arnett, *Supernovae and Nucleosynthesis: An Investigation of The History of Matter, From the Big Bang to the Present.* Princeton University Press (1996).

[6] J. N. Bahcall, *Neutrino Astrophysics.* Cambridge University Press (1989).

[7] T. Padmanabhan, *Theoretical Astrophysics, Volume II: Stars and Stellar Systems.* Cambridge University Press (2001).

[8] H. Suzuki, from *Physics and Astrophysics of Neutrinos* p. 763 (1994).

[9] S. E. Woosley *et al.*, Astrophys.J. **433** 229 (1994).

[10] T. Totani *et al.*, Astrophys.J. **496**, 216 (1998).

[11] K. Takahashi, M. Watanabe, and K. Sato, Phys. Lett. B **510**, 189 (2001).

[12] J. F. Beacom and P. Vogel, Phys. Rev. D **60**, 033007 (1999).

[13] J. F. Beacom, R. N. Boyd, and A. Mezzacappa, Phys. Rev. D **63**, 073011 (2001).

[14] K. Langanke, P. Vogel, and E. Kolbe, Phys. Rev. Lett. **76**, 2629 (1996).

[15] D. N. Schramm and J. W. Truran, Phys. Rep. **189**, 89 (1990).

[16] G. S. Bisnovatyi-Kogan, S. F. Seidov, Ann. N.Y. Acad. Sci. **422**, 319 (1984).

[17] L. M. Krauss, S. L. Glashow, and D. N. Schramm, Nature **310**, 191 (1984).

[18] S. E. Woosley, J. R. Wilson, and R. Mayle, Astrophys. J. **302**, 19 (1986).

[19] T. Totani and K. Sato, Astropart. Phys. **3**, 367 (1995).

[20] T. Totani, K. Sato, and Y. Yoshii, Astrophys. J. **460**, 303 (1996).

[21] R. A. Malaney, Astropart. Phys. **7**, 125 (1997).

[22] D. H. Hartmann and S. E. Woosley, Astropart. Phys. **7**, 137 (1997).

[23] M. Kaplinghat, G. Steigman, and T. P. Walker, Phys. Rev. D **62**, 043001 (2000).

[24] S. Ando, K. Sato, and T. Totani, Astropart. Phys. **18**, 307 (2003).

[25] L. Wolfenstein, Phys. Rev. D **17**, 2369 (1978).

[26] S. P. Mikheyev, A. S. Smirnov, Sov. J. Nucl. Phys. **42**, 913 (1985).

[27] Y. Fukuda *et al.* [The Super-Kamiokande Collaboration], Phys. Rev. Lett. **81**, 1562 (1998).

[28] S. Fukuda *et al.* [The Super-Kamiokande Collaboration], Phys. Rev. Lett. **86**, 5651 (2001).

[29] Q. R. Ahmad *et al.* [The SNO Collaboration], Phys. Rev. Lett. **87**, 071301 (2001).

[30] A. S. Dighe and A. Y. Smirnov, Phys. Rev. D **62**, 033007 (2000).

[31] C. Lunardini and A. Y. Smirnov, Phys. Rev. D **63**, 073009 (2001).

[32] S. Fukuda *et al.* [The Super-Kamiokande Collaboration], Phys. Rev. Lett. **86**, 5656 (2001).

[33] S. Fukuda *et al.* [The Super-Kamiokande Collaboration], Phys. Lett. B **539**, 179 (2002).

[34] Q. R. Ahmad *et al.* [The SNO Collaboration], Phys. Rev. Lett. **89**, 011302 (2002).

[35] K. Eguchi *et al.* [The KamLAND Collaboration], Phys. Rev. Lett. **90**, 021802 (2003)

[36] W. Zhang *et al.* [The Kamiokande Collaboration], Phys. Rev. Lett. **61**, 385 (1988)

[37] K. S. Hirata, *Search for Supernova Neutrinos at Kamiokande-II* PhD thesis, University of Tokyo (1991).

[38] M. Morii, *Search for relic neutrinos from past supernovae in Super-Kamiokande* Masters thesis, Tokyo Institute of Technology (2001).

[39] J. D. Jackson, *Classical Electrodynamics, Second Edition.* John Wiley & Sons (1975).

[40] E. Segrè, *Nuclei and Particles, Second Edition.* Benjamin/Cummings Publishing Company (1977).

[41] S. Fukuda *et al.* [The Super-Kamiokande Collaboration], Nucl. Instrum. Methods Phys. Res. Sect. A **501**, 418 (2003).

[42] Y. Takeuchi *et al.* [The Super-Kamiokande Collaboration], Phys. Lett. **452**, 418 (1999).

[43] C. Mitsuda *et al.*, Nucl. Instrum. Methods Phys. Res. A **497**, 414 (2003).

[44] KEK Data Acquisition Development Working Group, *TKO Specification*, KEK Report 85-10 (1985).

[45] *The ZEBRA Systen*, CERN Program Library Long Writeups Q100/Q101.

[46] Z. Conner, *A Study of Solar Neutrinos Using the Super-Kamiokande Detector* PhD thesis, University of Maryland (1997).

[47] M. Nakahata *et al.* [The Super-Kamiokande Collaboration], Nucl. Instrum. Methods Phys. Res. Sect. A **421**, 113 (1999).

[48] T. Suzuki, D. F. Measday, and J. P. Roalsvig, Phys. Rev. C **35**, 2212 (1987).

[49] E. Blaufuss *et al.* [The Super-Kamiokande Collaboration], Nucl. Instrum. Methods Phys. Res. Sect. A **458**, 638 (2001).

[50] A. Suzuki *et al.* [The Kamiokande Collaboration], Nucl. Instrum. Methods Phys. Res. Sect. A **329**, 299 (1993).

[51] C. Michael Lederer and Virginia S. Shirly, *Table of Isotopes*. John Wiley & Sons.

[52] H. Ishino, *Measurement of the Solar Neutrino Spectrum at Super-Kamiokande* PhD thesis, University of Tokyo (1999).

[53] N. Sakurai, *Constrains of the Neutrino Oscillation Parameters from 1117 Day Observation of Solar Neutrino Day and Night Spectra in Super-Kamiokande* PhD thesis, University of Tokyo (2000).

[54] J. Kameda, *Detailed Studies of Neutrino Oscillation with Atmospheric Neutrinos of Wide Energy Range from 100 MeV to 1000 GeV in Super-Kamiokande* PhD Thesis, University of Tokyo (2002).

[55] K. Hagiwara *et al.*, Phys. Rev. D **66**, 010001 (2002).

[56] J. F. Beacom and S. Palomares-Ruiz, Phys.Rev. D **67**, 093001 (2003).

[57] J. N. Bahcall, M. H. Pinsonneault, and S. Basu Astrophys. J. **555**, 990 (2001).

[58] P. Vogel and J. F. Beacom, Phys. Rev. D **60**, 053003 (1999).

[59] M. Honda *et al.*, Phys. Rev. D **52**, 4985 (1995).

[60] V. Agrawal *et al.*, Phys. Rev. D **53**, 1314 (1996).

[61] *GEANT Detector Description and Simulation Tool*, CERN Program Library W5013 (1994).

[62] A. Morel *et al.*, Limnology and Oceanography **22**, 709 (1977).

[63] Y. Koshio, *Study of Solar Neutrinos at Super-Kamiokande* PhD thesis, University of Tokyo (1998).

[64] S. Fukuda *et al.* [The Super-Kamiokande Collaboration], Phys. Rev. Lett. **85**, 3999 (2000).

[65] Y. Fukuda *et al.* [The Super-Kamiokande Collaboration], Phys. Lett. B **433**, 9 (1998).

[66] M. Malek *et al.* [The Super-Kamiokande Collaboration], Phys. Rev. Lett. **90**, 061101 (2003).

[67] T. Totani, Private communication (2000).

[68] W. D. Arnett, D. N. Schramm, and J. W. Truran, Astrophys. J. **339**, L25 (1989).

[69] J. F. Beacom and M. R. Vagins, paper in preparation

[70] G. Guillian, Private communication (2003).

[71] The Sudbury Neutrino Observatory (SNO) Homepage, http://www.sno.phy.queensu.ca/

[72] M. R. Vagins, Presentation at the Fourth Workshop on Neutrino Oscillations and their Origin: *Future Detection of Supernovas* (2003).

[73] J. F. Beacom, Presentation at the Eighth Conference on the Intersection of Particle and Nuclear Physics: *Particle and Nuclear Astrophysics* (2003).

[74] C. K. Jung, *Feasibility of a Next Generation Underground Water Cherenkov Detector: UNO*, Proceedings from the Next Generation Nucleon Decay and Neutrino Detector Workshop (2000).
E-print archive: hep-ex/0005046.

[75] *Physics Potential and Feasibility of UNO*, Stony Brook preprint SBHEP01-3 (2001). Available from http://nngroup.physics.sunysb.edu/

[76] K. Nakamura, Presentation at the October 2002 UNO Collaboration Meeting: *Hyper-Kamiokande R & D* (2002). Available from http://superk.physics.sunysb.edu/uno/uno-meeting/collab_oct02_talks/

[77] M. Fukugita and M. Kawasaki, Mon. Not. R. Astron. Soc. **340**, L7 (2003).

[78] The Official Web Site of The Nobel Foundation, http://www.nobel.se/physics/laureates/2002/press.html (2002).